HIGH-STRENGTH STAINLESS STEELS FOR CORROSION MITIGATION IN PRESTRESSED CONCRETE: DEVELOPMENT AND EVALUATION

A Dissertation
Presented to
The Academic Faculty

by

Robert D. Moser

In Partial Fulfillment
of the Requirements for the Degree
Doctor of Philosophy in the
School of Civil & Environmental Engineering

Georgia Institute of Technology

August 2011

HIGH-STRENGTH STAINLESS STEELS FOR CORROSION MITIGATION IN PRESTRESSED CONCRETE: DEVELOPMENT AND EVALUATION

Approved by:

Dr. Lawrence F. Kahn, Co-Advisor
School of Civil & Environmental Engineering
Georgia Institute of Technology

Dr. Kimberly E. Kurtis, Co-Advisor
School of Civil & Environmental Engineering
Georgia Institute of Technology

Dr. Preet M. Singh
School of Materials Science & Engineering
Georgia Institute of Technology

Dr. David W. Scott
School of Civil & Environmental Engineering
Georgia Institute of Technology

Dr. Paul G. Allison
Geotechnical & Structures Laboratory
U.S. Army Engineer Research and Development Center

Date Approved: April 29th, 2011

It so happens that the work which is likely to be our most durable monument and to convey some knowledge of us to the most remote posterity is a work of bare utility; not a shrine, not a fortress, not a palace, but a bridge.

-Montgomery Schuyler, "The Bridge as a Monument," Harper's Weekly, 1883

ACKNOWLEDGEMENTS

I would first like to express my utmost gratitude to my advisors, Dr. Lawrence F. Kahn, Dr. Kimberly E. Kurtis, and Dr. Preet M. Singh. I am truly fortunate to have had the opportunity to work on a novel topic with a group of such talented and sincere individuals who allowed me to carve my own path for this research. Dr. Kahn: I thank you for pushing me to strive for excellence and to always consider the practicality of my work. Dr. Kurtis: I thank you for getting me involved with research and for telling me to "chill out" every once in a while. Dr. Singh: I thank you for getting me acquainted with the field of corrosion and for never hesitating to sit down and talk about research and life.

Thesis committee members Dr. David W. Scott and Dr. Paul G. Allison also deserve many thanks for reading this dissertation, providing their useful insights, and always being helpful in answering any questions I had.

The bulk of this research project was funded by the Georgia Department of Transportation (GDOT) under research project number 07-70. I am also grateful for the financial assistance provided by the U.S. Department of Defense through its SMART Scholarship Program, the Georgia Tech Presidential Fellowship, the American Concrete Institute (ACI), the Georgia Chapter of ACI, and the NACE Foundation

This work would not have been possible without the assistance of Bill McClenathan, Jon Cornerlius, Brian Burr, and Chetan Patel of Sumiden Wire Products Corporation and Stig Forsberg of Fagersta Stainless. Their donation of materials and time to this research and willingness to answer my seemingly endless stream of questions is what truly made this research project a success.

I would like to acknowledge Jamshad Mahmood for helping with experimental setups and operation of equipment. Thanks also go to Jeremy Mitchell for all of his help through the years at the structures lab and our many light-hearted discussions. I would also like to thank Andy Udell and Mike Sorensen for their help with fabricating experimental setups and test specimens. Undergraduate research assistant Daniel Schuetz is thanked for his countless hours of valuable work fabricating specimens, polishing specimens, and testing specimens. Brett Holland must also be recognized for his contributions to understanding the durability of prestressed concrete bridge structures.

I would also like to acknowledge many mentors, colleagues, and friends who have been instrumental in my completion of this journey. I doubt I would be here today without the guidance of my Young Harris College calculus and physics professors, Dr. Bob Nichols and Dr. Hartmut Ramm, who urged me to further my education at Georgia Tech. Thanks also to my Hiawassee neighbors, Ed and Virginia Reynolds, who always told me that my future was brighter than cutting grass and doing trim carpentry.

In my time at Georgia Tech, my Mason 507 officemates Amal Jayapalan, Dr. Victor Garas, Dr. Jun Chen, Lisa Lindquist Hoeke, Chris Shearer, Bo Yeon Lee, Sarah Fredrich, and Bradley Dolphyn have always been a source of encouragement. I truly believe that I was blessed to be part of one of the most kind and welcoming research groups at Georgia Tech. Thanks also to Dr. Jonathan Hurff, Kevin Chasse, Lindsey Goodman, Di Yang, Andrew Bechtel, Dr. Benjamin Kosbab, Dr. Andrea Mezencevova, Dr. Kennan Crane, Dr. Xiaoyuan Lou, Jonah Kurth, Curtis O'Malley, Andrea Rose, Katherine Snedeker, Jennifer Dunbeck, and countless others who have been an invaluable part of my studies at Georgia Tech. I would be remiss in not thanking friends Kevin

Smith, Dr. Jonathan Hurff, Anthony Bentivegna, Chris Putman, Andrew and Anna Bechtel, James Torrance, Michael Holland, Dr. Benjamin Kosbab, Justin Cooner, Liz Kramer, Lauren DeBacker, Christine Chaney, Brett Holland, and Michael Jones for being an invaluable part of my life outside of Georgia Tech.

Most importantly, I must thank my parents, Calvin and MaryAnn Browning, and my brother, Stephen Moser, for their unending love and encouragement. The lives you lead and the sacrifices you make have taught me the values of hard work, dedication, and compassion which have become the foundation of who I am today.

TABLE OF CONTENTS

LIST OF TABLES

LIST OF FIGURES

LIST OF SYMBOLS AND ABBREVIATIONS

$\%_{red}$	Area reduction by cold drawing
A_{10}	Percent strain over 100 mm (4 in) gage length
A416	Prestressing strand conforming to ASTM A416
ACI	American Concrete Institute
AFRP	Aramid fiber reinforced polymer
ASTM	American Society for Testing and Materials
BCC	Body centered cubic crystal structure
CFRP	Carbon fiber reinforced polymer
CPP	Cyclic potentiodynamic polarization
CRR	Corrosion-resistant reinforcement
C_S	Surface Cl^- concentration
C_T	Cl^- threshold level (CTL)
CTL	Chloride threshold level
C_{Ts}	CTL of prestressing strand
C_{Tw}	CTL of prestressing wire
D	Cl^- diffusion coefficient or wire diameter
d_{rod}	Diameter of stainless steel rod coil
d_{wire}	Diameter of stainless steel wire
E	Elastic modulus or electrochemical potential
EAC	Environmentally assisted cracking
$E_{breakdown}$	Potential at which passive film breaks down

E_{corr}	Open circuit potential
EDX	Energy dispersive X-ray spectroscopy
f	AC frequency during induction heating
FCC	Face centered cubic crystal structure
FHWA	Federal Highway Administration
FRP	Fiber reinforced polymer
GDOT	Georgia Department of Transportation
HCP	Hydrated cement paste
HE	Hydrogen embrittlement
HPC	High performance concrete
HSSS	High-strength stainless steel
I	Corrosion current
i	Corrosion current density
J	Cl^- flux during diffusion
LDX	Lean duplex stainless steel
NACE	National Association of Corrosion Engineers
OCP	Open circuit potential
PREN	Pitting resistance equivalency number
PSC	Prestressed concrete
RC	Reinforced concrete
R_m	Ultimate tensile strength
SCC	Stress corrosion cracking
SCE	Saturated calomel reference electrode

SCM	Supplementary cementitious material
SEM	Scanning electron microscopy
SFE	Stacking fault energy
SHE	Standard hydrogen reference electrode
SSRT	Slow strain rate test
SWPC	Sumiden Wire Products Corporation
UHPC	Ultra-high performance concrete
UTS	Ultimate tensile strength
w/cm	Water-to-cementitious materials ratio
XRD	X-ray diffraction
Z	Reduction in area at fracture surface
α'	Strain-induced martensite
γ	Austenite phase of steel
δ	Ferrite phase of steel
ΔA	Reduction in area at fracture surface
ΔG	Gibb's free energy
ϵ_{ult}	Ultimate strain
μ_r	Relative magnetic permeability
ρ	Electrical resistivity
σ_{ult}	Ultimate tensile strength
σ_y	Yield strength by 0.2 % offset or 1 % yield criterion
$R_{p0.2}$	Yield strength by 0.2 % offset criterion
μ_o	Magnetic permeability of free space ($4\pi \cdot 10^{-7}$ N/A^2)

SUMMARY

Corrosion of prestressing reinforcement in concrete structures exposed to marine environments and/or deicing chemicals is a problem of critical concern. While many corrosion mitigation technologies are available for reinforced concrete (RC), those available for use in prestressed concrete (PSC) are limited and in many cases cannot provide the 100+ year service life needed in new construction, particularly when exposed to severe marine environments.

The use of stainless steel alloys in RC structures has shown great success in mitigating corrosion in even the most severe of exposures. However, the use of high-strength stainless steels (HSSSs) for corrosion mitigation in PSC structures has received limited attention. To address these deficiencies in knowledge, an experimental study was conducted to investigate the feasibility of using HSSSs for corrosion mitigation in PSC. The study examined mechanical behavior, corrosion resistance, and techniques for the production of HSSS prestressing strands. Stainless steel grades 304, 316, 2101, 2205, 2304, and 17-7 were produced as cold drawn wires with diameters of approximately 4 mm (0.16 in). A 1080 prestressing steel was also included to serve as a control.

Tensile strengths of 1250 to 1550 MPa (181 to 225 ksi) were achieved in the cold-drawn candidate HSSSs. Non-ductile failure modes with no post-yield strain hardening were observed in all candidate HSSSs. 1000 hr stress relaxation of all candidate HSSSs was predicted to be between 6 and 8 % based on the results of 200 hr tests conducted at 70 % of the ultimate tensile strength. Residual stresses due to the cold drawing had a significant influence on stress vs. strain behavior and stress relaxation.

Electrochemical corrosion testing found that in solutions simulating alkaline concrete, all candidate HSSSs showed exceptional corrosion resistance at chloride (Cl^-) concentrations from zero to 0.25 M. However, when exposed to solutions simulating carbonated concrete, corrosion resistance was reduced and the only candidate HSSSs with acceptable corrosion resistance were duplex grades 2205 and 2304, with 2205 being resistant to corrosion initiation at Cl^- concentrations of up to 1.0 M (twice the Cl^- concentration in seawater). A strong correlation between microstructural defects and corrosion damage was observed in the heavily cold-drawn HSSSs. Based on these results, duplex grades 2205 and 2304 were identified as optimal HSSSs and were included in additional studies which found that: (1) 2304 is susceptible to corrosion when tested in a stranded geometry, (2) 2205 and 2304 are not susceptible to stress corrosion cracking, and (3) 2205 and 2304 are susceptible to hydrogen embrittlement.

Efforts focused on the production of 2205 and 2304 prestressing strands showed that they could be produced as strands using existing ASTM A416 prestressing strand production facilities. Due to the ferromagnetic properties of 2205 and 2304, a low-relaxation heat treatment to reduce stress relaxation and improve mechanical properties was also found to be feasible.

The overall conclusion of the study was that HSSSs, especially duplex grades 2205 and 2304, show excellent promise to mitigate corrosion if utilized as prestressing reinforcement in PSC structures exposed to severe marine environments.

CHAPTER 1

INTRODUCTION

1.1 Research Purpose and Objectives

The purpose of this research was to investigate the feasibility of using high-strength stainless steels (HSSSs) as corrosion-resistant reinforcement in prestressed concrete (PSC) bridge substructures exposed to marine environments. The ultimate goals of the study were to identify optimal HSSSs based on their mechanical properties and corrosion resistance and to develop techniques for their production as prestressing strand to be implemented for the construction of durable PSC bridges with 100+ year service lives. The primary objectives of the research presented herein were:

1. To assess the current state-of-the-art of the use of stainless steels for corrosion mitigation in reinforced concrete (RC) and PSC structures while identifying areas requiring additional research.
2. To evaluate the mechanical properties and corrosion behavior of A416 prestressing strands and to indentify or develop test methods which can be used to evaluate the mechanical properties and corrosion resistance of new HSSSs.
3. To identify candidate stainless steels alloys which may be best suited for investigation as prestressing reinforcement considering factors such as potential mechanical properties, corrosion resistance, availability, and cost.
4. To experimentally assess key performance criteria, including stress vs. strain behavior, stress relaxation properties, and Cl^- induced corrosion resistance.

5. To develop materials selection and optimization criteria by correlating mechanical behavior and corrosion damage to microstructural features using various characterization techniques.
6. To identify optimal HSSSs from the candidate materials investigated based on the results of experimental studies.
7. To further evaluate the performance of optimal HSSSs by investigating the influence of stranding on corrosion resistance and susceptibility to damage by environmentally assisted cracking (EAC) mechanisms.
8. To investigate the feasibility of producing corrosion-resistant prestressing strands using optimal HSSSs in existing prestressing strand production facilities.

1.2 Scope of Experimental Program

The overall scope of the experimental program is shown in the flowchart in Figure 1.1. Initial research efforts focused on conducting a thorough literature review and assessing the current state of corrosion damage in Georgia's coastal bridges. The experimental program addressed the need for novel research in the area of HSSSs for corrosion mitigation in PSC bridge substructures. In order to develop a benchmark for comparison, the first phase of experimental studies focused on evaluating the mechanical properties and corrosion resistance of high-C eutectoid steels used for the production of A416 prestressing strand. The influence of crevice effects due to stranding and surface imperfections on the corrosion resistance of A416 prestressing strands was evaluated. The first phase of experiments was also useful in developing specimen geometries,

electrochemical testing methodologies, and characterization techniques which were subsequently used for the evaluation of candidate HSSSs.

Following the completion of studies on A416 prestressing strands, a series of studies investigating HSSSs was commenced. Candidate alloys were selected for the investigation through consultation with industry partners and the literature. Factors considered in the selection of candidate alloys included potential corrosion resistance, mechanical properties, cost, and availability. The tensile strength of candidate alloys was increased to approximately 1380 MPa (200 ksi) by cold drawing stainless steel rod to wire diameters commonly used for the production of A416 prestressing strand (4 mm (0.16 in)). As-received candidate HSSSs were characterized using chemical analysis, metallographic, and X-ray diffraction techniques. All candidate HSSSs were included as part of a screening study which examined their mechanical behavior and corrosion resistance. The stress vs. strain behavior and long-term stress relaxation was experimentally determined. Passivation behavior and Cl^- induced corrosion resistance was evaluated using electrochemical methods in solutions which simulated alkaline and carbonated concretes. Based on the results of the screening study, optimal alloys with acceptable mechanical properties and corrosion resistance were identified from the list of candidate materials.

Additional experiments were performed specifically on the optimal HSSSs indentified in the screening study to determine the influence of stranding on corrosion resistance and susceptibility to damage by EAC. Finally, techniques for the full-scale production of prestressing strands using optimal HSSSs were investigated, including specifications for wire drawing and stranding, and the development of a low-relaxation

thermomechanical heat treatment to improve mechanical properties and reduce stress relaxation.

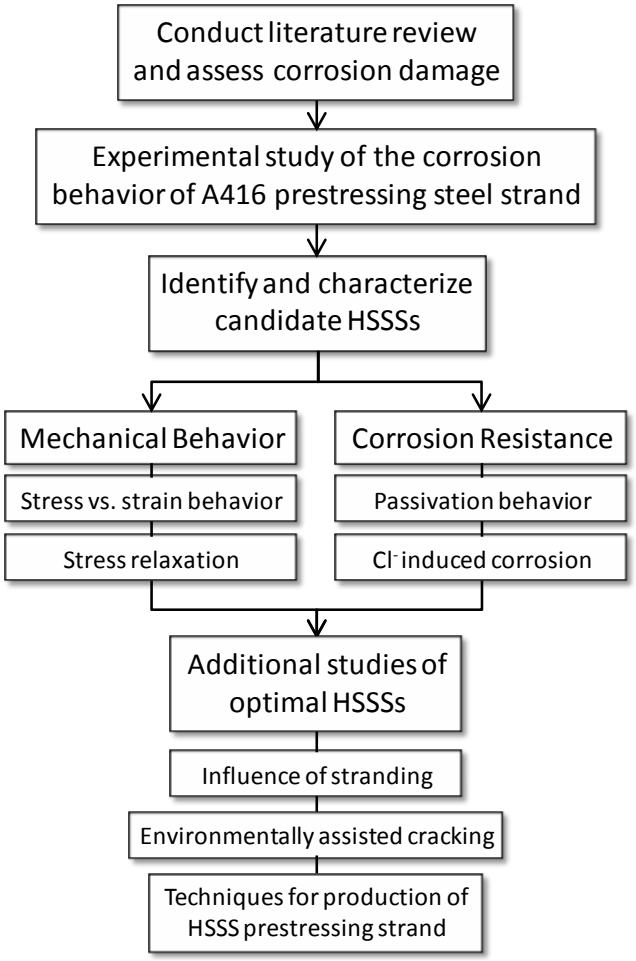

Figure 1.1 Scope of experimental program

1.3 Background

Corrosion of embedded steels has been one of the prevalent deterioration mechanisms in reinforced and prestressed concrete structures since their introduction. Previously thought to occur due to stray currents, it is now known that most corrosion in

concrete structures is caused by the ingress of aggressive ions such as chlorides (Cl^-) and/or CO_2. The corrosion of reinforcing steels became especially prevalent in the 1960's with the increased use of deicing salts, causing extensive corrosion of bridge decks in areas with harsh winters (Hartt, et al., 2004). Today, reinforcement corrosion affects all types of concrete elements, including bridge girders and decks, exposed members of buildings, concrete pavements, and precast prestressed concrete piles.

Steel embedded in concrete is typically very durable and resistant to corrosion. Alkali hydroxyls present in the pore solution of the hydrated cement paste and soluble products of cement hydration like $Ca(OH)_2$ provide the high pH (12.5-13.7) necessary for carbon steels to develop a protective, self-repairing passive film on their surface. The stability of this passive film is only jeopardized in the presence of chlorides or when pH is reduced by carbonation of the cover concrete (Revie, 2000). Structures exposed to severe marine environments, industrial conditions, and/or deicing salts are at the greatest risk of reinforcement corrosion caused by the ingress of Cl^-.

Once corrosion occurs, damage typically manifests itself as cracking and spalling of the cover concrete associated with the formation of expansive corrosion products on the surface of the reinforcing steel. Another result of corrosion is loss of reinforcement cross section and in turn member strength. These modes of damage lead to reduced service lives and eventually to structural deficiencies, making premature repair or replacement necessary. In PSC structures, EAC mechanisms (e.g., stress corrosion cracking and hydrogen embrittlement) may also lead to damage by the synergistic interaction between corrosion propagation and tensile stress, ultimately leading to brittle

fracture (Hope and Nmai, 2001a). Figure 1.2 depicts typical corrosion-induced spalling in the splash zone of a precast prestressed concrete substructure of a coastal bridge.

Figure 1.2 Spalling of cover concrete in splash zone of PSC piling caused by corrosion of prestressing strand and ties. Location: I-95 over the Turtle River in Brunswick, GA

Reinforcement corrosion can lead to premature damage of concrete structures. Almost all bridges include RC decks, with 50% of new bridges being all concrete, including precast PSC girders and piles. Approximately 13% of the nation's 595,000 bridges have been classified as structurally deficient according to the Federal Highway Administration's 2006 Report to Congress (Federal Highway Administration, 2006). Recent studies indicate that 15 % of structural deficiencies in U.S. bridges are the result of corrosion, with direct annual costs of $3.5 billion for the replacement of bridges damaged by corrosion and $4 billion to maintain and replace corroded concrete bridge

decks and substructures (Koch, et al., 2008). In addition to the direct costs of corrosion, indirect costs stemming from increased traffic congestion, bridge closures, affected businesses, and off-system structures like parking decks and piers have been estimated to be between $50 and $200 billion annually (NACE, 2008).

Bridges and other coastal structures in Georgia and throughout the Southeast are deteriorating prematurely due to corrosion (Griggs, 1987; Hamilton III, 2007). Numerous corrosion initiated failures have occurred in precast PSC piles and RC pile caps, leading to the costly repair and replacement of either the entire bridge or the affected members, if possible (Griggs, 1987). Figure 1.3 shows the results of a study of Georgia Department of Transportation (GDOT) bridge inspection records for bridges with concrete pile substructures along Georgia's coastal counties. Approximately 30 %, or 85 out of 290, of the bridges showed substructure ratings of 6 or less (shown by red dots in Figure 1.2), indicating that significant damage was present resulting from cracking and spalling caused by corrosion.

Reinforcement corrosion is also a durability concern around the world. Severe distress was found in over 100 bridges only 20 years after their construction in the Arabian Gulf due to the combined effects of a harsh environment and poor construction practices (Matta, 1993). Collapse of the roof of the Berlin Congress Hall in 1980 was caused by environmentally assisted cracking of the prestressing strands because of poor construction practices (Isecke, 1982). While other examples of reinforcement corrosion can be found throughout the literature, in today's society, it is believed that numerous corrosion-related failures go undocumented and are settled through litigation before any investigation or research is conducted (Hope and Nmai, 2001b).

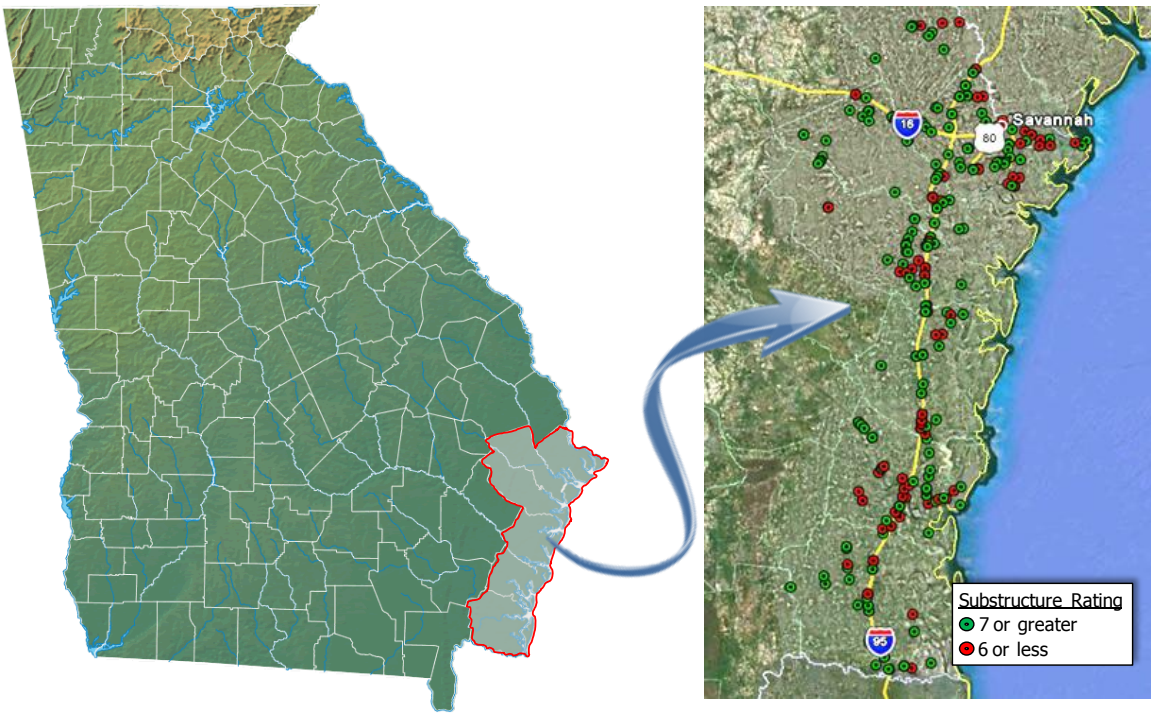

Figure 1.3 Bridge substructure deterioration in Georgia's coastal counties

Numerous studies examining chloride threshold levels (CTLs), the passivity of steel in concrete, models for service life estimation, and novel corrosion mitigation and rehabilitation strategies have been conducted in the laboratory and the field; yet, the problems associated with corrosion continue to plague concrete structures (Virmani and Clemena, 1998). Recent initiatives such as the Bridge Life Extension Act and the Federal Highway Administration's 100+ year bridge service life goal have provided a new impetus for the development and implementation of novel corrosion mitigation technologies in new concrete structures (Koch, et al., 2008). A majority of developed corrosion mitigation technologies have focused on RC structures reinforced with mild ferritic steels, including high performance concretes with reduced permeability(Hansson, 2005)(Hansson, 2005)(Hansson, 2005), epoxy or Zn-coated reinforcing steels,

electrochemical methods of protection, corrosion inhibitors, surface coatings and sealers, durable structural design and detailing methodologies, and, more recently, the use of corrosion-resistant stainless steel reinforcing bars.

In modern PSC bridges, corrosion mitigation it typically attempted with the use of high performance concretes (HPCs), large cover thicknesses, and proper design to limit cracking of the concrete. By this methodology, corrosion is mitigated primarily by decreasing diffusion coefficients, increasing the distance Cl^- must diffuse to reach the reinforcing steel, and preventing direct access of Cl^- to the steel in cracks. The use of HPCs has been shown to increase service lives to 100+ years using various service life modeling techniques (Boddy, et al., 1999). However, the brittle nature of HPCs makes them more susceptible to cracking caused by shrinkage and construction issues (e.g., overdriving of PSC piling) (Pfeifer, 2000). The presence of cracking HPCs is not accounted for in service life models and negates the effectiveness of reduced diffusion coefficients on limiting the ingress of Cl^-.

While other technologies such as ultra-high performance concretes (UHPCs), epoxy-coated prestressing strands, and fiber reinforced polymeric prestressing tendons have been investigated, their use in PSC construction has been limited due to increased cost and/or challenges associated with their implementation. Thus, the limitations associated with current corrosion mitigation technologies in PSC require an innovative approach to provide a corrosion prevention system which requires little to no maintenance, is cost effective over the 100+ year desired service life of the bridge, and is simple to implement by engineers and constructors.

One of the most effective methods of corrosion mitigation in RC structures is the use of corrosion resistant reinforcing (CRR) materials, typically austenitic or duplex (austenite + ferrite) stainless steel reinforcing bars. Stainless steels possess chloride CTLs typically more than one order of magnitude greater than mild reinforcing steels (Hartt, et al., 2004). However, the extension of CRRs from RC to PSC which requires high-strength prestressing reinforcement is a topic which has received limited attention in the literature, but is one which looks to provide many of the same durability benefits witnessed in RC structures. The growing use of PSC elements, especially in bridge structures (e.g., piles and girders), is a cause for increased awareness of corrosion issues and the development and assessment of novel corrosion mitigation techniques.

For stainless steels to be implemented for corrosion mitigation in PSC structures, strengthening techniques must be developed in order to form a new family of HSSSs which are better suited for prestressing. The challenges associated with optimizing mechanical properties, materials production and processing techniques, resistance to corrosion and EAC, and economic considerations have made research on HSSSs for PSC a difficult task which few have pursued. Thus, the motivation for the research presented in this dissertation – High-Strength Stainless Steels for Corrosion Mitigation in Prestressed Concrete: Development and Evaluation – which focused on addressing the need for more research in this area.

1.4 Organization of Dissertation

- Chapter 2 presents the results of a literature review which introduces many of the fundamental electrochemical aspects of corrosion, corrosion and EAC mechanisms in RC and PSC, and techniques for corrosion mitigation. In-depth discussion is provided relating to the use of stainless steels for corrosion mitigation in PSC structures; indentifying areas where additional research is necessary.
- Chapter 3 presents the results of a study examining the corrosion behavior of A416 prestressing strand considering the influence of crevice effects associated with stranding and surface imperfections on corrosion resistance.
- Chapter 4 introduces the stainless steels selected for investigation as HSSS prestressing reinforcement. Materials selection considerations and production techniques are discussed, followed by a description of each candidate HSSS including the results of microstructural characterization studies of the as-received materials.
- Chapter 5 presents the results of mechanical testing and stress relaxation experiments conducted as part of a screening study of all candidate HSSSs.
- Chapter 6 presents the results of electrochemical studies conducted to evaluate the resistance of all candidate HSSSs to Cl^- induced corrosion. Optimal alloys are identified based on corrosion resistance. The results of additional experiments evaluating the influence of stranding on corrosion resistance and EAC susceptibility are presented.
- Chapter 7 presents a review of the current techniques used for producing A416 prestressing strand and a discussion of the challenges in producing HSSS prestressing

strand. The results of a series of experimental studies examining methods for producing HSSS prestressing strand and a trial production run conducted at an A416 prestressing strand production facility are presented.

- Chapter 8 provides a summary of the research performed and its key conclusions. Recommendations regarding the implementation of HSSS prestressing strand for the construction of durable PSC structures and areas requiring future research are given.
- Appendices include additional results not provided in the body of the dissertation, detailed discussion of experimental methods and procedures for making specimens, and a list of references for all chapters.

CHAPTER 2

LITERATURE REVIEW

2.1 Introduction to the Electrochemistry of Corrosion

Corrosion reactions are controlled mainly by electrochemical phenomena – the interchange of chemical and electrical energy at the interface between a material and an ionically conductive electrolyte. The electrochemical reactivity of surfaces is mainly a result of changes in bonding present at the surface compared to the bulk of the material. In the bulk, atoms will coordinate themselves in a crystalline lattice structure to achieve the lowest energy structure. As the microstructure present in the bulk approaches the surface, the lack of atoms to complete the periodic crystal structure results in unsatisfied bonds at the surface – which in most cases leads to some buildup of charge (Skorchelletti, 1976).

In order to stabilize the surface and achieve charge neutrality, the metal will either alter its structure (a high activation energy process) or will react with the environment. Reactions with the environment for the surface to achieve energetic stability are the main cause of corrosion in metals. In the case of metallic corrosion, the charged surface will cause the adsorption of solvated compounds from the electrolyte, forming what is commonly referred to as a double layer at the surface as shown in Figure 2.1.

Two important features of the double layers must be noted: (1) ionized species migrate to the surface due to its charge and (2) a separation of charge exists between the metal surface and ionized species in the electrolyte. It is the presence of this separation of

charge which results the formation of a potential difference between the metal and electrolyte and thus the establishment of a driving force for electron transfer reactions (i.e., oxidation and reduction reactions) to occur at the metal/electrolyte interface.

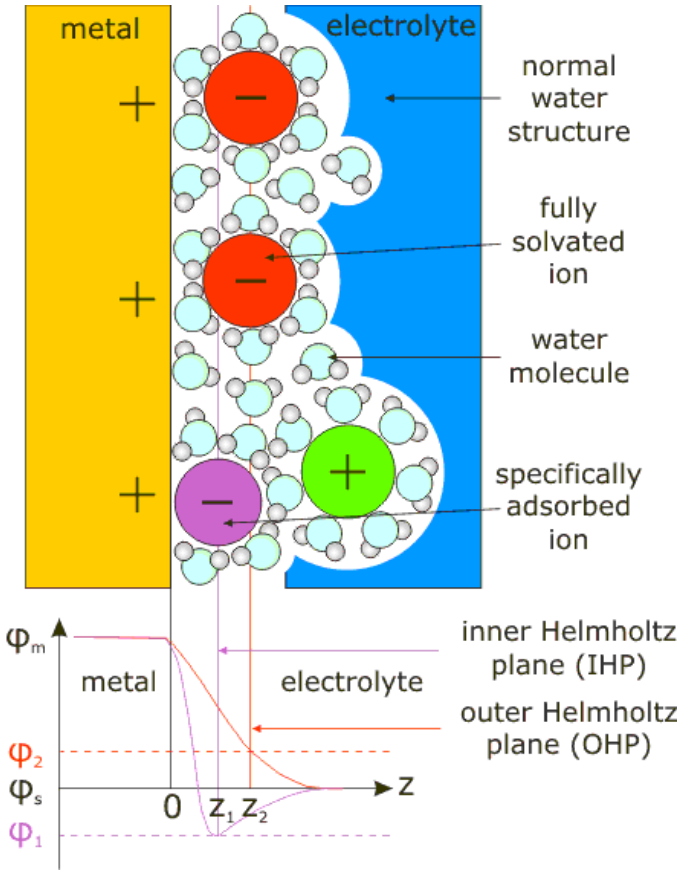

Figure 2.1 Double layer on metallic surface (from (Inst. Für Elektrochemie, 2011))

For an electrochemical (i.e., corrosion) reaction to occur, five components are necessary: (1) an anodic oxidation site ($Fe \rightarrow Fe^{2+} + 2e^-$), (2) a cathodic reduction site ($2H_2O + O_2 + 4e^- \rightarrow 4OH^-$), (3) an electrical connection between the anode and cathode to transfer electrons, (4) an electrolytic environment to transfer ions and complete the circuit, and (5) the availability of reactants at the site of corrosion such as O_2, Cl^-, H_2O.

The resulting products of these corrosion reactions vary greatly depending on the composition of the metal and the electrolyte. Pourbaix diagrams are typically used to map the regions of stability of products formed by corrosion reactions for various values of electrochemical potential and pH. A typical Pourbaix diagram for Fe exposed to an aqueous solution is shown in Figure 2.2. In general, three outcomes may be observed: (1) active corrosion, (2) passive protection, and (3) immunity. Active regions represent reactions where the product formed is not protective and anodic dissolution of metal occurs. Passive regions represent reactions where the product formed on the surface is protective, causing corrosion reactions to slow greatly. Immune regions represent reactions where the pure metal is stable and corrosion reactions are slowed to negligible rates (i.e. ΔG is negative for the reduction reaction).

Experimentally, the presence of a protective passive film may be shown on a polarization diagram, where corrosion current density remains constant or decreases over a wide range of E, indicating the presence of a reaction limiting product being formed on the surface. Figure 2.3 depicts the typical polarization behavior of a metal behaving in an active or passive manner with anodic polarization. The active region represents dissolution of the metal to ferrous ions in the electrolyte (e.g. $Fe \rightarrow Fe^{2+} + 2e^-$) which may then further react to form corrosion products. The passive region represents the buildup of a stable passive film on the surface (e.g., $2Fe^{2+} + 3H_2O + 2e^- \rightarrow Fe_2O_3 + 6H^+$). Once potentials reach the transpassive level, corrosion protection is lost as the passive film's structure begins to destabilize by anodic depassivation or localized dissolution caused by the initiation of pitting corrosion (Landolt, 2007).

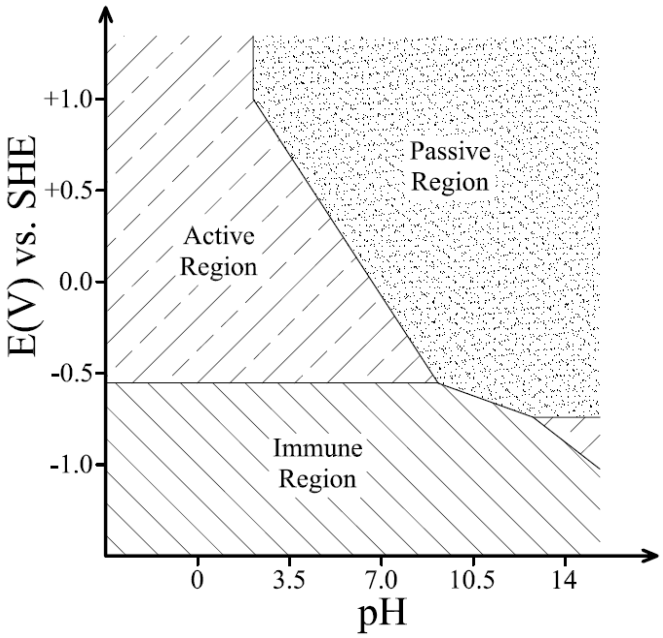

Figure 2.2 Example E vs. pH Pourbaix diagram for Fe

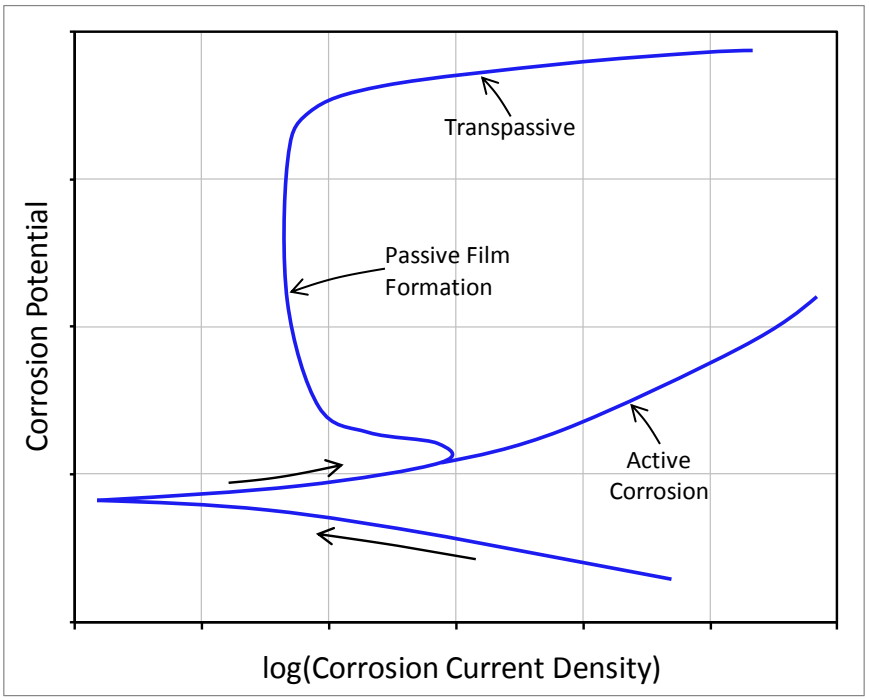

Figure 2.3 Polarization curve for active and passive metal

Corrosion reactions occur in cells where all five components of the electrochemical circuit are present. Corrosion cells can exist as macrocells as shown in Figure 2.4, or microcells as shown in Figure 2.5. Macrocells are created when there is a large separation between the anode and cathode (cm to m). A typical example of a corrosion macrocell is when the top mat of reinforcement in a bridge deck has begun corrosion due to Cl^- exposure from deicing salts and acts as the anode, while the unaffected bottom mat of reinforcing acts as the cathode. Microcells occur when the anode and cathode of the corrosion cell are very close in proximity (μm to mm). Metals generally have low resistivity and do not greatly limit the transfer of electrons between the anode and the cathode of an electrochemical cell. Concrete, being a high resistivity medium with a tortuous pore space, can limit distance of effective ionic transfer between the anode and the cathode (Böhni, 2005).

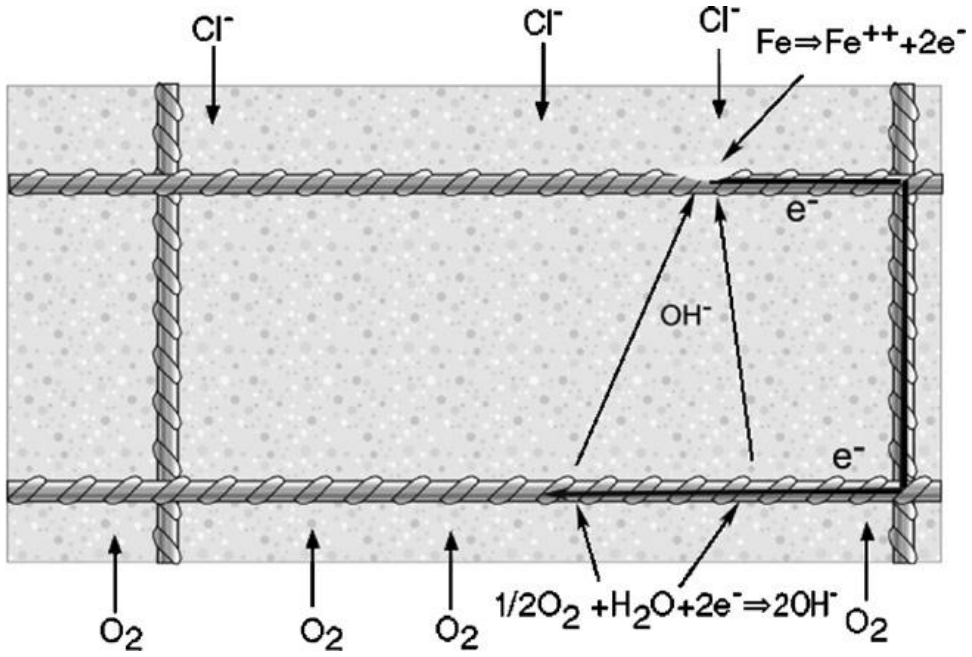

Figure 2.4 Corrosion macrocell on steel in concrete (from (Hansson, et al., 2006))

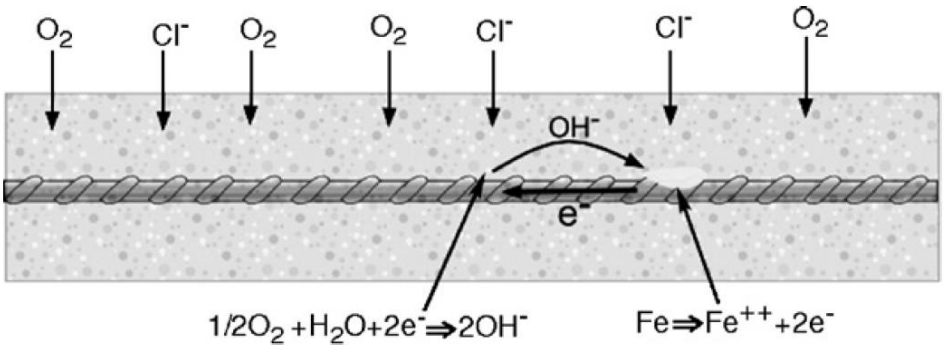

Figure 2.5 Corrosion microcell on steel in concrete (from (Hansson, et al., 2006))

The following section will provide a review of corrosion mechanisms in reinforced and prestressed concrete structures, techniques for corrosion mitigation, and in-depth discussion of the use of stainless steels for corrosion mitigation in concrete structure. Specific focus will be given to occurrence of corrosion and its mitigation using stainless steels in prestressed concrete structures.

2.2 Corrosion in Reinforced and Prestressed Concrete Structures

As discussed in Chapter 1, reinforcing and prestressing steels are typically highly resistant to corrosion when embedded in good quality concrete. The alkaline pore solution with pH 12.5 to 13.7 (Mehta and Monteiro, 2006) present in the capillary pore space of the hydrated cement paste (HCP) places in the material in a “passive” state (see Figure 2.2) by the formation of a stable passive film on the surface of the steel (Poursaee and Hansson, 2007). This nanometer-thick film, consists primarily of Fe oxides and oxy-hydroxides (Addari, et al., 2008; Rossi, et al., 2001) and been shown to decrease anodic dissolution rates to negligible levels (see Figure 2.6) by limiting corrosion reactions on

the metal surface. It is only when this film is degraded by the ingress of aggressive agents from the environment or when conditions for EAC are present that damage can occur.

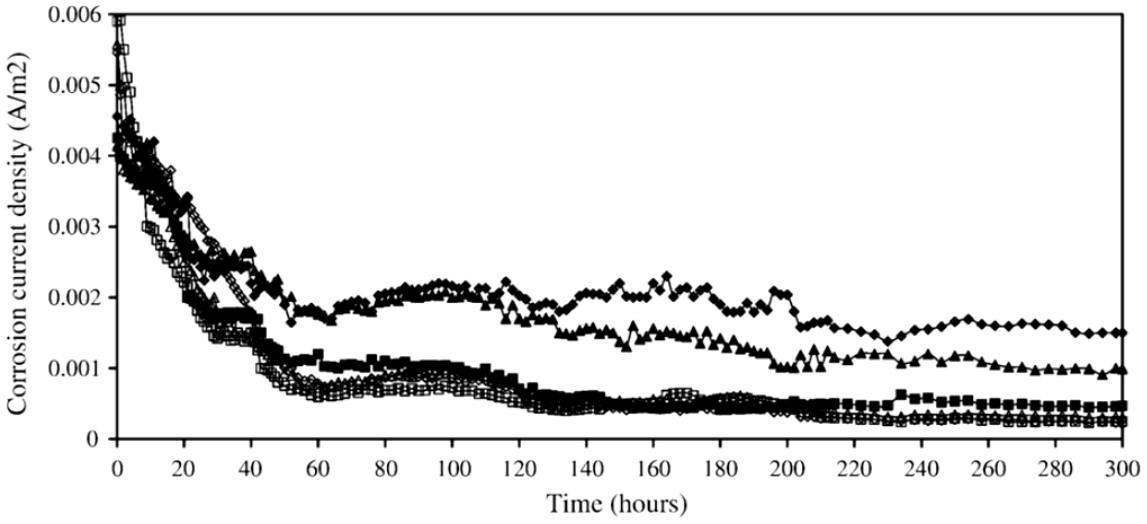

Figure 2.6 Corrosion current density vs. time indicating the formation of a passive film on the surface steel embedded in mortar (from (Poursaee and Hansson, 2007))

It must also be noted that much of the theoretical background of electrochemistry and aqueous corrosion discussed in this Section 2.1 are not fully applicable to steel embedded in concrete. The presence of mill scales on the surface of most reinforcing steels, mineral scales when embedded in concrete, and the heterogeneous distribution of phases and voids present in the hydrated cement paste (HCP) all influence the corrosion behavior of steels embedded in concrete. The following sections will review the relevant corrosion and EAC mechanisms in reinforced and prestressed concrete structures.

2.2.1 Carbonation-Induced Corrosion

Corrosion of reinforcement caused carbonation of the cover concrete occurs with the ingress of CO_2 from the atmosphere. For corrosion to occur, carbonation of the HCP

must occur to the level of the reinforcing steel. The ingress of CO_2 has been shown to occur at a rate approximately proportional to the square root of time as shown in Equation 2.1 (Bertolini, et al., 2004) :

$$d = K \cdot t^{1/n} \tag{2.1}$$

Where:
d = Depth of carbonation
K = Constant
t = time
n = Curve fitting factor (2 in PCC and >2 in HPC)

The ingress of CO_2 is greatly affected by environmental conditions such as relative humidity and temperature. At high levels of relative humidity, the void space present in the HCP is largely filled with H_2O, limiting the transport of gaseous CO_2 into the concrete. However, at low levels of relative humidity, insufficient moisture is available in the pore space to solubilize CO_2 and $Ca(OH)_2$ which are necessary for carbonation reactions to occur. Maximum carbonation rates occur approximately at a relative humidity of 50-60% (see Figure 2.7) (Papadakis, et al., 1991). Cyclic wet/dry cycles can also increase carbonation rates. Dry cycles allow CO_2 to permeate into the concrete, while wet cycles provide the H_2O needed for carbonation reactions to occur. CO_2 concentration can also have a large impact on carbonation rates. Under normal conditions CO_2 concentrations are on the order of 0.03%, with up to 10X higher concentrations in industrial or urban areas, and up to 100X higher concentrations in areas such as highway tunnels or power plants (ACI 222, 2001). As would be expected, increased temperatures also increase rates of carbonation and carbonation related corrosion.

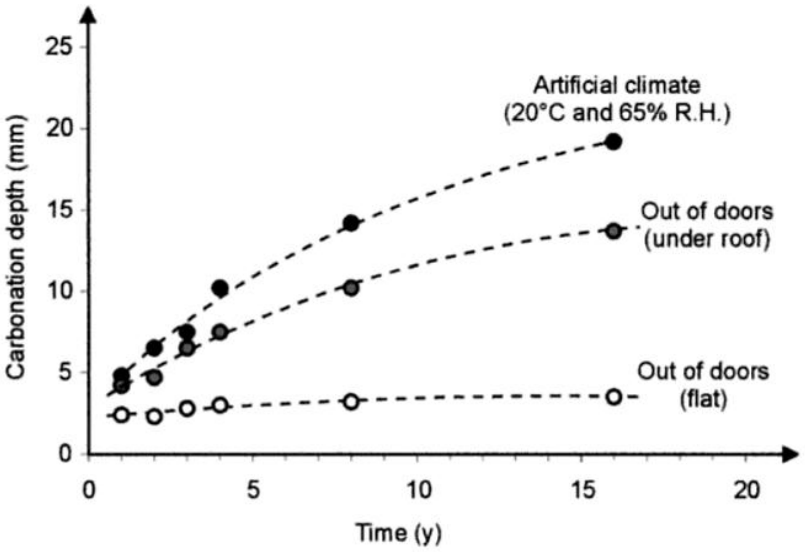

Figure 2.7 Carbonation depth vs. time (Wierig, 1984)

The pH of the pore solution falls as CO_2 reacts with the components of the concrete pore solution (Bohni, 2005), as shown in Equations 2.2 to 2.4.

$$2NaOH + H_2O + CO_2 \rightarrow Na_2CO_3 + 2H_2O \quad (2.2)$$

$$2KOH + H_2O + CO_2 \rightarrow K_2CO_3 + 2H_2O \quad (2.3)$$

$$Ca(OH)_2 + H_2O + CO_2 \rightarrow CaCO_3 + 2H_2O \quad (2.4)$$

Note in Equations 2.2 to 2.4 that H_2O has been included as both a reactant and product. The presence of H_2O as a reactant indicates the intermediate step to each carbonation reaction associated with the formation of carbonic acid in the presence of H_2O (i.e., $CO_2 + H_2O \rightarrow H_2CO_3$). The products of the carbonation reactions, sodium and potassium carbonates have a high solubility, therefore, they stay in solution while the calcium carbonate has a low solubility and precipitates out of solution, often filling the

pore space and reducing CO_2 ingress rates. The consumption of alkali hydroxyls present in the pore solution and dissolution of solid $Ca(OH)_2$ leads to a reduction in the pH of the pore solution to approximately 8 to 9. At the neutral pH, the protection offered by the passive film is lost. Thus, once the carbonation front reaches the depth of the reinforcing steel uniform corrosion initiation occurs (Broomfield, 2007). Figure 2.8 illustrates the typical distribution of pH with carbonation depth.

In the U.S., corrosion due to carbonation is of lesser concern than Cl^- induced corrosion in most modern structures as carbonation rates are typically on the order of 1 mm/yr (0.04 in/yr) or less (Hartt, et al., 2004). However, many regions around the globe where climates are more favorable to accelerated carbonation rates (moderate temperature with frequent wet / dry cycles) are subject to corrosion initiated by carbonation (Broomfield, 2007).

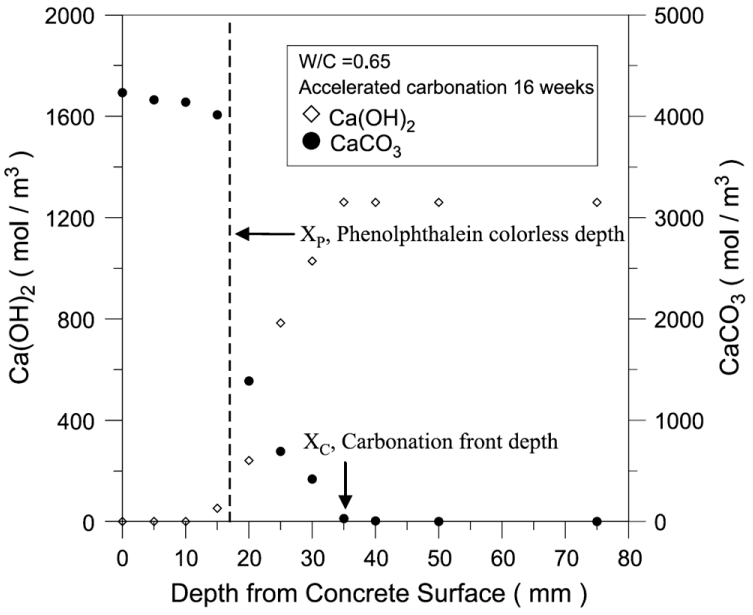

Figure 2.8 $Ca(OH)_2$ composition as an indicator of carbonation depth measured using thermogravimetric analysis (from (Chang and Chen, 2006))

2.2.2 Chloride Induced Corrosion

In modern structures, ingress of Cl^- ions from the environment is the predominant cause of corrosion in reinforced and prestressed concrete structures. Because corrosion by Cl^- is of utmost importance, this section will discuss the effect of marine and deicing salt exposure, Cl^- corrosion mechanisms, transport mechanisms, the effect of cracking, and a discussion of accepted Cl^- threshold values.

2.2.2.1 Marine and Deicing Salt Exposure

The most destructive component of a salt-bearing environment, from the perspective of metal preservation, is the Cl^- ion. In seawater, salt concentrations range from 33-38 parts per thousand (ppt) and is usually considered to be 35 ppt (or 3.5% by mass) in open ocean water (Mehta, 1991). While the salts are made up of various elements including sodium, potassium, and magnesium, the main ion present in seawater is Cl^-. Table 2.1 shows the typical anion and cation content is open ocean water. Chlorides can also ingress into concrete through the use of deicing salts in regions with severe winters, resulting in extensive corrosion of bridge decks and concrete pavements. Other potential sources for Cl^- include concrete mix water, washwater for aggregates, and Cl^- containing chemical admixtures (e.g., $CaCl_2$ accelerator). Degradation can also be accelerated in tropical regions, where marine conditions are accompanied by increased temperatures and relative humidity (Hartt and Nam, 2004).

Table 2.1 Seawater ion content (Chandler, 1984)

Seawater Ions	Content (g/kg)
Total Salts	35.10
Sodium	10.77
Magnesium	1.30
Calcium	0.409
Potassium	0.338
Chloride	19.37

Another important consideration in both bridge decks and marine exposures is the potential for periodic wet and dry cycling. Periodic wetting due to tidal or splash action in marine structures, or periods of rain/snow and dry on bridge decks can allow chlorides to ingress at high rates during wet periods facilitated by capillary suction and then precipitate during dry periods, eventually leading to a buildup of Cl^- in the surface of the concrete. Even though Cl^- contents can be very high in submerged areas, corrosion is of little concern due to the lack of O_2 to carry out reactions at the cathodic site. It is only in the wet/dry areas of the splash and tidal zone where a supply of both chlorides and oxygen is present and corrosion rates are accelerated (Sandberg, et al., 1998).

2.2.2.2 Chloride-Induced Corrosion Mechanisms

In Cl^- bearing environments, the main danger of corrosion is the localized breakdown of the passive film. Once Cl^- has reached a sufficient concentration at the level of the reinforcement, passivity can be lost locally, initiating corrosion. Breakdown of the passive film is caused primarily by diffusion of Cl^- into the passive film (Jones, 1996). Under normal conditions the passive film dissolves at a slow and steady rate. Cl^- at the passive layer – electrolyte interface can dissociate hydroxyl ions in the passive film, forming metal chlorides (halides) which dissolve into the electrolyte (pore solution

in this case). Degradation of the passive film occurs according to Equations 2.5 to 2.7 (Kurtis and Mehta, 1997). It should be noted that the reaction shown in Equation 2.7 involves the formation of $Fe(OH)_2$ corrosion product and, most importantly, the release of the Cl^-. Thus, the breakdown of the passive film is an autocatalytic reaction, with the Cl^- reactant not being bound into the corrosion products.

$$Fe^{2+} + 6Cl^- \rightarrow FeCl_6^{-4} \tag{2.5}$$

$$Fe^{3+} + 6Cl^- \rightarrow FeCl_6^{-3} \tag{2.6}$$

$$FeCl_6^{-3} + 2OH^- \rightarrow Fe(OH)_2 + 6Cl^- \tag{2.7}$$

Corrosion initiation will occur preferentially at inclusions in the metal (e.g., precipitates) and defect sites in the passive film. A typical corrosion pit is shown in Figure 2.9. Inside of the pit Cl^- is concentrated and pH falls to acidic levels approaching 1 due to the formation of H^+ (Revie, 2000). Once pitting has become extensive on the surface of the reinforcement, pits will eventually coalesce and transgress into general / uniform corrosion, causing the typical cracking and spalling of the cover concrete.

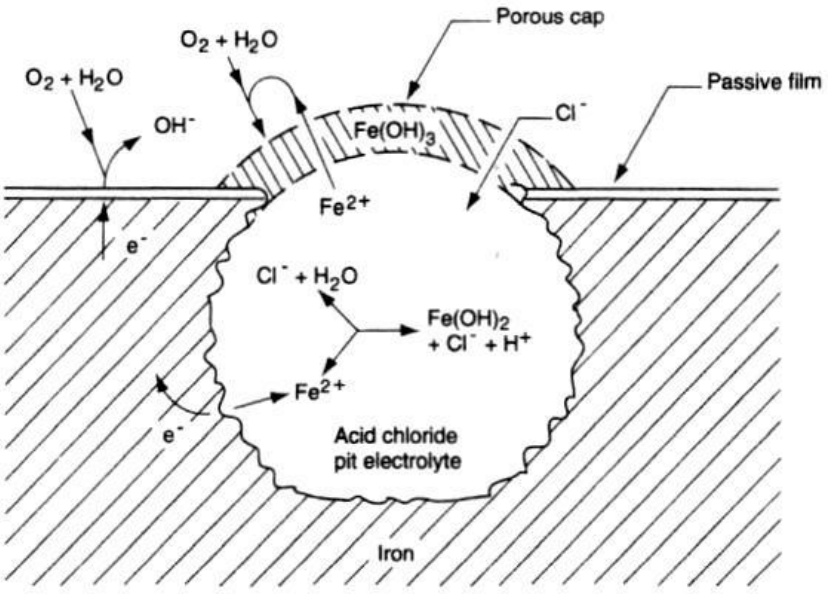

Figure 2.9 Typical corrosion pit morphology (Jones, 1996)

In addition to pitting corrosion mechanisms described above, crevice corrosion mechanisms may also be a concern in prestressing reinforcement used in PSC structures. This concern results from the stranded geometry most prestressing steels are produced in (shown in Figure 2.10). In the seven wire strand geometry, crevices are formed at the impingement sites between adjacent wires. The presence of crevice sites has been shown to accelerate localized corrosion by limiting access of O_2 within the crevice, attracting Cl^- to the crevice region, and accelerating acidification within the crevice by hydrolysis reactions with H_2O (Frankel, 1998; Sharland, 1992). In essence, the crevice acts as a corrosion pit that does not require a nucleation step (i.e., the geometry acts as an artificial pit). The existence of crevice corrosion mechanisms in prestressing strands has been the subject of limited qualitative research (Brooks, 2003; Proverbio and Bonaccorsi, 2002). Chapter 3 presents the results of an in-depth study conducted by the author to evaluate

the influence of crevice corrosion mechanisms on the corrosion resistance of prestressing strands.

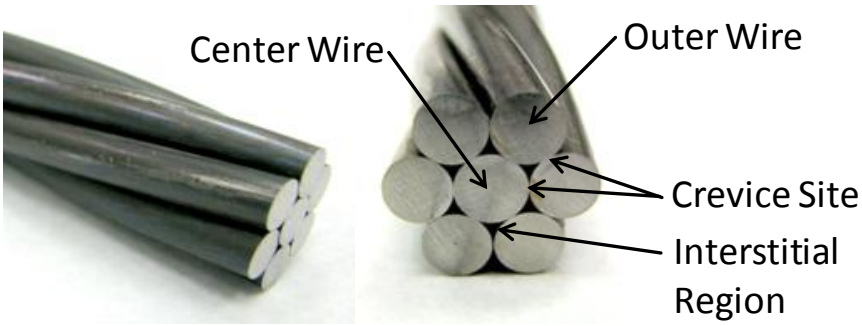

Figure 2.10 Seven-wire prestressing strand geometry including crevice sites

2.2.2.3 Chloride Transport Mechanisms in Concrete

For Cl^- induced corrosion to occur, Cl^- must reach the chloride threshold level (CTL) at the depth of steel by transport from the surface. Figure 2.11 illustrates this type of Cl^- transport phenomena based on a Collepardi-type model (Nilsson, 2009). Service life estimates can be made based on a knowledge of the relevant concrete transport phenomena and the corrosion resistance of the embedded steel. The ingress of Cl^- is controlled by many different mechanisms including diffusion, capillary suction, and chloride binding, and electromigration. Diffusion is defined as transport (in this case of Cl^-) into a material due to a concentration gradient. Capillary suction is the absorption of a fluid into a material due to capillary tension forces (also known as capillary action). Cl^- may be physically bound by adsorption on the surface of hydrated phases or chemical bound in aluminate phases like Friedel's salt ($3CaO \cdot Al_2O_3 \cdot CaCl_2 \cdot 10H_2O$) which can form by reaction with monosulfate and ettringite phases and residual anhydrous tricalcium aluminate. Electromigration effects may also be present due to the presence of

potential gradients within the concrete and the coulombic interaction between charged ions as they transport through the pore solution. When concrete is saturated, diffusion is the dominant transport mechanism. When concrete is dry, capillary suction upon first wetting is the main mode of transport for chlorides (Thomas, et al., 1999a). Concrete which is completely dry has almost no ability to absorb Cl^- and is resistant to corrosion.

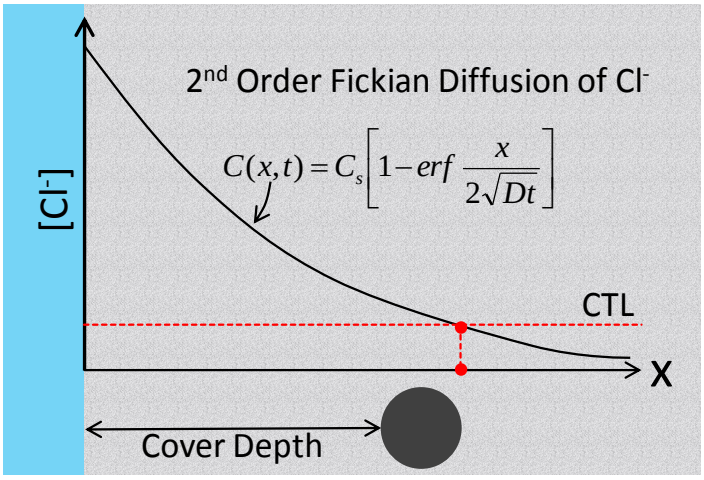

Figure 2.11 Collepardi model for Cl^- ingress into concrete

Fick's second law for diffusion is typically utilized for modelling the non-steady state Cl^- transport phenomena in saturated concrete. Fick's second law states that:

$$\frac{\partial C}{\partial t} = -div(\bar{J}) \tag{2.8}$$

Where:
C = Concentration
t = Time
$\bar{J}$ = Diffusional flux across a boundary

Using Fick's first law and taking D (the diffusion coefficient) to be constant, the usual form of Fick's second law, a 2nd order partial differential Equation 2.9, is obtained:

$$\frac{\partial C}{\partial t} = D\frac{\partial^2 C}{\partial x^2} \tag{2.9}$$

Where:
D = Diffusion coefficient
x = Depth of ingress

Through Boltzman substitution, $\eta = x/2\sqrt{Dt}$, Equation 2.9 can be transformed from a partial differential equation to an easily solved 2nd order homogeneous ordinary differential equation, which when incorporating boundary conditions and an error function to simplify calculations yields Equation 2.10.

$$C(x,t) = C_s\left(1 - erf\ \frac{x}{2\sqrt{Dt}}\right) \tag{2.10}$$

Where:
$C(x,t)$ = Concentration at depth x and time t
C_s = Concentration at surface

Many researchers have successfully used diffusion-based models to predict Cl^- ingress successfully (Bertolini, et al., 2004). However, many more sophisticated models are also available which consider the impact of capillary suction, Cl^- binding, and even electromigration effects on the ingress of Cl^- into concrete (Boddy, et al., 1999).

2.2.2.4 Effect of Cracking on Chloride Ingress

While much debate exists concerning the influence of cracking on Cl^- ingress, it is universally accepted that the presence of cracks will increase permeability. Numerous studies have been conducted to determine the effect of cracking and evaluate at which size of crack the ingress of Cl^- begins to accelerate. Most studies indicate that if a detectable crack is present, it will greatly increase the ingress of Cl^-, and the width of the crack has little effect on the rate of ingress (Rodriguez and Hooton, 2003; Schießl and Raupach, 1997). Others indicate that crack width can affect the ingress of Cl^-, finding that cracks less than approximately 0.1 mm (4 mil) in width have little influence on the ingress Cl^- (Hansson, 2005). Cracking of cover concrete not only allows for Cl^- to reach a direct point on the surface of the reinforcement, but also allows for additional ingress of Cl^- into the HCP through the interior surfaces of the crack. Figure 2.12 illustrates the effect of a crack on the ingress of H_2O in concrete.

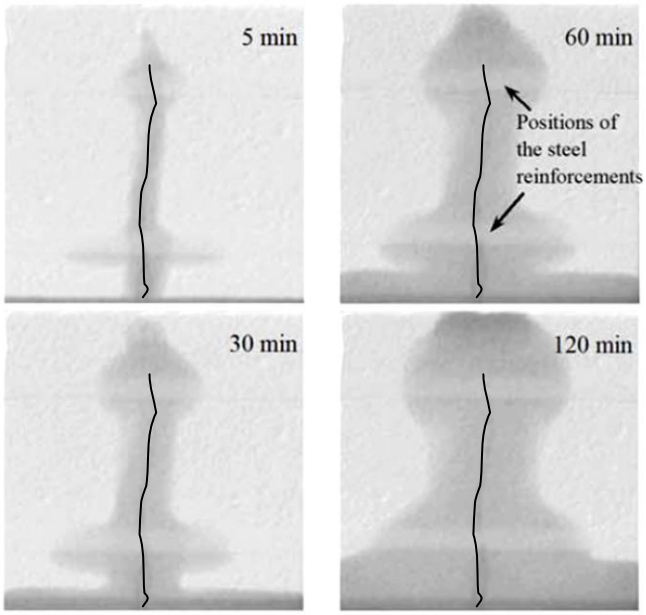

Figure 2.12 Effect of cracking on H_2O (dark) ingress (adapted from (Zhang, et al., 2010))

Much research has also been conducted on the possibility of autogenous self healing of cracks to limit permeability. Self healing is possible due to the combined effects of swelling and additional hydration of cement paste, precipitation of carbonates, (such as $CaCO_3$), and crack blocking by impurities or broken concrete. While self healing of cracks was not found to be possible when widths are large, healing was found to occur when crack widths were less than approximately 0.1 mm (4 mil), with almost a full recovery in impermeability (Edvardsen, 1999). In any case, researchers agree that over a long design life (as is the case in current bridges with a 100+ year design life) the presence of cracks only accelerates the initiation of corrosion (Ahern, 2005). In the case of prestressed concrete structures, crack closure and subsequent self healing due to the presence of precompressive stresses is possible. It has been shown that the self healing of cracks to restore original permeability properties is greatly accelerated at early ages by the presence of compressive stress to close the crack. In addition, it was found that only enough compressive stress to close the faces of the crack was needed to initiate self healing (Heide, 2005).

2.2.2.5 Chloride Threshold Level

The parameter utilized by most engineers for Cl^- limits is the chloride threshold level, commonly known as the CTL. This value is typically expressed as the weight percent of chloride vs. the weight of cement in a concrete mixture, or weight of chlorides per cubic volume of concrete and represents the concentration of Cl^- when corrosion is expected to initiate. In the United States, a CTL value of 0.6 to 0.9 kg/m^3 (1 to 1.5 lb/yd^3) has been agreed upon by most researchers for the initiation of corrosion of mild steel reinforcement in concrete (Ann and Song, 2007; Manera, et al., 2007). Due to the large

variability in values for the CTL reported by researchers, the American Concrete Institute (ACI) has taken a conservative stance on CTL values. CTL values given in the ACI 318-08 *Building Code Requirements for Structural Concrete and Commentary* are shown in Table 2.2. ACI 318-08 CTL values are much less than those of 0.4 to 0.6 % by weight of cement used in Europe and Canada (ACI 222, 2001).

Table 2.2 CTL values recommended in ACI 318-08 (ACI 318-08, 2008)

Type of member	Maximum water soluble Cl^- in concrete, percent by weight of cement
Prestressed Concrete	0.06
Reinforced concrete exposed to Cl^- in service	0.15
Reinforced concrete that will be dry or protected from moisture in service	1.00
Other reinforced concrete construction	0.30

Another measure of chloride content recommended by researchers is the use of a molar chloride-to-hydroxide ratio, $[Cl^-]:[OH^-]$ (Ann and Song, 2007). Researchers indicate that this value is more inclusive of the corrosion inhibiting behavior of concretes with higher OH^- contents wherein the constant buffering provided by the high pH of the pore solution results in the formation of a passive film with higher quality and stability. While ratios of 1 to 3 are typical, variability from 0.5 to 40 seems to make the $[Cl^-]:[OH^-]$ ratio an unreliable indicator of the CTL (Ann and Song, 2007; Thangavel and Rengaswamy, 1998).

In both the cases of the typical weight % measure of CTL and the $[Cl^-]:[OH^-]$ ratio, variability in laboratory and field conditions and concrete placement techniques makes any measure of CTL inherently unreliable (Hope and Nmai, 2001b). Figure 2.13

depicts the high variability present in CTL experimental results. The CTL is affected by numerous factors, including concrete quality, the presence of voids, temperature, relative humidity, cracking, oxygen availability, and, most importantly, the test method used to evaluate it. There likely exists a synergistic relationship present between the many possible variables which interact differently to give the true CTL of a particular reinforced concrete element in service. Figure 2.14 illustrates these interdependent relationships as determined by the CEB-FIP committee on Durable Concrete Structures.

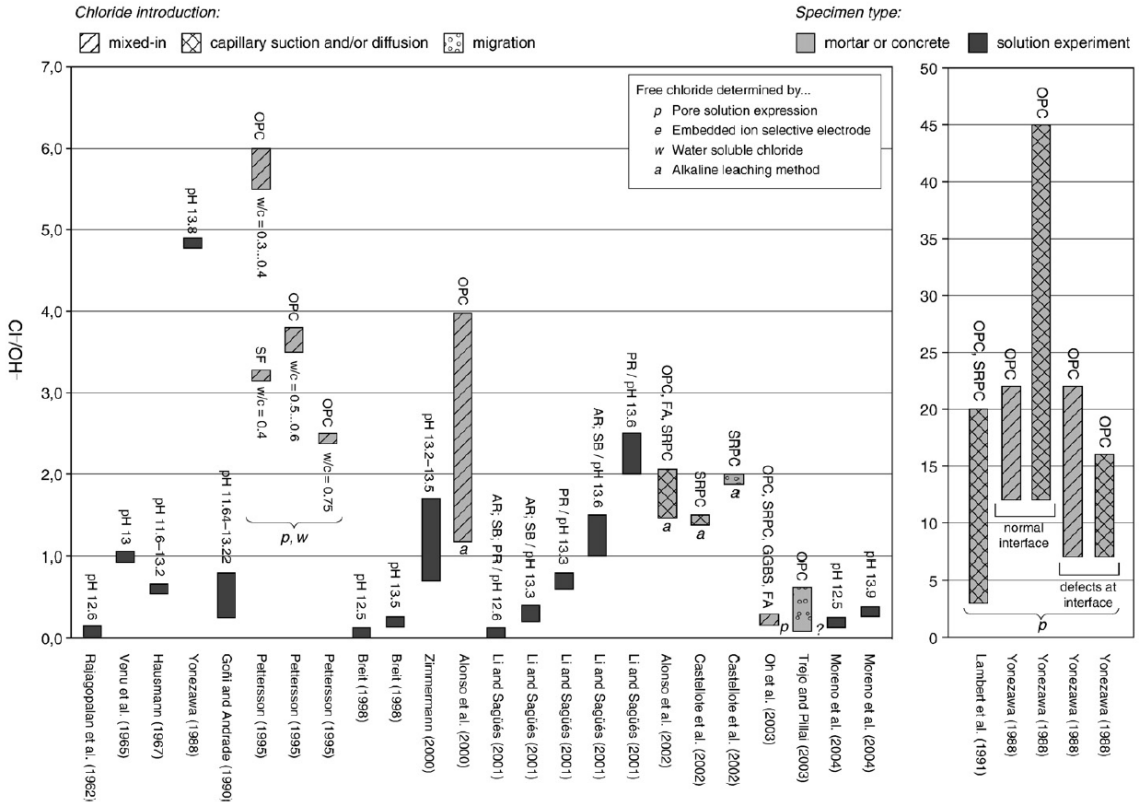

Figure 2.13 Variability in CTL defined as $[Cl^-]$:$[OH^-]$ in the literature (Angst, et al., 2009)

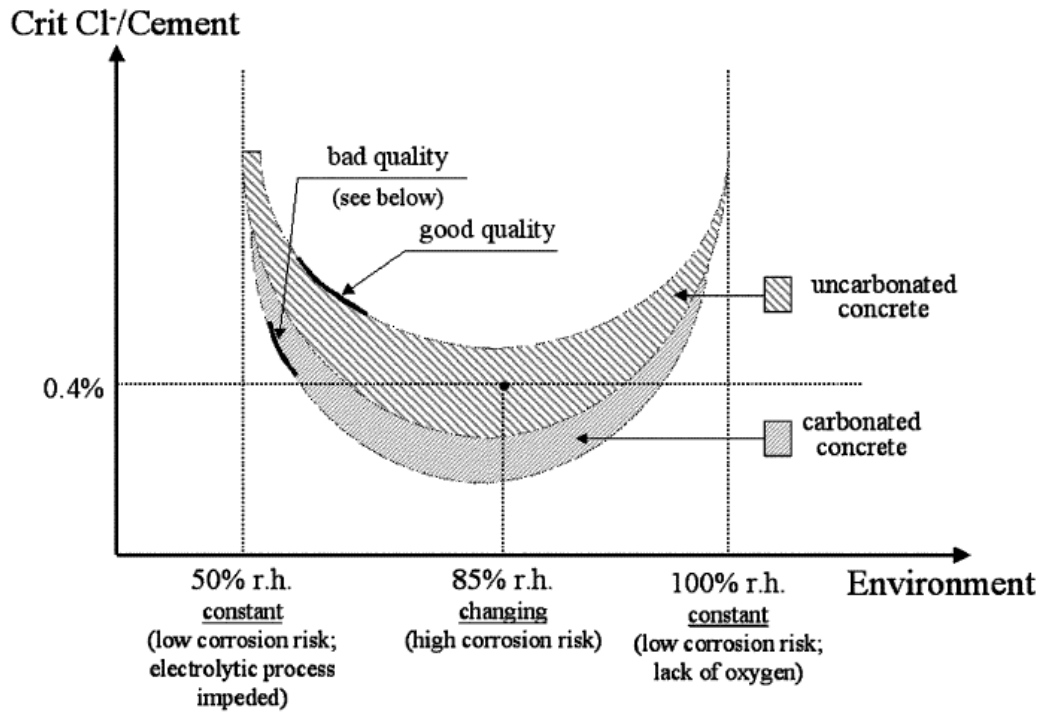

Figure 2.14 CTL recommendations by CEB – FIP (FIP, 1992)

2.2.4 Consequences of Carbonation and Cl^- Induced Corrosion

Damage to structures caused by corrosion occurs over an extended period of time. Depending on the quality of the concrete, the environment, cover, and many other factors, the time until failure of the structure occurs and/or rehabilitation is needed can vary greatly. Corrosion timelines include an initiation period where carbonation of the cover concrete or ingress of Cl^- to the level of the reinforcing steel occurs and a propagation period as corrosion is initiated and damage to the structure begins. As explained in Figure 2.15, the length of each period is affected by many factors.

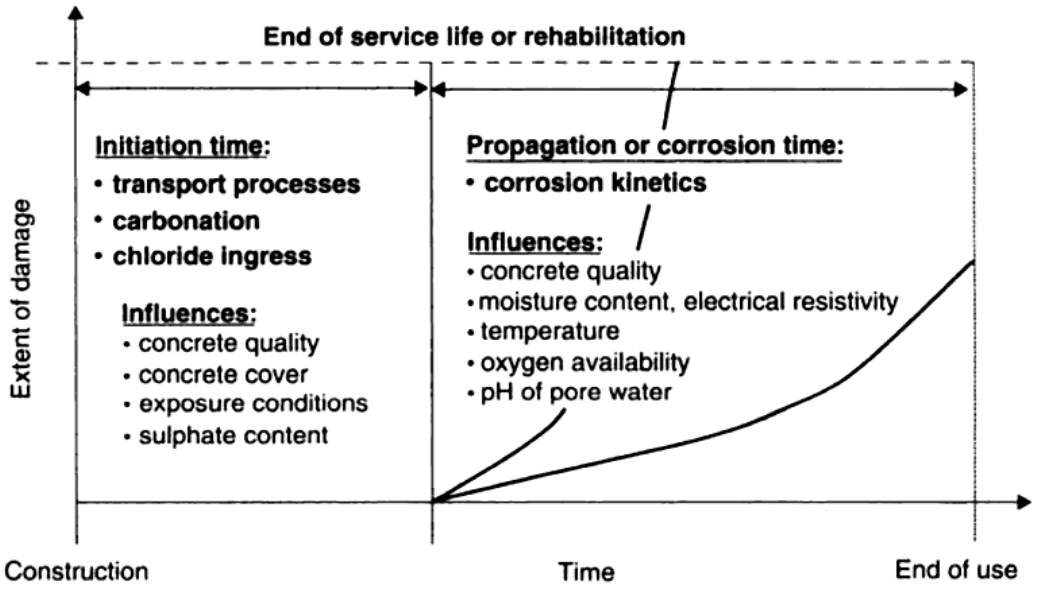

Figure 2.15 Corrosion damage timeline (Böhni, 2005)

Once corrosion of the reinforcement has initiated, it is the reaction itself and the corrosion products formed which degrade the integrity of the concrete structure. Corrosion reactions result is dissolution of metal, in this case Fe, from the surface of the reinforcement, resulting in a loss of cross sectional area. Due to decreased cross section, the design strength of the member may be decreased. However, in most cases general reinforcement corrosion is noted by cracks and brown rust stains like those depicted in Figure 2.16 well before strength is degraded to dangerously low levels. The far greater impact of corrosion is the formation of corrosion products on the surface of the reinforcement. As shown in Figure 2.17, products formed by corrosion reactions when hydrated can occupy up to 7 times the volume when compared to that of the reacted metal (Mehta and Monteiro, 2006).

Figure 2.16 Cracks and rust staining on precast PSC piling in coastal bridge substructure. Location: Island Expressway in Savannah, GA

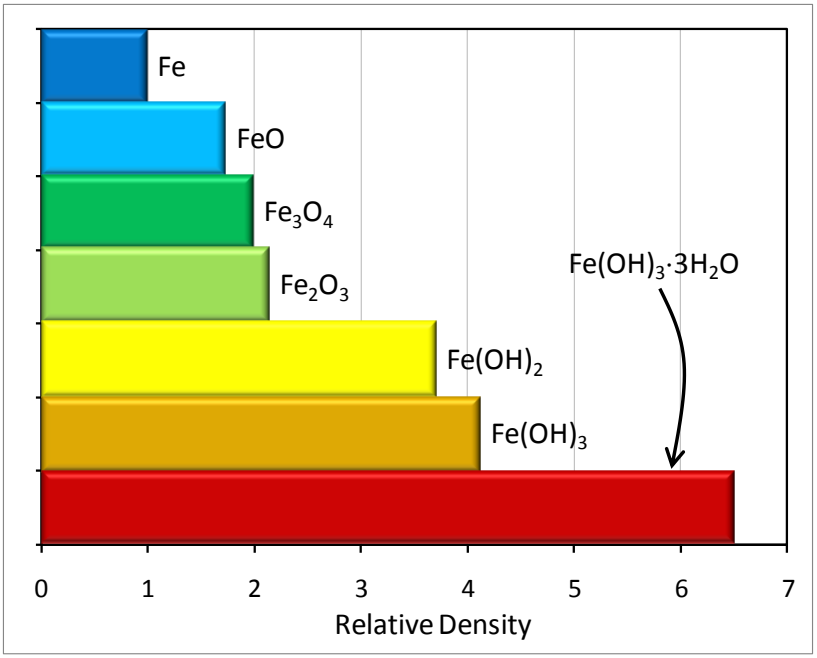

Figure 2.17 Relative density of corrosion products (adapted from (ACI 222, 2001))

The formation of expansive corrosion products on the surface of the steel results in the development of tensile hoop stresses around the perimeter of the reinforcing bar. With concrete being weak in tension, cracks develop perpendicular to the tensile hoop stresses, as shown in Figure 2.18. Eventually, cracks will become extensive and spalling of the cover concrete occurs (see Figure 1.1 and 2.16). In addition to reducing the member's strength, cracking and spalling greatly lowers the concrete's resistance to the ingress of Cl^- and other reactants such as CO_2 and O_2, leading to accelerated corrosion damage (Broomfield, 2007). The formation of corrosion products at the steel / concrete interface may also lead to bond degradation and the migration of these products through the concrete can embrittle the cover (Kurtis and Mehta, 1997).

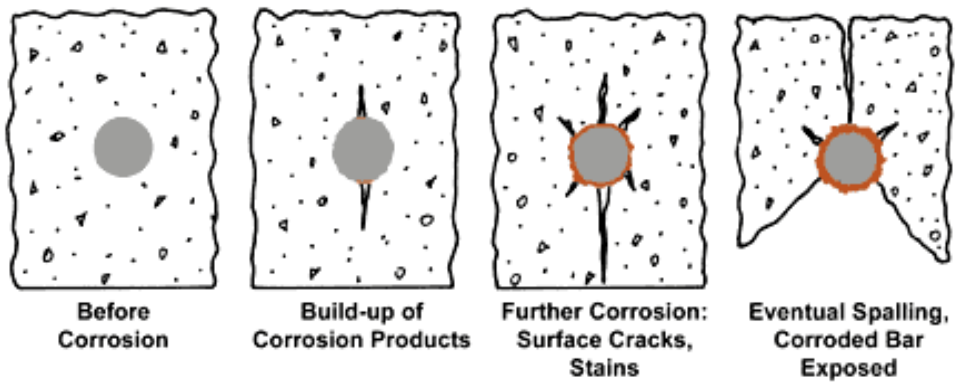

Figure 2.18 Cracking and spalling of concrete caused by corrosion (from (Rourke, 2008))

2.3 Environmentally Assisted Cracking in Prestressed Concrete

In addition to the corrosion mechanisms discussed in Section 2.2 present in reinforced and prestressed concrete, other dangers exist in prestressed concrete structures. Due to their high level of initial stress and inherent metallurgical properties, prestressing

steels may be susceptible degradation caused by environmentally assisted cracking (EAC) mechanisms. Two modes of EAC are of particular concern, stress corrosion cracking (SCC) and hydrogen embrittlement (HE) (Hope and Nmai, 2001a). The main danger of EAC is a reduction in both strength and ductility of the affected metal resulting in limited ductility and brittle modes of failure. Figure 2.19 demonstrates the influence of EAC (in this case SCC) on the stress vs. strain behavior of steel when exposed to seawater. Much like the timeline for Cl- corrosion initiation, EAC includes an initiation period when cracks begin to form, a propagation period as cracks grow through the microstructure, and a damage period when fast fracture and failure of the metal occurs (Landolt, 2007).

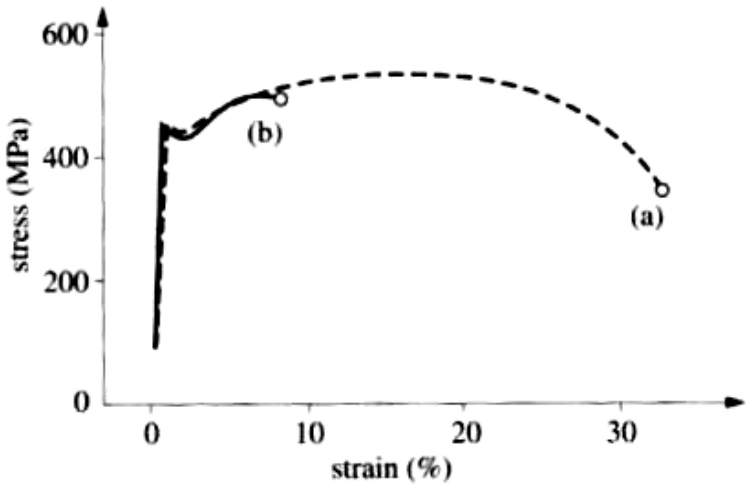

Figure 2.19 Slow strain rate test of steel in air (a) and seawater (b) (from (Landolt, 2007))

2.3.1 Stress Corrosion Cracking

Brittle failures caused by SCC may result when a susceptible alloy is placed in a corrosive environment while under a constant tensile loading (Schweitzer, 2003). In

many cases, only specific alloy / environment combinations may be susceptible to damage by SCC. High strength alloys are at the greatest risk of SCC, owed to their high defect density and possible microstructural inhomogeneities resulting from production (Jones, 1996). SCC may be intergranular or transgranular, as shown in Figure 2.20. Transgranular cracking results from reaction with the alloy itself along specific crystal planes and directions. Intergranular cracking results from inhomogeneities present at sites grain boundaries. This is especially prevalent in cases where metal processing has resulted in undesirable precipitates (such as chromium carbides) being formed at grain boundary sites due to improper heat treatment (Mietz, et al., 1997).

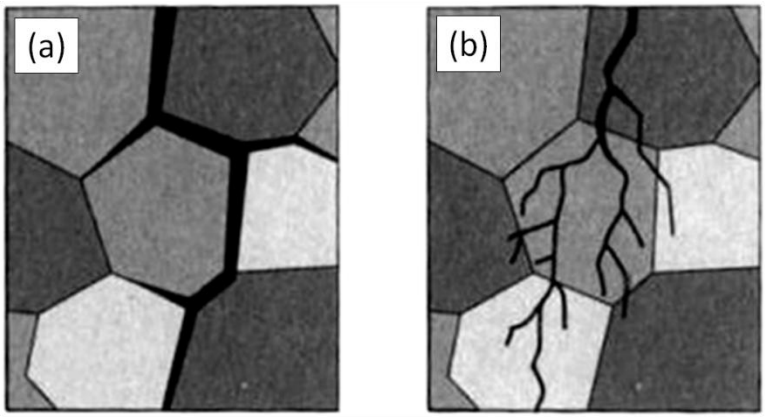

Figure 2.20 SCC (a) Intergranular, and (b) Transgranular (from (Landolt, 2007))

SCC is mainly limited to active – passive alloy / environment combinations, with damage occurring primarily in regions where passive film stability is easily jeopardized. Figure 2.21 shows zone 1 and 2 potential regions where SCC will most likely occur. In the transpassive region zone 1, the passive film is becoming destabilized as the film begins to breakdown. The presence of stress concentration sites on the surface of the

metal caused by pitting corrosion has also been shown to assist in the initiation of SCC, although it is not the only mechanism responsible for SCC. In zone 2, a stable passive film is just beginning to be formed and is not yet stable. Therefore, the metal's surface can easily transfer between active and passive states, resulting in randomly distributed local anodic sites with large cathodic regions driving the formation of electrochemically active crack tips in the presence of tensile stress (Jones, 1996; Landolt, 2007).

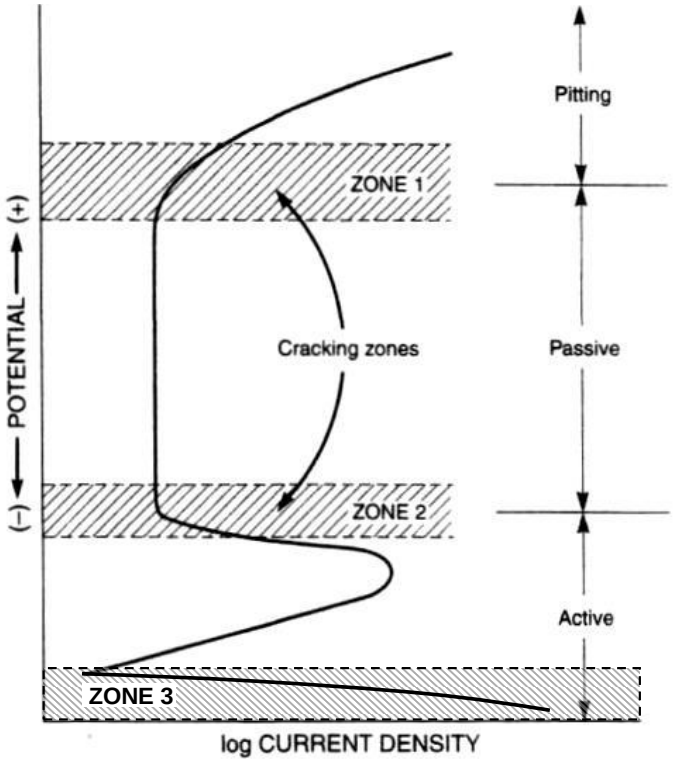

Figure 2.21 Regions of SCC susceptibility (from (Jones, 1996))

While most theories of SCC attribute anodic dissolution of metal at the crack tip to be the driving force for damage, examination of fracture surfaces shows little anodic dissolution of the faces of cracks, indicating combined SCC and mechanical modes of fracture. An example of intergranular SCC induced cracking in a prestressing steel is

shown in Figure 2.22. In Figure 2.22, note the intergranular cracking which is adjacent to the region of ductile fracture of the prestressing steel.

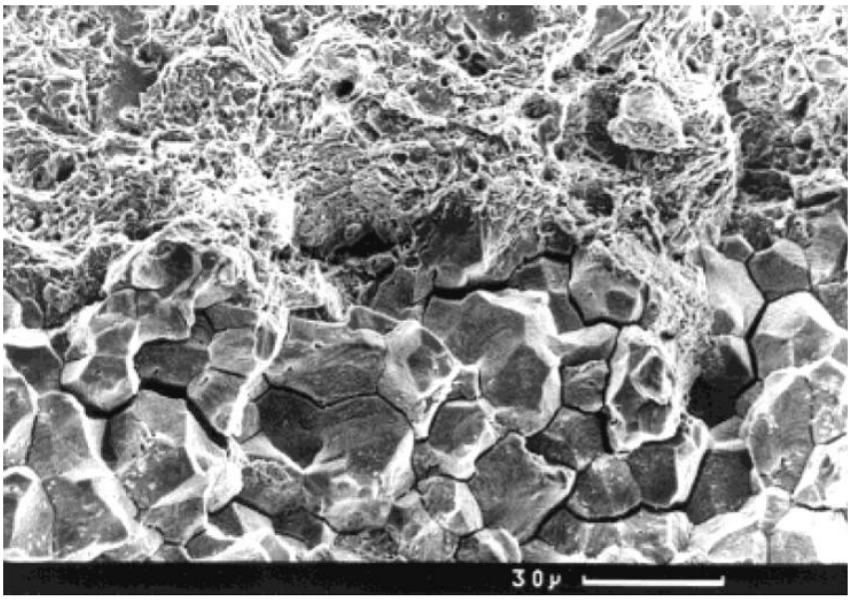

Figure 2.22 Intergranular SCC in eutectoid prestressing steel (from (Mietz, 2000))

2.3.2 Hydrogen Embrittlement of Metals

Damage of metals due to hydrogen diffusing into the crystal structure is referred to as hydrogen embrittlement (HE). Much like SCC, HE results in brittle modes of failure with the initiation of cracks upon tensile loading. Cracks formed by HE are mainly transgranular, as HE typically results in the most damage when occurring in the lattice structure and not at defects and grain boundaries where porosity is relatively high compared to the bulk. HE may occur only when atomic hydrogen is present due to high pressure hydrogen gas or through its generation by cathodic reactions (Nuernberger, 2002). Thus, in civil infrastructure applications, atomic hydrogen may only be generated at sufficient levels of cathodic polarization (under excessive cathodic protection) when

corrosion potentials are such that hydrogen is evolved (see Figure 2.23) (Bertolini, et al., 2004). The corrosion potential at which H_2 is evolved is calculated in V as E = -0.059·pH on the standard hydrogen electrode (SHE) scale.

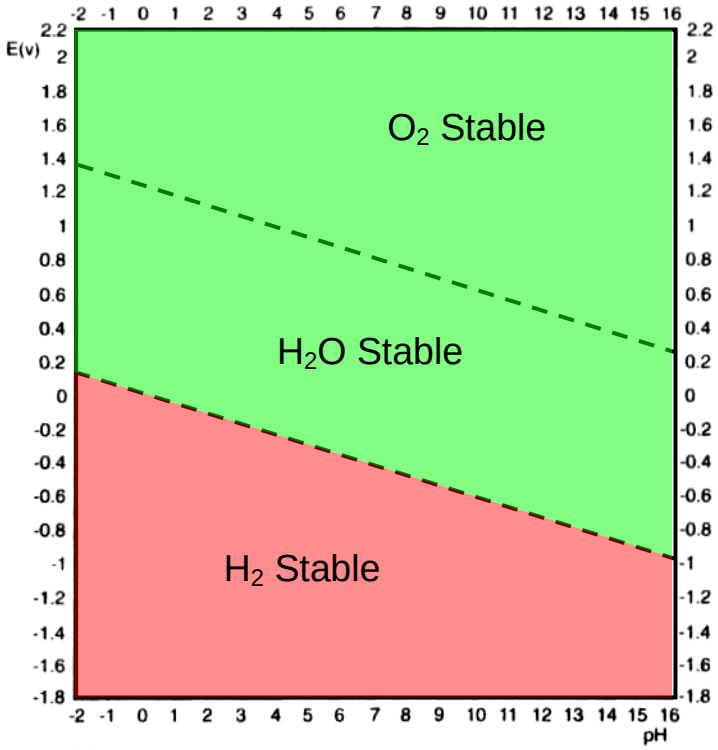

Figure 2.23 Regions of stability for H_2 generation (adapted from (Pourbaix, 1974))

Atomic hydrogen may be present at the metal surface by reduction of water or hydrogen cations in neutral and acidic solutions (Landolt, 2007), respectively:

$$H_2O + e^- \rightarrow H + OH^- \quad (2.11)$$

$$H^+ + e^- \rightarrow H \quad (2.12)$$

Because hydrogen exhibits a +1 oxidation state, it normally reacts to form covalently bonded molecular hydrogen by $H + H \rightarrow H_2$. However, reactions to form molecular hydrogen may be slow, allowing atomic hydrogen present on the surface of the metal to penetrate the lattice before reaction to form H_2 (Skorchelletti, 1976). The formation of expansive hydrides by reaction with Ti, Zn, Hf, V, Nb, Ta, and Pd are also mechanisms for HE (Jones, 1996), but these elements are not typically present in great quantities in alloys used for civil engineering applications. Once atomic hydrogen has entered the lattice, it will occupy interstitial sites and other regions of high porosity, such as grain boundaries and defect / dislocation regions. Interstitial sites for H occupation in BCC and FCC metals are shown in Figure 2.24.

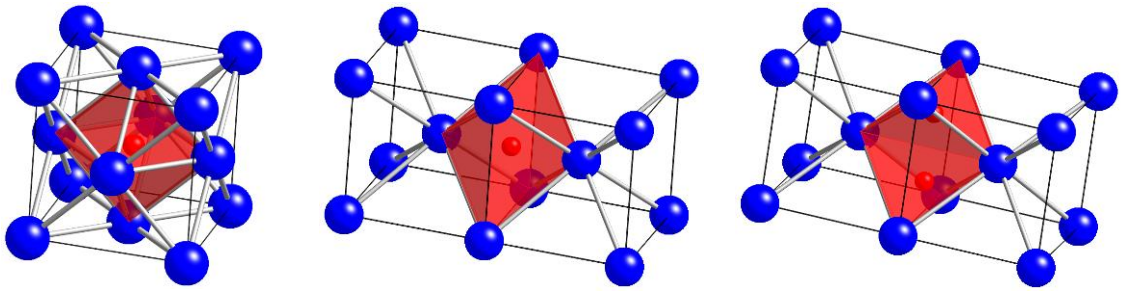

(a) FCC Octahedral Site (b) BCC Octahedral Site (c) BCC Tetrahedral Sites

Figure 2.24 Interstitial sites for H occupation in BCC and FCC metals

With atomic hydrogen present in the crystal lattice, reaction to form molecular H_2 results in expansion and dilation of the lattice as the larger molecule is formed at interstitial and defect sites (Jones, 1996; Skorchelletti, 1976). In addition to straining of the lattice, the present of absorbed hydrogen also limits ductile slip mechanisms, resulting in reduced toughness. Face centered cubic (FCC) metals with larger interstitial sites and

higher ductility are generally less affected than body centered cubic (BCC) metals which have lower H solubility and restricted slip capabilities. Cracks formed by HE are generally transgranular, as the lattice structure itself is most affected by the formation of molecular H_2 (Landolt, 2007). An example of transgranular HE induced cracking in a prestressing steel specimen is shown in Figure 2.25.

Figure 2.25 Transgranular HE of prestressing steel (from (Schroeder and Müller, 2003))

2.4 Corrosion Mitigation Methods in Prestressed Concrete

High performance concretes and large cover thicknesses along with proper design (i.e., limiting cracking) have found the greatest use for corrosion mitigation in PSC structures exposed to corrosive environments.

High performance concretes (HPCs) contribute to increased durability primarily by slowing the ingress of Cl^- with decreased diffusions coefficients. In HPCs, the partial

replacement of cement with supplementary cementitious materials (SCMs) like fly ash, blast furnace slag, silica fume, and metakaolin is common, as are lower water-to-cementitious materials ratios (w/cm). These SCMs participate in pozzolanic reactions in the presence of H_2O and $Ca(OH)_2$. Pozzolanic reactions form supplementary calcium silicate, aluminate, and alumino silicate hydrates which reduce permeability by increasing the tortuosity of the porosity. In addition, supplementary hydrates also provide additional sites for Cl^- binding. HPCs also exhibit lower water-to-cementitious materials ratio (w/cm) of 0.4 or less, resulting in a reduction in both porosity and permeability (the interconnectivity of the pore space). Figure 2.26 illustrates the effect of incorporating SCMs and using a reduced w/cm on the ingress of Cl^- into concrete.

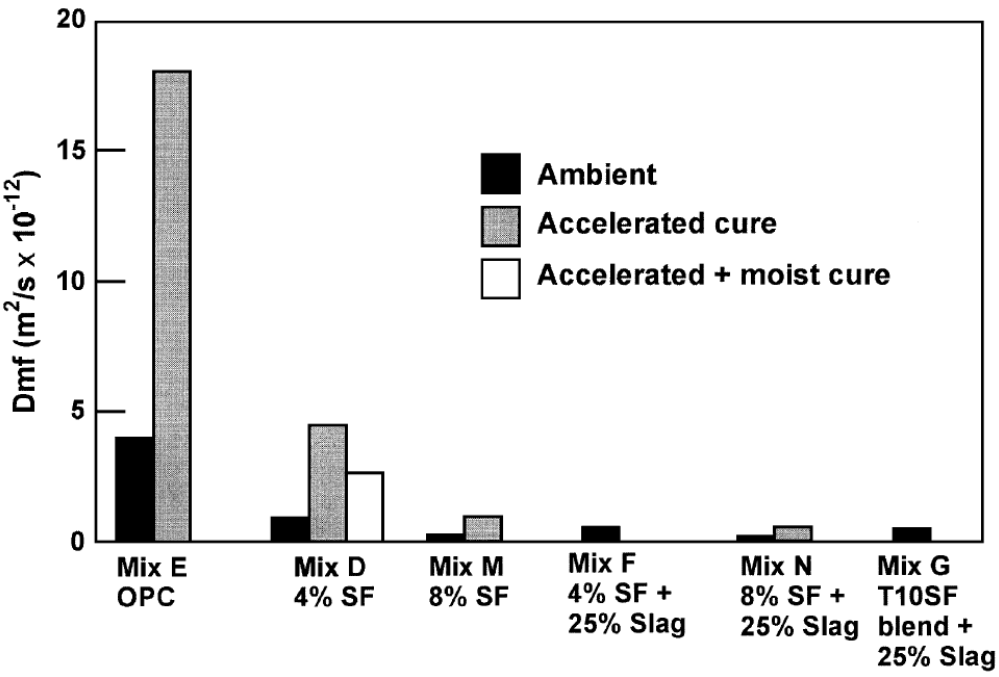

Figure 2.26 Reduction of Cl^- diffusion coefficient with use of SCMs at a w/cm of 0.30 (from (Hooton and Titherington, 2004))

Increased cover thicknesses lengthen the distance that Cl^- must travel ("x" in Equation 2.10), resulting in an increase in the time-to-corrosion initiation. Common cover thicknesses specified in modern construction vary from 25 to 100 mm (1 to 4 in) depending on exposure condition. For RC and PSC structures exposed to marine environments and/or deicing salts, cover thicknesses are generally specified as 75 to 100 mm (3 to 4 in). Finally, with the advent of PSC structural systems, engineers have been able to overcome the weak tensile strength of concrete by applying precompressive stress to the concrete; which through proper design can be tailored to negate tensile stress induced by self weight and external loadings, thus limiting deleterious tensile cracking and increasing durability.

Galvanized coatings and cathodic protection methods have fallen out of favor (and in fact are not allowed in many localities) due to concerns of HE resulting from the excessive generation of hydrogen due to the oxidation of the Zn coating in alkaline concrete or by unintentional cathodic "overprotection" of the steel substrate (Hartt, et al., 1993; Raharinaivo, 2005). Epoxy-coated prestressing strands are currently produced by many manufacturers but have suffered from the undesirable stigma of epoxy-coated reinforcing bars: potential breakdown of bond between the steel and epoxy, and coating defects caused by handling resulting in crevice corrosion (Salas, et al., 2008). In addition, older epoxy-coated prestressing strands were only coated on the external surface of the strand, allowing for moisture to ingress and cause severe corrosion of the interstitial region of the strand. Modern epoxy-coated prestressing strands are "flow-filled" with epoxy that completely filled the interstitial void in the strand.

Fiber reinforced polymeric (FRP) prestressing tendons have been investigated for use in prestressing systems. Investigations of FRP prestressing tendons have focused on reinforcing the matix with aramid (AFRP) and carbon (CFRP) fibers. The largest drawback of these materials is viscoelastic stress relaxation under constant strain. In PSC systems, it is most efficient to minimize any stress relaxation of the prestressing reinforcement (typically less than 2.5 % stress relaxation at 1000 hr with initial loading of 70% ultimate tensile strength). Experimental studies of AFRP and CFRP prestressing tendons have shown stress relaxation of 5 to 10 % with initial loadings of only 60 % of ultimate tensile strength (Saadatmanesh and Tannous, 1999). In addition to the drawback of high stress relaxation, the high cost of manufacturing (especially in CFRPs), limited applied research, shear lag deficiencies, lack of ductility, and concerns related to high temperature and high strain rate behavior have limited the use of FRP prestressing tendons in PSC structures (Salas, et al., 2004).

2.5 Applications of Stainless Steels in Reinforced Concrete

The use of stainless steels as concrete reinforcement can greatly extend the usable service lives of reinforced concrete structures exposed to even the most severe of environments (Hartt, et al., 2004). Such alloys provide exceptional corrosion resistance by the formation of a highly stable passive film resulting from alloying Fe with Cr, Ni, Mo, and N (among others) which maintains the film's integrity over a much wider range of pH and Cl^- concentration. In stainless steels, Cr is the main contributor to increased corrosion resistance by the formation of a high quality nanometer thick chromium oxide

(Cr_2O_3) passive film; the primary function of the film is to increase corrosion resistance by preventing pit nucleation. However, the effectiveness of Cr is only gained if addition is upwards of 12 % by mass in the stainless steel, as evidenced in Figure 2.27. If the passive film is broken down and corrosion pits nucleate, the presence of alloyed Ni, Mo, and N aid in repassivation of the pit. This repassivation can prevent metastable pitting from transforming into stable pit propagation (Newman, 2001). Recent studies in simulated concrete pore solutions have found that in alkaline conditions, the passive film developed on stainless steels may also be composed on Mo-containing compounds and Ni enrichment takes place on the stainless steel substrate below the passive film (Elsener, et al., 2011))

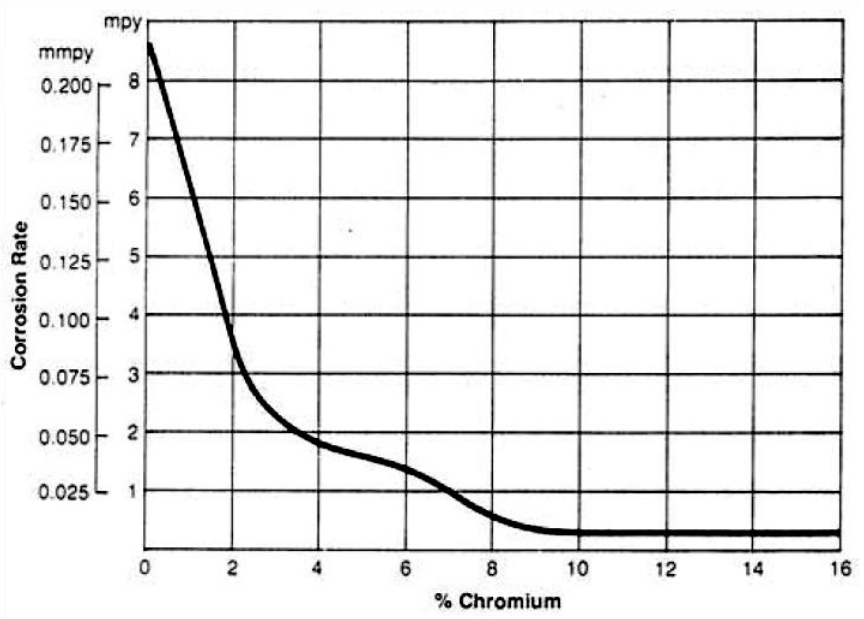

Figure 2.27 Effect of Cr addition on corrosion rate (from (Jacobs and Wozadlo, 1988))

Alloy composition, solution / electrolyte aggressiveness, temperature, and many other factors alter the behavior of polarization curves. For example, Figure 2.28

illustrates the increase in passivity resulting from addition of 10.5 % Cr to steel in an aqueous alkaline environment. The addition of 10.5 % Cr clearly results in increased passivity as evidenced by decreased current densities upon anodic polarization. Polarization curves are specific to the material and environment tested and cannot be used for broad applications of corrosion behavior.

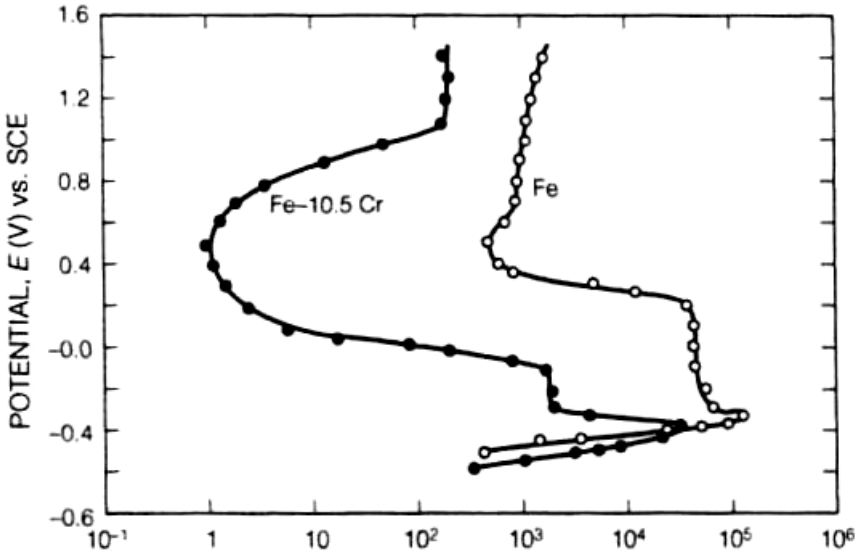

Figure 2.28 Polarization curve for Fe & Fe + 10.5% Cr alloys (from (Jones, 1996))

As shown in the Schaeffler constitution diagram in Figure 2.29, stainless steels can be divided into four different families: austenitic, ferritic, martensitic, and duplex (a mixture of γ-austenite and δ-ferrite). In Figure 2.29, the Ni equivalent has been shown including the DeLong correction to account for the effect of N on austenite stability (DeLong, et al., 1956). The stable phase depends primarily on composition, with Ni, C, Mn, and N acting as austenite stabilizers and Cr, Mo, and Si acting as ferrite stabilizers.

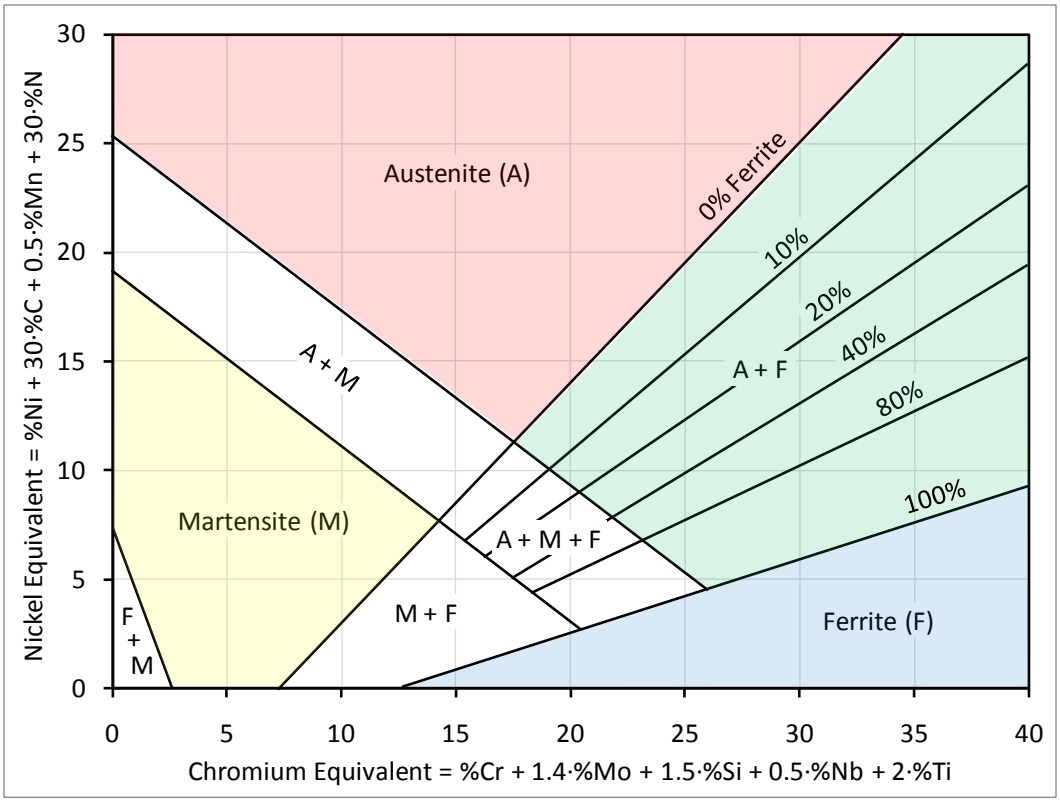

Figure 2.29 Schaeffler constitution diagram for stainless steels (adapted from (DeLong, et al., 1956; Schaeffler, 1949))

Austenitic stainless steels are the most widely used grades of stainless steels. Austenitic stainless steels possess a face centered cubic (FCC) crystal structure which results in high ductility, toughness, and workability when compared with other stainless steels. The corrosion resistance of typical austenitic stainless steels is generally good due to their alloying composition (typically greater than 18 % Cr and 8 % Ni). In the annealed condition, austenitic stainless steels exhibit a fully FCC microstructure and are nonmagnetic. However, phase transformations can occur in metastable alloys under plastic strain. Such phase transformations will be discussed in detail in subsequent sections.

Ferritic stainless steels possess a body centered cubic (BCC) crystal structure and exhibit mechanical properties similar to typical carbon steels. When compared with austenitic grades, ferritic stainless steels have higher yield and ultimate strengths but lower ductility and toughness. Ferritic grades also typically exhibit lower corrosion resistance than austenitic grades due to their lower Cr (12-16 %) and little Ni and Mo.

Martensitic stainless steel present very similar properties as ferritic stainless steels with the exception of increase C content, resulting in high hardness and strength. Corrosion resistance of martensitic stainless steels is thought to be similar to ferritic grades based on composition. Martensitic stainless steels have seen limited application as reinforcing steel due to their excessively high strengths of up to 1200 MPa (174 ksi) in the annealed condition. These high strengths may better suit martensitic stainless steels for use in PSC structures.

Duplex stainless steels contain a dual-phase microstructure of both austenite and ferrite. By combining these two phases together, superior strength is obtained from the ferrite phase and toughness, workability, and corrosion resistance are contributed by the austenite phase. Since 2000, duplex stainless steels have seen increasing use in civil infrastructure applications because of their increased corrosion resistance and decreased cost (lower Ni content) when compared with widely available austenitic grades (Hartt, 2005). In addition to commonly available "workhorse" duplex grades (e.g., 2205), lean duplex grades (e.g., 2003, 2101, 2202, 2304, and 2404) have been developed which display similar mechanical properties and corrosion resistance but with decreased cost by reducing Ni and Mo contents. Generally Mn and N are added to lean duplex grades to stabilize and strengthen the austenite phase.

In the U.S., Canada, and Europe, stainless steels have been increasingly used in bridge decks and coastal bridge substructures to mitigate corrosion. Austenitic grades 304 and 316 and duplex Type 2205 have seen the largest use as reinforcement in concrete, primarily owed to their high availability and the extensive amount of research conducted on their corrosion resistance in concrete (Hartt, 2005). Ferritic grades such as 430 have also been investigated for use as reinforcement in concrete but have seen limited application due to the superior corrosion resistance of readily available austenitic grades (Hartt, et al., 2004). Lower cost lean duplex alloys such as 2101 and 2304 have also been investigated for used as reinforcement in concrete and generally exhibit exceptional mechanical properties and corrosion resistance comparable with 304 and 316 (Clemena, 2003; Dupoiron and Audouard, 1996; Hartt, 2005; Hurley and Scully, 2006). Specialty alloys such as low-Ni, N-charged or Mn rich stainless steels (e.g., ASTM XM-29 / Nitronic® 33) and lean Cr microcomposite steels (e.g., MMFX-II^{TM}) have seen increasing interest recently due to their lower cost (decreased Ni and Mo content) when compared with traditional austenitic grades such as 316 (García-Alonso, et al., 2007; Presuel-Moreno, et al., 2010). Typical elemental compositions for these alloys are shown in Table 2.3. The relative resistance of these stainless steels to chloride-induced pitting corrosion has also been recorded in Table 2.3 as the pitting resistance equivalency number (PREN) calculated according to Eq. 2.13 (Markeset, et al., 2006).

$$PREN = \%Cr + 3.3 \times \%Mo + \beta \times N \tag{2.13}$$

Where: β = 30 for duplex grades
β = 16 for other grades

Table 2.3 Elemental composition and PREN for common stainless steels grades. Typical compositions from (Outokumpu, 2010) and (ASTM A1035, 2009)

Grade	Type	Composition (wt.%) – Fe Balance						PREN
		C	N	Cr	Ni	Mo	Other	
304	Austenitic	0.04	0.06	18.2	8.1	-	-	19.2
316	Austenitic	0.04	0.06	17	11	2.8	-	27.2
XM-29	Austenitic	0.08	0.30	18	3	-	13Mn	22.8
430	Ferritic	0.04	-	16.5	-	-	-	16.5
MMFX-II	Microcomposite	0.15	0.05	9	-	-	1.5Mn, 0.5Si	9.8
2101	Duplex	0.03	0.22	21.5	1.5	0.3	5Mn	29.1
2205	Duplex	0.02	0.17	22	5.5	3	-	37.0
2304	Duplex	0.02	0.10	23	4.8	0.3	-	27.0

The use of stainless steels to replace normal mild steel reinforcement has been shown to provide decreases in maintenance costs of greater than 50% while extending the structure's service life to far greater than 100 years in most applications with only modest increases in initial expenditures (Cramer, et al., 2002). Construction costs also can be decreased by utilizing stainless steels in only the most critical regions of a structure (e.g., the top map of a bridge deck or the piles and pile caps of a coastal bridge substructure). One of the best examples of the performance of stainless steel reinforcement is the Progreso Pier located on Mexico's Yucatan Peninsula, constructed using 220 tons of 304 reinforcing steel in an extremely corrosive environment. The pier, built in 1939 with poor quality concrete and a cover thickness of 25 mm (1 in), is now over 70 years old and remains is excellent condition (see Figure 2.30), while a companion pier built in 1979 with normal ferritic mild steel reinforcement had to be demolished due to corrosion damage after two decades of service (Knudson and Skovsgaard, 1999).

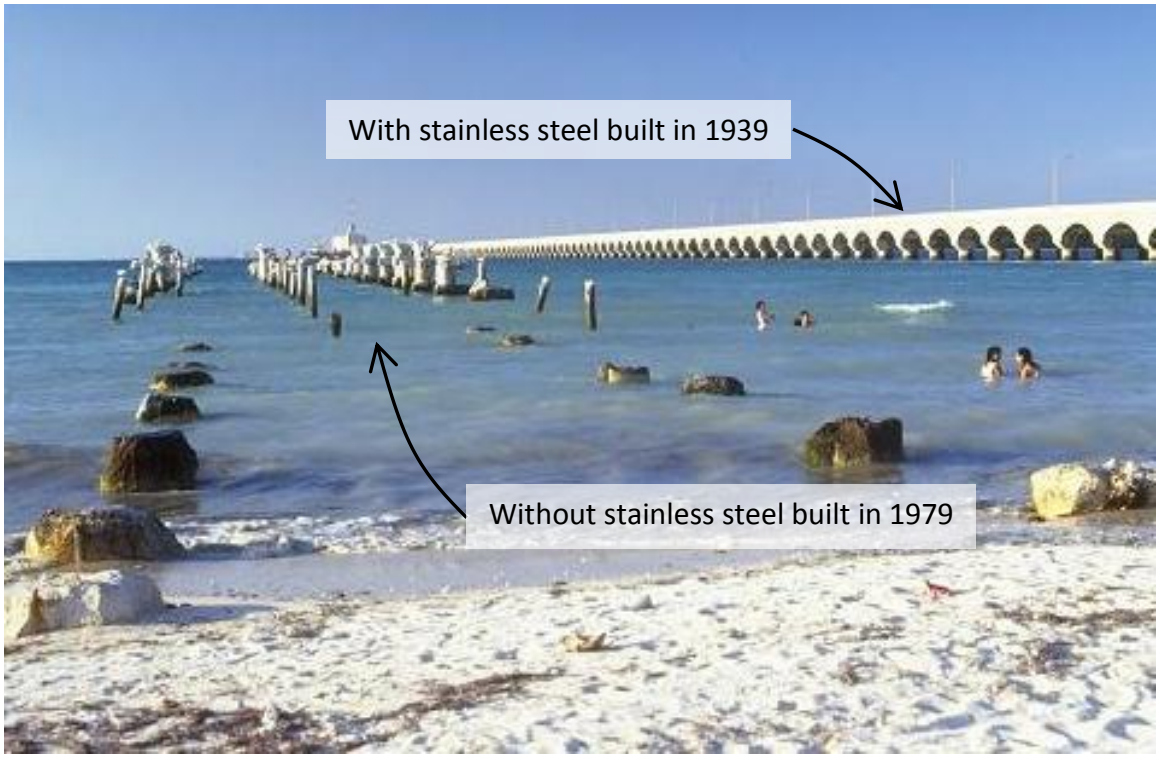

Figure 2.30 Progreso pier located on the Yucatan Peninsula in Mexico (from (Arnvig and Houska, 2010))

With the success of stainless steels when utilized in reinforced concrete structures, their use is PSC structures may provide a means to corrosion mitigation which warrants further investigation. As presented by Schupack (Schupack, 2001) and as discussed below, limited research (particularly applied research) has been conducted on the use of stainless steels as prestressing reinforcement for concrete structures. The following section reviews the limited previous research conducted on high-strength stainless steels (HSSSs) for application in PSC and in other industries.

2.6 High-Strength Stainless Steels for Corrosion Mitigation in Prestressed Concrete

2.6.1 Austenitic Stainless Steel Grades 304 and 316

The most significant investigations of austenitic HSSSs for PSC applications stem from recent research conducted as a part of COST Action 534 – New Materials and Systems in PSC Structures, an effort supported by the European Union (Alonso, 2007; Alonso and Recio, 2007; Alonso, et al., 2008; Nürnberger, 2003; Nürnberger and Wu, 2005; Nürnberger and Wu, 2008; Wu and Nürnberger, 2009). HSSSs of grades 304, 316, and 316LN (a low C, N-charged grade) were cold drawn until achieving ultimate strengths in the range of 1400 to 1850 MPa (203 to 268 ksi). Stress relaxation of these HSSSs was found to be approximately 7 % (much higher than the 2-3 % typical for prestressing steels). Higher strengths were achieved with 304 when compared with 316. This result is expected as metastable 304 likely transforms from face centered cubic (FCC) γ-austenite to body centered cubic (BCC) α′-martensite (Dash and Otte, 1963). Given the large cold reductions used to achieve these high strengths, α′-martensite volume contents exceeding 50 % can be expected in 304 (Milad, et al., 2008).

Corrosion susceptibility of these alloys was evaluated using potentiodynamic polarization techniques on samples exposed to simulated concrete pore solutions with Cl^- added up to 2.5 M concentration (Alonso, 2007) or embedded into alkaline or carbonated mortar cylinders with 5 wt.% Cl^- by weight of cement. Using this technique, corrosion susceptibility is clearly indicated by the formation of a breakdown potential as in Figure 2.31 prior to entering the O_2 evolution region (Hurley and Scully, 2006) indicating that the threshold resistance for chloride-induced corrosion has been exceeded. The results of

these studies suggest that 304, 316, and 316LN are resistant to corrosion initiation up to Cl^- concentrations of 1.5 M, above which SAE 304 becomes susceptible while 316 and 316LN remain resistant. Even though 304 was found to be susceptible to corrosion initiation above Cl^- concentrations of 1.5 M, the typical Cl^- concentration of seawater does not exceed 0.5 M.

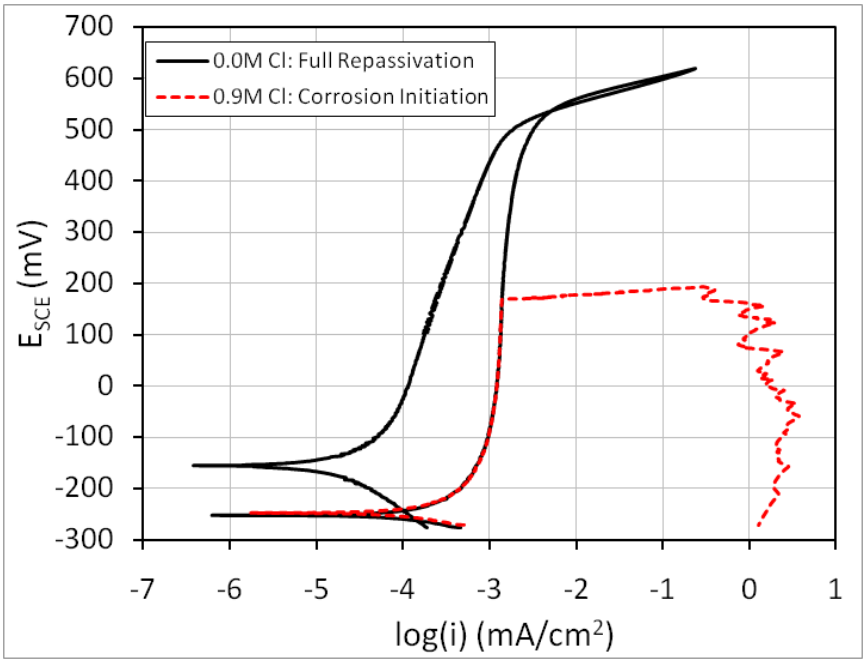

Figure 2.31 Polarization behavior of prestressing steel in simulated concrete pore solution with 0.0M Cl^- and 0.9M Cl^- exposure

Similar performance of 304 was also observed in tests conducted in Cl^- containing mortars (Wu and Nürnberger, 2009). Figure 2.32 summarizes the results of testing conducted in alkaline and carbonated mortars for samples with and without cold drawing. The researchers state that the poor performance of 304 was most likely due to the presence of ά-martensite which initiated pitting by galvanic microcells occurring between martensite inclusions (which function as anodic sites) and the surrounding austenite

phases. In all cases, 316LN provided the highest resistance to pitting corrosion, with little to no degradation even in the case of a carbonated Cl^- containing mortar embedments. Thus, the researchers concluded that 316 grades tested should provide acceptable corrosion resistance, while corrosion of 304 may be a concern.

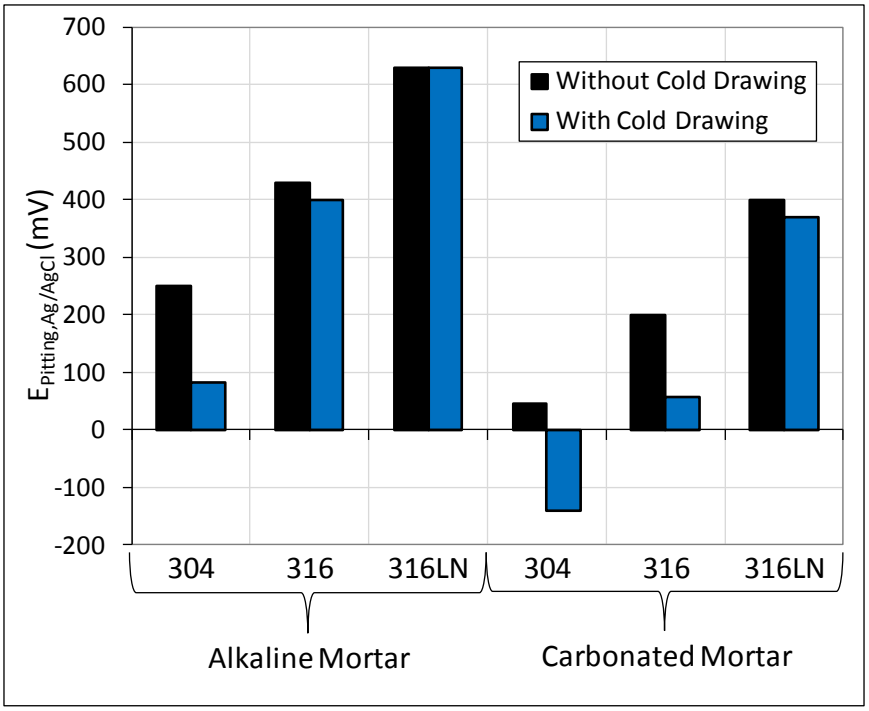

Figure 2.32 Pitting potential of HSSS embedded in alkaline and carbonated Cl^--containing mortars (adapted from (Wu and Nürnberger, 2009))

Chloride-assisted SCC was evaluated using U-bend specimens placed in Cl^--containing solutions with pH of 4.5 (such as in an ungrouted post-tensioning duct), 8.5 (typical of carbonated concrete), and 12.1 (alkaline concrete) at temperature between 30 and 80 ºC (176 ˚F). Only 304 was found to be susceptible to SCC in pH 4.5 and 8.5 environments and thus may not be acceptable for use if such exposure is anticipated. The

researchers again attributed the reduced stress corrosion performance of 304 to inclusions of α′-martensite. 316 maintained resistance to Cl^--induced SCC in all ranges of pH.

2.6.2 Nitronic® 33 Nitrogen-Strengthened Austenitic Stainless Steel

One of the first studies investigating the use of HSSS for PSC applications was lead by the Naval Facilities Engineering Command (Jenkins, 1987). The primary goal of this study was to develop a high-strength non-magnetic prestressing steel for use in concrete piling to be placed in a military deperming facility where ships and submarines are serviced to reduce their magnetic signature. Consequently, an austenitic stainless steel with high resistance to the formation of ferromagnetic α′-martensite was desired in order to preserve paramagnetic properties even under excessive cold drawing. A nitrogen-strengthened high Mn proprietary alloy known as Nitronic® 33 (ASTM XM-29) was cold drawn and produced as 7-wire prestressing strand. The resulting strand exhibited an ultimate strength of 938MPa (136 ksi), and ε_{ult} of 33.3 %. No stress relaxation values were reported. Mechanical properties were far below those required for most prestressing systems, although strengths as high as 1650 MPa (240 ksi) have been achieved using the same alloy in more recent unpublished studies (Insteel Industries, 2002).

Durability testing of the Nitronic® 33 HSSS focused on chloride-induced corrosion, with no investigation of SCC and HE. Preliminary testing conducted in mortar extracts with the addition of Cl^- at pH values between 10.0 and 12.1 found that normal carbon prestressing steel suffered significant corrosion at a pH of 11.6 with a small addition of 200 ppm Cl^-, while Nitronic 33 suffered no damage even at a pH of 10.0 and 6000 ppm Cl^-. Further testing performed in cracked concrete specimens exposed to seawater solutions showed that corrosion initiated on carbon prestressing steels, while

Nitronic 33 remained passive in all cases. Full-scale PSC piles constructed using Nitronic 33 prestressing strands were also included in the study. Nondestructive potential measurements indicated that corrosion may have initiated on the Nitronic 33 HSSS. Upon forensic autopsy of the piles, corrosion was only found to be occurring on carbon steel wire ties used to secure the Nitronic 33 HSSS prestressing strands with no damage found on the strands themselves. Subsequent inspection of piles using Nitronic 33 HSSS placed in the Port of Tacoma Washington has shown no corrosion initiation (Jenkins, 1987).

2.6.3 Duplex Stainless Steel Type 2205

The only documented research which has examined a duplex grade HSSS for PSC was performed by the Shinko Wire Company in collaboration with Kyoto University (Shirahama, et al., 1999). The duplex HSSS investigated was similar in composition to Type 2205 with σ_{ult} of 1636 MPa (237 ksi) and ε_{ult} of 4.0 % following cold drawing and stranding. Stress relaxation of 0.5 % for the duplex HSSS was also similar to normal prestressing steel when tested by an accelerated 10 hour method. These results indicate that the mechanical behavior of 2205 duplex HSSS may be far superior to the austenitic HSSSs discussed in Section 2.6.1.

In addition to mechanical testing, durability tests examined the susceptibility to damage by chloride-induced corrosion, exposure nitrate containing solutions, and HE. Pitting corrosion time-to-failure tests were performed on duplex HSSS stressed to 80 % σ_{ult} while immersed in a 3 % NaCl solution maintained at 90 ºC. The tests were stopped after 350 hours when failure had not occurred. H-SCC resistance was evaluated using the FIP test method (Elices, et al., 2008). The developed duplex HSSS did not fracture even after 350 hours of exposure, while the eutectoid prestressing steel failed after 8 hours.

These results, when combined with mechanical behavior, indicate that the developed duplex HSSS with composition similar to Type 2205 provides the better balance between mechanical performance and corrosion resistance, particularly when compared to austenitic HSSSs.

2.6.4 Developments in Other Industries

While the aforementioned studies have provided many useful insights into the use of HSSSs for corrosion mitigation in PSC systems, developments from other industries also warrant investigation. A majority of research on HSSSs has been conducted in the aerospace and spring wire industries. In the case of spring wire, it is not high tensile strength which is desired, but rather a high range of linear-elastic behavior. HSSS research in these industries has mainly focused on techniques to strengthen readily available grades such as 304 and 316. The replacement of C with N, or the addition of N along with C has been shown to be an extremely effective means of strengthening austenitic grades in conjunction with cold drawing (Shanina, et al., 2002). N has been shown to be an effective solid-solution strengthener, has a much higher solubility than C (0.4 wt.% and up to 1 wt.% if high pressure melting techniques are employed), and N also acts as an austenite stabilizer (i.e., prevents the formation of α′-martensite) (Simmons, 1996). Figure 2.13 illustrates the effectiveness of N addition along with cold drawing at increasing the strength of austenitic stainless steels to levels similar to those used in prestressing applications (i.e., 1500 to 1900 MPa (217 to 275 ksi)).

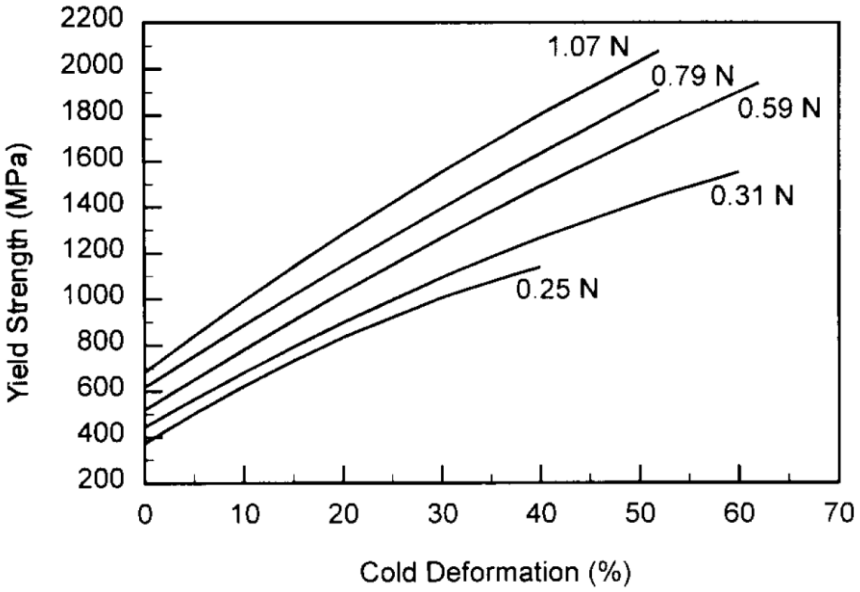

Figure 2.33 Influence of N addition and cold deformation on yield strength (from (Stein and Witulski, 1990))

Precipitation hardenable (PH) stainless steels such as 15-5, 17-4, and 17-7 have long been used in the aerospace industry for their moderate corrosion resistance and high tensile strengths (approximately 1000 MPa (145 ksi) in the annealed condition) which can be increased through cold drawing. PH stainless steels have received little attention as reinforcement in concrete as even their annealed strengths far exceed the typically required tensile strengths of reinforcing steels of approximately 500 MPa (72 ksi) . However, given the high desired tensile strengths of prestressing reinforcement, PH stainless steels may make an ideal candidate. Semiaustentic PH grade 17-7 is one of the most used HSSS in the spring wire industry as it readily work hardens by a transformation from an austenitic to fully martensitic microstructure, resulting in strengths of up to 1800 MPa (261 ksi) in the range of wire diameters used in prestressing strands (Izumida, et al., 2005).

More recent work in the spring wire industry has resulted in the development of high- and super-high-strength duplex stainless steels with tensile strengths exceeding 1500 MPa (217 ksi) in the range of wire diameters typically used in prestressing strand (Chai, et al., 2007). While limited research has been conducted on the corrosion resistance of these newly developed duplex HSSSs, based on the results presented in Section 2.4.3, further investigation of common duplex grades such as 2205 as well as new lean grades such as 2003, 2101, and 2304 for PSC applications is warranted.

2.6.5 Challenges of Development and Implementation

While the use of HSSSs will likely yield similar improvements in durability witnessed when using stainless steel in reinforced concrete structures, many challenges exist in implementing HSSSs in PSC structural systems, mostly stemming from the structural design and production standpoints. When compared with currently used eutectoid prestressing steels, most stainless steels exhibit very poor ductility and toughness when produced at strengths exceeding 1500 MPa (225 ksi). Figure 2.34 depicts the trends in stress vs. strain behavior for 304 stainless steel from the annealed condition up to a 50 % areal reduction by cold drawing. While there is an expected decrease in ductility corresponding to an increase in yield and ultimate strength, most troubling is the reduction in post-yield strain hardening. At cold reductions above 40 %, little to no post-yield strain hardening is observed, with failure occurring by immediate strain localization rather than ductile behavior. From a structural designer's perspective, this behavior is concerning in that energy dissipation resulting from post-yield strain hardening cannot be relied upon as a means to improving the redundancy of a PSC structural system.

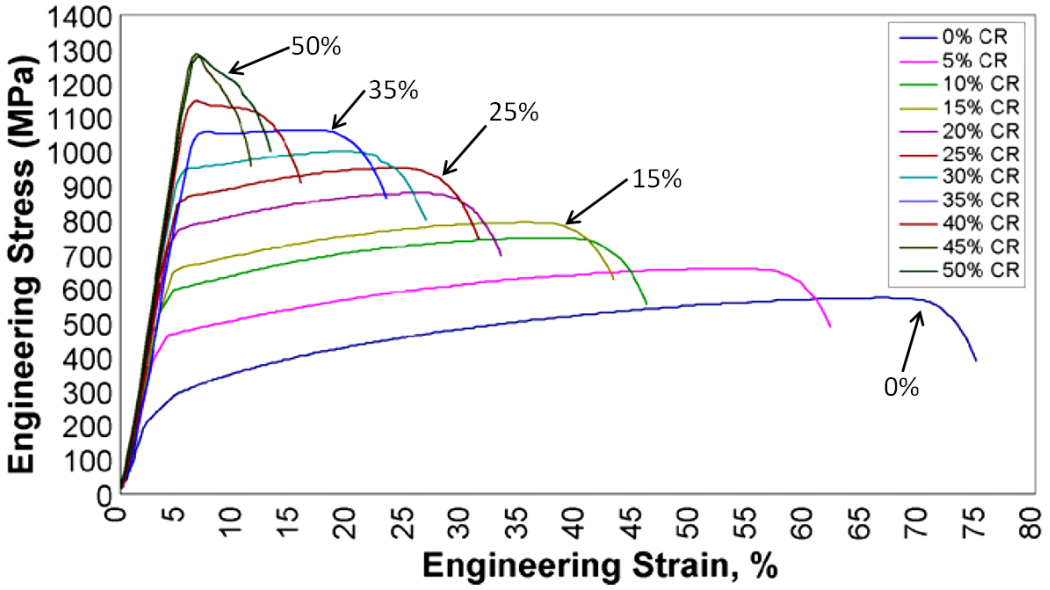

Figure 2.34 Influence of cold deformation on the stress vs. strain behavior of 304 stainless steel (from (Milad, et al., 2008))

Another factor to consider is the linear-elastic behavior of HSSS knowing that, if designed properly; prestressing steels will operate well below stress levels where global yielding occurs in service. Figure 2.35 shows the typical difference in stress vs. strain behavior between stainless and carbon steel, with stainless steels generally exhibiting a poorly defined yield point when compared with carbon steels (Gardner, 2005). When significant cold working is introduced, the yield point becomes even more poorly defined as illustrated in Figure 2.36.

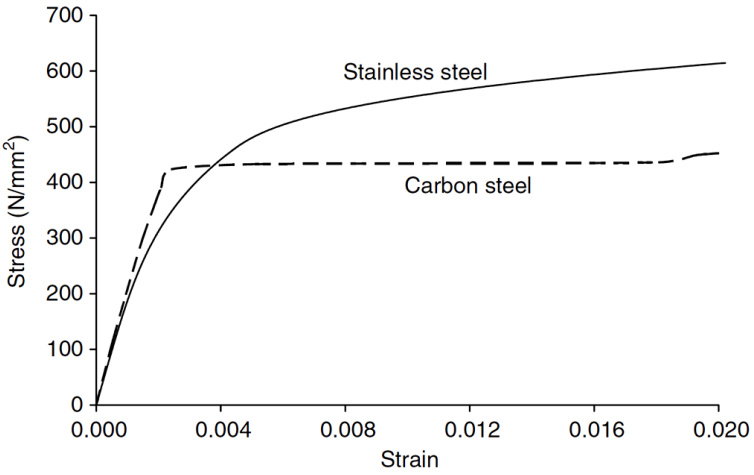

Figure 2.35 Comparison between the stress vs. strain behavior of stainless steel and carbon steel (from (Gardner, 2005))

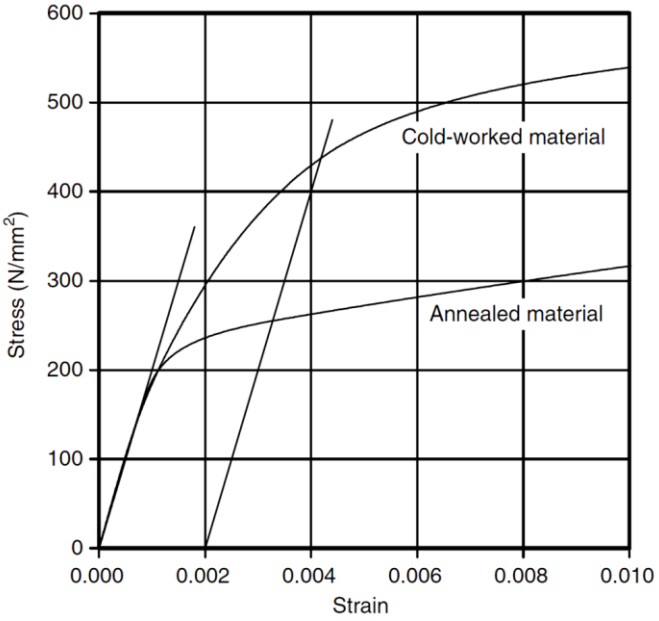

Figure 2.36 Influence of cold work on stress vs. strain behavior (from (Gardner, 2005))

In order to be applied in PSC operations, HSSSs will likely need to be manufactured in a stranded geometry similar to that of currently produced eutectoid prestressing steels. Stranding is performed in a skip strander by winding six wires

helically around a center wire with all stresses remaining elastic (if the strand was not confined the wires would unwind). To preserve the stranded geometry, the steel is heated to approximately 370 ˚C (700˚F) while under tensile stress, causing the steel to "relax" into the stranded geometry as a part of the low-relaxation treatment (Osborn, et al., 2008). In most modern prestressing strand production facilities, this heating of the strand is conducted using high efficiency induction heaters which take advantage of the ferromagnetic properties of eutectoid prestressing steels. This heating process raises the question of how to actually form a strand when using HSSSs, especially if the steel is paramagnetic (e.g., 304, 316, or Nitronic® 33). HSSSs which have been produced as strands in the past were generally stranded using older technologies which form a stranded geometry using plastic deformation of the individual wires while stranding. Considering these factors, HSSSs which exhibit ferromagnetic properties such as martensitic PH grades may be more viable for the large-scale production of stainless steel prestressing strand.

CHAPTER 3

CORROSION BEHAVIOR OF A416 PRESTRESSING STRAND

A majority of prior research has focused on the corrosion of mild steel reinforced concrete structures, with relatively less research effort devoted to prestressed concrete (PSC). When compared with low-carbon ferritic mild steels used in reinforced concrete structures, high-strength prestressing steels are fundamentally different in composition (Nawy, 2000), surface condition (Diaz, et al., 2009), and – most importantly – the stranded geometry they are typically produced in; all of which likely play a role in their corrosion behavior in concrete. Consequently, the vast amount of knowledge gained from research conducted on the corrosion of mild steel reinforcement in concrete is not directly applicable to PSC systems when considering the underlying mechanisms of corrosion initiation in prestressing steels.

Previous research evaluating the corrosion resistance of prestressing steels can generally be divided into two categories: (1) small-scale electrochemical studies conducted with and without stress in simulated concrete pore solutions using prestressing wires (Cherry and Price, 1980; Diaz, et al., 2009; Hartt, et al., 1993), and (2) large-scale studies using prestressing strand embedded in concrete and exposed to chloride containing solutions (Ahern, 2005; Trejo, et al., 2009). Relatively few studies have considered the crevice effects associated with stranded geometries or the influence of as-received surface coatings (i.e., most used polished samples) on the electrochemical behavior of prestressing steels (Brooks, 2003; Proverbio and Bonaccorsi, 2002). Of these,

only qualitative relationships between the presence of crevices between wires in a stranded geometry and alterations in corrosion resistance were examined.

3.1 Research Objectives

This chapter presents the results of a study examining the corrosion behavior of A416 prestressing steel strand considering crevice effects and surface imperfections. The primary objectives of this study were: to quantitatively determine the impact of crevices caused by stranding on the chloride-induced corrosion resistance of prestressing steels, to determine if the presence of imperfections in as-received surface coatings influences corrosion behavior, to develop a model describing corrosion initiation processes in prestressing strands in concrete, and to determine the influence of stranding on the service lives of PSC structures. In addition, specimen geometries and experimental methods developed for studying the corrosion behavior of A416 prestressing strand are used to evaluate the corrosion resistance of high-strength stainless steels, the results of which are presented in Chapter 6.

3.2 Experimental Program

Single wire and stranded prestressing steel specimens were produced with their as-received surface coatings left intact. Specimens were exposed to a simulated concrete pore solution with additions of NaCl and evaluated using cyclic potentiodynamic polarization (CPP) techniques. Following testing, samples were characterized using

optical and scanning electron microscopy (SEM) coupled with elemental analysis by energy dispersive X-ray spectroscopy (EDX). Select additional electrochemical experiments were performed to validate proposed corrosion damage mechanisms based on the results of polarization experiments.

3.2.1 Materials

Prestressing steel used for all experiments was produced by MMIStrandCo, LLC (Newnan, GA) with a diameter of 15.2 mm (0.6 in) in the stranded 7-wire geometry (see Figure 2.10). The chemical composition of the steel used was determined by Applied Technical Services Inc. using combustion and ion-coupled plasma atomic emission techniques and is recorded in Table 3.1. As is typical for cold drawn prestressing steels, a highly anisotropic pearlitic microstructure was observed with alternating lamellae of ferrite (white) and cementite (black) oriented longitudinally in the direction of cold drawing as illustrated in the electron micrographs shown in Figure 3.1 by wet etching in a 2 % Nital solution. The electron micrograph shown in Figure 3.2 depicts the disordered morphology of the as-received $ZnPO_4$ surface coating on the prestressing steel. Both the morphology and composition of the as-received surface coating are evidence of flaws generated during cold drawing and subsequent thermomechanical processing during strand production (Osborn, et al., 2008).

Table 3.1 Elemental composition of prestressing steel

Element	C	Mn	P	S	Si	Cr	Ni	Mo	Cu	V	Fe
Weight %	0.81	0.73	0.009	0.005	0.24	0.04	0.06	0.01	0.11	0.08	Bal.

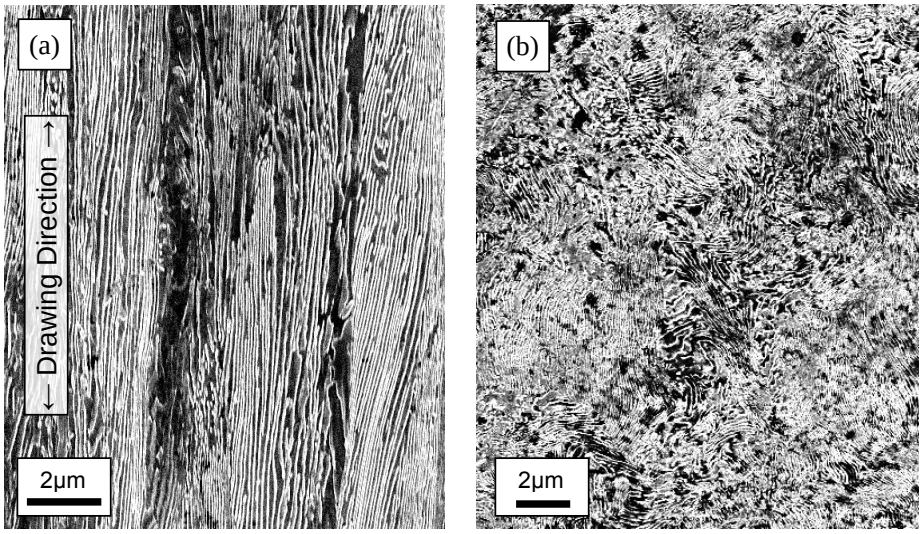

Figure 3.1 Pearlitic microstructure of prestressing steel obtained by wet etching in a 2% Nital solution in (a) longitudinal and (b) transverse orientations

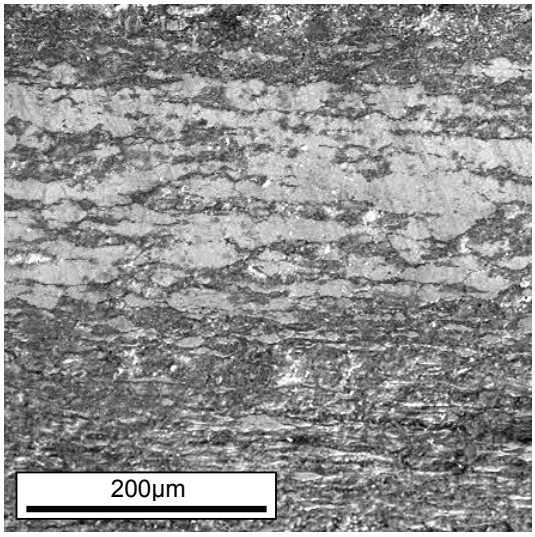

Figure 3.2 As-received $ZnPO_4$ surface coating on prestressing steel

3.2.2 Fabrication of Test Specimens

Two specimen geometries were developed through numerous trials to simulate a single prestressing wire and a 7-wire prestressing strand. The fabrication techniques used to produce both specimen geometries are described briefly below.

3.2.2.1 Wire Specimen Geometry

Figure 3.3 depicts a typical completed wire specimen. The center wire of a 7-wire prestressing strand was extracted and used to fabricate prestressing wire corrosion test specimens. A slow-speed diamond wafering saw was used to cut 63.5 mm (2.5 in) long segments of the center wire. Polyolefin heat-shrink tubing was applied to the upper portion of the specimen to eliminate any air / solution interface effects. A polytetrafluoroethylene (PTFE) plug was affixed with epoxy to the end of the specimen to be immersed in the solution to isolate only the $ZnPO_4$ coated surface to the testing solution. Silicon adhesive sealant was applied circumferentially around the top and bottom of the area to be exposed to the testing solution as to prevent crevice corrosion from occurring under the heat shrink tubing or the PTFE plug. The wire specimen had an exposed area of 3.5 cm^2 (0.54 in^2).

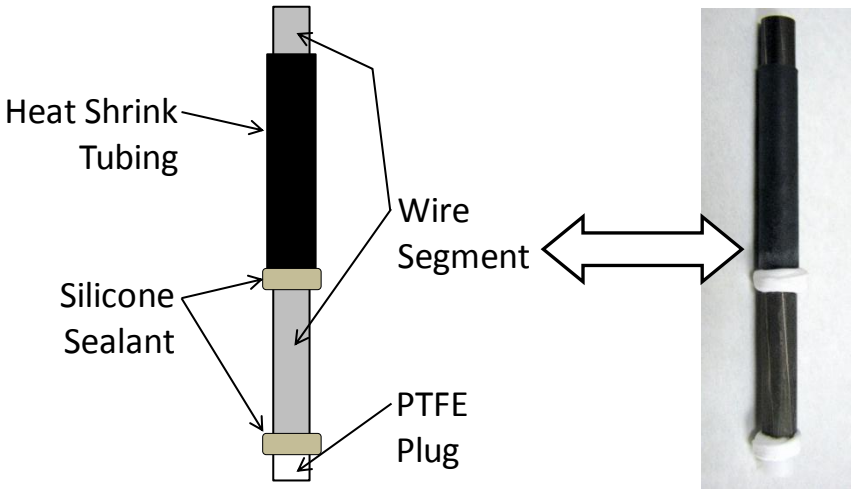

Figure 3.3 Overview of prestressing wire specimen configuration

3.2.2.2 Strand Specimen Geometry

Figure 3.4 depicts a typical completed strand specimen. All strand specimens were fabricated using as-received 7-wire prestressing strand. A slow-speed diamond wafering saw was used to cut 37 mm (1.46 in) long segments of the prestressing strand. In order to preserve the original geometry of the strand (helical twist and impingement locations between wires), plastic cable ties were secured along the segment prior to prevent movement of the wires during cutting. Following cutting, the segments were ultrasonicated in ethanol to remove any oils, metal shavings, or debris lodged in the interstices of the strand. The seven wires of the strand were then soldered together and to an electrical lead to be connected to the potentiostat. To ensure that only the $ZnPO_4$ coated surface would be exposed to the testing solution and to seal off the soldered connections, both ends of the specimens were potted in epoxy (Sikadur 32 Hi-Mod) which had a viscosity that allowed it to properly encapsulate the strand without wicking up into the interstices. Once the epoxy had cured, the cable ties were removed and the specimen could be tested. The strand specimen had an exposed area of 24.5 cm^2 (3.80 in^2).

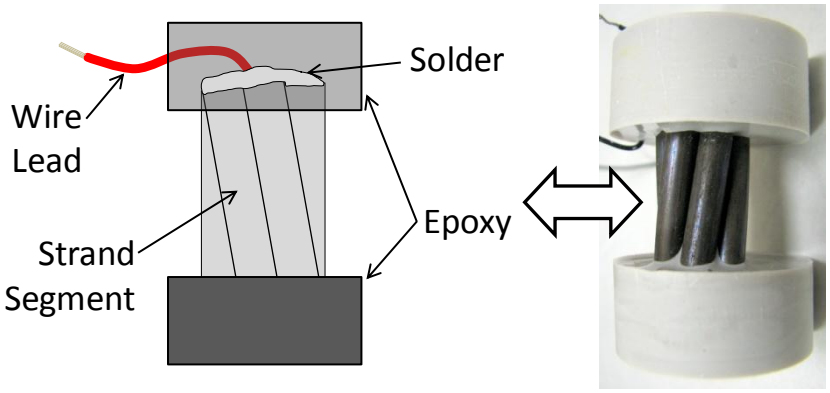

Figure 3.4 Overview of prestressing strand specimen configuration

3.2.3 Testing Procedures

All experiments were performed at 24 ˚C (75˚F) in a solution prepared using deionized water based on a composition present in the pore space (i.e., a pore solution) of the hydrated cement paste of a typical concrete with composition shown in Table 3.2 (Page and Vennesland, 1983; Poursaee and Hansson, 2007). The resulting solution possessed a pH of approximately 13.6. Chlorides (Cl^-) were added to solutions with NaCl up to 1.0 M concentration in steps of 0.1 M (i.e., 0.0 M, 0.1 M, 0.2 M, and so on). It should be noted that testing conducted in simulated concrete pore solutions is not fully representative of the actual conditions present in concrete and should only be used as a comparative indicator of performance (Trejo and Pillai, 2004). All CPP experiments were conducted in a basic three-electrode electrochemical cell similar to that shown in Figure 3.5 with a platinum foil counter electrode with surface area of 4 cm^2 (0.62 in^2), a saturated calomel reference electrode (SCE), and the working electrode being either the wire or strand specimen. Wire specimens were tested in a solution volume of 250 ml (8.45 oz) while strand specimens were tested in a solution volume of 700 ml (23.67 oz). These solution volumes were used in order to meet minimum solution volume-to-specimen surface area requirements of 0.2 ml/mm^2 (4.36oz/in^2) outlined in ASTM G 31.

Table 3.2 Composition of simulated concrete pore solution

Compound	KOH	NaOH	$CaSO_4 \cdot 2H_2O$	$Ca(OH)_2$	NaCl
Conc. (g/L)	17.94	5.24	0.55	2.40*	Varies

*Mostly precipitated out of solution

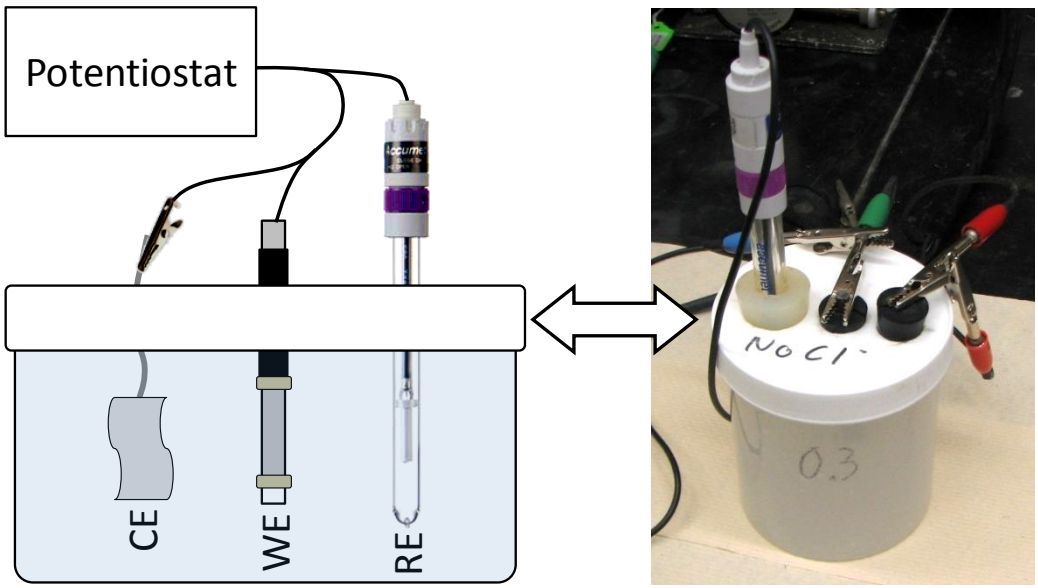

Figure 3.5 Three electrode electrochemical cell used for CPP experiments

Prior to CPP testing, a two-step sample conditioning procedure was used for each sample tested in order to ensure that a stable passive film had formed prior to Cl^- exposure. First, specimens were exposed to the simulated pore solution without Cl^- for 90 min in order to stabilize the passive film as it would be in the field prior to any Cl^- exposure. Following the 90 min passivation period, specimens were transferred without drying into a pore solution containing the Cl^- concentration to be tested and allowed to acclimate for an additional 30 min, yielding total sample conditioning time of 120 min prior to testing. Time periods selected for sample conditioning were based on open circuit potential (OCP) vs. time studies which showed that after approximately 90 min the OCP began to stabilize as shown in Figure 3.6.

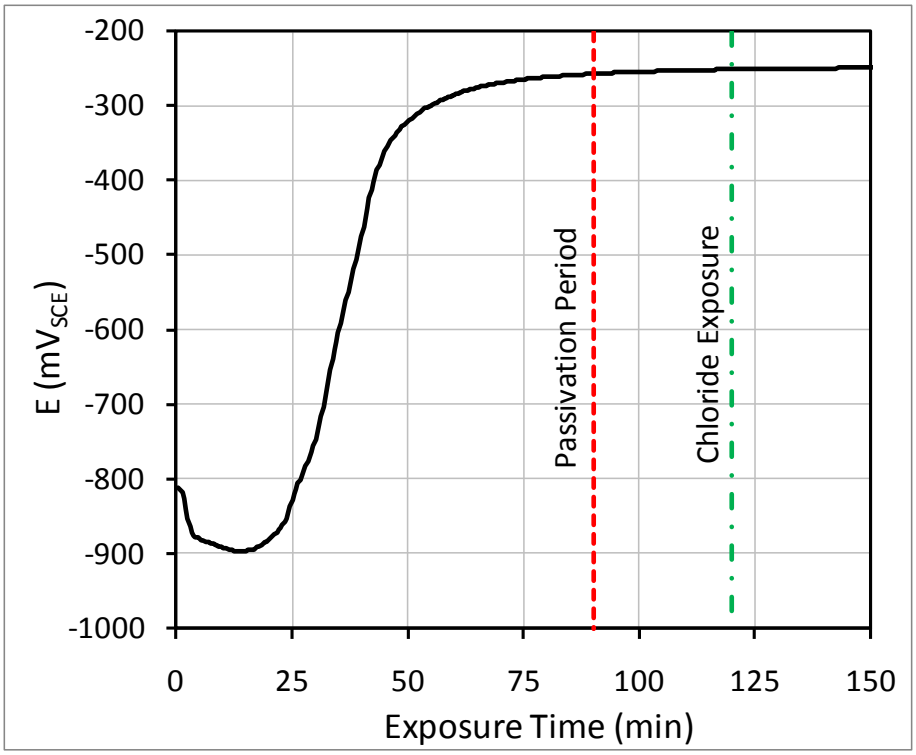

Figure 3.6 Open circuit potential vs. time for prestressing wire immersed in simulated concrete pore solution without chlorides

Following the 120 min sample conditioning period, CPP was used to evaluate each specimen's resistance to corrosion initiation when exposed to a given Cl^- concentration. It is important to note that each experiment utilized a new sample that underwent its own sample conditioning procedure. CPP experiments were performed using GAMRY PC3/300, PC4/750, and Reference 600 potentiostats and an EG&G-PAR 263A potentiostat. A scan rate of 0.1 mV/s was used for all tests. Scans began at -25 mV vs. OCP (to limit cathodic film removal) and were run until reaching a current density of 0.25 mA/cm^2 (1.62 mA/in^2), at which point the scan rate was reversed and the potential was brought back down to -25 mV vs. the original OCP. The maximum current density of 0.25 mA/cm^2 (1.62mA/in^2) generally corresponded to an increase in current of

approximately two decades due to either O_2 evolution or the initiation of localized corrosion. Following each experiment, tested samples were thoroughly examined to ensure that no unintended crevice corrosion had occurred due to poor sample preparation techniques. If, for example, unintended corrosion was found under heat shrink tubing in one of the wire specimens, the data were disregarded, and a new test was performed with a new specimen.

Using CPP techniques, corrosion initiation was clearly indicated by a sudden increase in current density during the anodic scan occurring at the breakdown potential ($E_{breakdown}$), with the current density remaining high even as the potential is reduced during the reversed scan (Alonso, et al., 2002; Bertolini and Redaelli, 2009). An example of this is shown in Figure 6 for prestressing wire specimens, where no corrosion initiation occurs under a 0.0 M Cl^- exposure whereas when exposed to a 0.9 M Cl^- solution localized corrosion clearly initiates with the current density remaining high through the remainder of the test. If corrosion was observed to initiate during CPP scans, the post-test E_{corr} was measured by leaving the sample in the testing cell until it achieved a stable OCP. Samples generally required at least 6 hr following CPP testing to achieve a stable OCP. If corrosion did not initiate, the post-test E_{corr} was recorded using the reverse portion of the CPP scan.

One important factor to consider in any electrochemical experiment (particularly CPP studies) is the inherent variability in corrosion initiation and the $E_{breakdown}$ at which it may occur (Li and Sagues, 2002). These effects become especially important when evaluating localized corrosion which is highly dependent on the random presence of

surface defects to provide initiation sites. An example of the typical variability in CPP results obtained for triplicate specimens in the present study is shown in Figure 3.7.

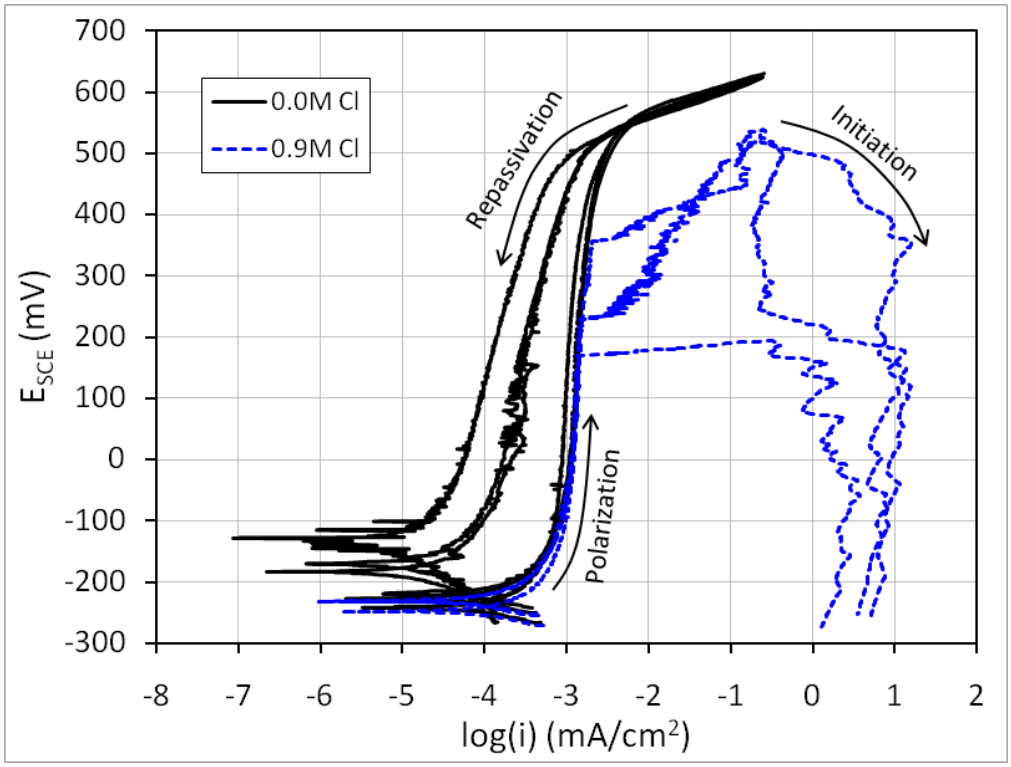

Figure 3.7 Cyclic polarization behavior of triplicate wire specimens under 0.0M and 0.9M Cl^- exposure

When no Cl^- is present polarization behavior is easily replicated as the electrochemical reactions occur uniformly across the surface of the steel (e.g., uniform passive film formation or the evolution of O_2). However, when Cl^- is added to the solution, while corrosion does initiate in all cases, the $E_{breakdown}$ at which it occurs varies over a range of approximately 200 mV. In order to account for these effects, triplicate tests were performed at all Cl^- concentrations studied. Additionally, five to six replicate

tests were performed near Cl^- concentrations that resulted in corrosion initiation to capture any stochastic variability in observed polarization behavior.

3.2.4 Materials Characterization

Following testing, corrosion damage was characterized using either a LEO 1530 thermally-assisted field emission SEM or a Hitachi S-3700N variable pressure SEM. All images were acquired using backscattered electron detectors. Both systems are equipped with Oxford INCA EDX detectors for performing elemental analysis in conjunction with imaging. The Hitachi S-3700N is capable of imaging non-conductive samples at low vacuum. Samples analyzed using the LEO 1530 required sputter coating with Au for imaging. Samples with extensive buildup of corrosion products were imaged using the Hitachi S-3700N as it does not require the products be removed or sputter coated for imaging. A Leica MZ6 stereomicroscope was also used to characterize corrosion damage at low magnifications after testing.

3.3 Results and Discussion

3.3.1 Chloride-Induced Corrosion

3.3.1.1 Prestressing Wire

Figure 3.8 shows the polarization curves obtained from CPP experiments conducted on prestressing wire specimens in 0.0, 0.7, 0.8, 0.9, and 1.0 M Cl^- exposures. Cl^- concentrations which showed little effect (i.e., no corrosion initiation) have not been included in Figure 3.8 for brevity.

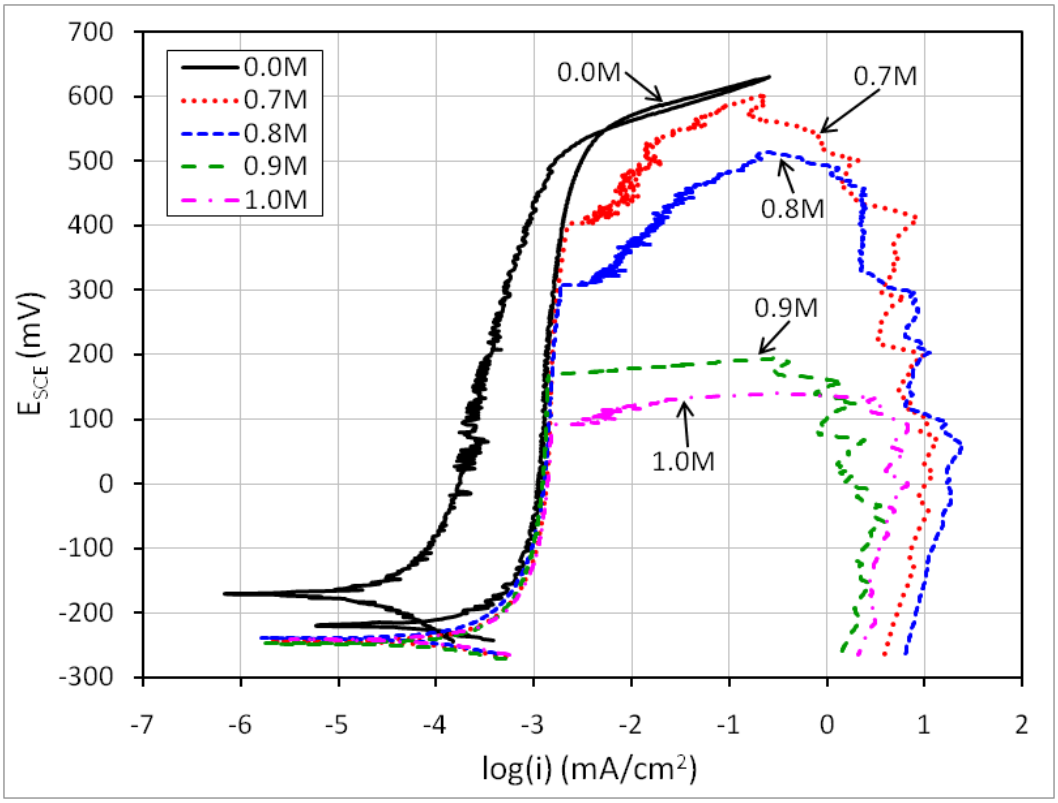

Figure 3.8 Cyclic polarization curves for prestressing wire specimens

Following the 120 min sample conditioning period, an open circuit corrosion potential (E_{corr}) of approximately -240 mV_{SCE} was measured for all wire specimens regardless of Cl^- concentration. When no Cl^- was present in solution, full repassivation was observed during the reverse potential scan following polarization into the O_2 evolution region (E above approximately 500 mV_{SCE}). Little influence of Cl^- was detectable until reaching a concentration of 0.6 M, at which point localized corrosion initiated during the anodic scan with the formation of an $E_{breakdown}$ prior to entering the O_2 evolution region. Based on the simulated concrete pore solution used for all experiments with pH of 13.6 (an $[OH^-]$ of 0.4 M), this Cl^- concentration (0.6 M) would correspond to a $[Cl^-]/[OH^-]$ ratio of approximately 1.5, a value which is comparable to CTLs of mild

steel reinforcing bars in simulated concrete pore solutions (Alonso and Sanchez, 2009; Angst, et al., 2009). Additionally, CPP experiments conducted on sandblasted mild steel reinforcing bars in a similar concrete pore solution (pH of 13.6 but without $CaSO_4 \cdot 2H_2O$) have shown that corrosion initiated at Cl^- concentrations above 0.6 M as well (Li and Sagues, 2002). Therefore, it is hypothesized that the corrosion behavior of prestressing steel wire in simulated concrete pore solutions is similar to that of mild steel reinforcement.

When compared with previous studies on the corrosion behavior of prestressing steels, Cl^- concentrations resulting in corrosion initiation in the present study are generally much higher (Cherry and Price, 1980; Diaz, et al., 2009). This difference is likely the result of many factors including the following:

- Previous studies on the corrosion behavior of prestressing steels has been conducted using simulated concrete pore solutions with lower pH compared with the data presented herein (Cherry and Price, 1980; Diaz, et al., 2009). Knowing that, in general, as pH increases, resistance to Cl^- induced corrosion increases, higher Cl^- concentrations for corrosion initiation are expected (Poursaee and Hansson, 2009).
- When evaluating corrosion susceptibility, most previous research has been conducted by directly immersing samples into simulated concrete pore solutions containing the specified Cl^- concentration without conditioning the steel to first develop a stable passive film non-chloride bearing solution. This procedure is unrealistic knowing that steel embedded in concrete will have developed a stable passive film long before it is ever exposed to Cl^- (Poursaee and Hansson, 2009).

- Polished samples have been used in almost all previous electrochemical studies of prestressing steels in simulated concrete pore solutions (Cherry and Price, 1980; Diaz, et al., 2009; Hartt, et al., 1993). As will be discussed in subsequent sections, the surface coating present on prestressing steel has a large effect on its corrosion behavior.

As expected, Figure 3.8 also shows that as Cl^- concentration increased, the barriers to corrosion initiation decreased as evidenced by the a continual decrease in $E_{breakdown}$. One other key result shown in Figure 3.8 is that no protection potential (E_{prot}) was formed during the reverse potential scan portion of the CPP scan above the original E_{corr}; that is, once corrosion initiated, anodic dissolution continued to occur even without the application of an overpotential by the potentiostat. These effects become particularly apparent as shown in Figure 3.9 when comparing values of E_{corr} before and after conducting CPP experiments for the Cl^- concentrations studied.

Prior to the CPP scan, the influence of Cl^- concentration on E_{corr} was negligible even up to 1.0 M exposure for 30 min during the second portion of the sample condition procedure. Following the CPP scan, as Cl^- concentrations increased from 0.0 M to 0.6 M a slight decrease of 60 mV in E_{corr} was measured, indicating a weak interaction between Cl^- and the passive film that did not result in corrosion initiation. However, above 0.6 M Cl^-, on the reverse scan E_{corr} shifted drastically to near -900 mV_{SCE}, representing a potential range wherein autocatalytic corrosion persists following testing. Typical corroding steel in concrete exhibits a E_{corr} of approximately -600 mV_{SCE}.(Alonso, et al., 2002) This negative shift in E_{corr} to near -900 mV_{SCE} may be the result of excessive corrosion damage occurring during the reverse portion of the CPP scan as potentials are

held at high levels of anodic polarization and in turn corrosion current densities remain high for extended periods of time.

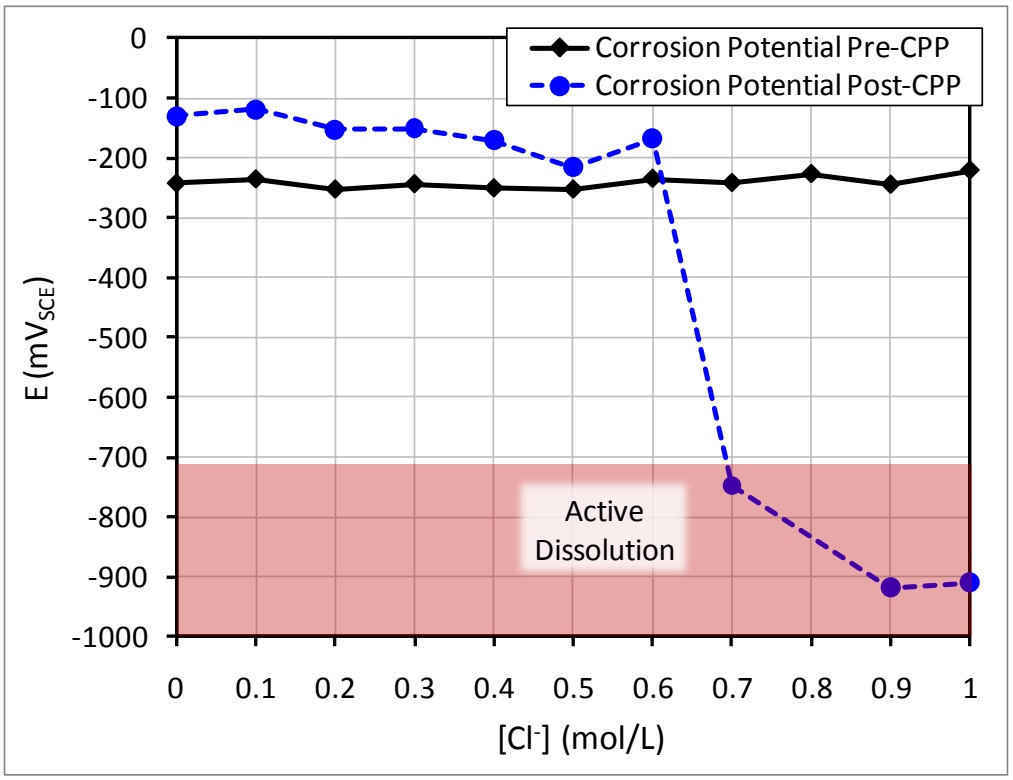

Figure 3.9 Ecorr vs. [Cl-] for prestressing wire specimens before and after CPP testing

3.3.1.2 Prestressing Strand

Figure 3.10 shows the polarization curves obtained from CPP experiments conducted on prestressing strand specimens in pore solutions with 0.0, 0.2, 0.3, 0.4, and 1.0 M Cl^-. Results for other Cl^- concentrations have not been included in Figure 3.10 for brevity. Following the 120 min sample conditioning period, E_{corr} was approximately -330 mV_{SCE}; 90 mV less than the E_{corr} of prestressing wire specimens. This shift in E_{corr} relative to prestressing wires is likely an indication of the formation of concentration /

aeration cells between the outer portion and inner (mass transport limited) portion of the prestressing strand resulting in a measured cathodic polarization of E_{corr} (Landolt, 2007).

At Cl^- concentrations of 0.0 and 0.1 M, no corrosion initiation occurred with full repassivation after polarization into the O_2 evolution region. Corrosion initiation in prestressing strands occurred at a Cl^- concentration of 0.2 M (a $[Cl^-]/[OH^-]$ of 0.5) and higher – significantly less than that of prestressing wire specimens and clear evidence that stranding geometry does have a significant influence on the prestressing steel's resistance to chloride-induced corrosion. Similar to the behavior observed for prestressing wires, as Cl^- concentration increased $E_{breakdown}$ continued to shift negatively until reaching -100 mV_{SCE} at 1.0 M Cl^-.

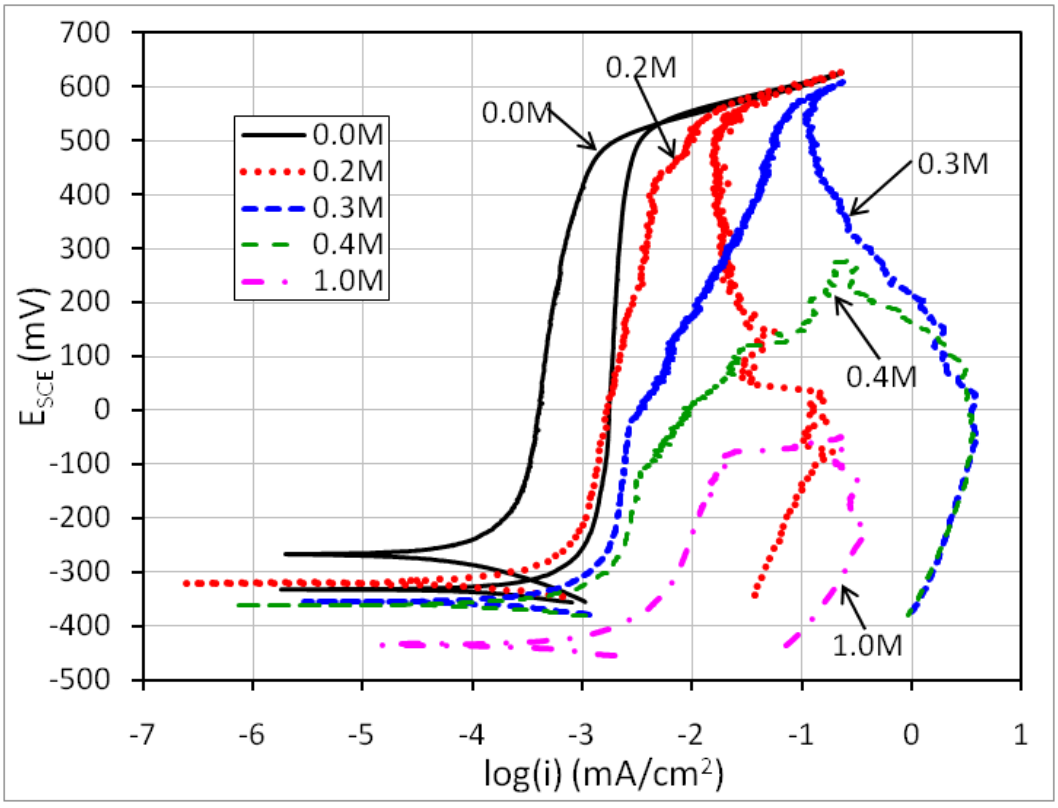

Figure 3.10 Cyclic polarization curves for prestressing strand specimens

Measurements of E_{corr} made before and after CPP testing of prestressing strand samples are shown in Figure 3.11. At Cl^- concentrations below 0.5 M, E_{corr} values were fairly stable near -330 mV_{SCE}, while at higher concentrations, values of E_{corr} varied significantly between -300 and -450 mV_{SCE} and generally began to shift negatively immediately after being transferred from the non-Cl^- pore solution to Cl^- containing pore solution during sample conditioning – an indication that Cl^- were beginning to interact with the specimen prior to polarization. Analogous to the results obtained for prestressing wires, once corrosion initiated (at [Cl^-] greater than 0.2 M) repassivation with the formation of an E_{prot} did not occur and E_{corr} continued to decrease to less than -900 mV_{SCE} following CPP testing.

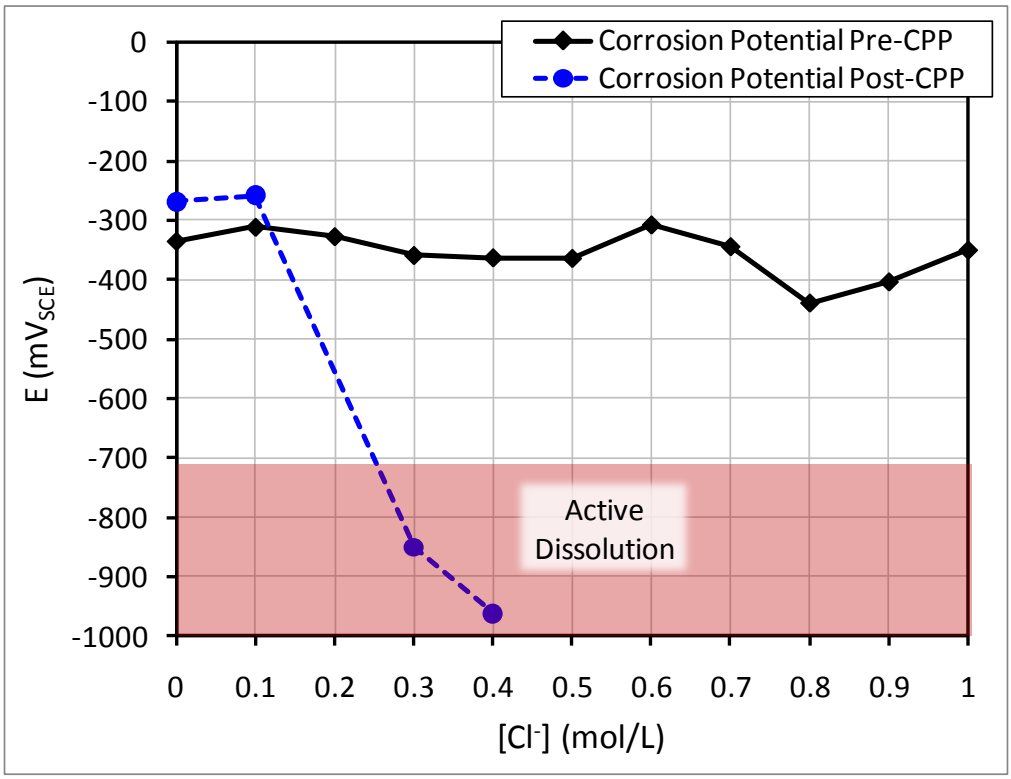

Figure 3.11 Ecorr vs. [Cl-] for prestressing strand specimens before and after CPP testing

3.3.1.3 Prestressing Strand vs. Wire

Figure 3.12 presents a comparison between the mean $E_{breakdown}$ determined for all replicate prestressing wire and strand specimens at each Cl^- concentration tested. The limiting $E_{breakdown}$ of 500 mV_{SCE} shown for both prestressing wire and strand specimens represents the potential above which O_2 evolves.

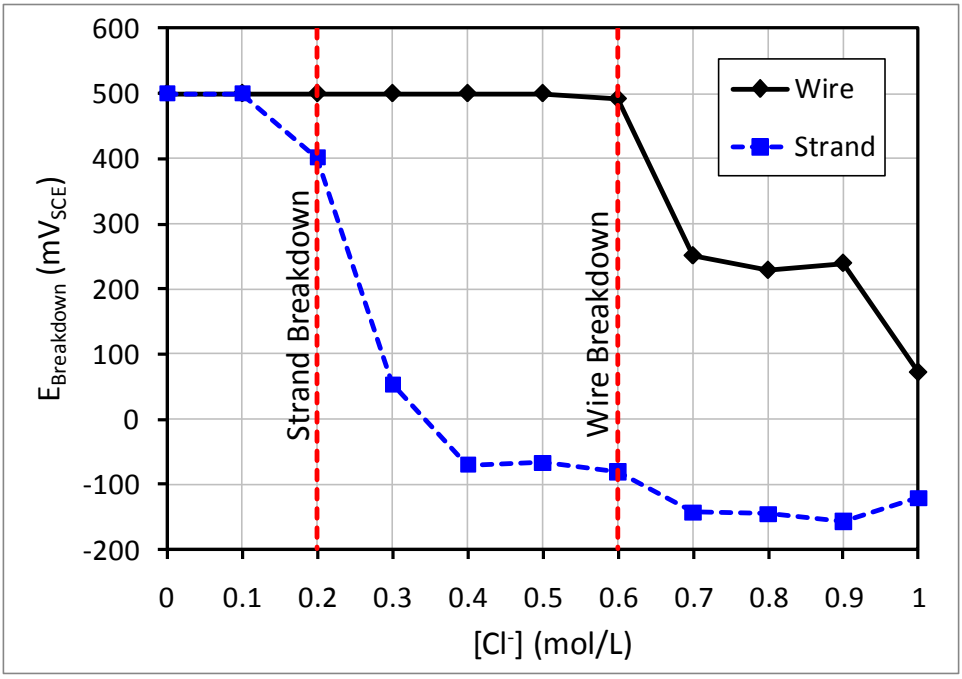

Figure 3.12 Breakdown potential vs. Cl- concentration for prestressing wire and strand

As discussed previously, for prestressing wires, $E_{breakdown}$ began to decrease above Cl^- concentration of 0.6 M, while for prestressing strands corrosion initiated at Cl^- concentrations as low as 0.2 M. For prestressing strands, at Cl^- concentrations above 0.4 M, $E_{breakdown}$ reached a limiting potential of approximately -100 mV_{SCE}. This limit was not observed for prestressing wires, although perhaps of wires had been tested at higher

Cl^- concentrations a limiting in $E_{breakdown}$ may have occurred. Nonetheless, when compared with prestressing wires which were found have similar corrosion behavior as mild steel reinforcing bars (see Section 3.3.1.1), stranding was found to have a significant impact on resistance to chloride-induced corrosion initiation, resulting in a 67 % reduction in the Cl^- concentration required to initiate corrosion. This reduction in corrosion resistance is consistent with Cl^- ion content limits for corrosion protection in ACI 318 which prescribes a limit of 0.15 % water soluble Cl^- by weight of cement in reinforced concrete exposed to Cl^- and 0.06 % for prestressed concrete (i.e., a 60 % reduction) (ACI 318-05, 2005).

3.3.2 Morphology of Corrosion Damage

Following all CPP experiments, each specimen was examined to characterize the morphology of corrosion damage. Once corrosion initiated for each specimen geometry, the damage observed and products formed were similar for both prestressing wires and strands. Figure 3.13 depicts the typical damage observed before and after testing at Cl^- concentrations that resulted in corrosion initiation. Observed corrosion damage on prestressing wires and strands could generally be divided into two types: (1) localized pitting or crevice corrosion associated with corrosion initiation, and (2) uniform surface attack associated with corrosion propagation following initiation.

In prestressing wires (Figure 3.13 (a) and (b)), corrosion was observed to initiate at surface imperfections with the formation of localized pitting type of corrosion attack, followed by uniform attack of the surface. Additional details on the influence of surface imperfections on corrosion initiation are provided in Section 3.3.3. In prestressing strands (Figure 3.13 (c) and (d)), corrosion was observed to initiate first in the crevice regions of

the strand with products forming between wires, followed by more uniform attack spreading onto the outer portions of the strand.

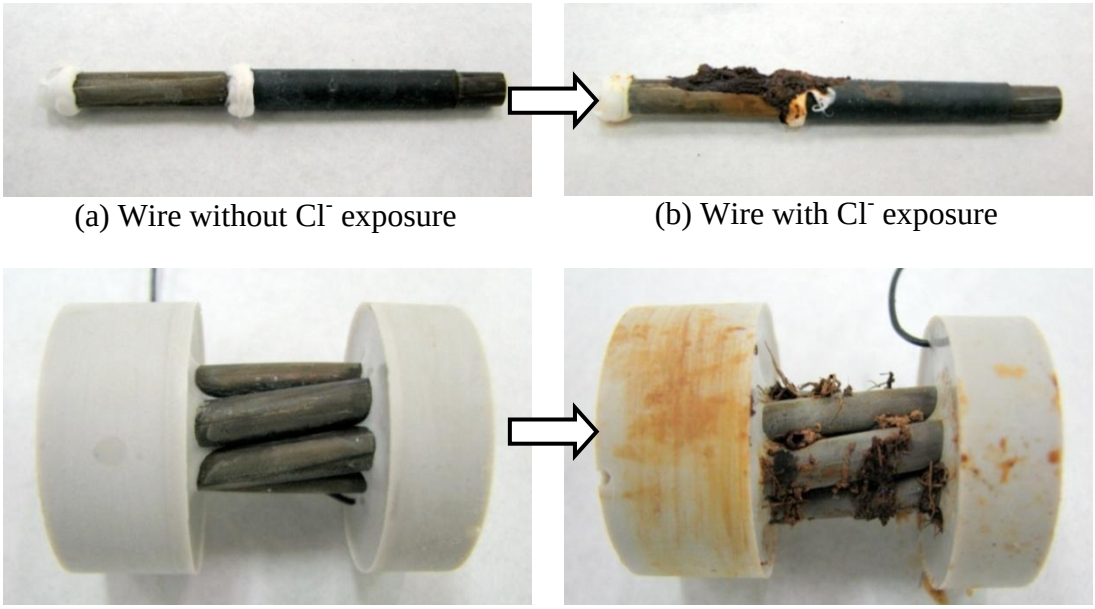

(a) Wire without Cl^- exposure (b) Wire with Cl^- exposure

(c) Strand without Cl^- exposure (d) Strand with Cl^- exposure

Figure 3.13 Specimens before and after corrosion initiation by CPP experiments

Cross sections of strands imaged using optical microscopy before and after testing (see Figure 3.14) showed that attack was also occurring in the interstices of the strand, with the formation of corrosion products adjacent to the impingement sites between wires. Interestingly, at sites of localized corrosion (i.e., surface pitting or crevice corrosion) products formed as hollow "whiskers" with a morphology similar to that reported by Cherry and Price (Cherry and Price, 1980). In many cases whiskers were up to 1 cm long suspended in solution. X-ray diffractions patterns obtained from whisker formations ground into a powder showed that the whiskers were primarily goethite

(FeOOH). Extensive pitting was observed at the base of the whisker formations when removed.

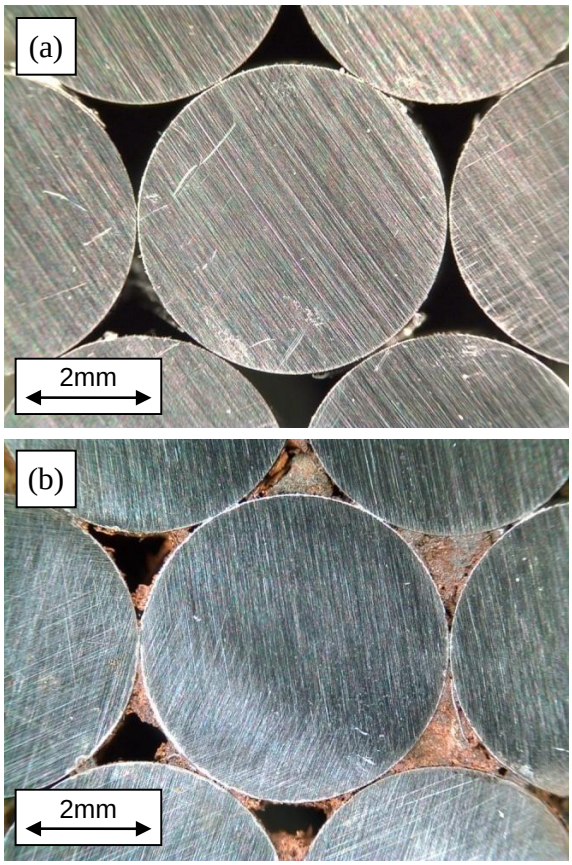

Figure 3.14 Cross section of prestressing strand (a) without exposure to Cl^- and (b) after corrosion initiation

Figure 3.15 depicts a typical pit observed at the base of a whisker formation using SEM. Pits ranged in diameter from 5 to 20 μm (0.2 to 0.8 mils) and typically exhibited concentric circular deposits of corrosion products on the pit walls as shown in Figure 3.15. This layered structure of corrosion products along with the erratic current densities following corrosion initiation (see Figures 3.8 and 3.10) suggest a highly dynamic form of metastable pitting prior to uniform surface attack (Frankel, 1998). With corrosion

products removed in regions of uniform surface attack, corrosion damage was found to be preferentially aligned in the drawing direction of the steel as shown in Figure 3.16. This type of damage mechanism was first described by Trejo et. al (Trejo, et al., 2000), who proposed that given the dual phase microstructure of pearlitic steels, microgalvanic cells may form on the surface of the steel with ferrite acting as the anode and cementite acting as the cathode.

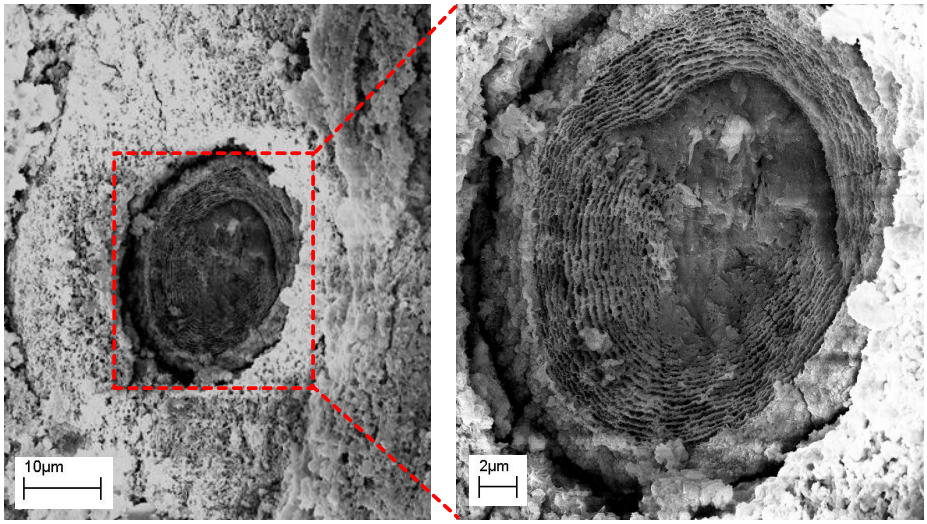

Figure 3.15 Typical pitting site on surface of prestressing steel with concentric circular deposits of corrosion production on the pit wall

Based on this investigation of corrosion damage, it was concluded that corrosion initiation in prestressing strands is controlled primarily by the presence of crevices at the impingement sites between wires along with imperfections in surface coatings, while in prestressing wires corrosion is influenced by the presence of surface imperfections which provide initiation sites. Once corrosion has initiated, its propagation occurs in a similar

manner in both prestressing wires and strands, spreading from sites of localized corrosion into a more uniform attack of the surface.

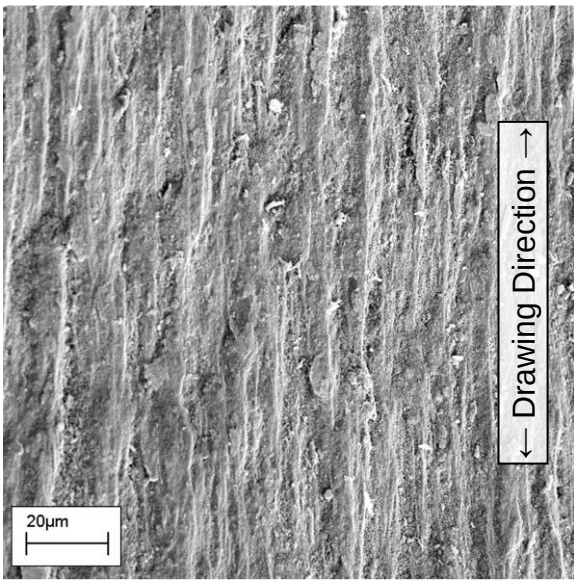

Figure 3.16 Uniform surface corrosion damage preferentially aligned in the drawing direction of the prestressing steel

3.3.3 Influence of Surface Imperfections

Through the characterization of corrosion damage discussed in Section 3.3.2, it became apparent that imperfections in the surface coating of the prestressing steel (along with crevices in prestressing strands) were typically the sites where corrosion would initiate. Imperfections in the $ZnPO_4$ surface coating can be divided into two categories: (1) scratches and blemishes in the coating due to cold-drawing prior to stranding operations, and (2) abrasion of the coating due to relative displacement between the wires which can occur during stranding and tensioning. Type 1 imperfections are typically present as either carbon rich (from wearing of the drawing die) or bare metal "streaks" aligned in the drawing direction of the wire. Type 2 imperfections are typically present as

bare metal “streaks” running helically with the twist of the strand and can only be seen if the strand is dissected.

SEM and EDX analyses were performed on prestressing steel samples to characterize imperfections in their as-received surface coatings. Figure 3.17 details the heterogeneity present in a 1 mm^2 area of the coating at a Type 2 imperfection site (i.e., at the impingement site between two wires in a strand). EDX analyses performed at three sites are also shown. In the center of the backscattered image shown in Figure 3.17, a bright diagonal Type 2 imperfection band (marked by dashed lines) is evident making a helical twist at the impingement site between an outer wire and center wire of the prestressing strand. EDX analysis of this region indicates that most of the $ZnPO_4$ coating has been abraded off, leaving only Fe exposed. Adjacent to this imperfection, the surface coating remains intact with EDX analyses showing the presence of both Zn and P. In many cases trace amounts of Ca were also detected in the surface coating. These Ca deposits are likely residual coatings of stearate-type drawing lubricants which were not completely removed during post-processing stress relief and cleaning treatments (Osborn, et al., 2008).

In order to elucidate the effects of surface imperfections, additional CPP experiments were conducted on prestressing wire specimens. These tests were conducted using similar procedures to those presented in Section 3.1.3; however, when corrosion initiated at $E_{breakdown}$ the test was halted and the sample was removed and flushed with acetone. Using this technique, sites of corrosion initiation could be identified prior to the extensive formation of corrosion products like those shown in Figure 3.13. Figure 3.18 depicts two sample tested using this procedure to determine preferential surface sites for

corrosion initiation. Initiation was found to occur at Type 1 and Type 2 imperfections prior to general attack of the $ZnPO_4$ coated steel surface.

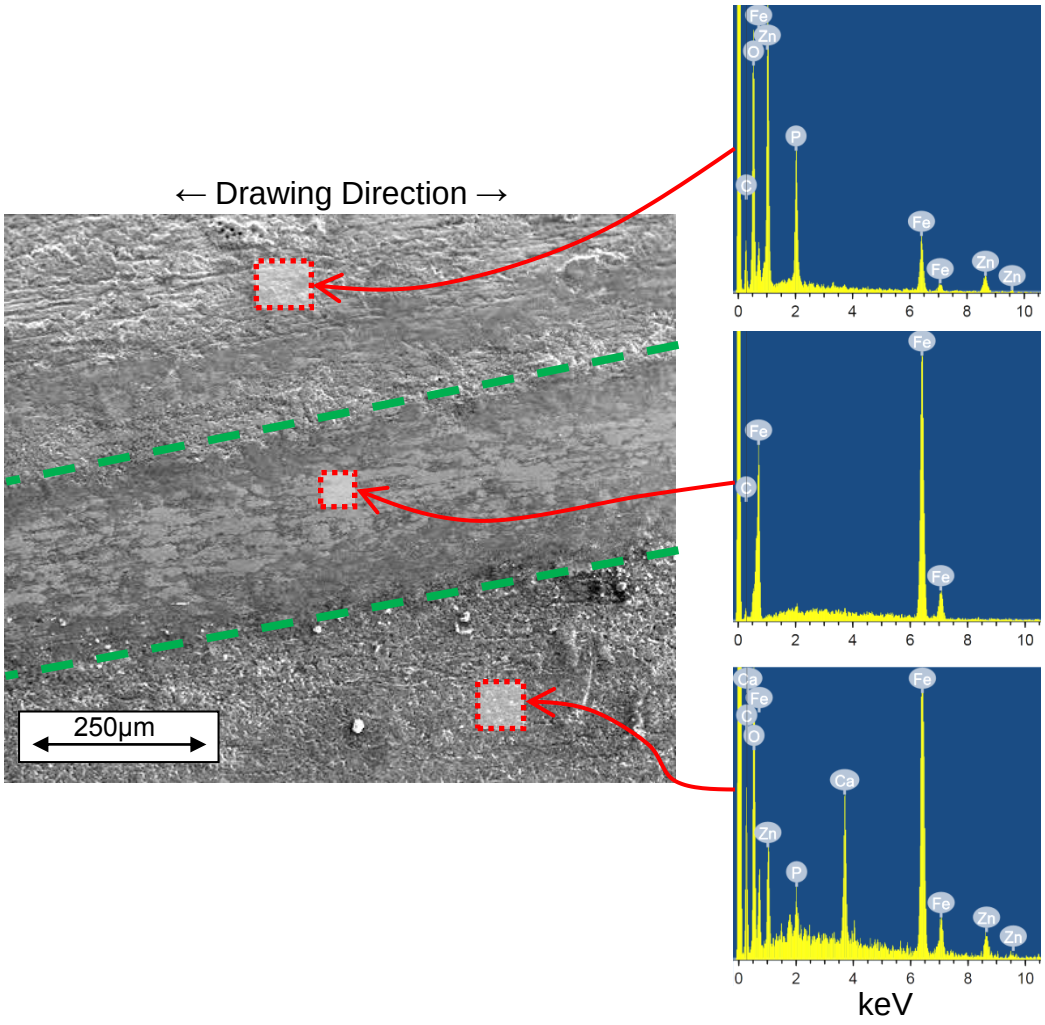

Figure 3.17 Typical Type 2 imperfection in $ZnPO_4$ surface coating of prestressing steel

Type 1 attack is clearly shown in Figure 3.18 on sample #2 with corrosion products forming on the carbon rich black streaks aligned in the drawing direction. Corrosion initiation at Type 2 imperfections is also shown in Figure 3.18, with corrosion products aligned with the helical twist of outer prestressing wires around the central

prestressing wire. These results suggest that the presence of, and more importantly imperfections in, as-received surface coatings play an integral role in providing sites for corrosion to initiate. Such effects would not be detected by experiments conducted on polished samples. Moreover, considering that Type 2 imperfections occur at the same location as crevices in prestressing strands (impingement sites between wires), surface imperfections may act synergistically with crevice mechanisms to reduce the barriers to corrosion initiation in prestressing strands.

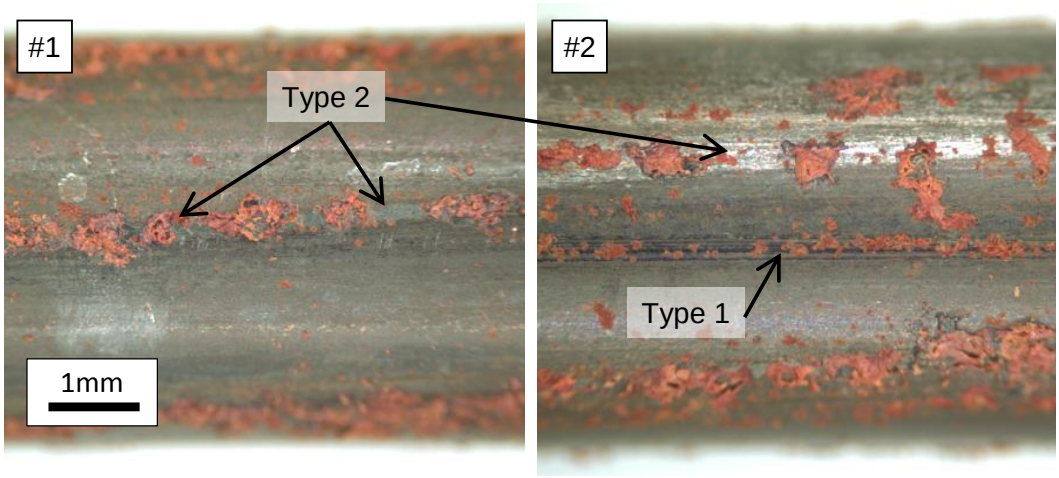

Figure 3.18 Attack of surface imperfections during CPP corrosion initiation experiments

3.3.4 A Model for Corrosion Initiation in Prestressing Strands

Based on these data, many insights into the fundamental mechanisms of corrosion initiation in prestressing strands can be made. The results presented in Sections 3.3.1 and 3.3.2 have shown that both the electrochemical behavior and morphology of damage observed in prestressing strands is fundamentally different than that of prestressing wires. Crevice corrosion phenomena have been studied extensively in other fields of corrosion

science but have only recently been noted as a possible mechanism for corrosion initiation in prestressing strands. Crevice mechanisms which may occur in the Cl^- containing pore solution system include:

- O_2 deficiencies in crevice regions due to mass transport limitations causing impaired passivity (Sharland, 1992). Lack of O_2 within the crevice may also result in the attraction of higher mobility Cl^- into the crevice in order to preserve charge neutrality (Jones, 1996).
- Acidification of the crevice region due to the hydrolysis of water in the presence of Cl^- leading to the formation of HCl and corrosion products (Frankel, 1998; Jones, 1996) according to the reaction: $Fe^{2+} + 2H_2O + 2Cl^- \rightarrow Fe(OH)_2 + 2HCl$

In addition to crevice mechanisms, results presented in Section 3.3.3 showed that imperfections in as-received coatings also play a role in corrosion initiation. Key in the case of prestressing strands is the fact that the locations of Type 2 surface imperfections coincide with the location of crevices formed at the impingement site between adjacent prestressing wires. Another factor to consider is that prestressing strand is embedded into concrete wherein the outer surface of the strand is in direct contact with cement hydration products (including $Ca(OH)_2$) while the interstitial space of the strand is not. Once corrosion initiates within crevices and acidification occurs in the interstitial region of the strand, the outer surface of the strand will be buffered by solid $Ca(OH)_2$ while the inner portion likely continues to acidify, thus amplifying concentration cell effects between the inner and outer portions of the strand.

Building on these mechanisms and the results presented herein, a three-step "thought" model has been proposed to describe the corrosion initiation and propagation

process in prestressing strands. An overview of the model is shown diagrammatically in Figures 3.19 (a) to (c) and is described as follows:

- Step 1 – Figure 3.19 (a): Crevice corrosion initiates at the impingement sites between adjacent prestressing wires once Cl^- concentration exceeds the CTL.
- Step 2 – Figure 3.19 (b): Following initiation, localized corrosion continues to occur at crevice sites accompanied by acidification of the interstitial region of the prestressing strand as indicated by change in color from black to white.
- Step 3 – Figure 3.19 (c): Once corrosion products have built up to a sufficient amount such that the mass transport of reactants to crevice sites is limited, corrosion attack spreads to the surface of the strand resulting in damage similar to what was observed on prestressing wires.

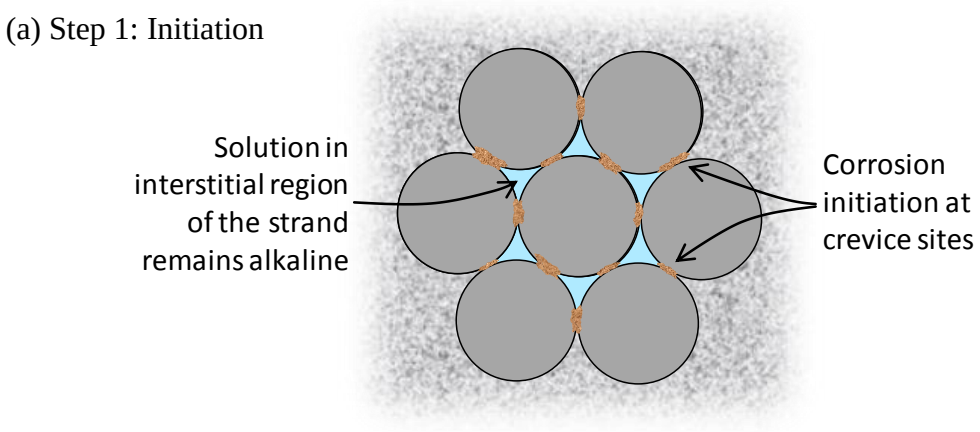

Figure 3.19 Model for corrosion initiation in prestressing strands

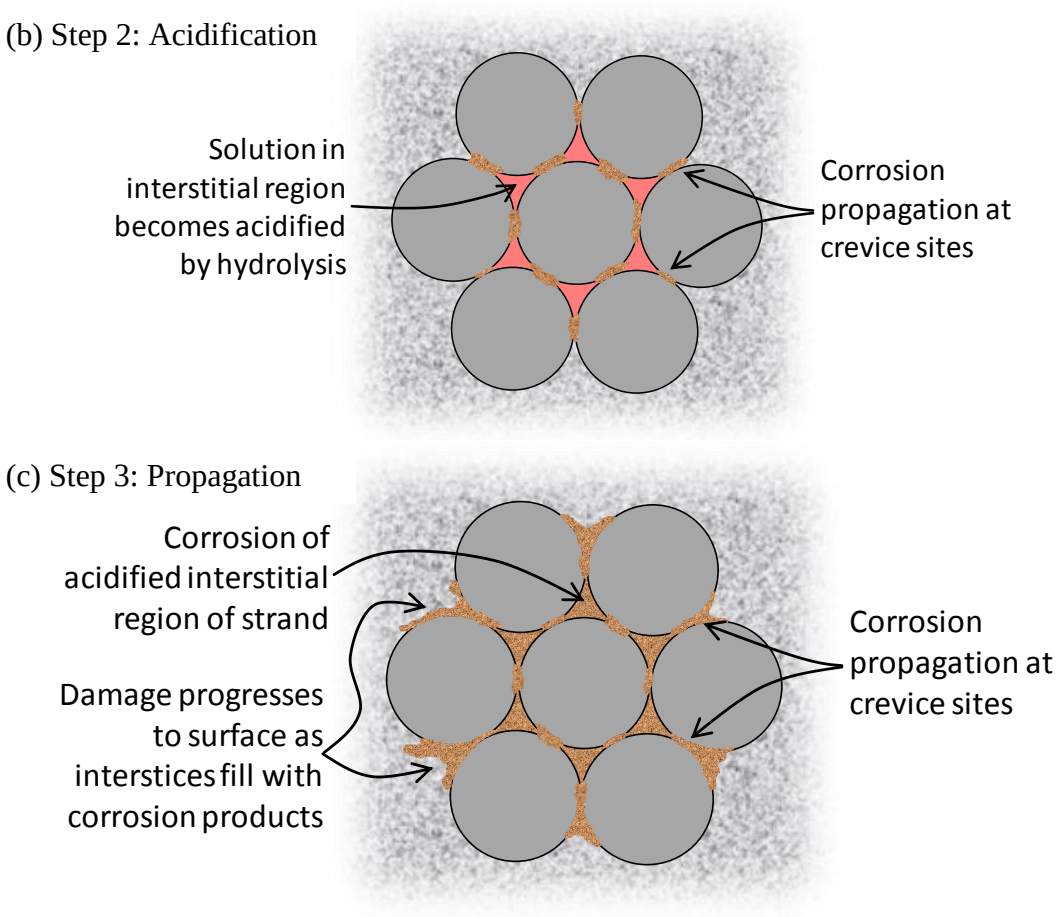

Figure 3.19 (cont'd) Model for corrosion initiation in prestressing strands

3.3.5 Impact on Time-to-Corrosion

A final point warranting further discussion is the impact of reductions in corrosion resistance in stranded prestressing steels on the time-to-corrosion initiation. Using a basic Collepardi type 2nd order Fickian diffusion model (Nilsson, 2009), reducing corrosion resistance from that of a prestressing wire (similar to mild steel reinforcement) to that of a prestressing strand can result in premature corrosion initiation provided that Cl^- has reached a sufficient concentration at the cover depth. One-dimensional 2nd order diffusion of Cl^- is typically modeled using Crank's solution to Fick's second law shown in

Equation 1, where C(x,t) is the Cl^- concentration at depth x and time t, C_s is the Cl^- concentration at the surface, x is the depth of interest, D is the diffusion coefficient, and t is time (Crank, 1980).

$$C(x,t) = C_s\left[1 - \text{erf}\left(\frac{\text{x}}{2\sqrt{\text{D}\cdot\text{t}}}\right)\right] \tag{3.1}$$

Equation 3.2 can be determined by solving for t in Equation 1 using inverse error functions. For the purpose of service life estimation, t can be considered the time-to-corrosion, x the cover thickness, and C_T the CTL for the material of interest. Equation 3 can be derived from Equation 2 to represent the percentage difference in time-to-corrosion between a stranded prestressing steel (C_{T_S}) and a prestressing wire (C_{T_W}). Because the percentage reduction in service life is just a difference ratio of the time-to-corrosion for two different systems, it is not a function of the cover thickness x or diffusion coefficient D, varying only with C_S and C_T. Using Equation 3.3, estimates of reductions in time-to-corrosion due to crevice effects in prestressing strands and their associated effects on corrosion resistance were made by varying values of C_S and C_T.

$$t = \frac{x^2}{4\cdot D}\left[erf^{-1}\left(1 - \frac{C_T(x,t)}{C_s}\right)\right]^{-2} \tag{3.2}$$

$$Reduction = \left[\frac{\left[erf^{-1}\left(1 - \frac{C_{T_S}(x,t)}{C_s}\right)\right]^2 - \left[erf^{-1}\left(1 - \frac{C_{T_W}(x,t)}{C_s}\right)\right]^2}{\left[erf^{-1}\left(1 - \frac{C_{T_S}(x,t)}{C_s}\right)\right]^2}\right] \tag{3.3}$$

The surface Cl^- concentration C_S was varied between 15 and 20 kg/m^3 (25 and 34 lb/yd^3) of concrete based on diffusion studies of field concrete in the literature (Hartt, 2010; Thomas, et al., 1999b). Based on the results presented in section 3.3.1 which have shown that the corrosion resistance of prestressing wire is similar to that of mild steel reinforcement when evaluated using similar methods, C_{T_W} was selected from commonly accepted values in the literature for mild steel reinforcement varying between 0.5 and 1 kg/m^3 (0.85 and 1.69 lb/yd^3) (ACI 222R-01, 2001; Frederiksen, 2009; Markeset, 2009). Values of C_{T_S} were simply determined by reducing values of C_{T_W} by 67 % based on the reduction in corrosion resistance in prestressing strands (i.e., $C_{T_S} = 0.33 \times C_{T_W}$). It should be noted that there is still much debate as to accurate values for C_T and C_S and thus these calculations should only serve as an example of the potential reductions in time-to-corrosion due to crevice effects present in prestressing strands.

Figure 3.20 illustrates the percentage reduction in time-to-corrosion for the different levels of C_S and C_T examined. Reductions in C_T from C_{T_W} to C_{T_S} did lead to a decrease in the time-to-corrosion. However, this decrease was not linearly related to the change in C_T. For a 67 % reduction in C_T values, the reduction in time-to-corrosion varied between 28 and 36 %. While the authors accept that additional research is required to validate the laboratory-based electrochemical experiments and time-to-corrosion studies presented herein, these results clearly demonstrate that stranding and any associated reductions in the corrosion resistance does have an impact on time-to-corrosion and affirms the need for reduced Cl^- content limits for prestressed concrete to be included in building codes.

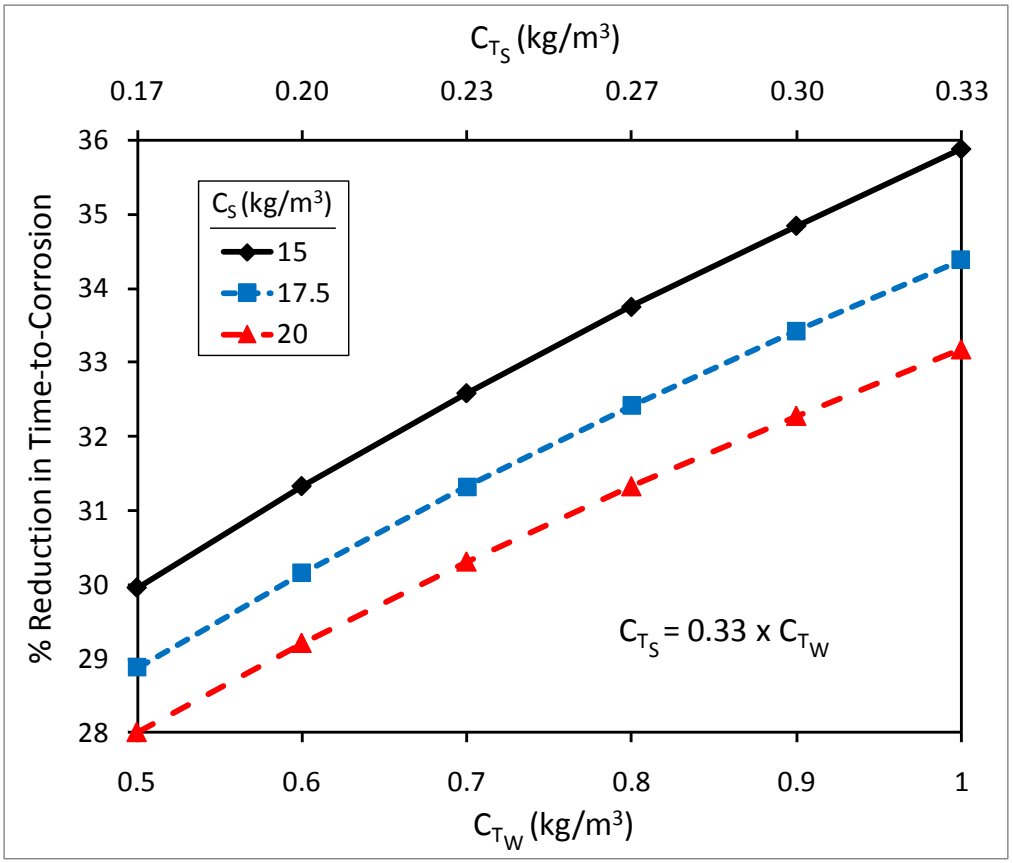

Figure 3.20 Influence of reductions in corrosion resistance on time-to-corrosion for various values of C_S and C_T (note: 1 kg/m^3 = 1.69 lb/yd^3)

CHAPTER 4

CANDIDATE STAINLESS STEELS SELECTED FOR INVESTIGATION

Following the completion of corrosion behavior studies performed on A416 prestressing strand presented in Chapter 3, the study focused on the development and evaluation of corrosion-resistant high-strength stainless steels (HSSSs) was commenced. This chapter presents the candidate stainless steels selected for the investigation, the strengthening techniques used for their production as HSSSs, and studies performed to characterize the as-received materials.

4.1 Materials Selection

4.1.1 Materials Selection Considerations

With a target application of corrosion resistant prestressing reinforcement, stainless steel alloys were selected for the investigation considering many factors. The primary factors considered for materials selection were potential corrosion resistance, potential mechanical properties, cost, and availability. Considering these factors, materials were selected through a thorough review of the available literature (see Sections 2.5 and 2.6) and consultation with industry experts familiar with the manufacture of stainless steel wire and of A416 prestressing strand.

4.1.2 Materials Selected for Investigation

Six stainless steel alloys were selected for the investigation. High carbon 1080 steel used in the production of A416 prestressing strand was also included as a control in most corrosion and mechanical testing. Table 4.1 lists the candidate stainless steels selected and the control along with their crystal structure, nominal composition, pitting resistance equivalency number (PREN, calculated by Equation 2.13), and approximate relative cost for rod coil material, including base cost plus the alloy surcharge for January 2011 (quotes obtained from MEPS Ltd, Outokumpu, and Fagersta Stainless).

Table 4.1 Candidate stainless steels selected for investigation

Alloy	Structure	Composition (%) – Balance Fe				PREN	Relative Cost*
		Cr	Ni	Mo	Other		
1080	Pearlitic	-	-	-	0.8C, 0.73Mn, 0.24Si	0.1	1.0
304	Austenitic	18.2	8.1	-	-	19.2	6.9
316	Austenitic	17	11	2.8	-	27.2	9.6
2101	Duplex	21.5	1.5	-	5Mn, 0.22N	29.1	5.0
2205	Duplex	22	5.5	3	0.17N	37.0	8.8
2304	Duplex	23	4.8	0.3	0.10N	27.0	6.4
17-7	Martensitic	17	7	-	1Al, 1Si	17.0	8.2

* Approximate relative cost normalized against carbon steel

4.1.2.1 Austentic Grades 304 and 316

Two austenitic stainless steel grades (304 and 316) were selected for investigation. Grades 304 and 316 are the most widely used stainless steels and are commonly produced as cold drawn high-strength wires in the spring wire industry. Austenitic stainless steels also exhibit exceptional work hardening during cold drawing associated with dislocation entanglement and the formation of strain-induced martensite

(particularly in metastable 304). Grades 304 and 316 have also been used extensively in reinforced concrete applications with exceptional corrosion resistance. In addition, previous studies of HSSSs for PSC conducted under Cost Action 534 focused on 304 and 316, providing a means for corroborating the results of the present study with those obtained by other researchers.

4.1.2.2 Duplex Grades 2101, 2205, and 2304

Three duplex grades (2101, 2205, and 2304) were selected for the investigation. Duplex stainless steels typically exhibit toughness, formability, and corrosion resistance provided by the austenite phase and high strength provided by the ferrite phase. With these phases combined, duplex stainless steels exhibit exceptional mechanical properties and can be strengthened by cold drawing. Duplex stainless steels also exhibit exceptional resistance to corrosion and stress corrosion cracking. Grade 2205 was selected as it is the most widely used "workhorse" duplex stainless steel (Alvarez-Armas, 2008). The more recently developed grades 2101 and 2304 were also selected based on their use as reinforcing steel in concrete. Duplex grades 2101 and 2304 are also referred to as "lean duplex" or LDX, due to their lower Ni and Mo contents when compared with 2205, leading to lower initial raw material cost and lower cost volatility. In lean duplex grades, the reduced Ni and Mo contents are typically compensated for by the addition of Mn and N to preserve austenite stability and pitting resistance (Alvarez, et al., 2011).

4.1.2.3 Precipitation Hardened Grade 17-7

One precipitation hardened stainless steel grade 17-7 was also selected for the investigation based on its high tensile strength. Grade 17-7 is commonly used in the U.S. for the production of high-strength stainless steel spring wire. 17-7 is typically supplied

to producers in the annealed condition with an austenitic crystal structure. Through cold drawing, a total martensitic phase transformation occurs, resulting in strengthening. Following cold drawing, a "precipitation hardening" heat treatment can also be applied at 482 ˚C (900 ˚F) for 60 min followed by air cooling, resulting in the formation of intermetallic precipitates (17-7 has a high Mn, Cu, Si, and Al content) and additional strengthening. In the precipitation hardened condition, 17-7 exhibits tensile strengths in excess of 1550 MPa (225 ksi) (ATI, 2008).

4.2 Production of HSSS Wires

Stainless steel grades selected for the investigation were cold drawn in order to achieve desired tensile strengths. At this stage of the study no heat treatments were applied after cold drawing and stranding of the cold drawn wires was not performed as it requires large quantities of material (typically at least 1000 kg (2200 lb)) which would be cost prohibitive for the evaluation of all six stainless steels. Cold drawing of 304, 316, and 17-7 was performed at the spring wire and prestressing strand production facility of Sumiden Wire Products Corporation (SWPC) located in Dickson, TN. Cold drawing of 2101, 2205, and 2304 was performed at the stainless steel production facility of Fagersta Stainless located in Fagersta, Sweden. Wires of the control steel were obtained from the center wire of the same A416 prestressing strands presented in Chapter 3.

4.2.1 Specifications for Wire Drawing

Cold drawing of candidate stainless steels was performed to achieve tensile strengths in excess of 1380 MPa (200 ksi) with a wire diameter similar to that used in

seven-wire prestressing strand. A416 prestressing strands are typically produced in 11.1, 12.7, and 15.2 mm (0.44, 0.5, and 0.6 in) nominal diameters, with 12.7 mm being the most commonly used strand size for prestressed concrete construction. Therefore, a target final wire diameter of 3.5 to 5 mm (0.146 to 0.2 in) was selected. Based on desired tensile strengths and wire diameters, work hardening diagrams developed by SWPC and Fagersta Stainless were used to calculate the required initial rod diameter. Figure 4.1 shows the work hardening behavior of all candidate HSSSs investigated. Area reductions of 55 to 80 % are necessary in order to achieve tensile strengths in excess of 1500 MPa.

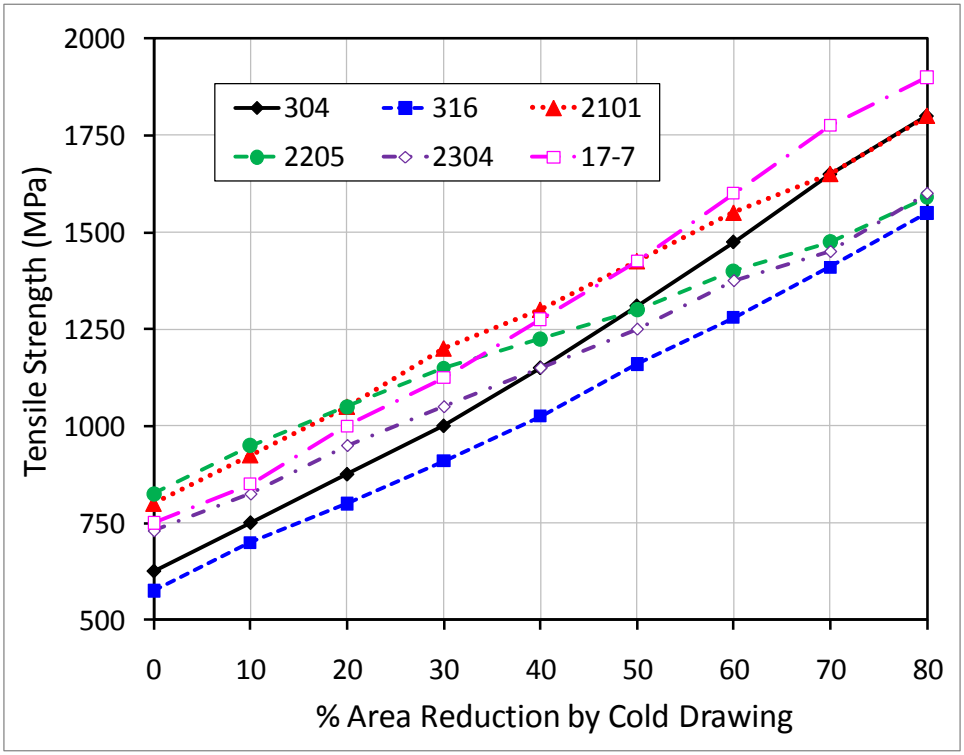

Figure 4.1 Work hardening behavior of all candidate HSSSs (adapted Fagersta Stainless Material Datasheets)

Initial rod diameter (d_{rod}) can be computed based on desired wire diameter (d_{wire}) and percent area reduction ($\%_{red}$) obtained from work hardening diagrams like that shown in Figure 4.1 to achieve desired tensile strengths according to Equation 4.1.

$$d_{rod} = d_{wire}\sqrt{\frac{100}{100 - \%_{red}}} \tag{4.1}$$

For example, if a 2304 wire was desired with tensile strength of 1500 MPa, it would require a reduction in area of approximately 72.5 % by cold drawing. Based on the 72.5 % area reduction value and a desired final wire diameter of 4.2 mm (0.167 in) corresponding to a 12.7 mm (0.5 in) seven-wire prestressing strand, an initial rod diameter of approximately 8 mm (0.31 in) would be used. Area reduction of approximately 70 % was necessary for all candidate HSSSs in order to achieve desired tensile strengths.

4.2.2 The Wire Drawing Process

With the initial rod size and necessary area reduction known, cold drawing of each stainless steel rod was performed until reaching the desired wire diameter. Cold drawing was performed using a process similar to that shown in Figure 4.2. Stainless steel rod coil is fed into the wire drawing machine, wherein the cross sectional area of the rod is reduced by pulling through multiple dies. Typical wire drawing machines may utilize up to ten dies. Each level of reduction consists of a single water-cooled die which successively apply a reduction in area of 10-25 % until reaching the desired wire diameter. Prior to entering each die, the wire passes through a box containing drawing

lubricants (typically animal fat or stearate lubricants). Capstans located at each die are used to pull the wire though the die and must run at an increasing speed as the diameter of the wire is reduced to compensate for the increase in length. Finally, the wire is wound onto a spool. For the purpose of our study, only 45 m (150 ft) of wire produced from each candidate stainless steel was necessary.

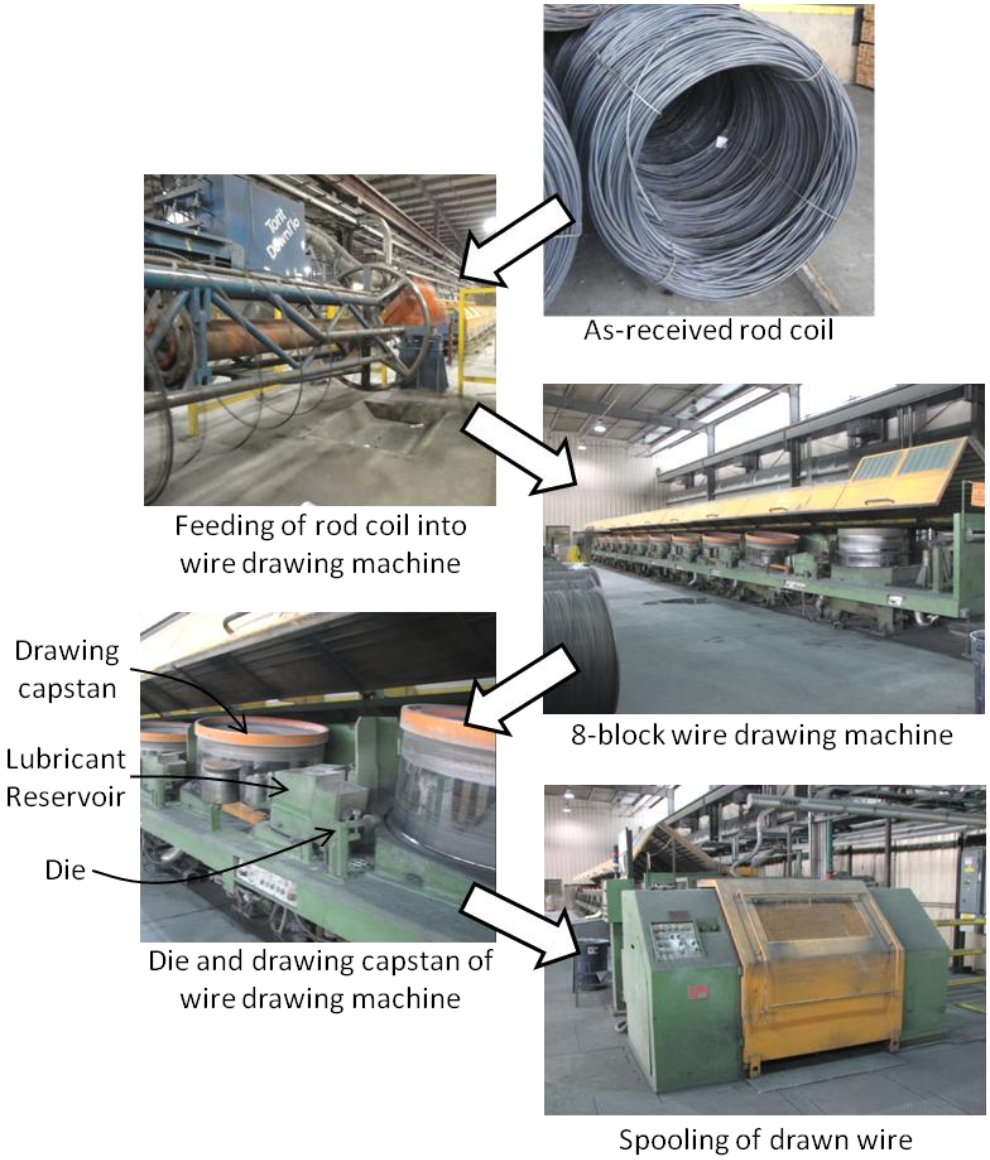

Figure 4.2 Typical cold drawing process used for the production of high-strength wire. Location: Sumiden Wire Products Corp. (Dickson, TN) and RettCo Steel (Newnan, GA)

Final wire diameters of candidate HSSSs and the control are recorded in Table 4.2. With the exception of 316, all candidate alloys were produced with diameters similar to that of A416 prestressing strand. 316 required deeper drawing in order to achieve desired tensile strengths as it does not work harden as readily as the other candidate alloys (primarily due to limited strengthening by strain-induced α′-martensite).

Table 4.2 Average wire diameter of candidate HSSSs and the control

Alloy	1080	304	316	2101	2205	2304	17-7
Diameter (mm)	5.21	4.29	3.23	4.19	4.19	4.19	4.50
Diameter (in)	0.205	0.169	0.127	0.165	0.165	0.165	0.177

4.3 Composition and Microstructure of Candidate High-Strength Stainless Steels

4.3.1 Chemical Composition

The chemical composition of each candidate HSSS was analyzed in its as-received condition by Applied Technical Services Inc. (Marietta, GA) using X-ray fluorescence, combustion, inert gas fusion, and ion coupled plasma atomic emission techniques (ASTM A751, 2008). Results of composition analyses are shown in Table 4.3. The chemical composition of all candidate HSSSs was within the limits specified in ASTM A276 (ASTM A276, 2008). The austentic grade 316 exhibited a sulfur content just at the specified limit of 0.030 %.

Table 4.3 Chemical composition of candidate HSSSs

Alloy	Composition (%) – Fe Balance											
	C	Mn	P	S	Si	Ni	Cr	Mo	Cu	V	N	Al
1080	0.81	0.73	0.009	0.005	0.24	0.06	0.04	0.01	0.11	0.08	-	-
304	0.07	1.02	0.028	0.001	0.33	8.3	17.8	0.33	0.47	0.10	0.09	-
316	0.03	1.67	0.030	0.030	0.21	10.8	16.4	2.23	0.46	0.16	0.05	-
2101	0.027	5.0	0.018	<0.001	0.71	1.56	20.9	0.16	0.25	0.12	0.29	-
2205	0.004	0.82	0.023	<0.001	0.51	5.1	22.1	3.2	0.21	0.12	0.22	-
2304	0.018	0.87	0.011	0.001	0.43	4.8	22.3	0.31	0.23	0.07	0.14	-
17-7	0.07	0.82	0.023	0.001	0.23	7.83	16.1	0.19	0.30	0.15	0.02	0.81

4.3.2 Microstructural Characterization

In order to characterize the microstructural morphology of each candidate HSSS, metallographic techniques were used to investigate grain orientation, the presence of deleterious precipitates, and to determine if deformation-induced phase transformations had occurred during drawing. X-ray diffraction (XRD) was also used to investigate for possible deformation-induced phase transformations which may not be fully evidenced by traditional metallographic techniques. Additional studies were performed to determine the condition of the as-received surface of HSSS wires.

4.3.2.1 Metallography

Specimens were sectioned from cold drawn wires using a water-cooled slow-speed diamond saw and potted in epoxy in longitudinal and transverse orientations with respect to the direction of cold drawing. Once the epoxy had cured, specimens were polished with SiC paper up to 1200 grit (approximately 6 μm (0.24mil)) followed by polishing in alumina (Al_2O_3) suspensions in H_2O to 50 nm (0.002mil). Specimens of grades 304, 316, and 17-7 were wet-etched in a dilute aqua regia solution of equal parts H_2O, HNO_3, and HCl. Specimens of duplex grades 2101, 2205, and 2304 were

electroetched using a 20 % NaOH solution with an applied potential of 4 V. The 1080 steel control was wet-etched in a 2% Nital solution (2 ml HNO_3 in 98 ml of ethanol (C_2H_5OH)). Specimens etched with aqua regia were imaged using polarized light optical microscopy. Due to their small grain size, duplex grades and the 1080 control required the use of scanning electron microscopy (SEM) for imaging. Most specimens were easily imaged using a Hitachi S-3700N variable pressure SEM. A Leo 1530 field-emission SEM was also used to obtain high resolution images at higher magnifications (generally above 5kX). In conjunction with SEM imaging, energy dispersive X-ray spectroscopy (EDX) was used to determine the chemical composition of specific phases and precipitates.

4.3.2.2 X-ray Diffraction

Specimens of cold drawn wires were sectioned and polished until reaching the midsection of the wire. Once a planar polished surface was achieved, the specimen was fixed into a slide for XRD analysis. XRD patterns were obtained using a PANalytical X'Pert Materials Research Diffractometer equipped with a Cu-Kα X-ray source operated at a voltage of 40 kV and current of 40 mA. The X-ray beam was narrowed using electronically controlled divergence slits to ensure that the beam only interacted with the planar polished sample surface (analysis area of approximately 3 mm by 5 mm). The experimental setup used for XRD measurements is shown in Figure 4.3. XRD patterns were obtained over a 2θ range of 40˚ to 100˚ on the Cu-Kα scale with a scan step size of 0.02˚ and time per step of 1 s.

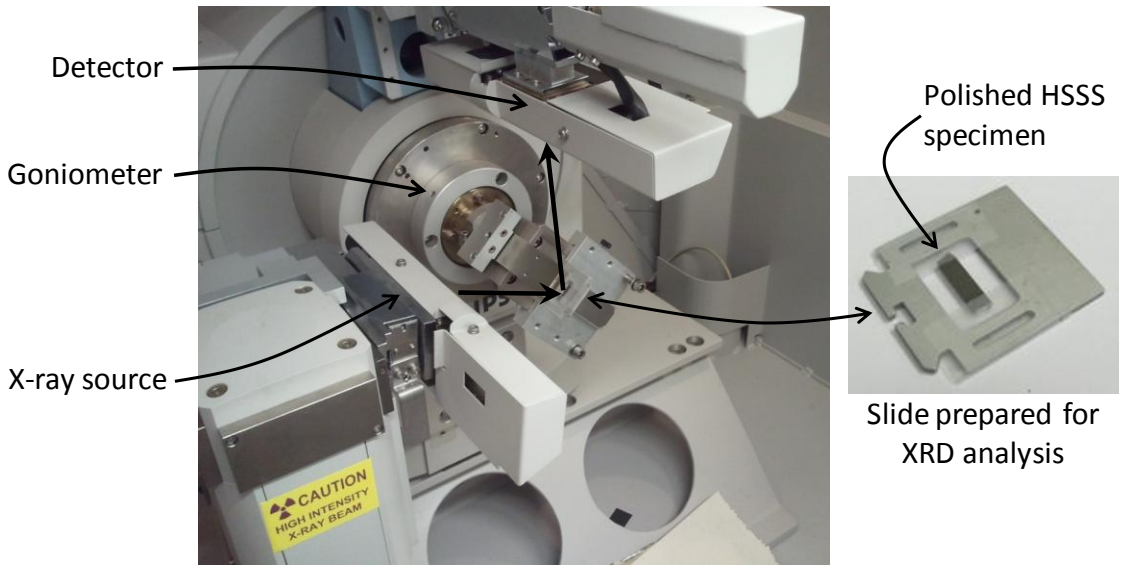

Figure 4.3 Experimental setup used for XRD analysis of HSSS wire specimens

4.3.2.3 High-C 1080 Control

Figure 4.4 (a) and (b) shows the transverse and longitudinal SEM micrographs of the etched 1080 control wire, respectively. The 1080 steel exhibited a microstructure orientated in the direction of cold drawing with a pearlitic structure of alternating lamellae of ferrite (bright) and cementite (dark). This microstructure is consistent with typical prestressing steels produced with a eutectoid C content (approx. 0.8 % C). Diffraction patterns revealed a primarily ferritic crystal structure (see Figure 4.5), although previous studies have shown that cementite peaks are overshadowed by ferrite (Lv, et al., 2008). Additional details on the 1080 steel used and its as-received surface condition are given in Section 3.2.1.

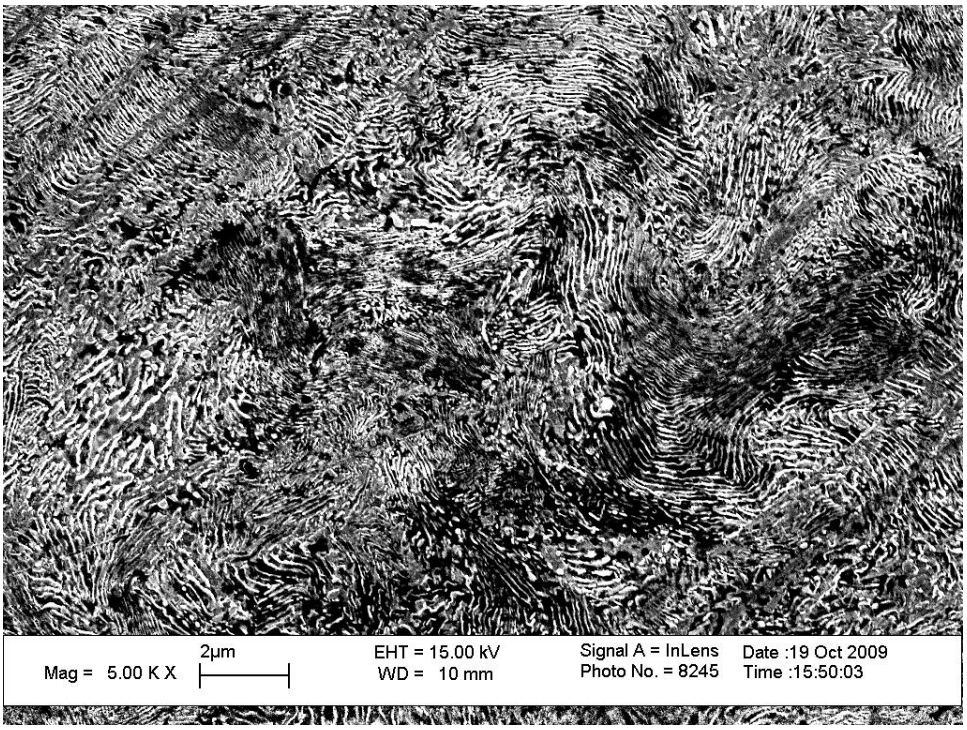

(a) Transverse orientation

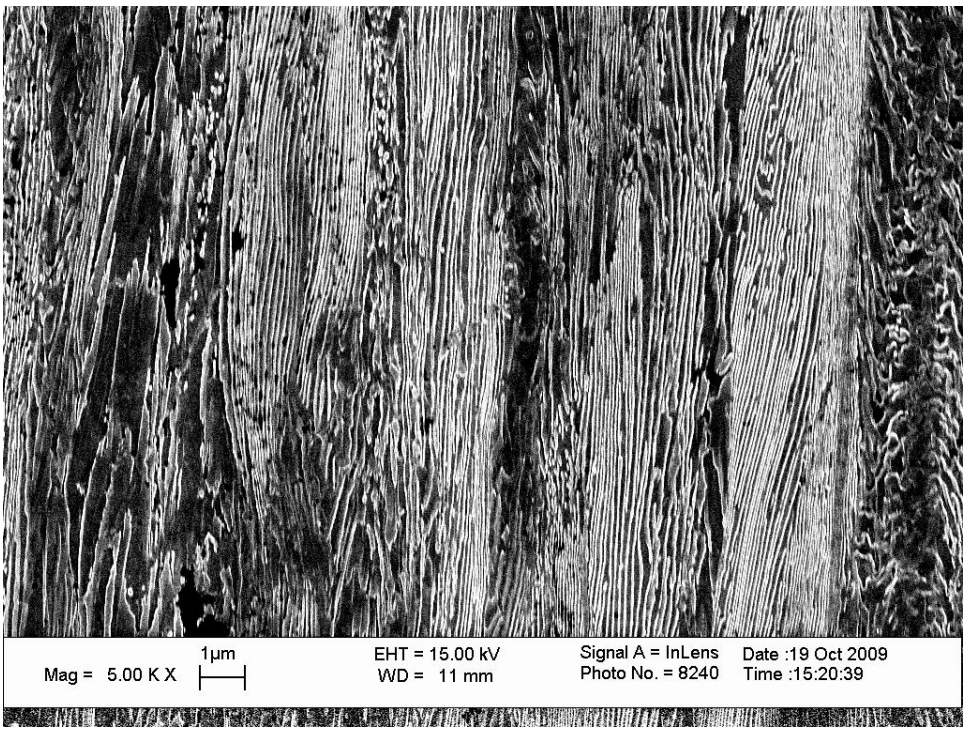

(b) Longitudinal orientation

Figure 4.4 Etched microstructure of High-C 1080 steel

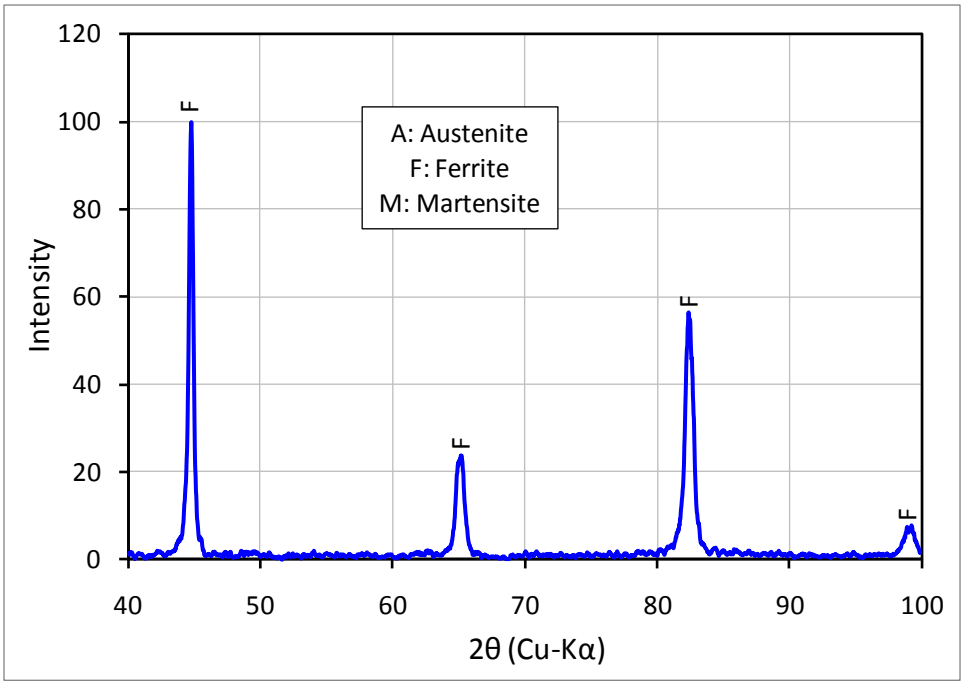

Figure 4.5 Diffraction pattern of High-C 1080 steel

4.3.2.4 Austenitic Grades 304 and 316

Both 304 and 316 exhibited similar microstructures, with grains elongated in the drawing direction and dense formations of strain-induced (α) martensite. Figure 4.6 depicts the typical microstructure observed in longitudinal and transverse orientations of 304. Bright regions correspond to retained austenite (γ) and dark regions correspond to α′-martensite. The presence of α′-martensite has been reported previously in heavily cold drawn 304 (a metastable austenitic stainless steel) (Cook, 1987) and 316 (Shyr, et al., 2010). Heavy slip banding was also observed in retained austenite grains. The density of α′was also observed to be higher at the surface of the 304 and 316 wires where significant plasticity occurs as the wire contacts the drawing die (see Figure 4.7).

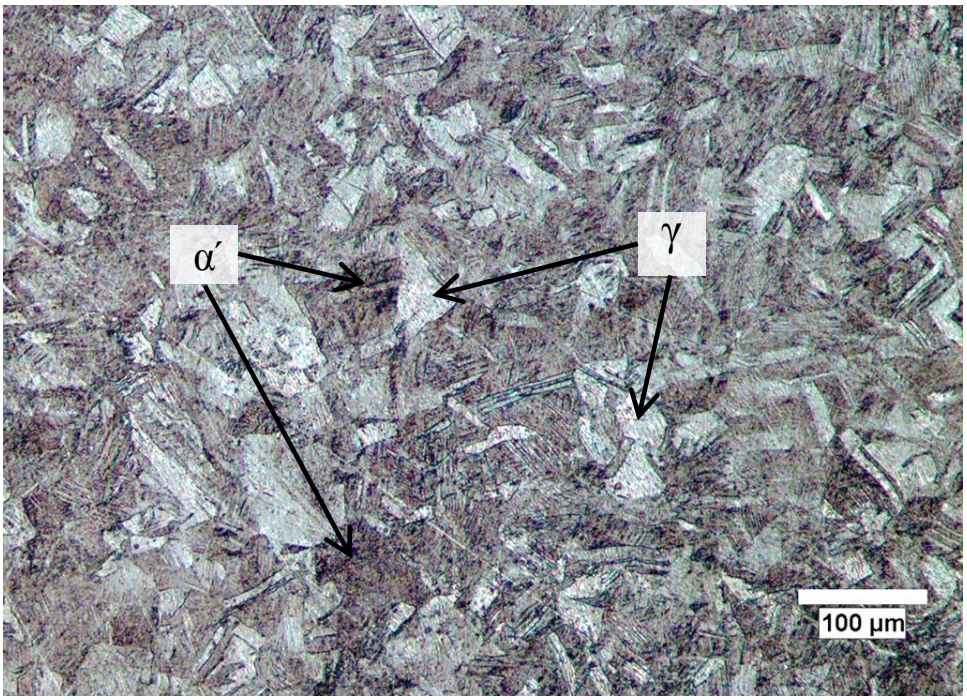

(a) Transverse orientation

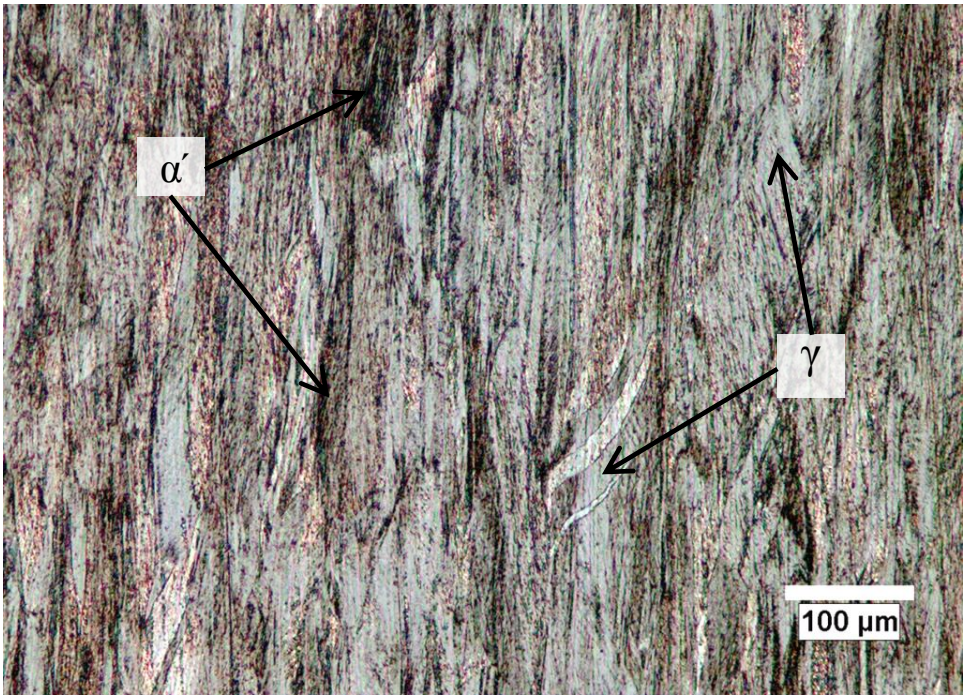

(b) Longitudinal orientation

Figure 4.6 Etched microstructure of 304 HSSS

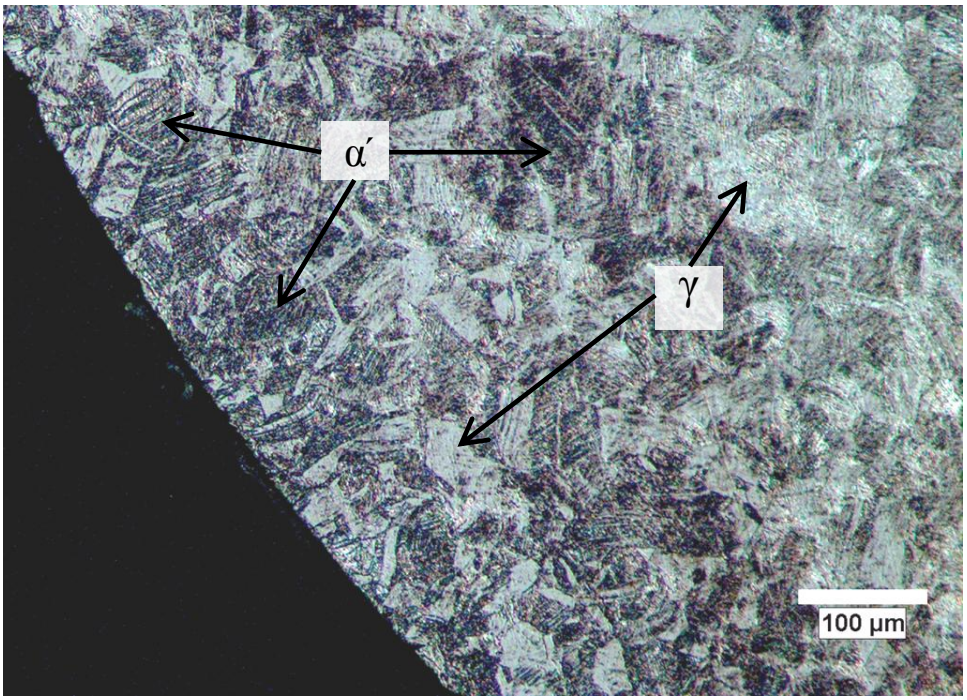

Figure 4.7 Increased density of α′-martensite at surface of 304 HSSS

The only apparent difference between 304 and 316 was the presence of distributed precipitates in 316 specimens. Unfortunately, precipitates were not retained in etched specimens, leaving voids in their place. The SEM micrograph shown in Figure 4.8 depicts a typical etched 316 microstructure with black dots at the site formerly occupied by precipitates. Precipitates seemed to be uniformly distributed throughout the microstructure with little tendency for locating at grain boundaries. Because the precipitates were removed during etching, EDX analysis to determine their composition could not be performed. However, based on the high sulfur content (0.030 %) of the as-received 316 HSSS, precipitates are likely sulfur-containing. The presence of such precipitates in the as-received 316 HSSS may result in decreased corrosion resistance when compared with a more pure alloy with lower sulfur content.

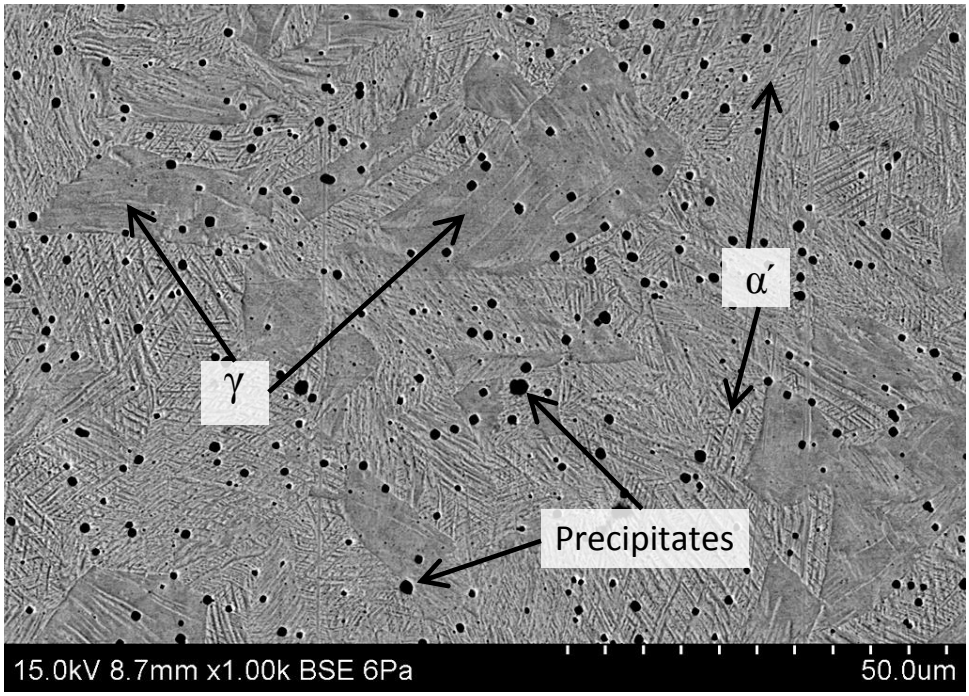

Figure 4.8 SEM micrograph of etched 316 showing distributed precipitates

While the metallographic techniques employed were useful to visualize the presence of α′-martensite and retained austenite, in many cases it is difficult to distinguish between heavy slip banding in retained austenite and α′. As a result, qualitative XRD was used to investigate the presence of α′ in 304 and 316 HSSSs. Figures 4.9 and 4.10 present the diffraction patterns obtained for 304 and 316, respectively. The phase α′-martensite was present in both 304 and 316. Grade 316 is traditionally thought to be more resistant to the formation of α′-martensite when deformed due to its high Ni content which increases the stability of the austenite phase (stacking fault energy (SFE) of 316 is 50 mJ/m^2 vs. 18 mJ/m^2 for 304) (Tavares, et al., 2006). However, at the high levels of cold drawing of HSSSs in the present study, 316 appears to contain similar levels of α′-martensite as 304 which may further jeopardize its typically higher corrosion resistance when compared with 304.

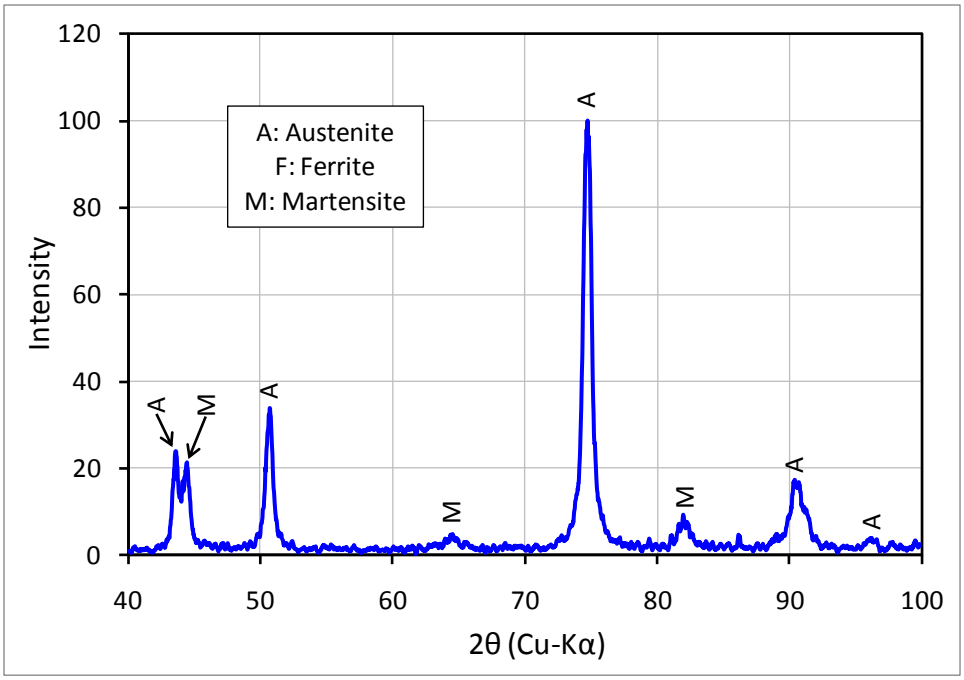

Figure 4.9 Diffraction pattern of 304 HSSS

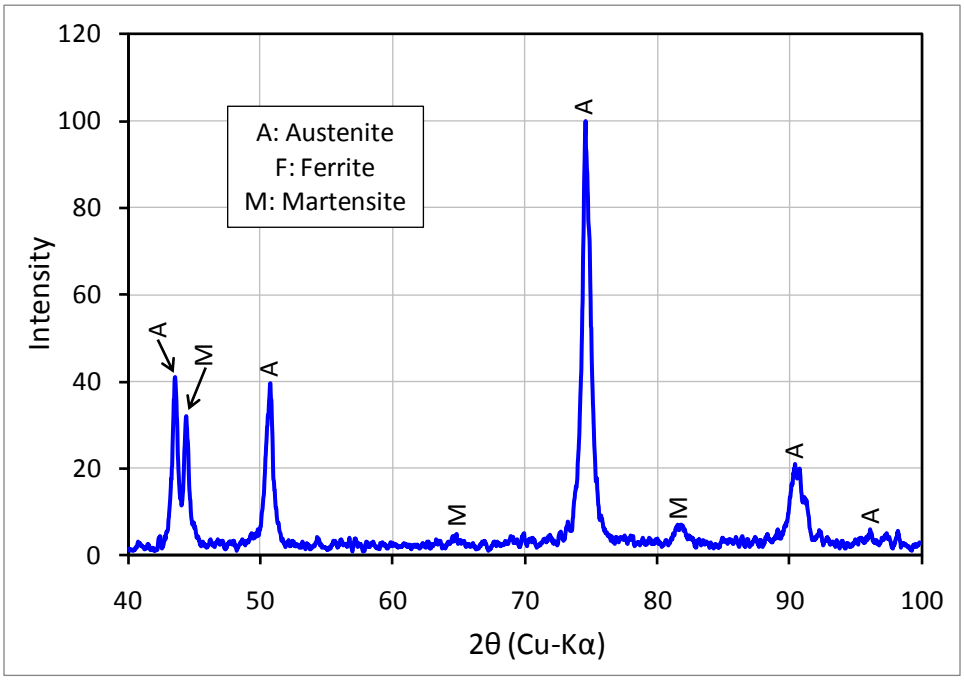

Figure 4.10 Diffraction pattern of 316 HSSS

4.3.2.5 Duplex Grades 2101, 2205, and 2304

Duplex grades 2101, 2205, and 2304 exhibited similar microstructures with grains oriented in the longitudinal drawing direction. Figure 4.11 depicts the typical microstructure observed (2205 shown) with alternating lamellae of brighter austenite (γ) and darker ferrite (δ). Quantitative image analysis was performed using ImageJ to determine the proportion of austenite and ferrite in each duplex HSSS. SEM images of electroetched transverse microstructures were thresholded to isolate a particular phase so an area fraction measurement could be made based on pixel count. Austenite (ferrite) contents were found to be 58.8 % (41.2 %), 49.6 % (50.4 %), and 56.3 % (43.7 %) for 2101, 2205, and 2304, respectively. However, these calculations assume that the only two phases present are austenite and ferrite. Previous research has shown that, like austenitic grades, duplex grades may be susceptible to the formation of α′-martensite in the austenite phase with heavy cold drawing (Baldo and Meszaros, 2010; Tavares, et al., 2006). These previous research efforts have focused on 2205 and 2101, with no examination of 2304. Typical microstructural etchants (like those employed in the present study) used for metallography of duplex stainless steels do not simultaneously indicate the presence of α′ in the austenite phase and ferrite. Therefore, other techniques like XRD must be used to confirm the presence of α′ in duplex stainless steels. One of the challenges in detecting α′-matertensite in duplex stainless steels is that, like ferrite, it possesses a BCC crystal structure and therefore similar diffraction peak locations. As a result, determination of the presence of α′ in duplex stainless is best performed by comparing the cold drawn material with the annealed condition. Figure 4.12 shows the diffraction patterns from 40˚ to 70˚ 2θ of annealed 2101, 2205, and 2304 duplex stainless steel obtained by other researchers.

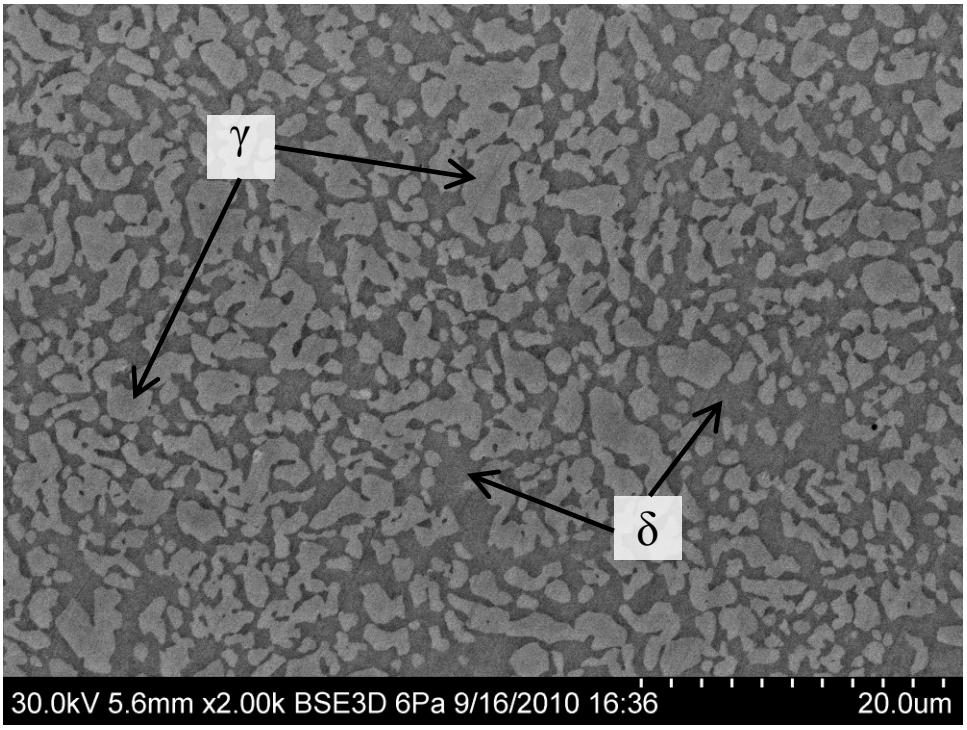

(a) Transverse orientation

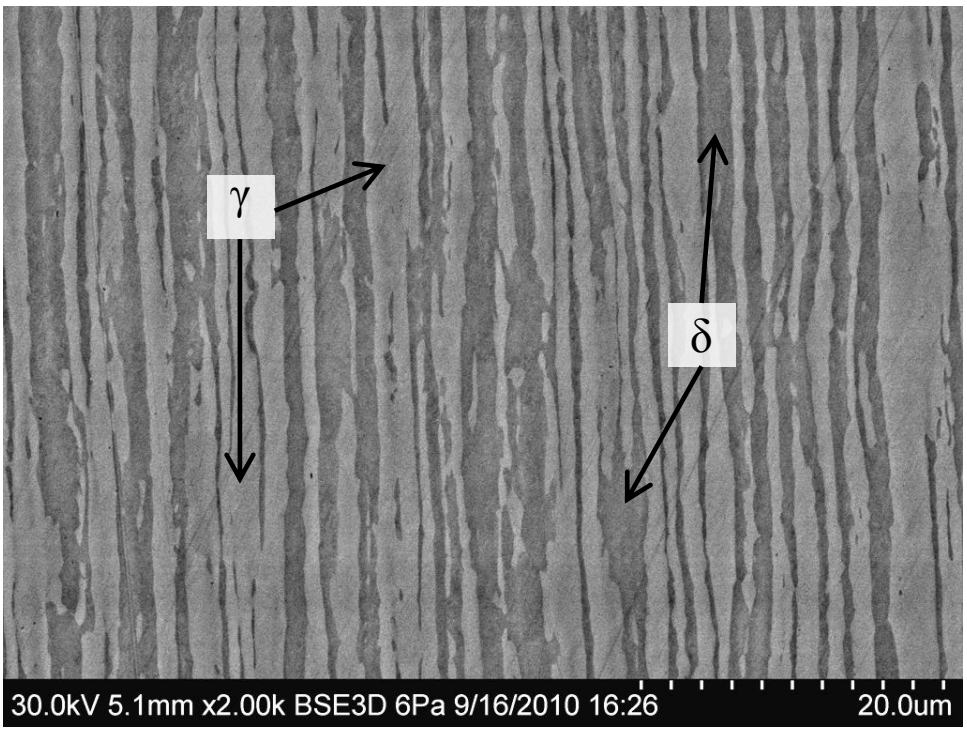

(b) Longitudinal orientation

Figure 4.11 Etched microstructure of 2205 HSSS

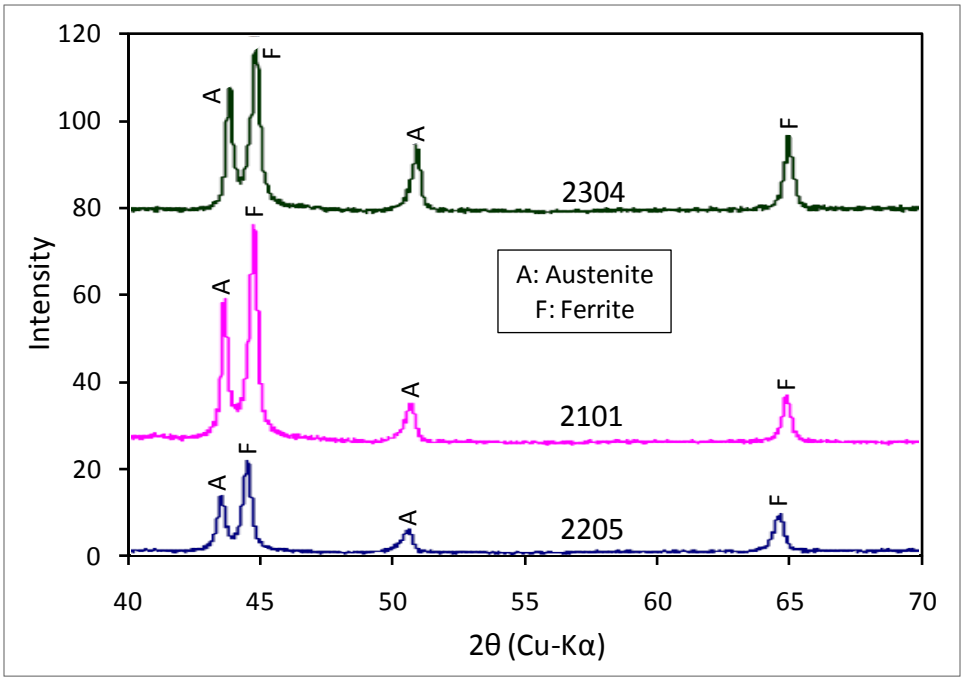

Figure 4.12 XRD patterns of annealed 2101, 2205, and 2304 (from (Bhattacharya, 2008))

From the diffraction patterns shown in Figure 4.12, a consistent peak high ratio between austenite and ferrite can be seen in 2101, 2205, and 2304, consistent with the approximately 50/50 content of austenite and ferrite. Based on these diffraction patterns in the annealed condition, qualitative comparisons can be made with duplex HSSSs in the present study. Figures 4.13, 4.14, and 4.15 present the diffraction patterns of 2101, 2205, and 2304, respectively. In duplex HSSS, a reduction in austenite peak heights (primarily at 44˚ and 51˚) was observed, with the greatest reductions in lean duplex grades 2101, and 2304. In conjunction with reduced austenite peak heights, increases in composite ferrite and martensite peaks was observed (strongest in 2304, see 65˚ and 83˚ peaks in Figure 4.15). Primary peak locations of 2101, 2205, and 2304 were 44.56˚, 44.91˚, and 44.49˚, respectively. These peak shifts to larger d-spacings in 2101 and 2304 indicate a more complete transformation to ά-martensite when compared with 2205.

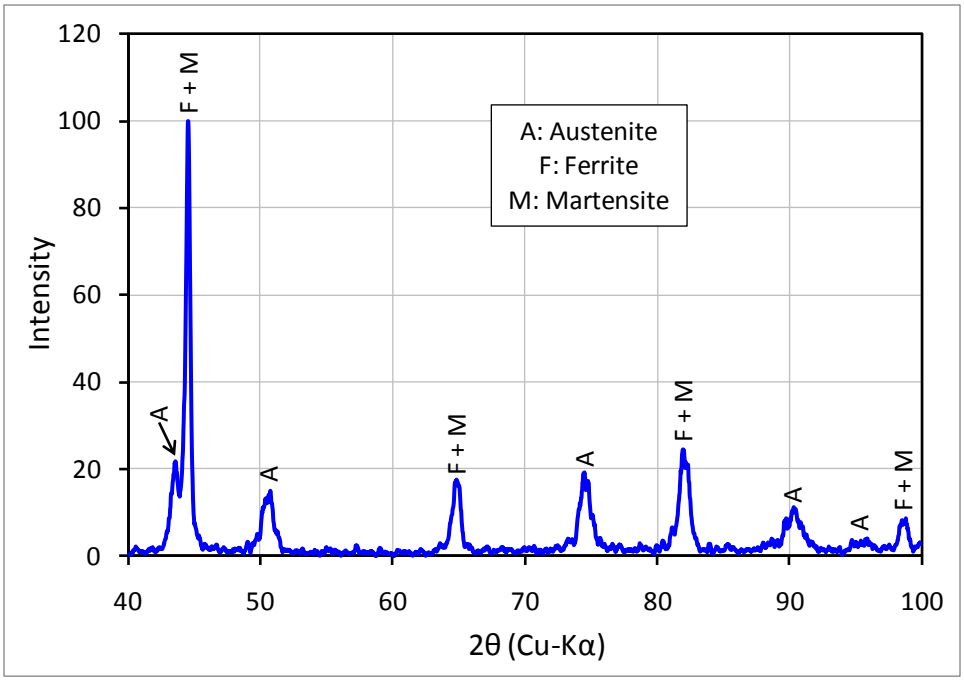

Figure 4.13 Diffraction pattern of 2101 HSSS

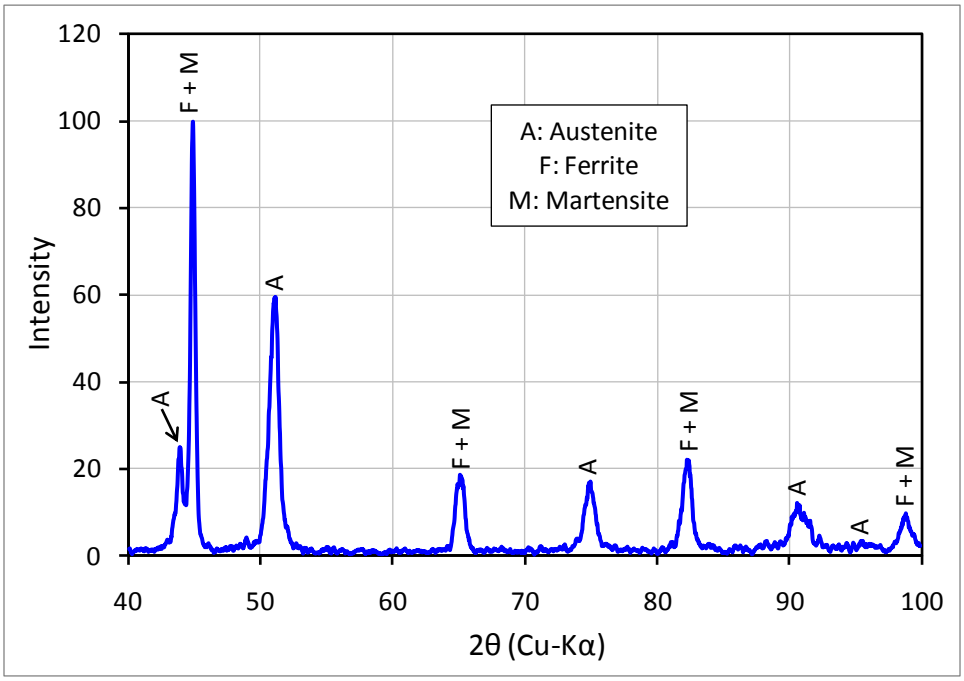

Figure 4.14 Diffraction pattern of 2205 HSSS

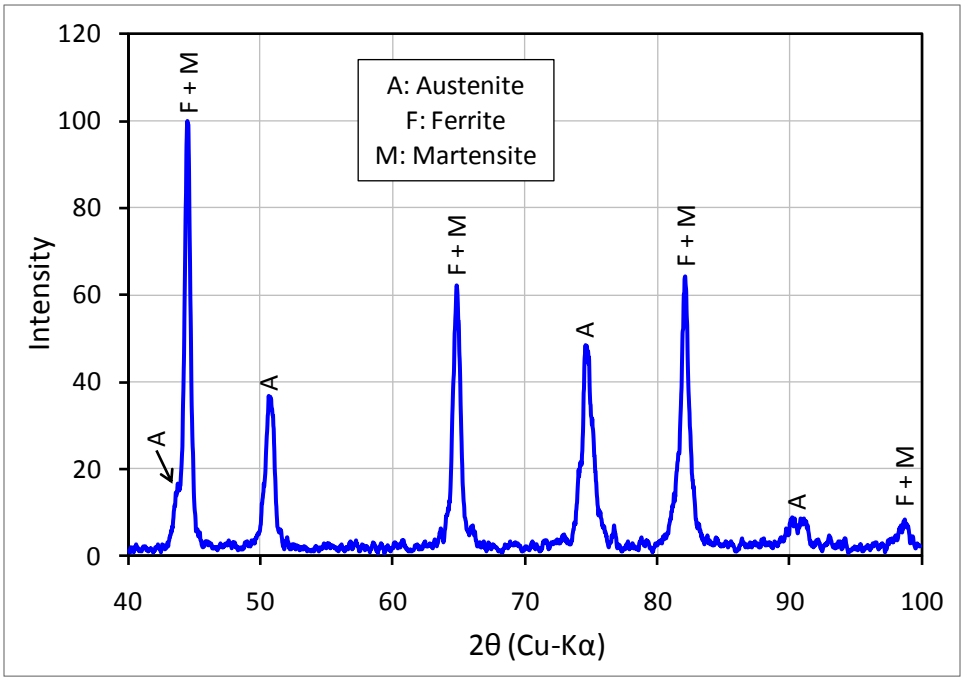

Figure 4.15 Diffraction pattern of 2304 HSSS

One final observation warranting discussion is the presence of precipitates in duplex HSSSs. With the electroetching method used, precipitates are revealed as rounded black features (voids) in backscattered SEM images corresponding to the sites where precipitates once resided. No precipitates were present in 2205 HSSSs. However, precipitates were found in lean duplex grades 2101 and 2304. Figure 4.16 depicts the typical distribution in precipitates in an etched 2101 specimen. Precipitates were exclusively located at austenite/ferrite phase boundaries in 2101 and 2304 HSSSs. The presence of such precipitates, along with α′-martensite, may further degrade the corrosion resistance of 2101 and 2304 when compared with 2205 HSSS.

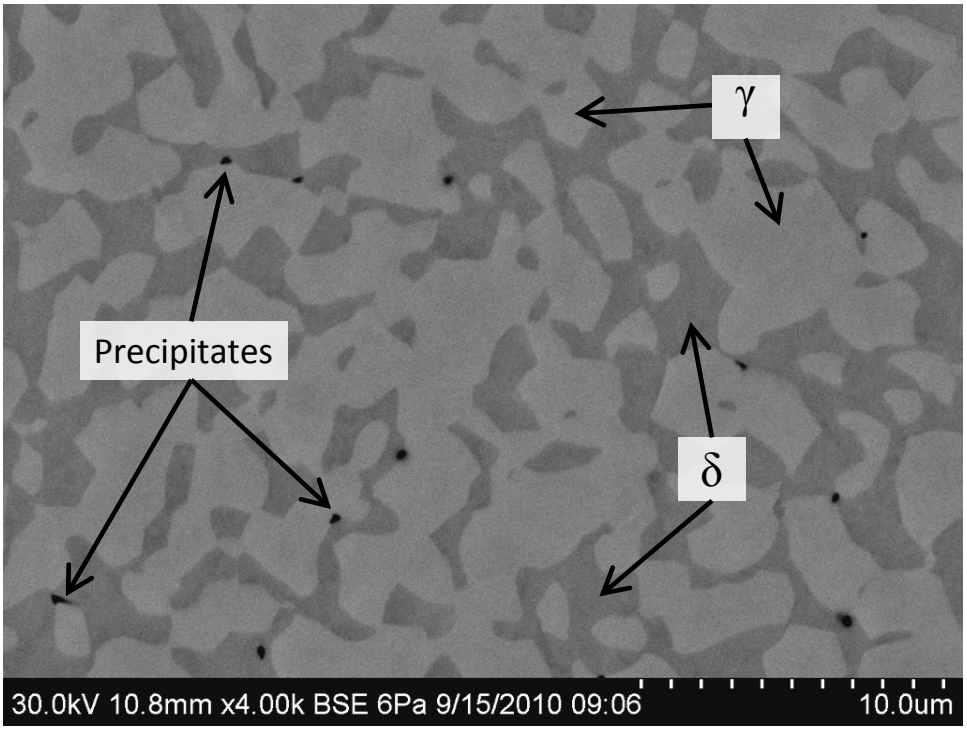

Figure 4.16 Precipitates present at austenite/ferrite phase boundaries in 2101 HSSS

4.3.2.5 Precipitation Hardened Martensitic Grade 17-7

Precipitation hardened 17-7 exhibited a primarily martensitic microstructure with distributed grains of retained austenite. Figure 4.17 shows the etched microstructure of 17-7 in transverse and longitudinal orientations. When examined using SEM, distributed Al-containing precipitates resulting from the precipitation hardening heat treatment were observed throughout the microstructure (see Figure 4.18). Like the austenitic grades, it was difficult to distinguish between heavy slip banding in retained austenite regions and regions of martensite. Diffraction patterns (Figure 4.19) indicate that the 17-7 HSSS has almost fully transformed to martensite with little austenite retained.

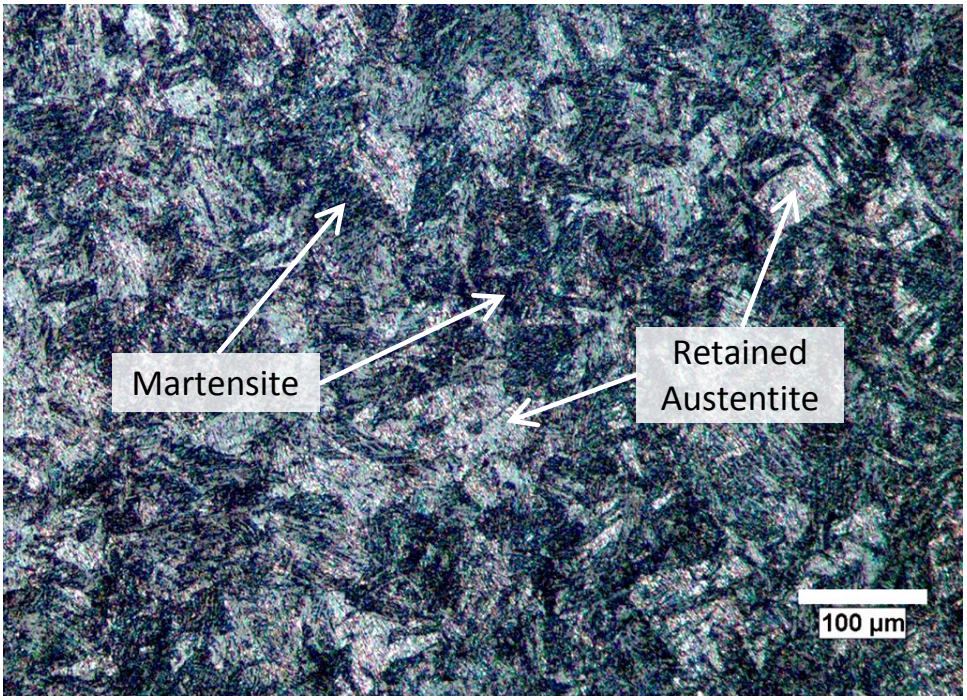

(a) Transverse orientation

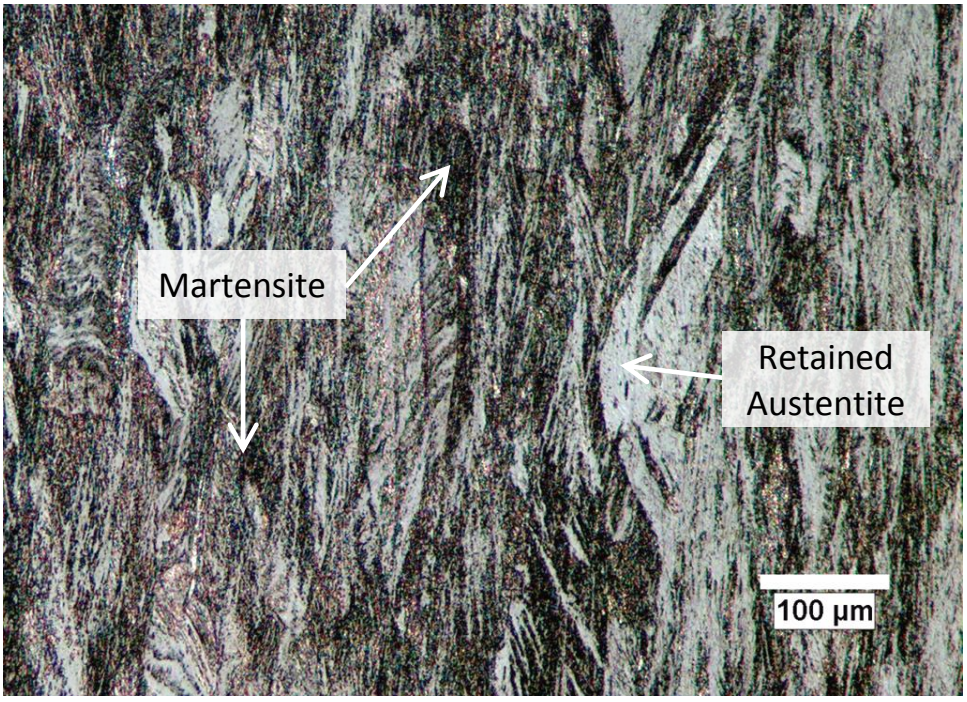

(b) Longitudinal orientation

Figure 4.17 Etched microstructure of 17-7 HSSS

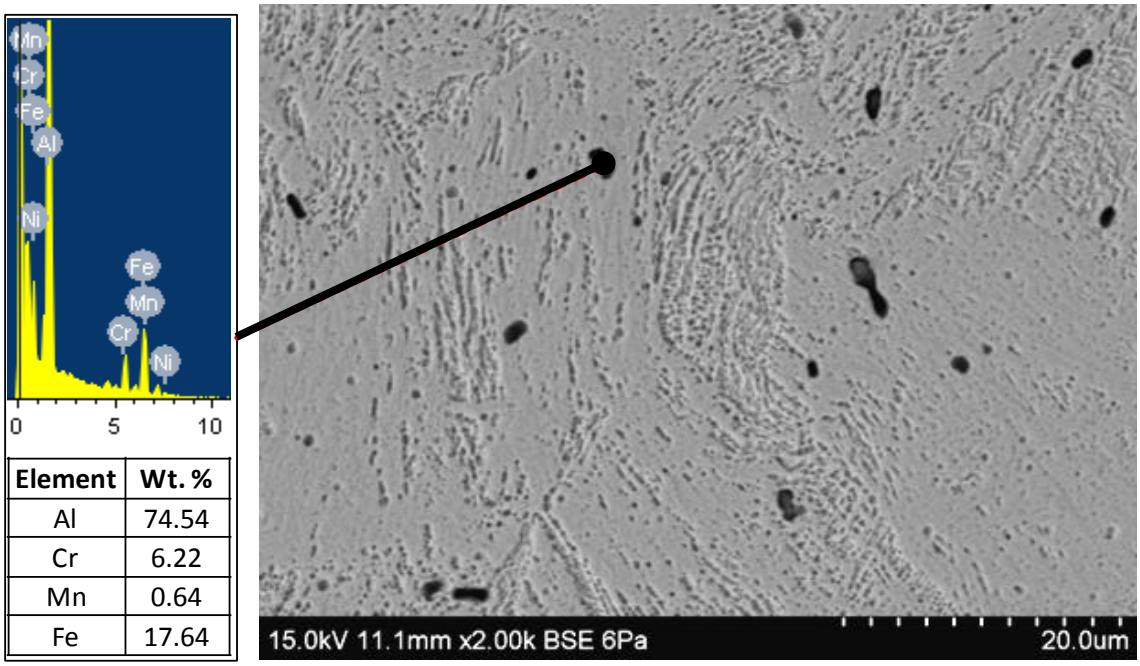

Element	Wt. %
Al	74.54
Cr	6.22
Mn	0.64
Fe	17.64

Figure 4.18 Distributed precipitates shown in etched 17-7 HSSS

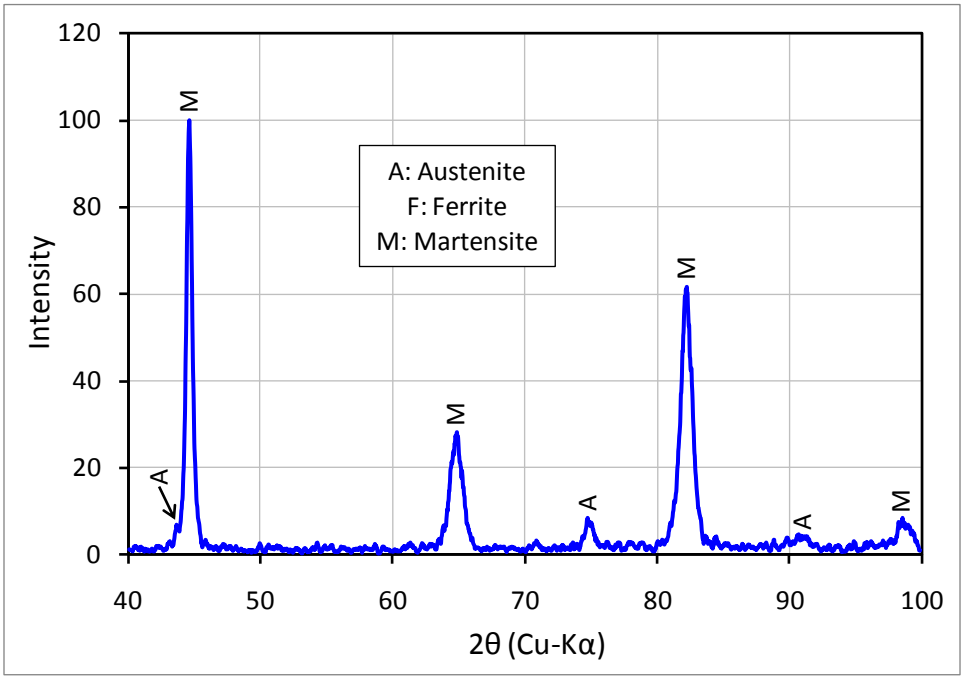

Figure 4.19 Diffraction pattern of 17-7 HSSS

4.3.2.6 Surface Condition of As-Received HSSSs

In practice, HSSSs utilized as prestressing reinforcement in concrete will not be polished, sand-blasted, or thoroughly cleaned prior to use. Therefore, there is a need to assess the surface condition of these materials as it may have an influence on corrosion initiation and propagation. Each candidate HSSS was examined using SEM and EDX to determine both the morphology and chemistry of the as-received surface. Detailed discussion of the as-received surface condition of the High-C 1080 steel is given in Sections 3.2.1 and 3.3.3. In general, surface conditions varied depending on manufacturing sites (i.e., either 304, 316, and 17-7 produced at Sumiden Wire Products Corp. or 2101, 2205, and 2304 produced at Fagersta Stainless). SEM micrographs shown in Figure 4.20 depict the typical surface of HSSSs produced by Sumiden and Fagersta.

Grades 304, 316, and 17-7 produced by Sumiden displayed a heterogeneous surface with deformed grains and voids at grain boundaries. The voids were filled with drawing lubricants which were determined to be largely Ca based when analyzed using EDX (common for animal fat or stearate drawing lubricants). Figure 4.21 shows the results of elemental mapping performed using EDX to determine the distribution of Ca and Fe and thus location of drawing lubrication. Grades 2101, 2205, and 2304 produced by Fagersta displayed a deformed surface with no remnants of drawing lubricants. These studies have shown that in the cold drawn condition, HSSSs have a deformed surface with many sites which may aid in the initiation and propagation of corrosion (Newman, 2001). In addition, from these images, the cleaning techniques following cold drawing at Fagersta Stainless appear to be more effective in removing drawing lubricants off the wire surface than those utilized by Sumiden Wire Products Corporation.

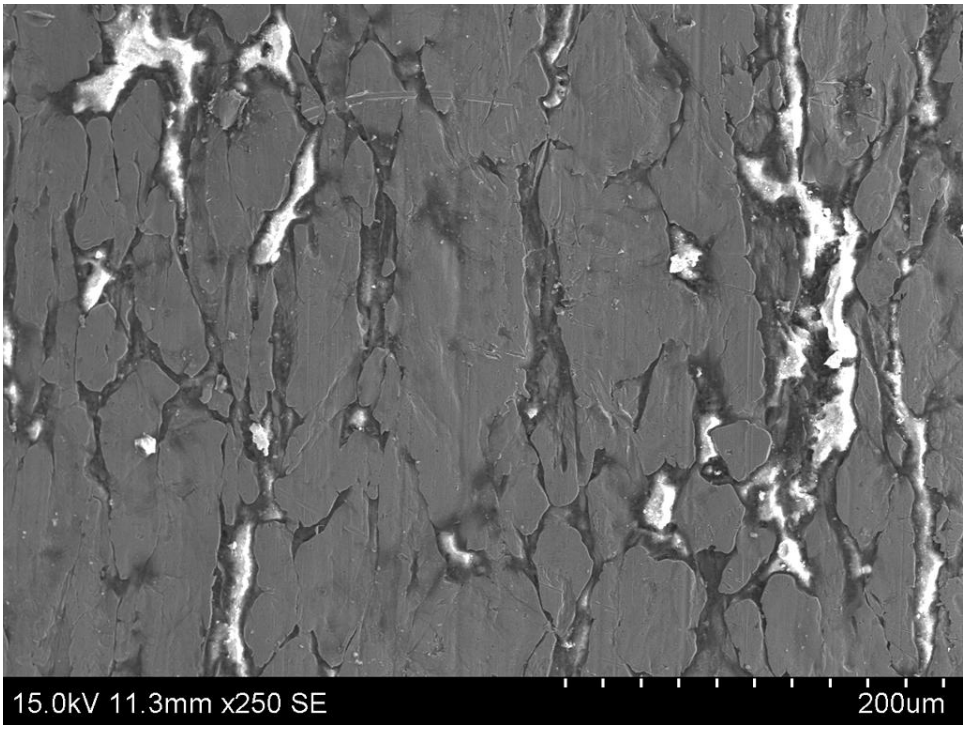

(a) HSSSs produced by Sumiden Wires Products Corporation (304 shown)

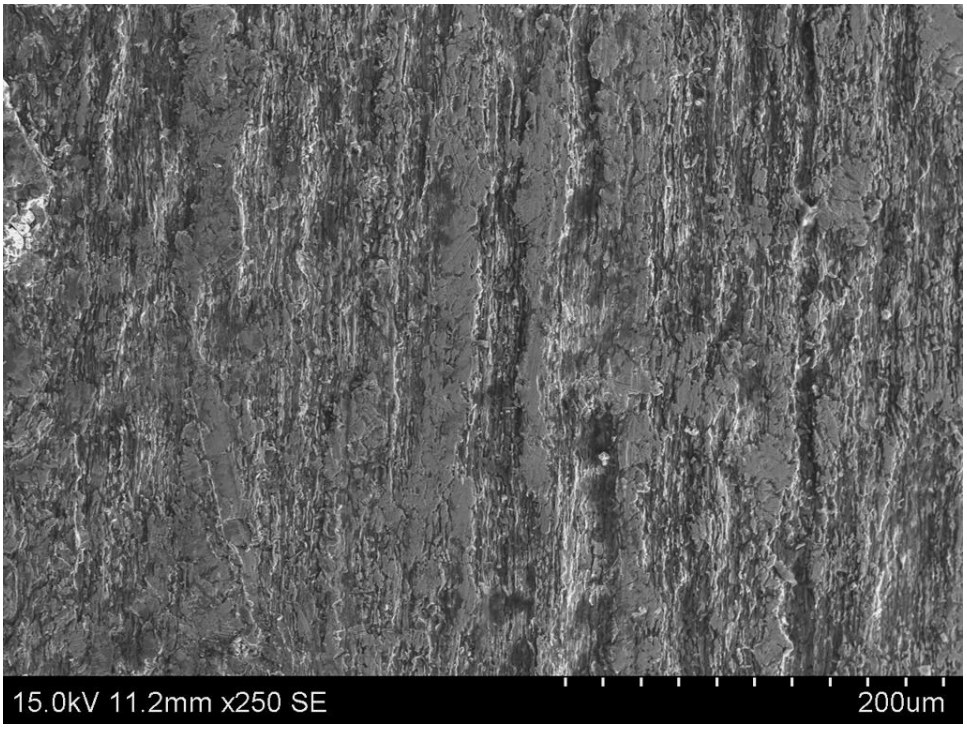

(b) HSSSs produced by Fagersta stainless (2101 shown)

Figure 4.20 Surface condition of as-received HSSS wires

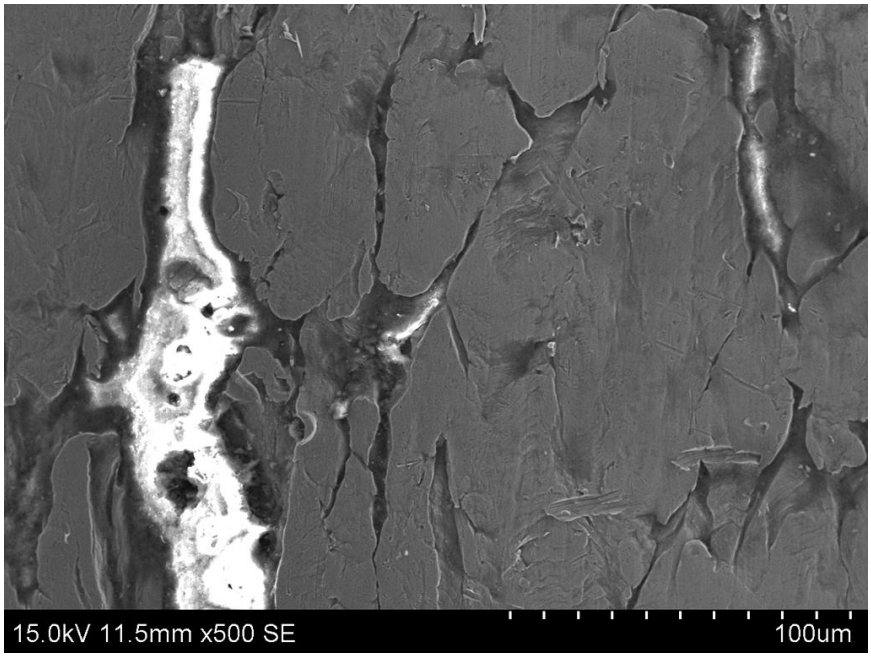

(a) SEM micrograph of surface of 304 HSSS

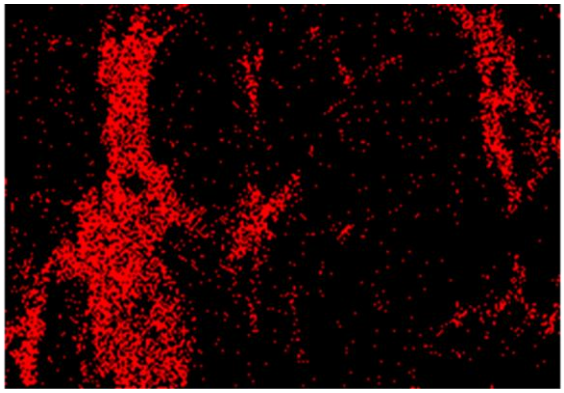

(b) Ca elemental map

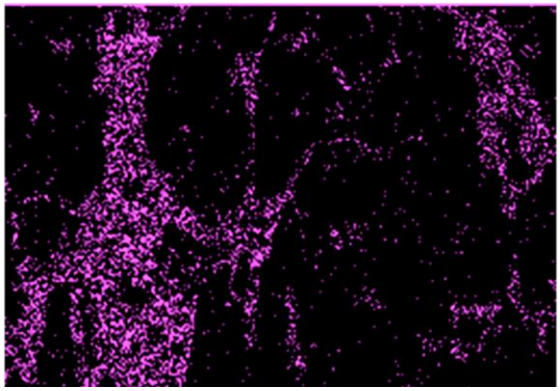

(c) C elemental map

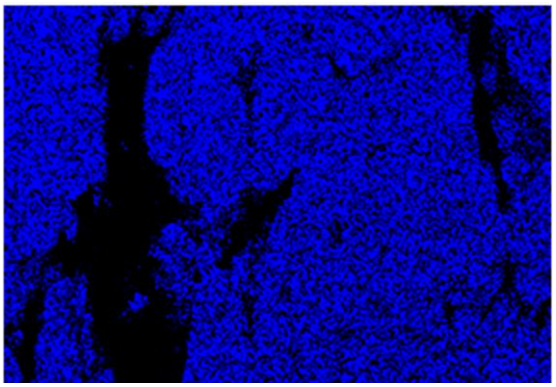

(d) Fe elemental map

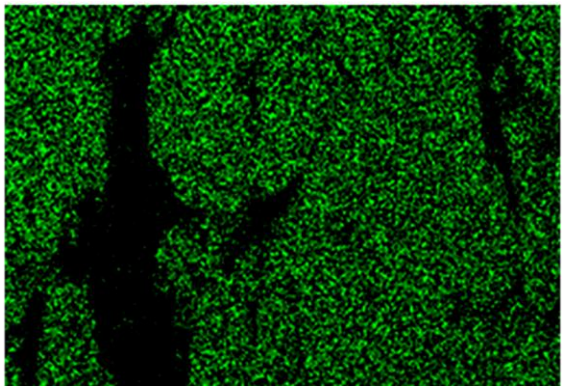

(e) Ni elemental map

Figure 4.21 Ca, C, Fe, and Ni elemental mapping corresponding to SEM micrograph of 304 HSSS shown in (a)

CHAPTER 5

MECHANICAL PROPERTIES OF HIGH-STRENGTH STAINLESS STEELS

With an intended application as prestressing reinforcement in concrete, determination of the mechanical properties was essential for all candidate HSSSs investigated. Experimental efforts focused on evaluating stress vs. strain behavior and stress relaxation of candidate HSSSs. A high-C 1080 prestressing steel was also included to serve as a baseline for comparison. A series of experiments were also conducted to compare the stress vs. strain behavior of wires with that of seven-wire prestressing strands.

5.1 Stress vs. Strain Behavior of Wires

5.1.1 Experimental Methods

Tensile testing of wires was performed according to the provisions outlined in ASTM A370. Specimens for tensile testing were cut directly from the coil of wire to a total length of 30.5 cm (12 in). Triplicate specimens were tested with their full cross section (i.e., without milling to reduce the diameter within the gage length) to preserve any residual stress distributions which would influence stress vs. strain behavior. The gage length of wire specimens tested was approximately 20 cm (8 in). Triplicate tests of each alloy were conducted. All experiments were performed using a screw-driven Instron electromechanical testing frame with maximum capacity of 100 kN (22.5 kips).

Specimens were secured in the testing frame using flat wedge grips as is typical for the testing of stainless steel spring wire. Strain measurements were made using a calibrated Epsilon extensometer with 50.8 mm (2 in) gage length. The extensometer was attached to each specimen using a spring loaded arm and rubber bands to prevent slipping of the knife edge that would result in erroneous strain measurements. A constant displacement rate of 5 mm/min (0.2 in/min) corresponding to a strain rate of approximately 0.025 min^{-1} was used for all tensile tests. The experimental setup is shown in Figure 5.1.

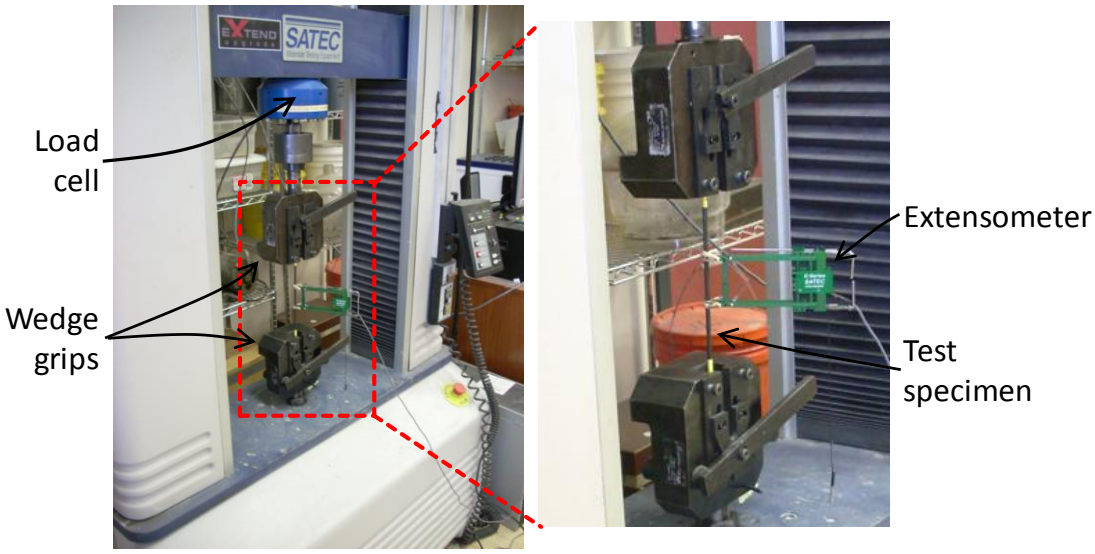

Figure 5.1 Experimental setup used for tensile testing of HSSS wires

One issue encountered during testing was residual curvature of the HSSS wires. In order to lessen the effect of curvature on stress vs. strain behavior, each wire was pre-loaded to a tensile stress of approximately 170 MPa (25 ksi) prior to attaching the extensometer. To prevent damage to the extensometer during sample fracture, it was removed from test specimens at approximately 2 % strain for HSSSs and 5 % strain for the 1080 prestressing steel. These strain levels approximately correspond to just prior to

ultimate strength (i.e., as loading rate → 0). Measurements of strain after removing the extensometer were based on cross head displacement and were calculated using a calibration between displacement and strain from the extensometer for the 0.5 % of strain prior to removing the extensometer. Figure 5.2 shows an example displacement vs. strain calibration for 304 HSSS. Using this method, more accurate values of strain are obtained by accounting for compliance of the testing machine (note: nonlinearity in strain vs. displacement shown in Figure 5.2) and fluctuations in the true gage length between the grips. Yield strength (σ_y) was calculated using 0.2 % offset and 1 % strain criteria. Elastic modulus was calculated between 250 MPa (36 ksi) and 500 MPa (72 ksi). Ultimate strength (σ_{ult}), ultimate strain (ϵ_{ult}), and fracture surface area reduction (ΔA) were also calculated. Following tensile testing, fracture surfaces were characterized using optical and scanning electron microscopy.

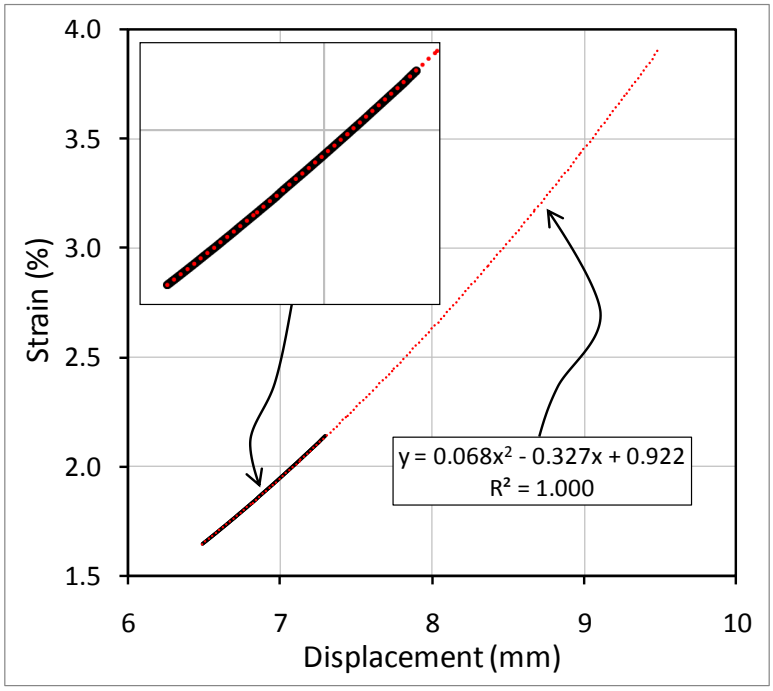

Figure 5.2 Crosshead displacement vs. strain calibration of 304 HSSS

5.1.2 Results and Discussion

Representative tensile engineering stress vs. strain curves for candidate HSSSs and the control are shown in Figure 5.3. Mechanical properties are recorded in Table 5.1, including the mean and standard deviation of the triplicate tensile tests. Tensile strengths of 1250 to 1550 MPa (181 to 225 ksi) were achieved in candidate HSSSs. These strengths were in the 1380 MPa (200 ksi) range expected based on the work hardening behavior shown in Figure 4.1. The 1963 MPa (285 ksi) tensile strength of the 1080 prestressing steel is also similar to what has been reported in the literature for wire used in A416 prestressing strands which has a guaranteed tensile strength of 1860 MPa (270 ksi) (Atienza and Elices, 2007). Further cold drawing and a reduction in residual stresses is likely necessary to increase tensile strengths of HSSSs to the levels similar to 1080.

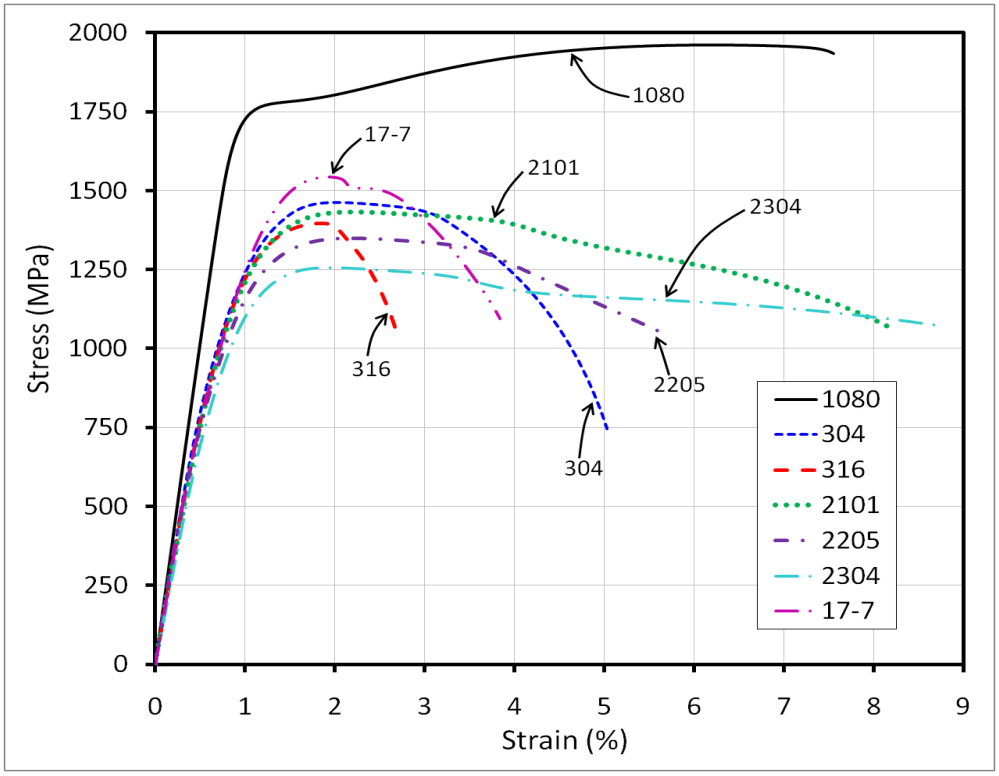

Figure 5.3 Tensile stress vs. strain behavior of candidate HSSS and 1080 control

Table 5.1 Mechanical properties

Alloy		σ_y 0.2% MPa/ksi	σ_y 1% MPa/ksi	σ_{ult} MPa/ksi	ϵ_{ult} (%)	E GPa/ksi	ΔA^* (%)
Mean	1080	1750/254	1738/252	1963/285	7.5	202/29300	34.9
	304	1173/170	1227/178	1461/212	5.5	164/23770	72.5
	316	1185/172	1220/177	1401/203	2.7	160/23160	61.6
	2101	1101/160	1211/176	1433/208	8.0	172/24990	67.9
	2205	1026/149	1145/166	1349/196	5.7	169/24190	84.6
	2304	1035/150	1097/159	1247/181	8.7	151/21850	77.2
	17-7	1226/178	1352/196	1556/226	3.8	176/25590	62.3
Standard Deviation	1080	5.5/0.8	11.7/1.7	2.3/0.3	0.23	5.8/847	4.1
	304	19.6/2.8	11.9/1.7	1.3/0.2	3.21	7.9/1142	2.0
	316	12.8/1.9	6.1/0.9	4.6/0.7	0.38	4.0/587	0.6
	2101	28.1/4.1	5.8/0.8	1.6/0.2	0.42	8.4/1217	3.4
	2205	19.6/2.8	7.2/1.0	1.6/0.2	0.73	6.2/904	1.0
	2304	9.4/1.4	14.4/2.1	1.2/0.2	0.16	4.4/632	2.8
	17-7	10.4/1.5	27.0/3.9	16.8/2.4	0.14	8.2/1196	0.8

* Change in cross sectional area before and after testing at fracture surface

From these data, two important characteristics of the stress vs. strain behavior of HSSSs arise: (1) stress vs. strain nonlinearity below yield and (2) a lack of strain hardening following yield.

In the annealed condition, most metals (including stainless steels) exhibit negligible residual stresses, resulting in linear stress vs. strain behavior prior to yielding. When cold drawn, significant residual stresses can form inside of the metal and produce low-strain nonlinearity. In high-strength cold drawn wire, residual stresses are typically tensile at the surface of the wire and compressive at the center of the wire (Atienza and Elices, 2007). Therefore, upon tensile loading, the surface of the wire will begin to yield prior to the center, resulting in observed nonlinearity. Figure 5.4 shows the typical residual stress distribution in cold drawn 1080 prestressing steel.

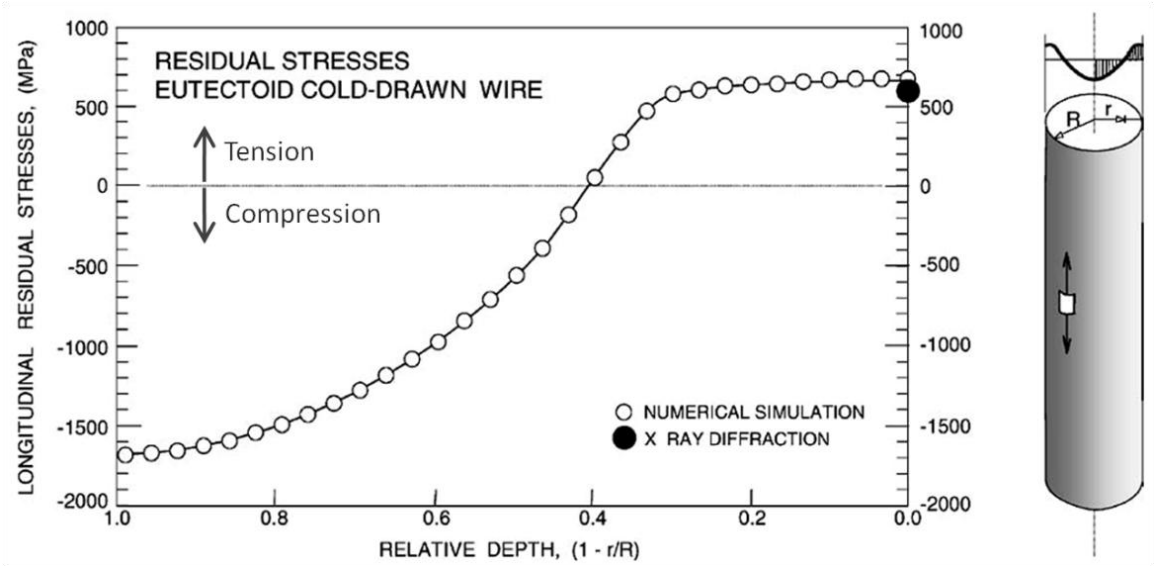

Figure 5.4 Residual stresses in 1080 prestressing steel (from (Elices, 2004))

Figure 5.5 shows stress vs. strain curves for 1080 and 304 from 0 % to 1.5 % strain. Lines have been included to show the proportional limit and 0.2 % offset and 1 % yield strengths. In 1080 which has received a low-relaxation stabilizing heat treatment, linear-elastic behavior is observed up to 1250 MPa (181 ksi), followed by increased compliance as the yield strength is approached. In this case, both the 0.2 % offset and 1 % yield strength are similar. However, in 304 HSSS which has not received a stabilizing heat treatment, nonlinear stress vs. strain behavior is observed at stresses above 600 MPa (87 ksi), indicating the presence of residual stresses. This nonlinearity also results in anomalous measures of yield strength by both the 0.2 % offset and 1 % strain techniques. Similar behavior was observed in all candidate HSSSs.

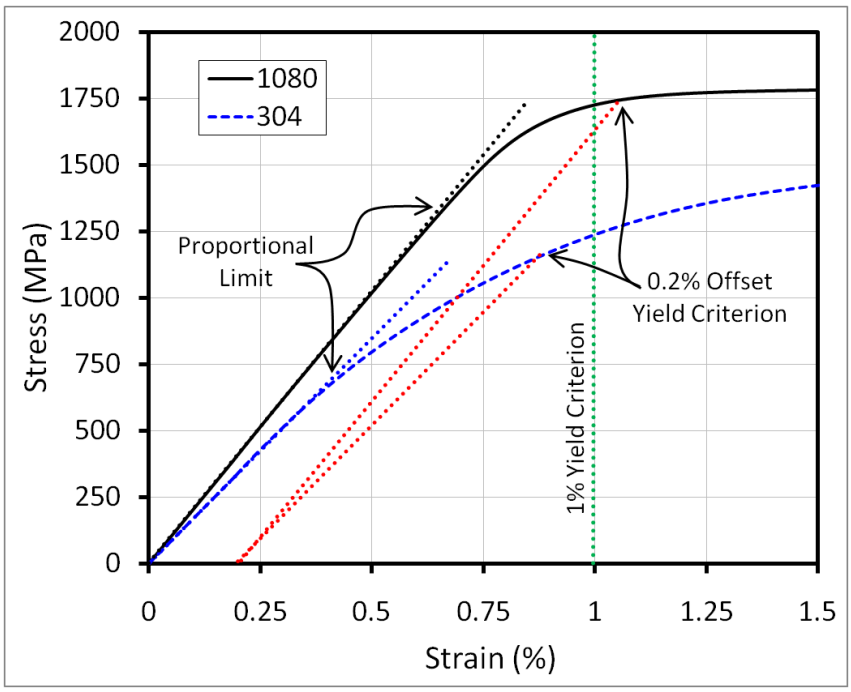

Figure 5.5 Close up of stress vs. strain behavior of 1080 and 304 HSSS

When compared with 1080 prestressing steels, all candidate HSSSs exhibited relatively ductile modes of fracture. This is most clearly observed in the area reduction values shown in Table 5.1, failure morphologies shown in Figure 5.6, and fracture surfaces shown in Figure 5.7. Fracture of 1080 prestressing steel was found to be brittle, with limited necking (see Figure 5.6 (a)) and a fracture surface dominated by cleavage planes (see Figure 5.7 (b)). In HSSSs, ductile necking failures were observed (see Figure 5.6 (b)) with a classic cup-and-cone fracture surface comprised of a shear lip around the perimeter of the neck and coalesced voids at the center.

While the HSSSs exhibited ductile modes of fracture, it is most important to note that none of the HSSSs tested exhibited any post-yield strain hardening; that is, failures were controlled by immediate strain localization following full yielding of the cross section – a non-ductile failure mode. This necessitates the definition of two types of

ductile failure: (1) microstructural ductile failure associated with a classic necking failure and (2) structural ductile failure associated with increased load carrying capacity by strain hardening prior to failure. In most cases, microstructural ductile failure coincides with structural ductile failure. This is not the case in heavily cold drawn HSSSs which exhibit non-ductile structural failures even though fracture surfaces appear to be ductile.

(a) Typical 1080 steel fracture surface

(b) Typical HSSS fracture surface (304 shown)

Figure 5.6 Fracture morphology of 1080 and 304 HSSS

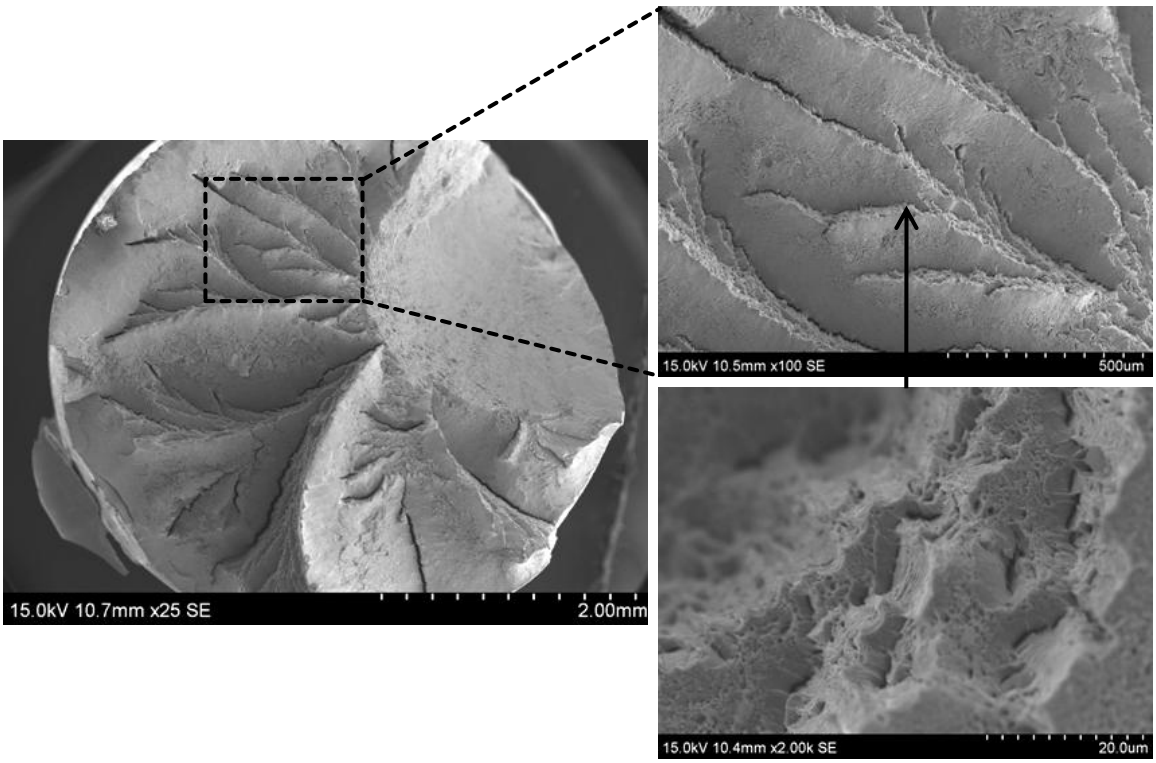

(a) Typical 1080 prestressing steel fracture surface

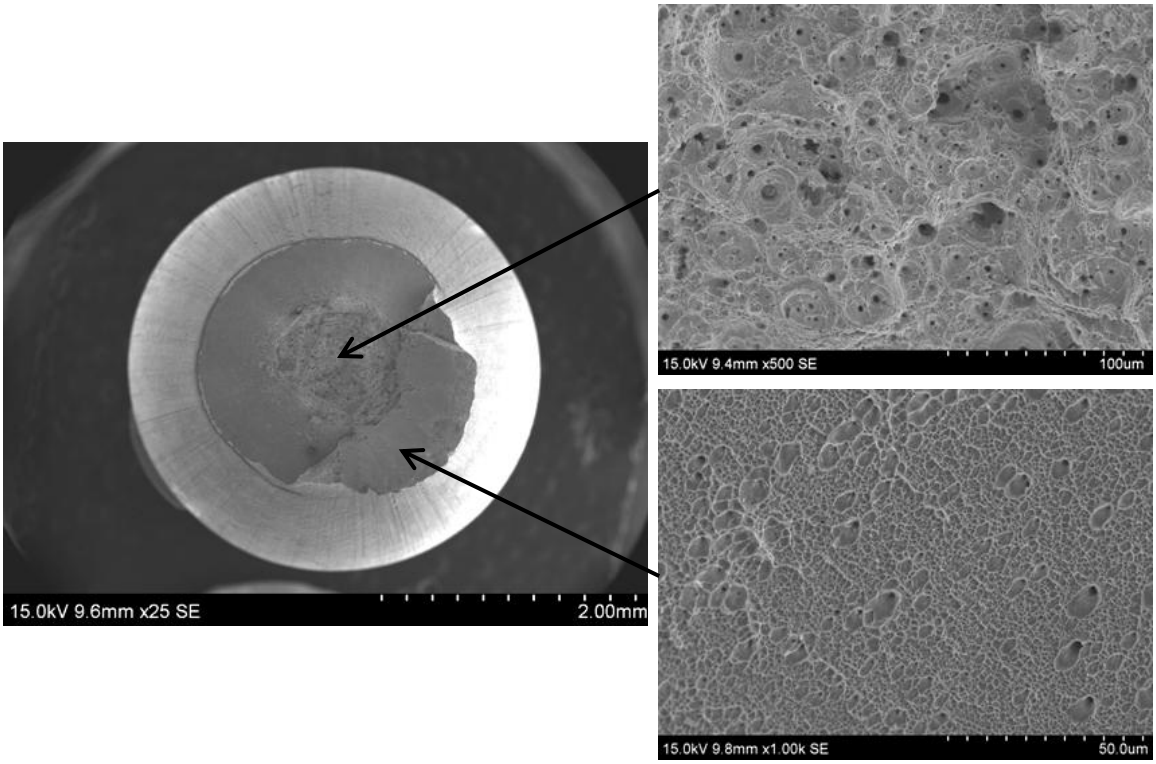

(b) Typical HSSS fracture surface (2205 shown)

Figure 5.7 SEM micrograph of fracture surface of 1080 and 2205 HSSS

This non-ductile failure mode is troubling from a structural design standpoint and indicates that stainless steels produced at these high strengths actually possess limited ductility wherein ϵ_{ult} approaches the yield strain as the gage length approaches ∞. In order to verify this hypothesis, additional tensile tests were performed on 304 HSSS wires with gage lengths of 20, 40, and 60 cm (8, 16, and 24 in) using the same procedures discussed in Section 5.1.1. Figure 5.8 illustrates the reduction in ϵ_{ult} as the gage length is increased, confirming the effect of strain localization on the stress vs. strain behavior of HSSSs. Therefore, when HSSSs are used at length scales applicable to PSC structures, any measure of ϵ_{ult}, ductility, or toughness should be calculated based on the strain prior to necking which, in HSSSs, corresponds to σ_{ult}. These reductions in strain hardening and ductility when compared with 1080 prestressing steels will likely make it necessary to develop new resistance factors or reduce permissible stresses when HSSSs are used as prestressing reinforcement in PSC structures.

A final result warranting discussion is the reduced elastic modulus typical of stainless steels. The elastic moduli of candidate HSSSs evaluated in the present study were 12.9 % to 25.2 % less than 1080 prestressing steel (see Table 5.1). The reduced elastic modulus in stainless steels can actually provide benefits in the case of PSC applications by decreasing the prestress loss caused by elastic shortening, shrinkage, and viscoelastic creep of the concrete (Wu and Nürnberger, 2009). However, the measured elastic moduli of candidate HSSSs are less than typical values for annealed stainless steels of 200 GPa (28900 ksi). Low elastic moduli measured in candidate HSSSs likely results from early yielding caused by residual stresses (increased strain) and possible geometric nonlinearity associated with straightening of the wire as it is loaded.

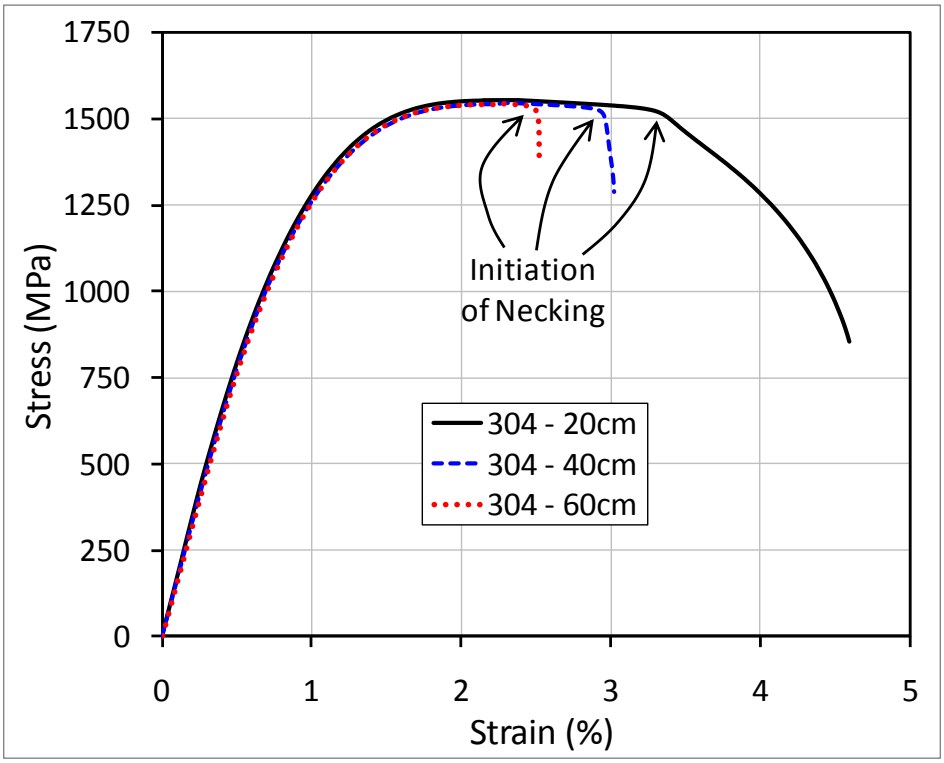

Figure 5.8 Stress vs. strain behavior of 304 HSSS with varying gage lengths

5.2 Stress vs. Strain Behavior of Strands

Previous studies have shown that the mechanical behavior of prestressing steels produced in a seven-wire stranded geometry can differ from single wires due to geometric effects and circumferential tightening of the strand during loading. A series of tensile tests were conducted on 1080 prestressing steel in single wire and seven-wire strand geometry. The results of this study were to predict the effect of stranding on the mechanical behavior of candidate HSSSs.

5.2.1 Experimental Methods

All specimens were fabricated from 15.2 mm (0.6 in) seven-wire A416 prestressing strand. Single wire specimens were produced with the same geometry and

tested using methods presented in Section 5.1.1. Full seven-wire strand specimens were cut to a length of 152 cm (60 in). Five replicate experiments were performed in the single wire and seven-wire strand geometry.

Testing of seven-wire strand was performed on a 2 MN (450 kip) Baldwin tension/compression testing frame. One of the greatest challenges of testing seven-wire prestressing strand is proper gripping of the strand in the testing frame. Through many trials, a system of 12.7 mm x 12.7 mm (0.5 in x 0.5 in) aluminum angles packed with moist fine sand and secured to the ends of the strand was developed which prevented slippage of the strand during testing and improved the quality of breaks by lessening the possibility of fracture occurring within the grip.

Strain was monitored using a calibrated linear variable differential transformer (LVDT) attached to the strand using brackets with an internal knife edge to define the proper gage length. A gage length of 76 cm (30 in) was used for LVDT strain measurements. The LVDT extensometer was removed at approximately 3 % strain. Ultimate strain was determined by measuring the final length between two gage length marks and adding 1 % strain as prescribed to account for elastic recovery of the strand after fracture (ASTM A416, 2006). Continuous load measurements were made using an LVDT attached to the analog readout of the Baldwin testing frame. All data were collected using an OPTIM MEGADAC data acquisition system. LVDTs used for load and strain measurements were calibrated prior to testing. Figure 5.9 shows the experimental setup for testing of strands.

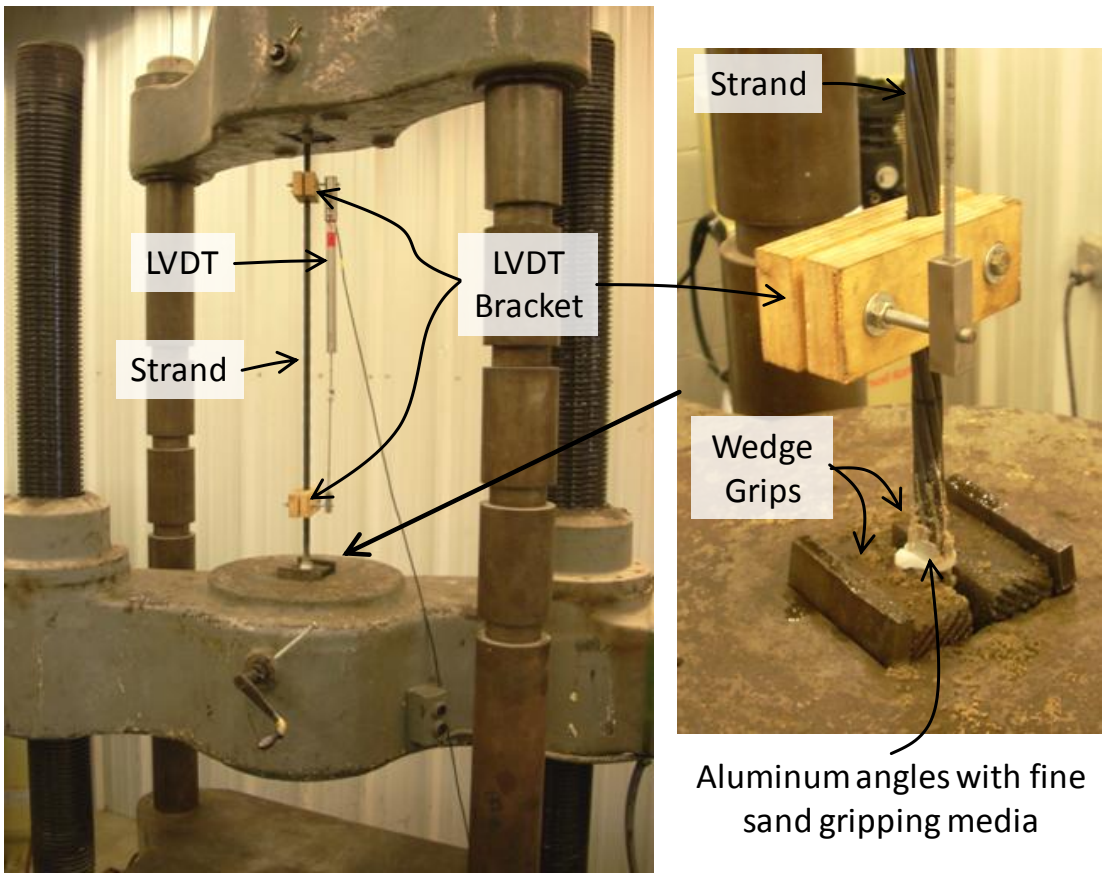

Figure 5.9 Experimental setup for tensile testing of prestressing strands

5.2.2 Results and Discussion

Figure 5.10 shows tensile stress vs. strain curves for wire and strand specimens produced from A416 prestressing strands. One wire and one strand test were deemed aberrant due to failure occurring prematurely in the grip. Mechanical properties are recorded in Table 5.2. Prestressing wire and strand exhibited similar elastic moduli (less than 0.4 % difference in the mean) with small reductions in σ_y, σ_{ult} of less than 2 % and reductions in ϵ_{ult} of approximately 22 % in the stranded geometry. The primary cause for reduction in strength and ductility is the much larger specimen size – a single 250 mm (10 in) long wire vs. a 152 cm (60 in) long strand made up of seven wires. As a result, the

probability of a microstructural defect which initiates fracture within the gage length is approximately 42 times higher in the strand tested than in the single wire. In addition, external wires in the stranded geometry are helically wound around the center wire and are not axially aligned with the tensile load which may also reduce the tensile strength of the seven-wire strand. Based on these data, tensile testing of wires can be used to predict the mechanical behavior of strands if a 1.5 % reduction in strengths in applied.

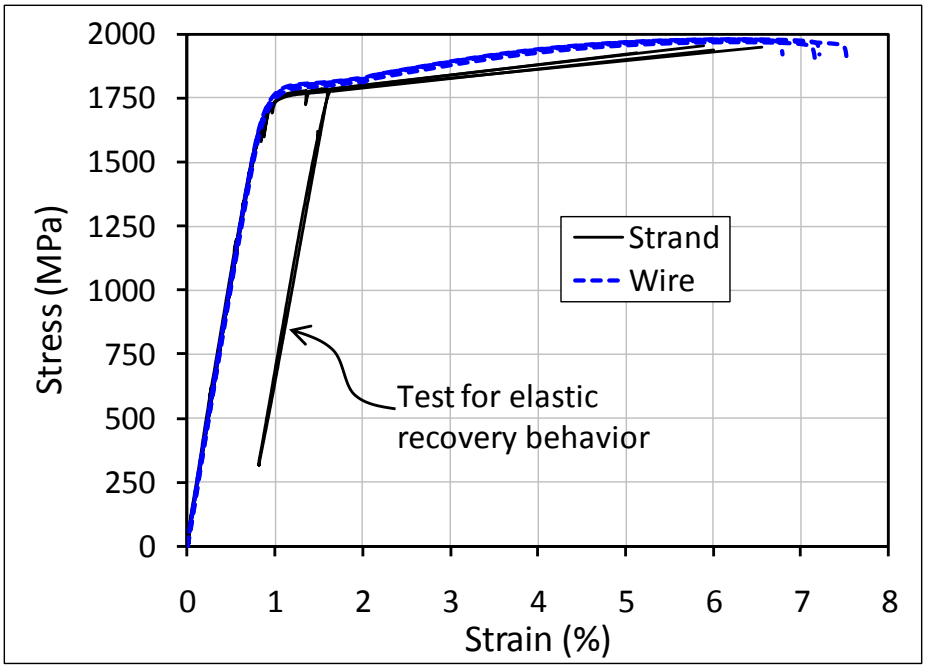

Figure 5.10 A416 prestressing wire and strand stress vs. strain curves

Table 5.2 Mechanical properties of A416 prestressing wire and strand

Specimen	Mean or Std. Dev.	σ_y 0.2% MPa/ksi	σ_y 1% MPa/ksi	σ_{ult} MPa/ksi	ϵ_{ult} (%)	E GPa/ksi
Wire	Mean	1772/257	1758/255	1972/286	7.2	203/29400
	Std. Dev.	10.6/1.5	10.3/1.5	4.5/0.7	0.36	1.8/261
Strand	Mean	1758/255	1731/251	1944/282	5.9	202/29300
	Std. Dev.	4.4/0.6	5.9/0.9	13.8/2.0	0.59	0.9/132
% Difference	Mean	0.79	1.56	1.44	22.03	0.34

5.3 Stress Relaxation

5.3.1 Experimental Methods

Tensile stress relaxation studies were performed in the temperature and relative humidity (RH) controlled creep room located at the Georgia Tech Structural Engineering and Materials Laboratory. The creep room was designed to maintain a temperature of 20 ˚C (68 ˚F). Temperature histories collected in the creep room showed small fluctuations of ±0.5 % from the desired operating temperature of 20 ˚C (68 ˚F). The experimental setup was fabricated by adapting existing frames designed and constructed for testing the tensile creep (constant load) properties of ultra-high performance concrete by Dr. Victor Y. Garas (Garas, 2009). Three frames were adapted to conduct the stress relaxation tests (constant strain) by replacing steel loading plates with threaded rods anchored to the base of the frames which extended into the loading arms that were used to apply a constant displacement (constant strain) to the specimen being tested. An in-line calibrated compression load cell was placed at the top of the frame and monitored using an OPTIM MEGADAC data acquisition system. Specialty small diameter prestressing wire chucks manufactured by CCL Stressing Systems were used to anchor the wire in the test setup. An overview of the tensile stress relaxation test setup is shown in Figure 5.11.

Once the specimen was secured in the testing frame using wire chucks, the loading arm was released, resulting in approximately 4.5 kN (1 kip) of tensile load (10:1 mechanical advantage). The remaining load was applied by placing a long Dywidag bar in the open end of the loading arm (to increase the mechanical advantage) and manually displacing it until reaching the desired load. Once the desired load was reached, a washer

and nut were secured on the threaded bar to preserve a constant strain condition. The entire loading process took less than 1 min to complete.

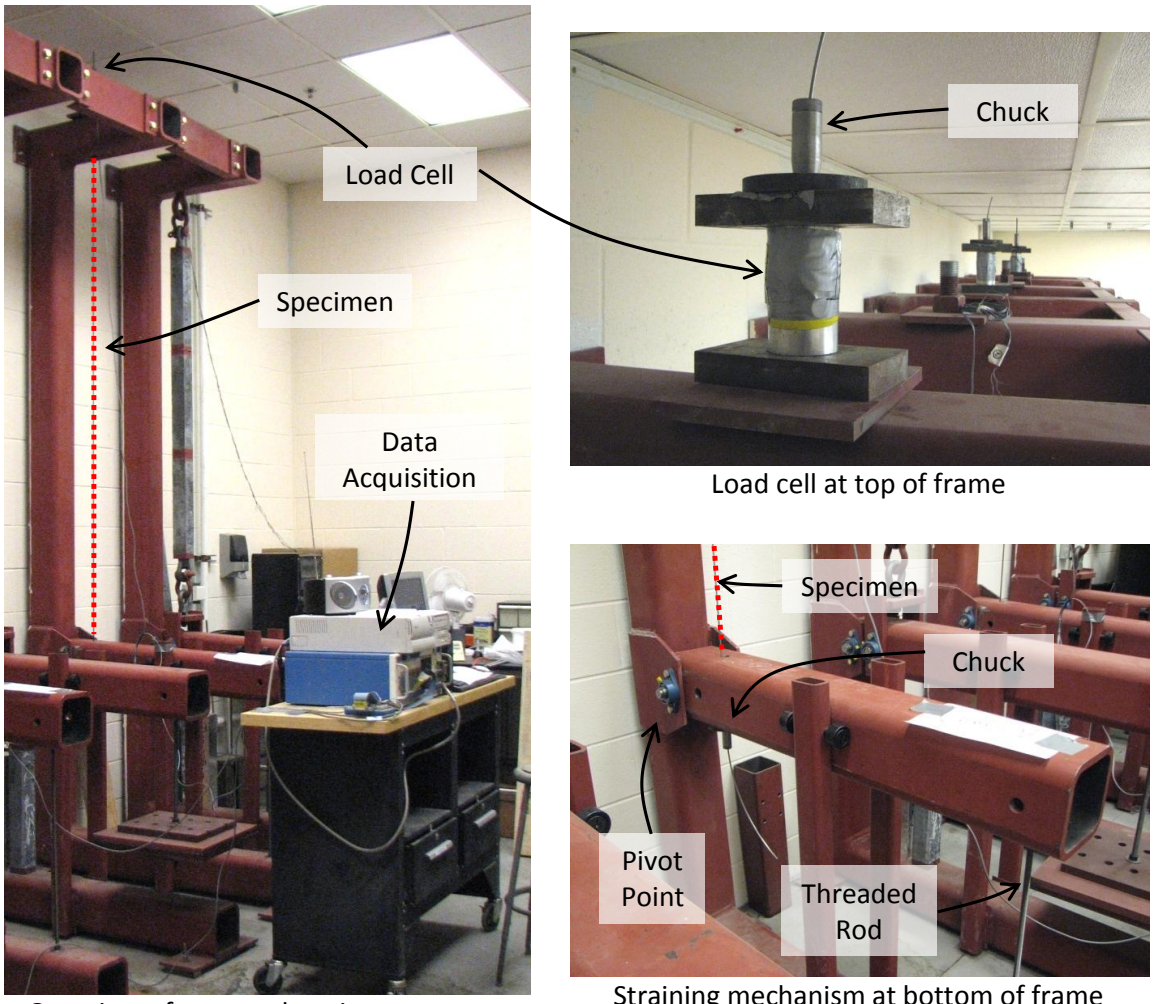

Figure 5.11 Tensile stress relaxation experimental setup

A416 prestressing strand manufacturers typically conduct stress relaxation tests at 70 % of the guaranteed ultimate tensile strength of 1860 MPa (270 ksi). In the present study, all specimens were loaded to an initial tensile stress of 70 % of the measured ultimate tensile strength of each alloy (see Table 5.1). As a result, the tensile stress in the

1080 prestressing steel (from A416 prestressing strand) tested in the present study is 74.2 % of the guaranteed ultimate tensile strength. Therefore, stress relaxation of 1080 prestressing steel is likely higher than that typically measured by manufacturers.

The total test duration for each stress relaxation experiment was 100 hr. Readings of load in each specimen were commenced 1 min after the initial loading was applied. A sampling rate of 0.1 Hz (one sample every 10 s) was used for the first 3 hours of testing followed by a sampling rate of 0.0033 Hz (one sample every 5 min). Based on these results, 1000 hr stress relaxation was predicted using logarithmic extrapolation with time. ASTM A416 states that stress relaxation at 1000 hr should be less than 2.5 % when initially loaded to 70 % of σ_{ult} and should be less than 3.5 % when initially loaded to 80 % of σ_{ult}. No standards are available that specify tensile stress relaxation limits for stainless steel prestressing reinforcement.

5.3.2 Results and Discussion

Figure 5.12 shows stress relaxation results of all candidate HSSSs and the 1080 prestressing steel control for the 100 hr test duration. Unfortunately, data were not reliable past 50 hr in 316, 2101, and 2304 HSSSs due to deleterious temperature instability in the creep room which resulted in temperature-induced deformations in the stress relaxation testing frame. All materials tested exhibited classic low-temperature logarithmic stress relaxation behavior as evidenced by a diminishing rate of relaxation with time (Nabarro, 2001). Such relaxation trends are typically attributed to dislocation creep under stress/strain which subsides over time as dislocations become pinned at obstacles such as foreign particles (e.g., precipitates), “forests” of saturated dislocations, and grain boundaries (Cottrell, 1997).

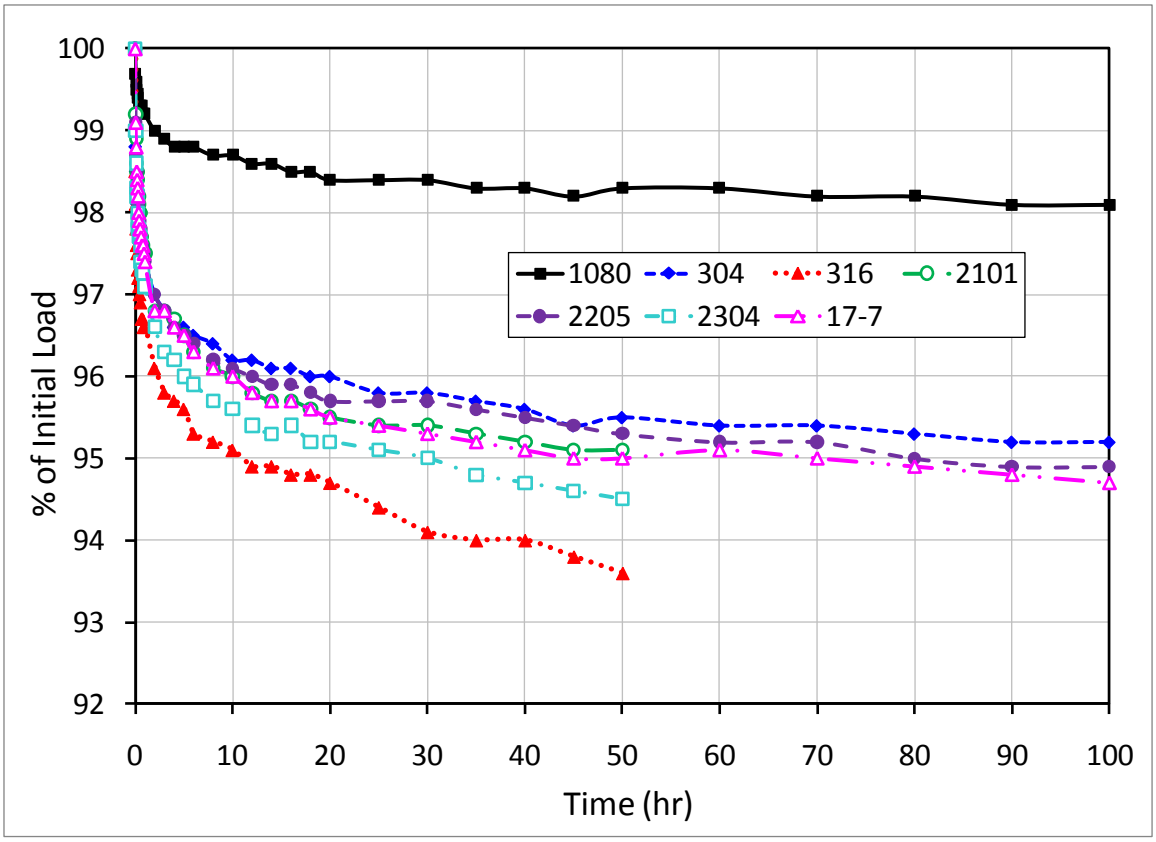

Figure 5.12 Stress relaxation results of all candidate HSSSs and the control

Figure 5.13 depicts the stress relaxation results when plotted vs. the logarithm of time. A green dashed line has also been included in Figure 5.13 to indicate the 2.5 % relaxation limit at 1000 hr specified by ASTM A416. A clearly linear relationship between stress relaxation and the log(time) further supports the low-temperature logarithmic creep mechanism. This linear relationship was used to predict stress relaxation at 1000 hr based on the linear trendlines which were least squares fitted to the results of 100 hr experiments (R^2 was greater than 0.995 for all materials tested). Stress relaxation results and the 1000 hr prediction are recorded in Table 5.3.

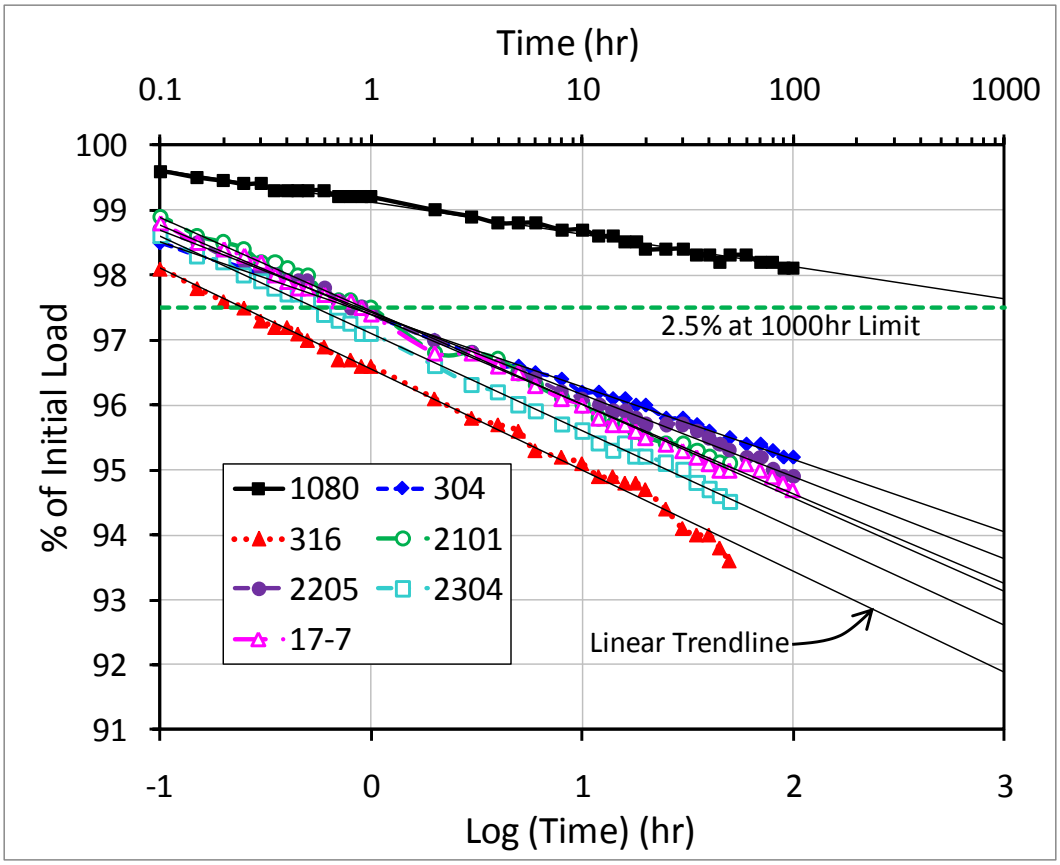

Figure 5.13 Stress relaxation results plotted vs. the logarithm of time

Table 5.3 Stress relaxation results

Alloy	Stress Relaxation	
	During Test (%)	1000hr Prediction† (%)
1080	1.9	2.4
304	4.8	6.0
316	6.4*	8.1
2101	4.9*	6.8
2205	5.1	6.3
2304	5.5*	7.4
17-7	5.3	6.9

* Test stopped at 50hr
† Based on linear extrapolation

Predicted 1000 hr stress relaxation of the 1080 prestressing steel was higher than the 1.5 to 2 % typical for A416 prestressing strands (Hill, 2006). This increase in relaxation is likely due to the application of an initial stress of 70 % of the true σ_{ult} rather than the guaranteed σ_{ult}. As discussed previously, initial stresses used in the present study correspond to 74.2 % of the guaranteed σ_{ult} of the 1080 prestressing steel.

Stress relaxation of candidate HSSSs was 3 to 4 times higher than that of the 1080 prestressing steel. However, it should be noted that the 1080 steel tested has undergone a low-relaxation thermomechanical heat treatment (see details in Section 7.1.1.2) which reduces stress relaxation by accelerating it during production with increased temperature and applied stress. 1080 prestressing steel which has not undergone this low-relaxation heat treatment exhibits 1000 hr stress relaxation of 5 to 6 % (similar to candidate HSSSs) (Atienza and Elices, 2007). In HSSSs, approximately 75 % of the stress relaxation occurred during the first 10 hr of testing, followed by relaxation trends which were similar to those of 1080 prestressing steels. This high initial relaxation indicates a dense, highly mobile network of dislocations in the cold drawn HSSSs.

One other factor which likely influenced stress relaxation behavior of candidate HSSSs was residual stresses. As discussed in Section 5.1.2, high-strength cold drawn wires can have tensile residual stresses at their surface as high as 600 MPa (87 ksi) and compressive residual stresses at their center as high as 1200 MPa (174 ksi). As a result, during the stress relaxation test, the internal stress state in the wire is actually a superposition of the stress induced by the externally applied displacement (strain) and the internal residual stresses.

With an initial applied stress of 70 % of σ_{ult}, it is likely that the surface of the wire is undergoing plastic deformation while the center of the wire has just overcome its compressive residual stresses. Previous studies have shown that as applied stress increases, stress relaxation increases exponentially (see Figure 5.14) (Atienza and Elices, 2007). In addition, the nucleation of additional dislocations associated with plastic deformation at the surface may also amplify stress relaxation. Therefore, it is hypothesized that the presence of tensile residual stresses at the surface of the cold drawn HSSS wires accelerates their stress relaxation. This hypothesis also implies that if a low-relaxation thermomechanical heat treatment were developed and applied to candidate HSSS wires (to reduced residual stresses and accelerate the diffusion of highly mobile dislocations during production), stress relaxation could be reduced to levels similar to those of the 1080 prestressing steel.

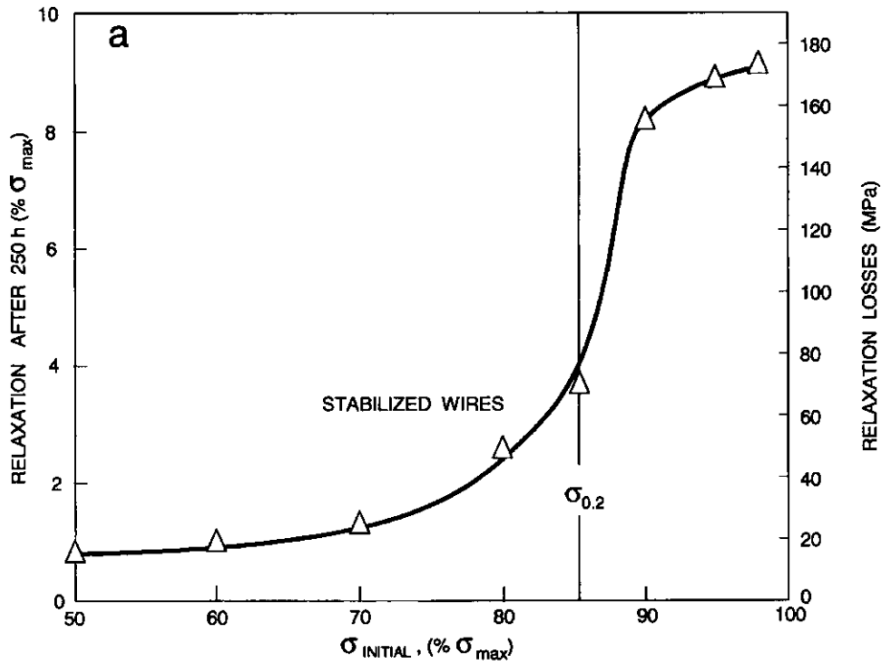

Figure 5.14 Stress relaxation vs. initial loading (from (Atienza and Elices, 2007))

CHAPTER 6

CORROSION BEHAVIOR OF HIGH-STRENGTH STAINLESS STEELS

This chapter presents the results of experimental studies investigating the corrosion behavior of candidate HSSSs. The bulk of the experimental program utilized electrochemical cyclic potentiodynamic polarization (CPP) techniques to evaluate the corrosion resistance of candidate HSSSs in environments simulating alkaline and carbonated concrete contaminated with Cl^-. A 1080 prestressing steel was also included as a control in the electrochemical studies. From the results of the electrochemical studies, optimal HSSSs were identified based on their corrosion resistance. Additional studies were performed to determine the influence of stranding on corrosion resistance and evaluate susceptibility to environmentally assisted cracking of optimal HSSSs.

6.1 Studies of Candidate High-Strength Stainless Steels

6.1.1 Experimental Program

6.1.1.1 Materials

Single wire test specimens of candidate HSSSs were produced using the same techniques as those discussed in Section 3.2.2.1. Each specimen was produced with a standard exposed length of 2.15 cm (0.85 in). However, because each HSSS was produced with a different wire diameter, each grade of HSSS had a different exposed surface area (see Table 6.1). All specimens were tested with their as-received surface

condition and were only flushed with H_2O prior to testing (i.e., no polishing). The goal of testing an unpolished surface was to simulate the true surface condition of the HSSS wire in the field.

Table 6.1 Exposed surface area of wire test specimens

Area	1080	304	316	2101	2205	2304	17-7
(cm^2)	3.5	2.9	2.2	2.8	2.8	2.8	3.1
(in^2)	0.54	0.45	0.34	0.43	0.43	0.43	0.48

6.1.1.2 Testing Procedures

All experiments were conducted at a temperature of 24 ˚C (75˚F). Two simulated concrete pore solutions were used to represent alkaline and carbonated concrete. Alkaline solutions consisted of 4 g/L of $Ca(OH)_2$ with a pH of 12.5. This alkaline solution was used to simulate concrete at later ages after the lixiviation of cations such as K^+ and Na^+ has taken place, resulting in a pore solution pH which is primarily buffered by soluble $Ca(OH)_2$ hydration products. The 4 g/L concentration of $Ca(OH)_2$ used was 2.3 times the solubility limit in order to create a saturated solution that was resistant to pH reduction by carbonation during testing. Carbonated solutions used to simulate concrete which has fully carbonated or acidified through the cover depth contained 0.3 M $NaHCO_3$ and 0.1 M Na_2CO_3 with pH of 9.5. In order to simulate a marine exposure, Cl^- was added as NaCl at concentrations of 0.00 M (no Cl^- exposure), 0.25 M (brackish water), 0.50 M (seawater), and 1.00 M. The 1.00 M Cl^- concentration was included as a worst case exposure which may result from capillary suction and/or evaporative precipitation causing the concentration of Cl^- within the concrete to reach higher levels than the Cl^- source at the surface. These solution compositions and Cl^- concentrations were selected

considering that at 100+ years Cl^- concentrations at the cover depth may begin to approach or exceed that present at the surface of the concrete and the concrete may show a reduction in pH due to carbonation and/or acidification through the cover depth.

Prior to Cl^- exposure used in CPP experiments, each specimen was conditioned to form a stable passive film on its surface. This procedure was developed to simulate conditions in the field where the passive film forms and is present for years prior to any exposure to Cl^- which must ingress from the surface. In order to determine the proper conditioning time, specimens were immersed in alkaline and carbonated solutions along with a saturated calomel reference electrode (SCE). A GAMRY 8-channel multiplexer connected to a GAMRY PC3 potentiostat was used to monitor open circuit potentials (E_{corr}) over time. Final values of E_{corr} at the completion of the conditioning period are recorded in Table 6.2. Figures 6.1 and 6.2 illustrate E_{corr} trends in alkaline and carbonated solutions, respectively. Continuous data collection in carbonated solutions (Figure 6.2) was interrupted after 112 hr of exposure due to an equipment malfunction.

Table 6.2 E_{corr} at end of specimen conditioning period

Alloy	E_{corr} (mV_{SCE})	
	Alkaline	Carbonated
1080	-166	-95
304	-230	-146
316	-225	-91
2101	-160	-144
2205	-187	-181
2304	-187	-157
17-7	-239	-139

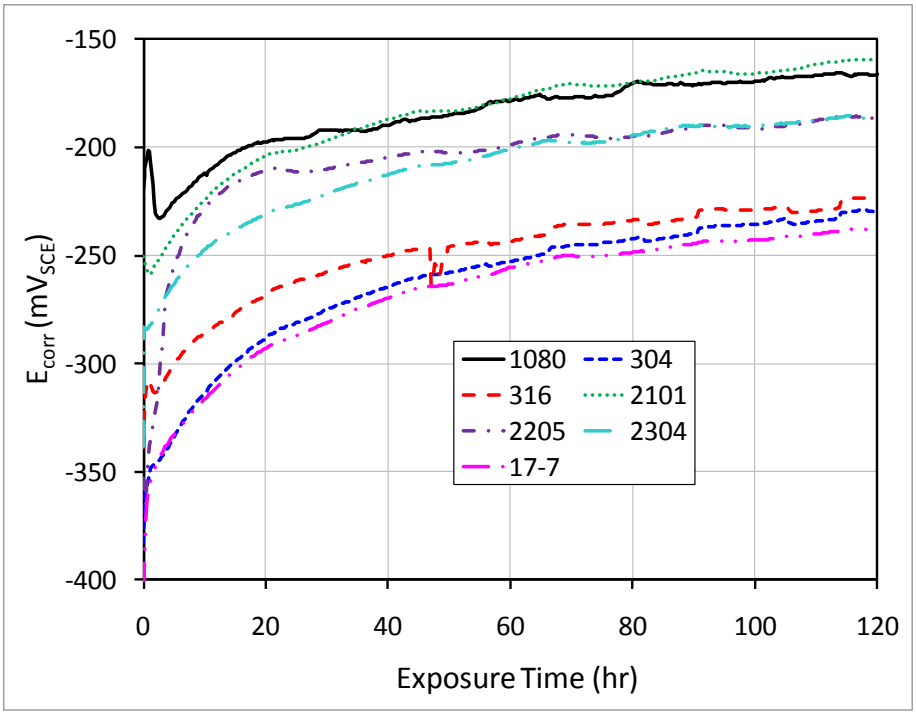

Figure 6.1 E_{corr} vs. time in alkaline solutions

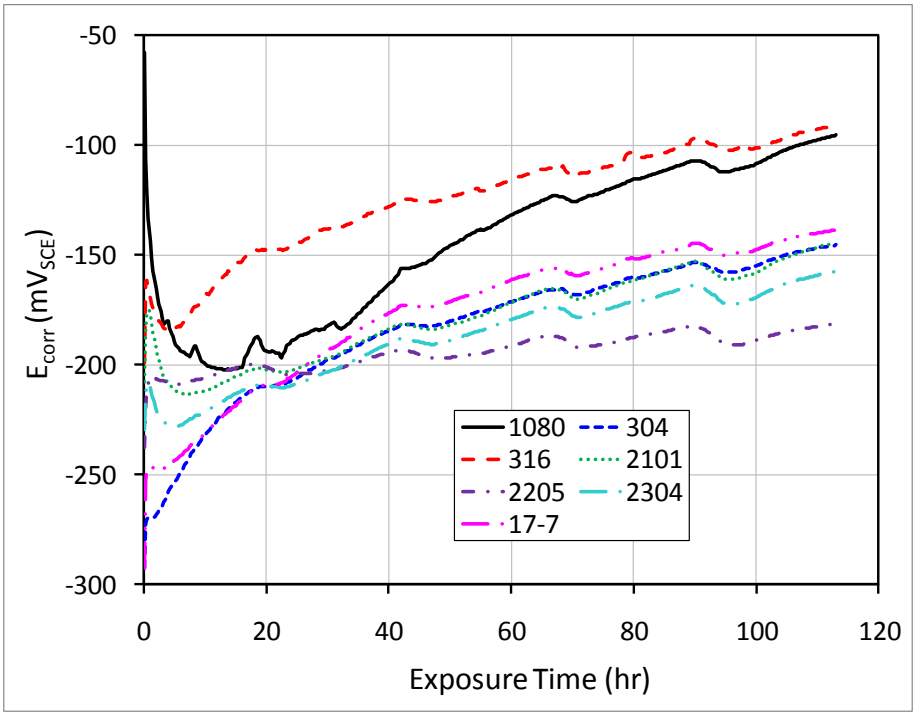

Figure 6.2 E_{corr} vs. time in carbonated solutions

Expected passivation trends were observed in candidate HSSSs and the 1080 prestressing steel, with E_{corr} rising to more noble (passive) potentials when exposed to alkaline and carbonated solutions. More active (negative) values of E_{corr} were observed in alkaline solutions associated with the higher pH of 12.5. In addition, candidate HSSSs exhibited more active values of E_{corr} when compared the 1080 prestressing steel. E_{corr} rose to passive potentials faster in alkaline solutions than in carbonated solutions, indicating the greater capacity of the alkaline solution to form a passive film in equilibrium with the aqueous solution. It was observed that after approximately 5 days of exposure, the E_{corr} of all samples remained fairly stable. This result is similar to previous passivation studies conducted on mild steel reinforcing bars which have shown at least 5 days of conditioning is necessary to form a stable passive film (Poursaee and Hansson, 2007). Hence, it was concluded that specimens could be transferred into a Cl^- containing solution after 5 days of conditioning to evaluate susceptibility to corrosion initiation using CPP techniques.

All CPP experiments were conducted using a three electrode cell like that shown in Figure 3.5, consisting of a Pt foil counter electrode with surface area of 4 cm^2 (0.62 in^2), an SCE reference electrode, and the working electrode being the wire test specimen. A solution volume of 250 ml (8.45 oz) was used to ensure a minimum solution volume-to-specimen surface area ratio of 0.2 ml/mm^2 (4.36 oz/in^2) as specified in ASTM G31. CPP experiments were conducted using GAMRY PC4 and Reference 600 potentiostats. A scan rate of 1 mV/s was used for all experiments. All potentials are given on the SCE scale. Potentials were anodically scanned from -25 mV vs. the steady open circuit potential (OCP) until either O_2 was evolved or corrosion initiation occurred. In both

cases, potential scans were reversed after a current increase of approximately two orders of magnitude beyond the passive condition. Using this method, corrosion susceptibility is clearly indicated by an abrupt increase in anodic current density in the passive region prior to reaching the O_2 evolution potential (see Figure 3.7).

Each experiment utilized a new sample which underwent its own conditioning procedure. Following testing, specimens were examined for unintended crevice corrosion underneath heat shrink tubing and silicone sealant. If unintended crevice corrosion had occurred, the data were deemed aberrant and the experiment was redone with a new specimen. Duplicate experiments were performed for all candidate HSSSs and the control in alkaline and carbonated solutions at all Cl^- concentrations considered. If variability in results was observed (e.g., corrosion initiated in one specimen but not in the other) a third experiment was performed. Such variability typically results from solution exposures and/or Cl^- concentrations which are near the limits of corrosion resistance of a given alloy. A total of 117 CPP experiments were conducted.

Following CPP testing, corrosion damage was characterized using optical and scanning electron microscopy (SEM). The SEM used was equipped with an energy dispersive X-ray spectroscopy (EDX) detector capable of performing elemental analyses in conjunction with imaging. Surface damage was characterized without the removal of corrosion products (only flushing with acetone) using optical and SEM/EDX. Select tested specimens were also sectioned in the transverse orientation with respect to the drawing direction and polished to reveal the cross sections of corrosion pits. Polished cross sections were also etched (see techniques in Section 4.3.2.1) to correlate microstructural features with corrosion damage.

6.1.2 Results and Discussion

6.1.2.1 Cl^- Induced Corrosion Resistance in Alkaline Solutions

Figures 6.3, 6.4, 6.5, and 6.6 present polarization curves of candidate HSSSs obtained in alkaline solutions with 0.00, 0.25, 0.50, and 1.00 M Cl^- concentrations, respectively. The 1080 prestressing steel control was found to be susceptible to corrosion initiation in even the least aggressive Cl^- bearing solution (alkaline solution with 0.25 M Cl^-). As a result, polarization curves for the 1080 prestressing steel have not been included in Figures 6.3 to 6.6 due to its disjoint corrosion behavior when compared with the candidate HSSSs evaluated.

When no Cl^- was present (Figure 6.3), two distinct changes in electrochemical behavior were observed upon anodic polarization above E_{corr}. At a potential of approximately 200 mV, a change in polarization behavior is observed likely resulting from the oxidation of Cr_2O_3 contained in the passive film to form CrO_4^{2-} (by $Cr_2O_3 + 5H_2O \rightarrow 2CrO_4^{2-} + 10H^+ + 6e^-$), which will occur at potentials above 225 mV when pH is 12.5 (Jones, 1996). Following the breakdown of the Cr_2O_3 film, current densities actually decrease, which indicates the role of Ni and Fe at potentials above 200 mV. Upon further anodic polarization, current density rises at a potential of approximately 650 mV as H_2O is reduced and O_2 is evolved ($2H_2O \rightarrow O_2 + 4H^+ + 4e^-$) (Bard and Faulkner, 2001). The evolution of O_2 dominates the current density measured and diminishes the ability to monitor the electrochemical behavior of the working electrode. It is also important to note that oxidation reactions to form CrO_4^{2-} and O_2 also result in the formation of H^+. As a result, the 200 mV and 650 mV potential levels may also be associated with acidification of the local environment present at the surface of the working electrode.

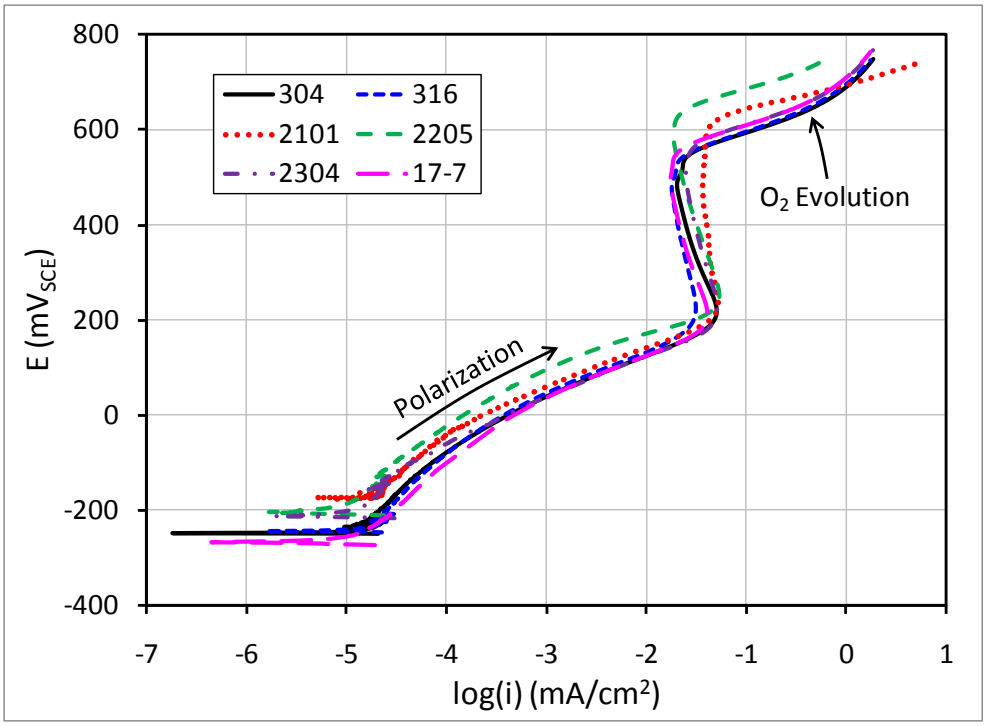

Figure 6.3 Polarization curves in alkaline solutions with 0.00 M Cl^-

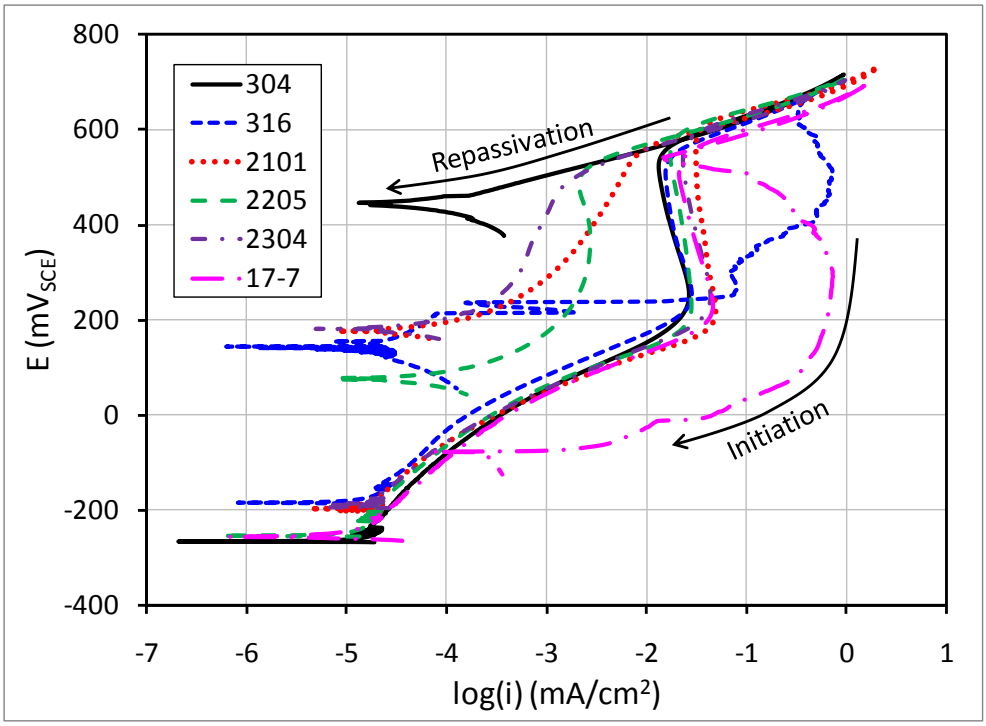

Figure 6.4 Polarization curves in alkaline solutions with 0.25 M Cl^-

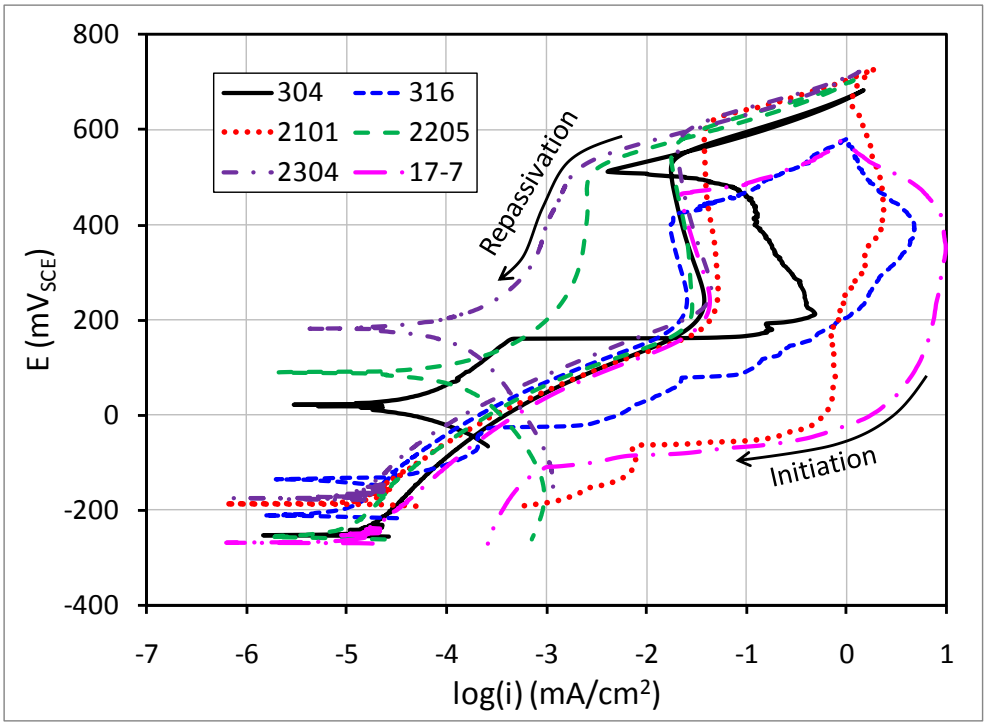

Figure 6.5 Polarization curves in alkaline solutions with 0.50 M Cl^-

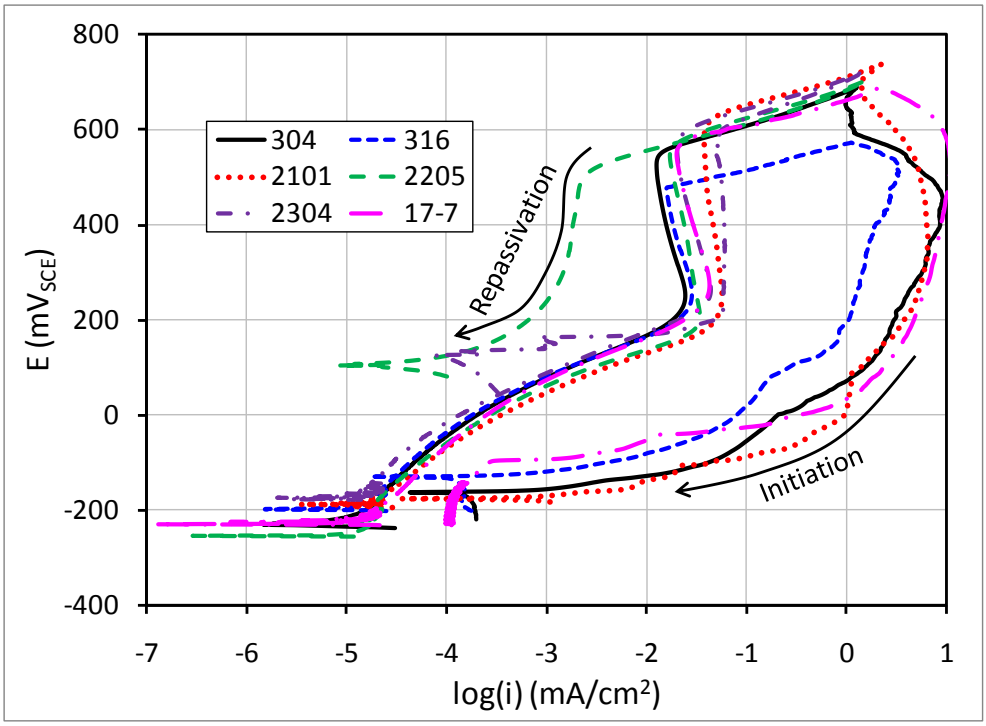

Figure 6.6 Polarization curves in alkaline solutions with 1.00 M Cl^-

As Cl^- was added to alkaline solutions, corrosion initiation occurred in more lowly alloyed HSSSs. At Cl^- concentrations of 0.25 M, corrosion initiation occurred only at the highly levels of anodic polarization as O_2 was evolved in 316 and 17-7 HSSSs. When the Cl^- concentration was increased to 0.5 M, only 2205 and 2304 exhibited full repassivation on the reverse potential scan. At the highest Cl^- concentration of 1 M, only 2205 (the most highly alloyed duplex HSSS with no precipitates observed in its etched microstructure) was resistant to corrosion. All breakdown potentials (the potential at which corrosion initiates) were above the 200 mV range where the Cr_2O_3 rich passive film begins to destabilize and into the O_2 evolution region. As discussed above, corrosion initiation may be assisted in these regions by degradation of the passive film and acidification caused by the formation of H^+. Once corrosion initiation occurred, current densities remained high (greater than 10 mA/cm^2) and repassivation potentials were at or below the 100 to 200 mV range that is considered to be the highest value of E_{corr} that the embedded steel possess in aerated concrete (Bertolini and Redaelli, 2009). All pitting potentials were above the 200 mV Cr_2O_3 oxidation potential, indicating that the Cr_2O_3 film must be destabilized for metastable pitting to transform into stable pit propagation.

Figure 6.7 shows optical micrographs of candidate HSSSs after CPP testing in alkaline 1 M Cl^- solutions. Two different morphologies of corrosion damage were observed following testing. In 304, 316, and 17-7 which exhibited the lowest corrosion resistance of the candidate HSSS tested, pitting corrosion was evident across the exposed surface area of the specimen. In duplex grades 2101 and 2304, only sparse pitting was observed at the highest Cl^- concentration of 1 M. Corroborating the results of electrochemical studies, no pitting was observed on the surface of 2205.

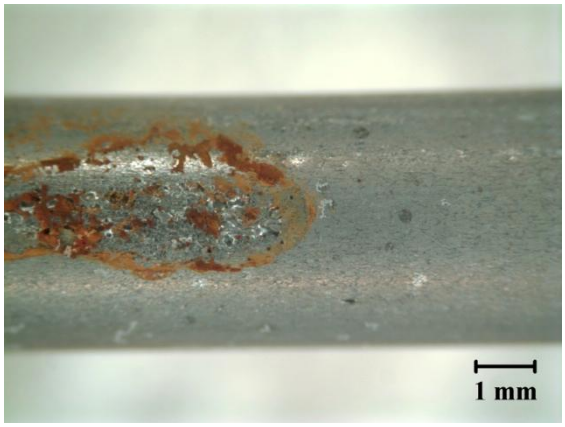

(a) 304

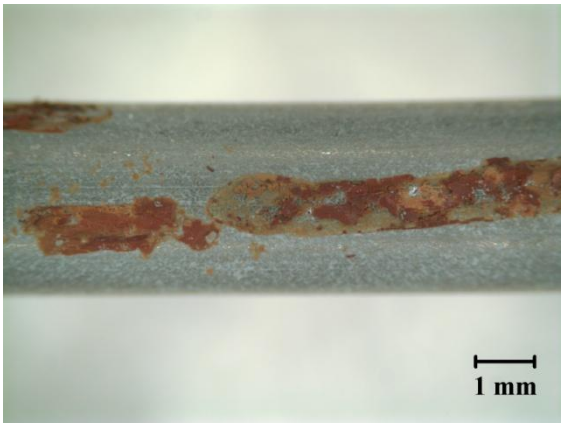

(b) 316

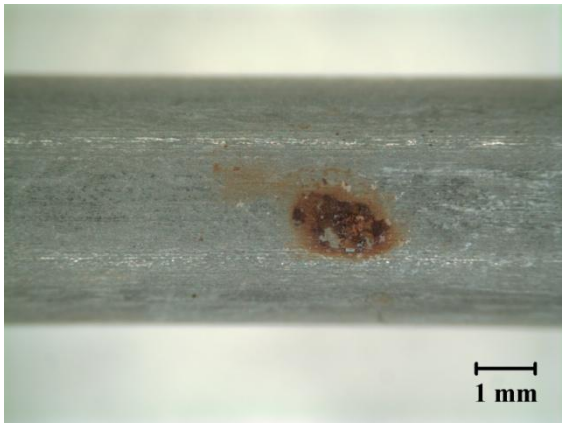

(c) 2101

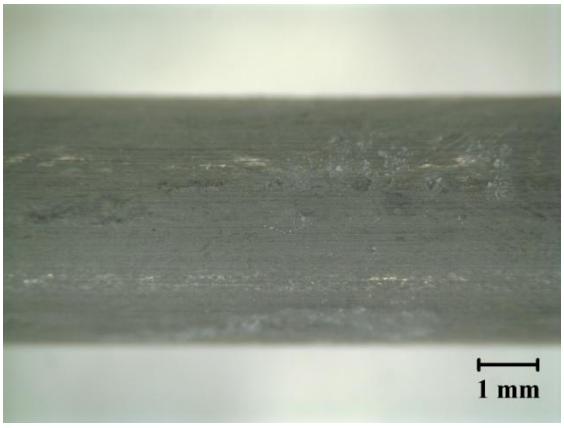

(d) 2205

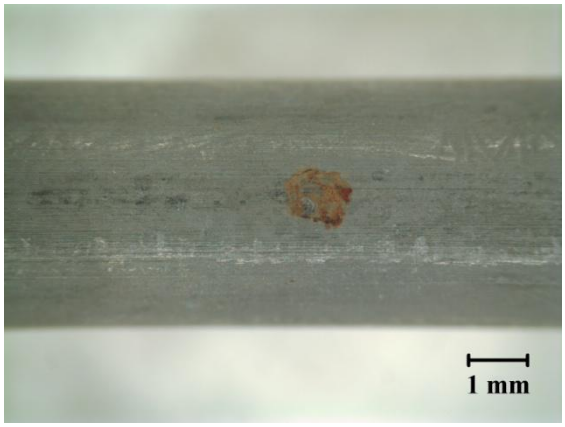

(e) 2304

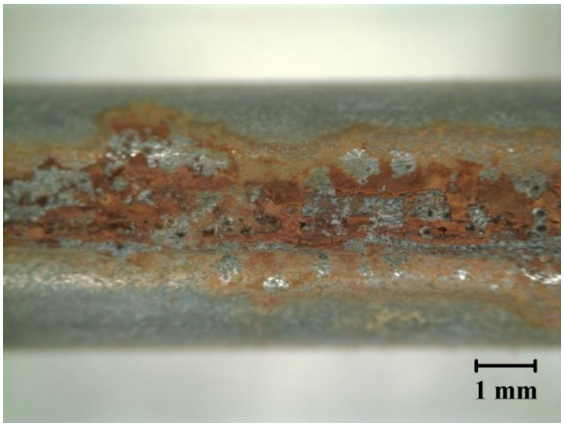

(f) 17-7

Figure 6.7 Corrosion damage in alkaline solutions with 1.00 M Cl^-

When compared with similar studies where CPP techniques were used on stainless steel reinforcing bars, Cl^- concentrations in the present study at which corrosion initiated in HSSS, were reduced significantly. For example, studies conducted by Hurley and Scully have CTLs as high as 2 M for 316 and 2101 reinforcing bars in saturated $Ca(OH)_2$ solutions (Hurley and Scully, 2006). Studies conducted by Elsener et. al on 2205 reinforcing bars have found CTLs as high as 4 M in alkaline solutions (Elsener, et al., 2011). Reductions in corrosion resistance of HSSSs likely stems from microstructural changes during cold drawing of the wires as discussed in Section 4.3.2. In addition, the deformed surface of the cold drawn wires may also result in reduced corrosion resistance in HSSSs when compared with reinforcing bars.

Limited data are available in the literature to compare with the corrosion behavior of candidate HSSSs evaluated in the present study (see Section 2.6). Alonso et. al have shown CTLs in excess of 1.5 M for 304 and 316 HSSSs using CPP techniques (Alonso, et al., 2008). However, studies by Alonso et. al were conducted in solutions with a pH of 13.2 which, based on much previous research (Thangavel and Rengaswamy, 1998), will result in a higher measured value of the CTL. No other study was available with which to compare the corrosion behavior of 2101, 2205, 2304, and 17-7.

The most anomalous result observed in CPP experiments was the behavior of the 316 HSSS tested. In all CPP experiments conducted, 316 HSSS consistently exhibited less resistance to corrosion initiation than 304, 2101, 2205, and 2304. Only 17-7 exhibited lower corrosion resistance than 316. Grade 316 is typically thought to have much higher corrosion resistance than 304 and lean duplex grades like 2101 and 2304 due to its Ni and Mo content (approximately 11 % Ni and 2.5 % Mo). One explanation

for the decreased corrosion resistance of the 316 HSSS evaluated is its high S content of 0.03 % and the precipitates observed in etched microstructures (see Section 4.3.2.4). The presence of these nonmetallic precipitates is known to reduce the barriers to localized corrosion initiation in the presence of Cl^- (Newman, 2001). Corrosion of 316 may also be aided by its Mo content causing molybdates to form which are known to be soluble in alkaline solutions, particularly at high temperature (Wensley and Dykstra, 1997).

6.1.2.2 Cl^- Induced Corrosion Resistance in Carbonated Solutions

Figures 6.8, 6.9, 6.10, and 6.11 present polarization curves of candidate HSSSs obtained in carbonated solutions with 0.00, 0.25, 0.50, and 1.00 M Cl^- concentrations, respectively. Similar to the electrochemical behavior observed in alkaline solutions, a change in polarization behavior was observed as the Cr_2O_3 was oxidized and as O_2 was evolved. However, in carbonated solutions, potentials at which these two reactions occurred were increased by approximately 200 mV due to the reduced pH.

As Cl^- was introduced to carbonated solutions, a decrease in corrosion resistance was observed by CPP testing. At a Cl^- concentration of 0.25 M, severe corrosion initiation occurred in 316, 2101, and 17-7 HSSSs when polarized above the Cr_2O_3 dissolution potential of 400 mV. Corrosion initiation also occurred in 304 HSSS during the reverse scan following O_2 evolution. When Cl^- concentration was increased to 0.5 M, corrosion initiated in all candidate HSSSs except for duplex grades 2205 and 2304. At the highest Cl^- concentration tested of 1 M, corrosion initiated in 2304 during the reverse potential scan while 2205 continued to exhibit high corrosion resistance. Here again, 316 exhibited lower corrosion resistance than 304 which has a lower Ni and Mo content. Once corrosion initiation occurred, current densities remained high (greater than 10

mA/cm^2) and repassivation potentials were much lower than the 100 to 200 mV threshold and even approached the original E_{corr} as Cl^- concentrations approached 1 M. All pitting potentials were above the 400 mV Cr_2O_3 oxidation potential, indicating that the Cr_2O_3 film must be destabilized for metastable pitting to transform into stable pit propagation.

These data clearly demonstrate the deleterious influence of reduction in pH on corrosion resistance. CPP experiments on 304 and 316 HSSSs in carbonated mortars conducted by Wu and Nürnberger (2009) have also shown similar reductions in corrosion resistance when compared with uncarbonated mortar (see Figure 2.32). Such reductions in pH can occur by carbonation of the cover concrete or, as seen in coastal Georgia bridges, due to acidification of the cover concrete (Moser, et al., 2010). In the case of Georgia bridges, it is expected that Cl^- ingress will more likely accompany acidification of the cover concrete than carbonation. However, at service lives well beyond 100 years, carbonation may be a concern as well and thus deserves consideration.

Figure 6.12 shows optical micrographs of candidate HSSSs after CPP testing in carbonated 1 M Cl^- solutions. When tested in carbonated solutions, 304, 316, 2101, and 17-7 exhibited surface pitting which was more uniformly distributed across the surface of the specimen than in alkaline solutions, indicating the presence of a less protective passive film. Duplex grade 2304 showed only sparse pitting in 1 M Cl^- corresponding to the brief increase in current density during the reverse potential scan (see polarization curve Figure 6.11). In alkaline solutions, lean duplex grades 2101and 2304 displayed similar corrosion damage. In carbonated solutions, widespread pitting was observed on 2101, while only sparse pits were found on 2304. In all cases, 2205 exhibited corrosion resistance far superior to the other candidate HSSSs investigated.

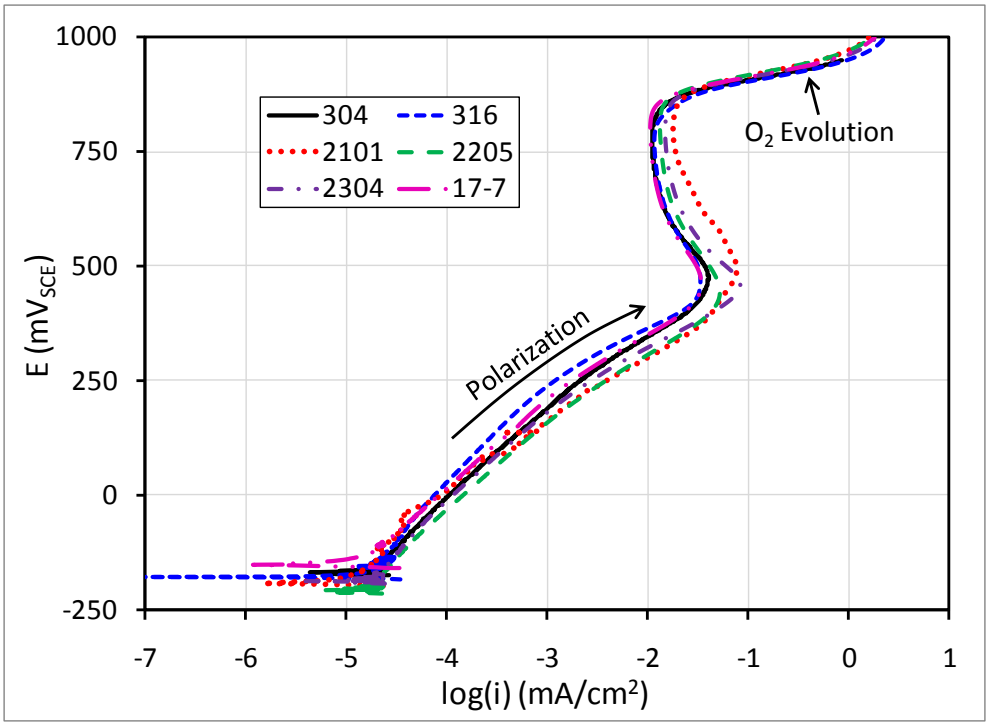

Figure 6.8 Polarization curves in carbonated solutions with 0.00 M Cl^-

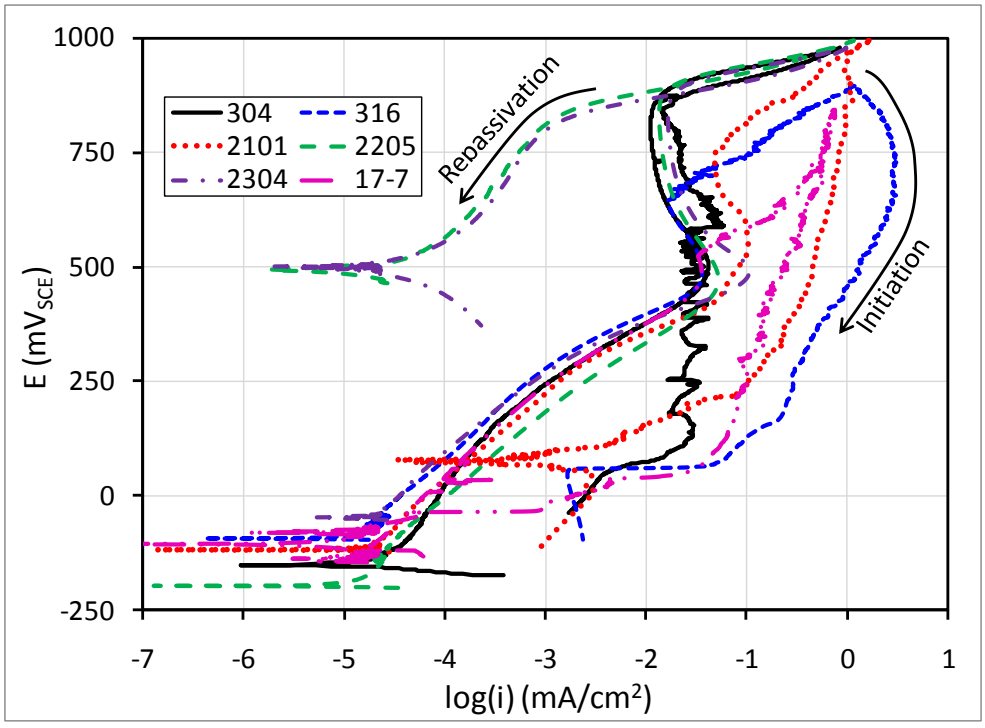

Figure 6.9 Polarization curves in carbonated solutions with 0.25 M Cl^-

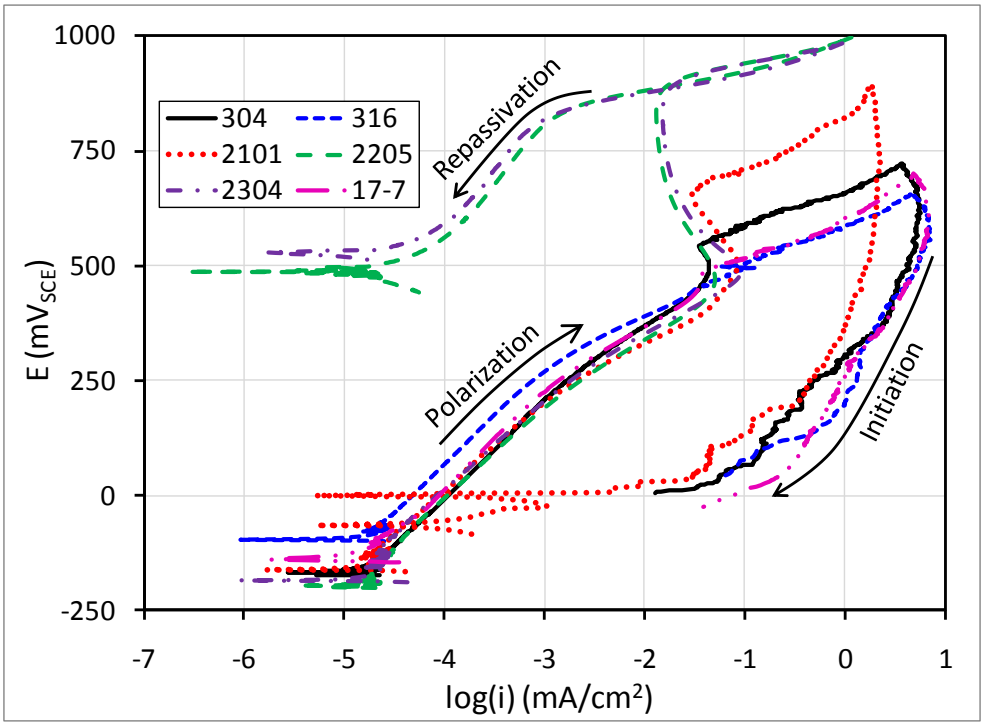

Figure 6.10 Polarization curves in carbonated solutions with 0.50 M Cl^-

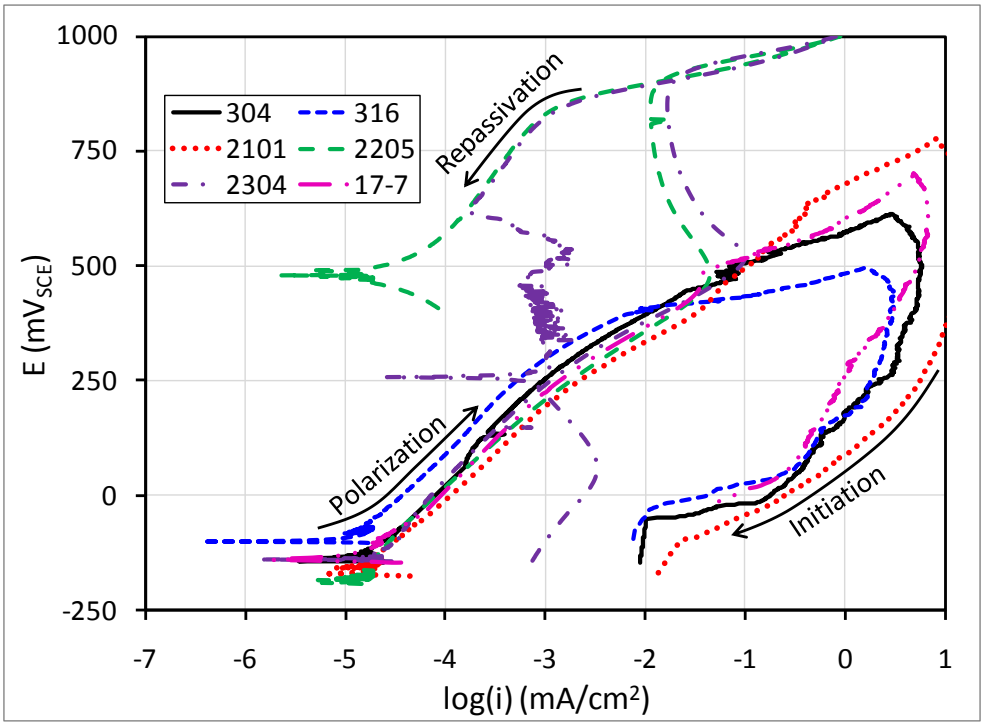

Figure 6.11 Polarization curves in carbonated solutions with 1.00 M Cl^-

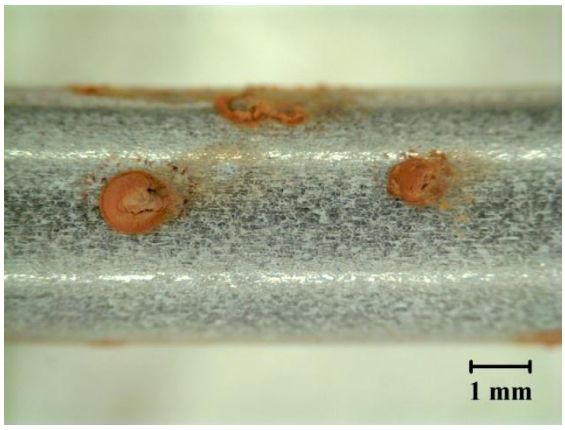

(a) 304

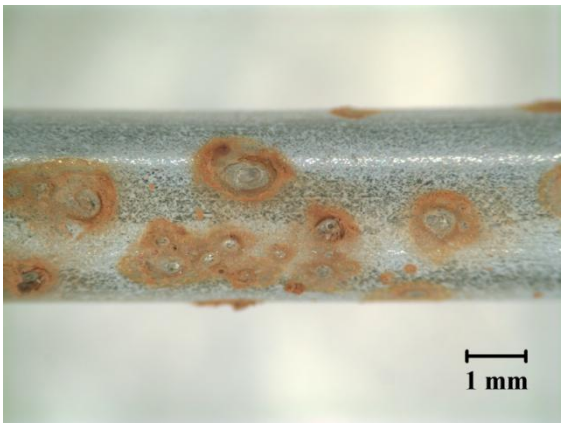

(b) 316

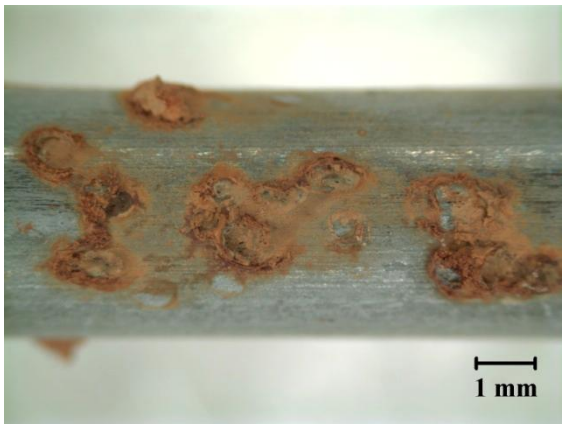

(c) 2101

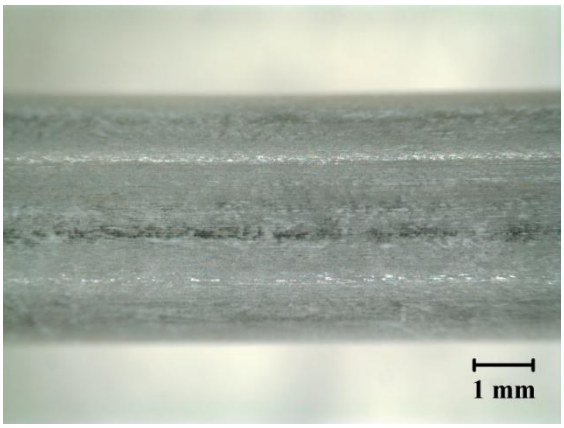

(d) 2205

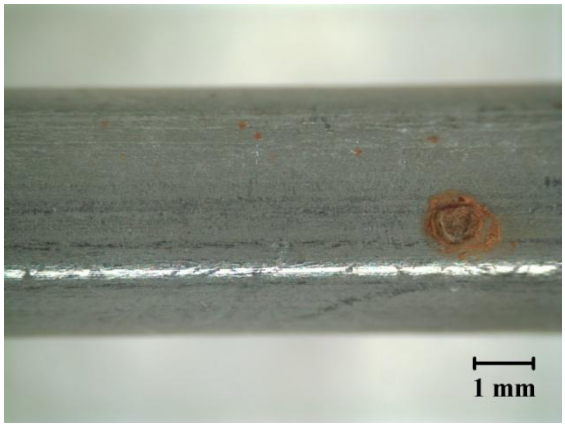

(e) 2304

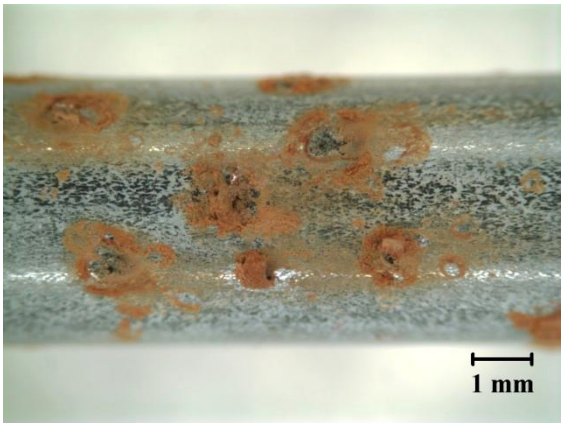

(f) 17-7

Figure 6.12 Corrosion damage in carbonated solutions with 1.00 M Cl^-

6.1.2.3 Morphology of Corrosion Damage

6.1.2.3.1 Austenitic Grades 304 and 316

Corrosion damage in austenitic HSSSs was dominated by surface pitting. Figure 6.13 depicts the typical pitting corrosion observed on the surface of 304 and 316 HSSSs. In addition to pitting, preferential dissolution occurred at grooves in the deformed surface of the cold drawn wires. The presence of these grooves may provide crevice sites which promote corrosion initiation and propagation. The grooves in the deformed surface were also filled with corrosion products which spread onto the surface of the specimen. In many cases, small pits like those shown in Figure 6.13 coalesced to form large pits (diameter greater than 100 μm (3.9 mil)) like those shown in Figure 6.14.

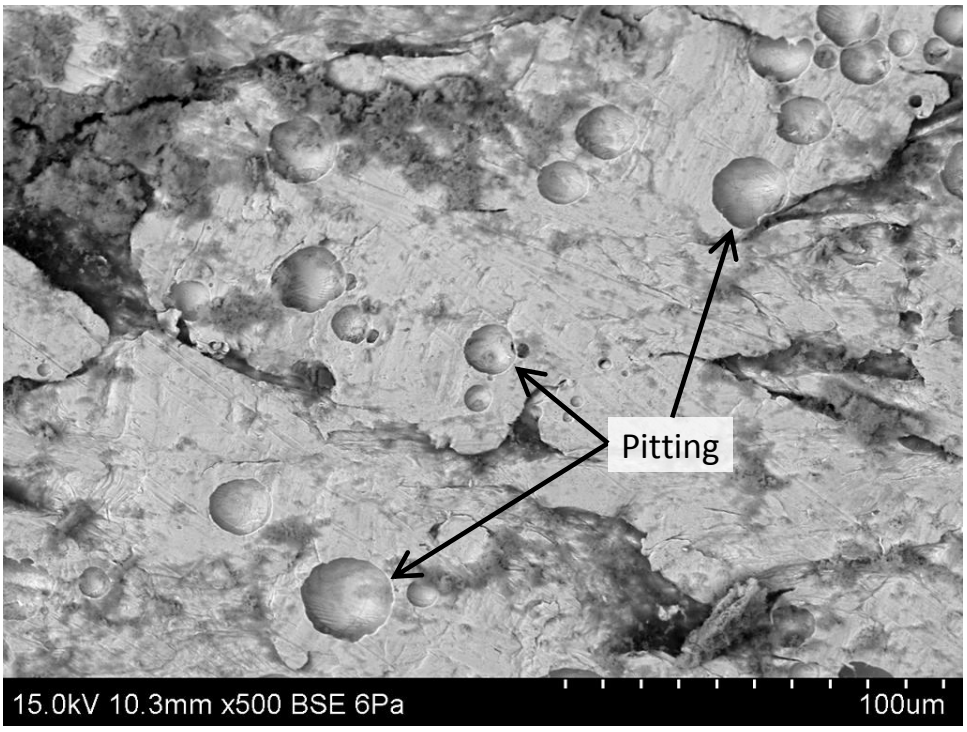

Figure 6.13 Pitting of 304 HSSS tested in a carbonated solution with 0.5 M Cl^-

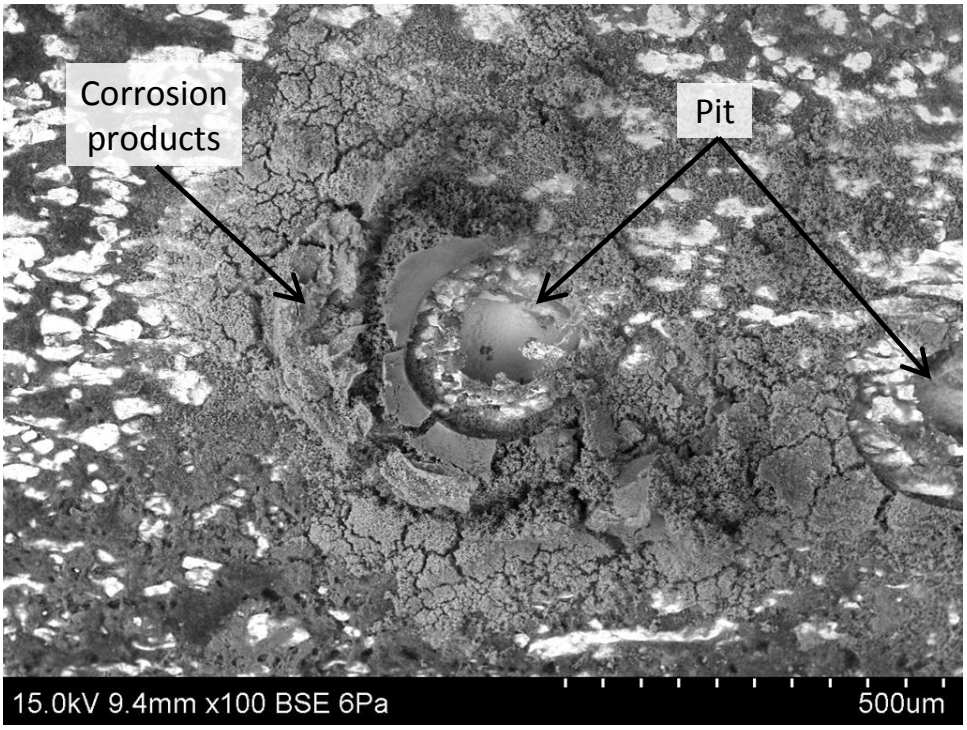

Figure 6.14 Large corrosion pit in 316 HSSS tested in an alkaline solution with 0.5M Cl^-

Large pits like that shown in Figure 6.14 had smooth walls and dense corrosion products deposited on the surface of the specimen around the rim of the pit. In 316 HSSSs, small MnS precipitates were found in the base of pits. One of the most interesting observations was the microstructure present at the rim of pits in austenitic HSSSs which appeared to be a thin foil of stainless steel with a lacy, perforated damage morphology. Figure 6.15 depicts one such pit in 304 HSSS. This damage was ubiquitous in all of the austenitic HSSS specimens examined. Figures 6.16 and 6.17 show close-ups of the microstructure present at the rim of the pit along with EDX data. Based on EDX data, the lacy microstructure at the rim of the pit is metallic and composed of Fe, Cr, and Ni; although, these elements are present at slightly higher concentrations than typical for 304 stainless steel (17.8 % Cr and 8.3 % Ni in bulk 304 HSSS).

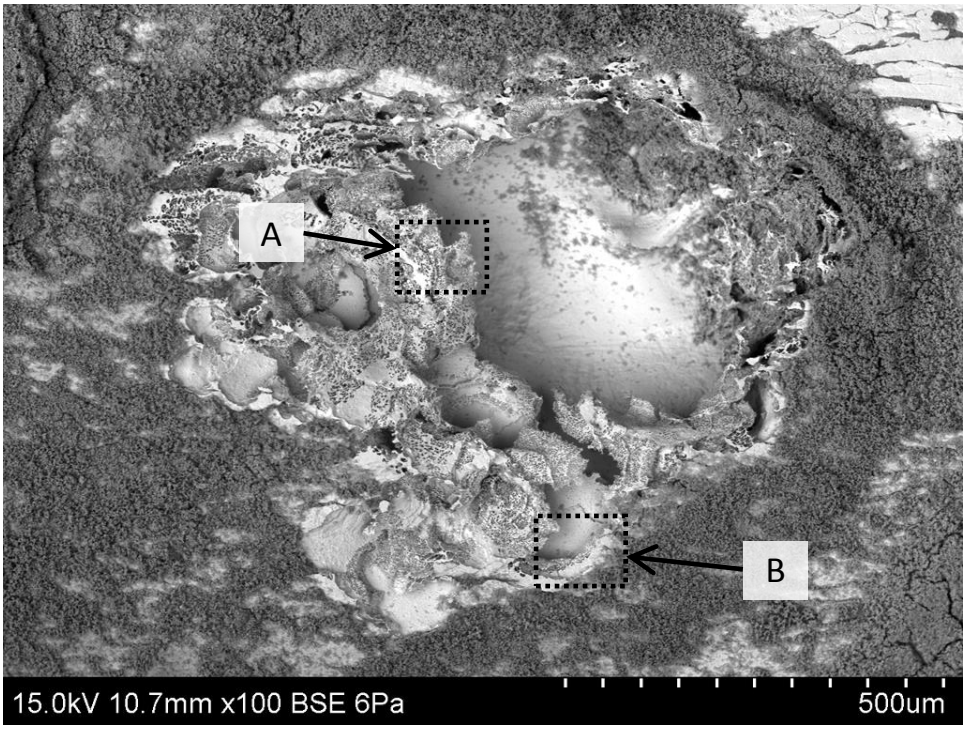

Figure 6.15 Large pit in 304 HSSS tested in a carbonated solution with 1 M Cl^-

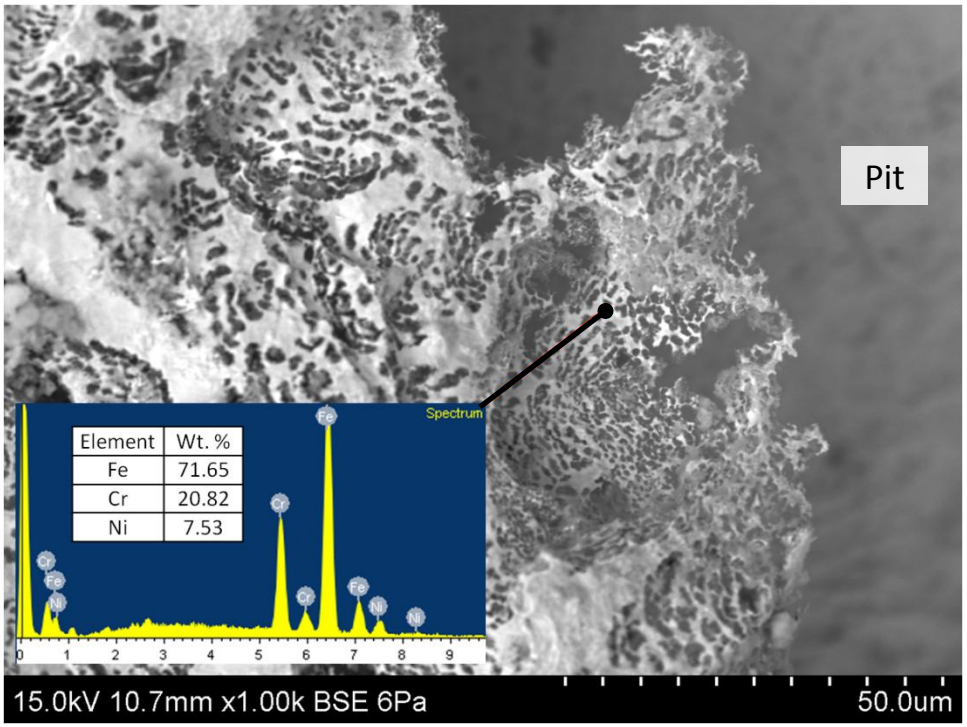

Figure 6.16 Close-up and EDX of region A in Figure 6.15

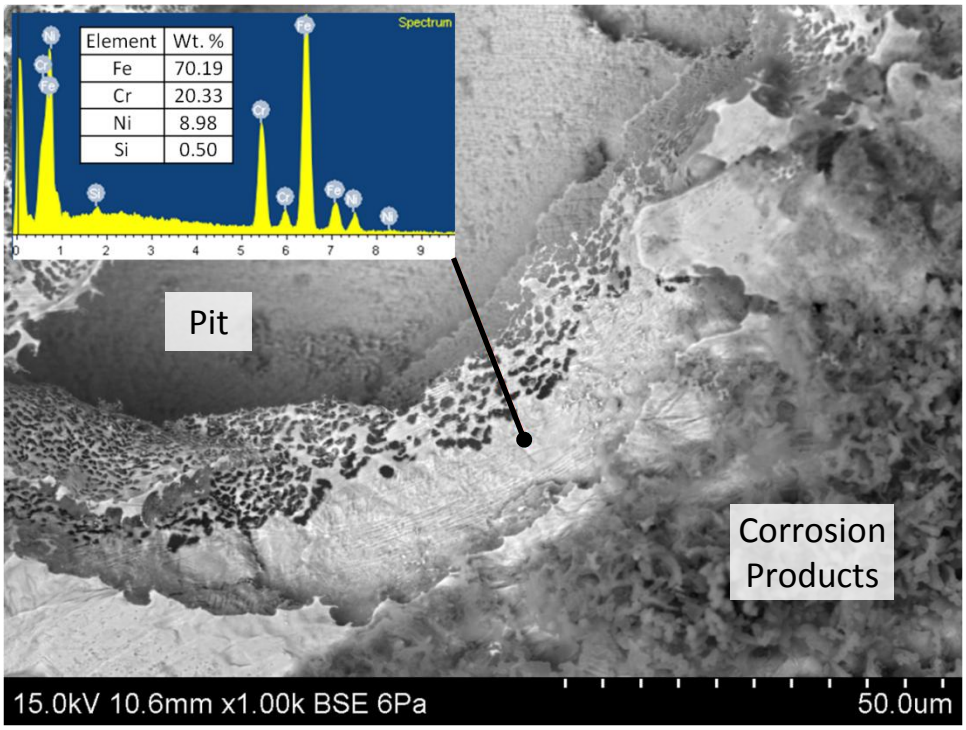

Figure 6.17 Close-up and EDX of region B in Figure 6.15

Similar lacy pitting corrosion has also been observed in grade 304 austenitic stainless steel by Ernst et. al (Ernst, et al., 1997; Ernst and Newman, 2002). According to Ernst, lacy corrosion damage is attributed to a highly metastable form of pitting where:

- Early pit growth following corrosion initiation will occur in a hemispherical geometry with the solution present in the pit being isolated from mixing with the bulk solution by remnants of the passive film that cover the pit and limit mass transport.
- As corrosion propagation occurs, the pit will eventually reach a critical size that causes the barrier covering the pit to become unstable. As the pit cover breaks down, the pit becomes an open hemispherical cavity which allows mixing of the corrosive solution in the pit with the bulk solution.

- With the hemispherical pit open, regions of the pit nearest to the bulk solution will repassivate while regions furthest away will continue to undergo anodic dissolution. This will cause the pit to shift from a hemispherical geometry to a saucer-shaped geometry which propagates underneath the surface of the metal.
- The sauce-shaped pit will continue to grow underneath the metal surface until intersecting the surface, causing holes to form like those shown in Figures 6.16 and 6.17. When the hole forms, solution in the pit mixes with solution in the bulk, causing the metal nearest to the hole to repassivate and pitting to shift to the adjacent metal.
- As this process occurs, eventually the lacy pitting morphology will develop as a result of sequential hole opening and repassivation events.

This process is shown diagrammatically in Figure 6.18. When tested specimens were cross sectioned, polished, and etched, the proposed saucer-shaped pitting was observed (see Figure 6.19). However, this mechanism assumes pitting occurs in a fairly homogenous equiaxed microstructure. As discussed in Section 4.3.2.4, the microstructure of austenitic HSSSs is comprised of heavily slip banded retained austenite and strain-induced α′-martensite. Phase α′-martensite is known to form in a lattice-like network at the location of slip band intersections (Suzuki, et al., 1977). At higher magnifications, selective attack of heavily slip banded austentite and α′-martensite was observed (see Figure 6.20). Previous electrochemical studies of austenitic HSSSs have also noted that α′-martensite displays selective attack when exposed to alkaline Cl^- bearing solutions (Alonso, et al., 2008; Wu and Nürnberger, 2009). Based on these previous studies and the data presented herein, it is hypothesized that lacy pitting along with selective attack of α′-martensite and precipitates are the predominant damage mechanisms in austenitic HSSSs.

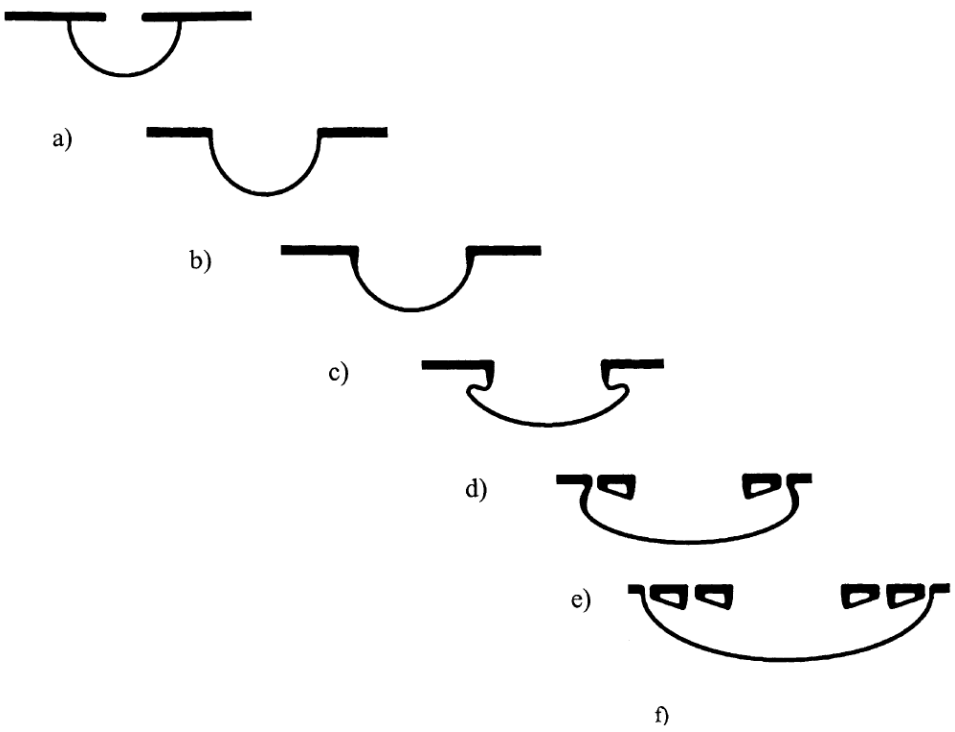

Figure 6.18 Process as the hemispherical pit (a) transforms to the saucer-shaped pit (f) with lacy pitting. Thick lines indicate passivated metal. (Ernst and Newman, 2002)

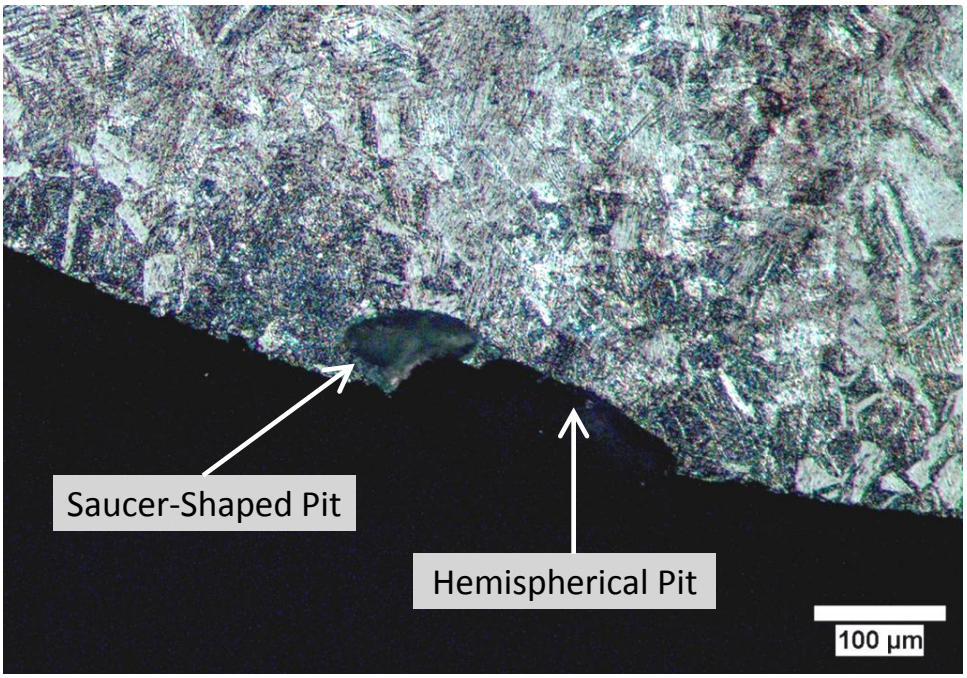

Figure 6.19 Hemispherical and saucer-shaped pitting of 304 HSSS

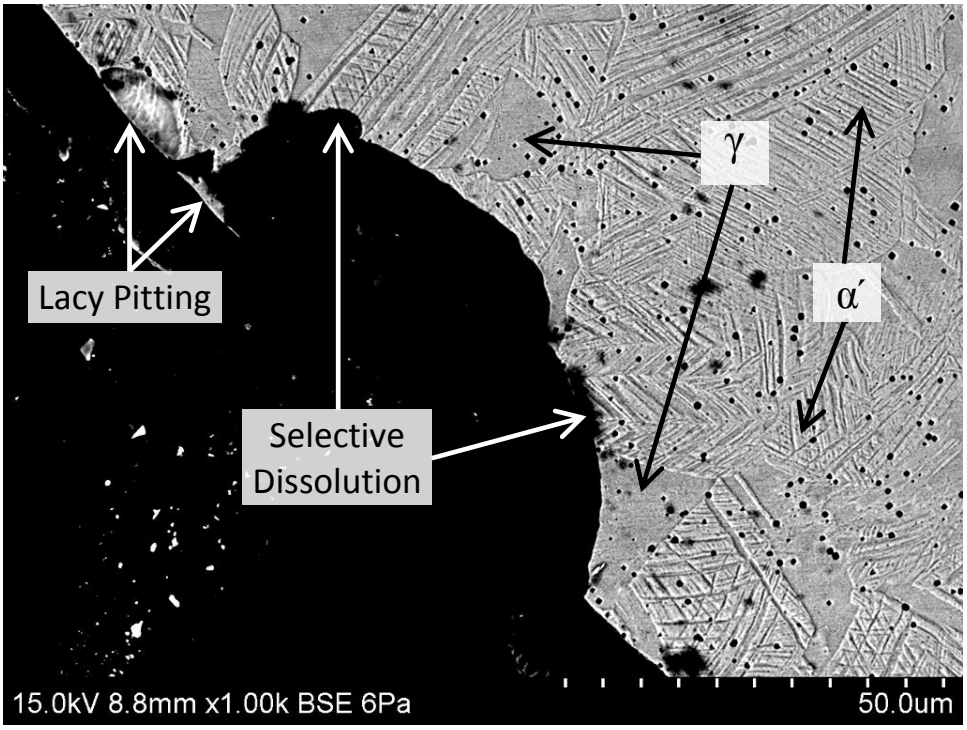

Figure 6.20 SEM micrograph of selective corrosion pit in 316 HSSS

6.1.2.3.2 Duplex Grades 2101, 2205, and 2304

Confirming the electrochemical behavior observed in CPP experiments, no corrosion damage was evident on any of the 2205 HSSS specimens examined (see Figures 6.21 and 6.22). Corrosion damage was evident on 2101 and 2304 HSSS specimens if corrosion initiation occurred during CPP experiments. Large regions of selective dissolution dominated corrosion damage in 2101 and 2304. Figures 6.23 and 6.24 depict typical selective dissolution in 2101 HSSS specimens following testing in carbonated solutions with 1 M Cl^-. Selective dissolution was isolated to regions with large corrosion pits and was aligned with the drawing direction.

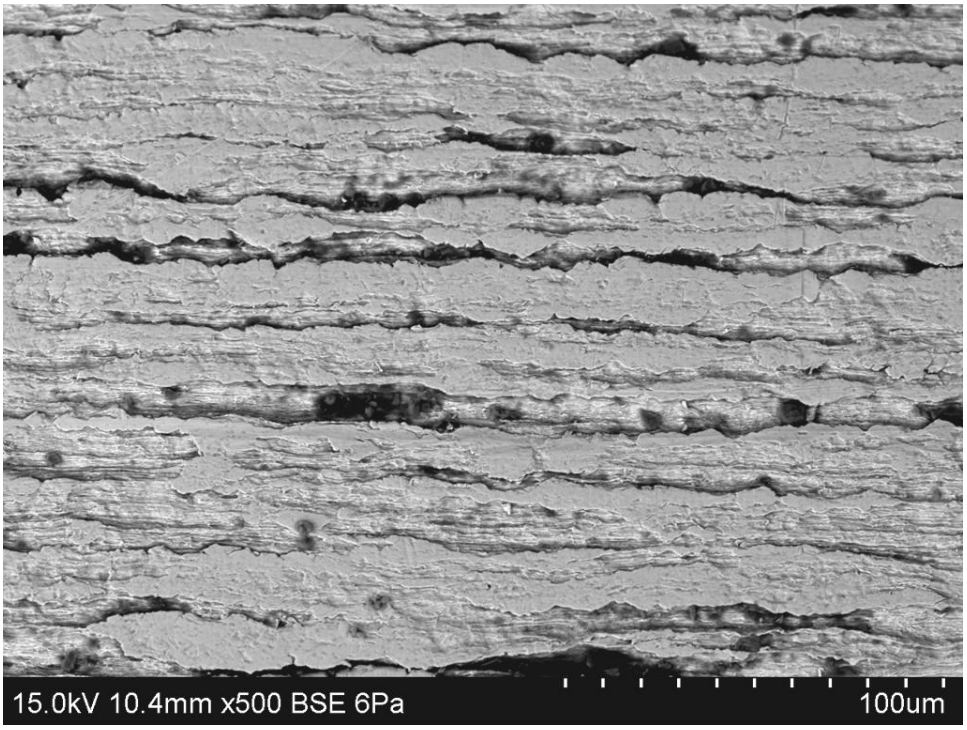

Figure 6.21 Surface of 2205 HSSS with no corrosion damage evident

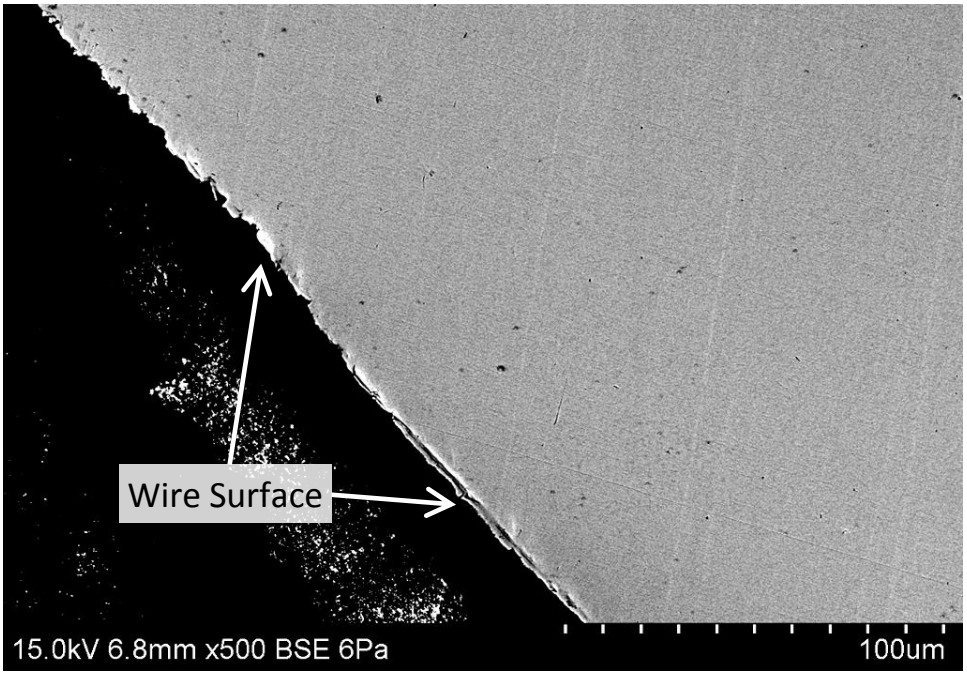

Figure 6.22 No pitting evident in transverse cross section of 2205 tested in carbonated solution with 1 M Cl^-

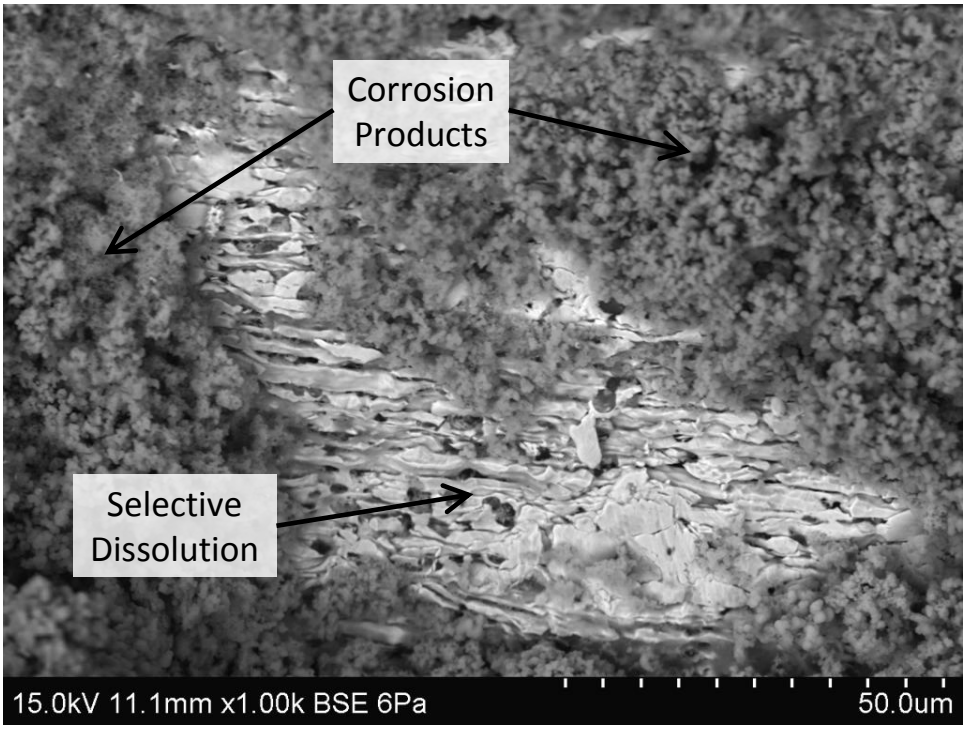

Figure 6.23 Selective dissolution in 2101 HSSS in carbonated solution with 1 M Cl^-

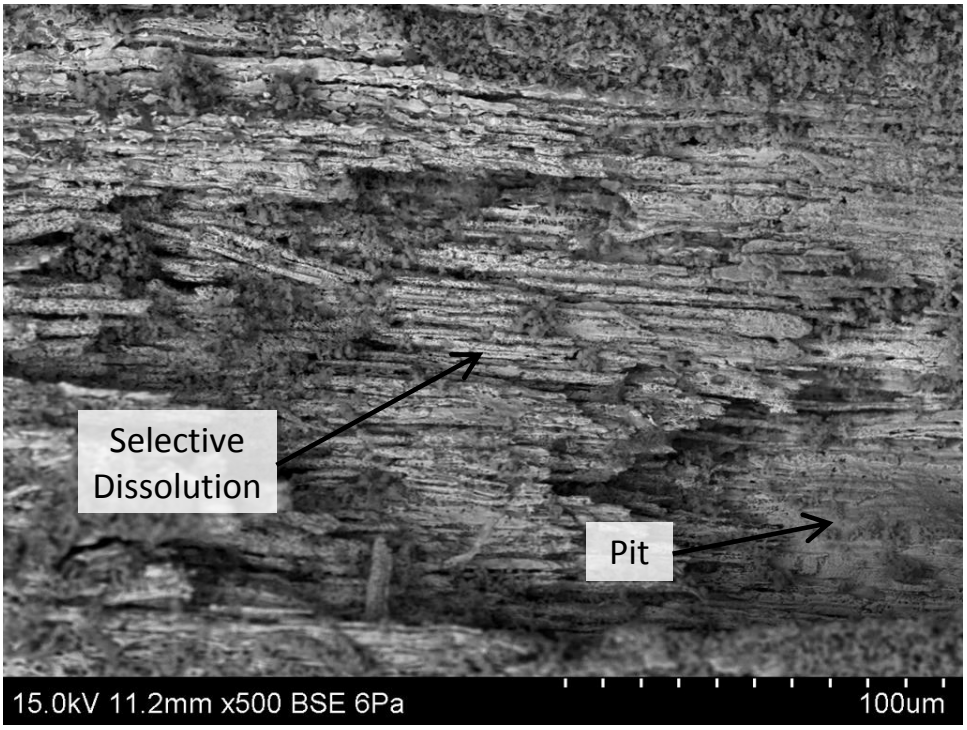

Figure 6.24 Selective dissolution in 2101 HSSS in carbonated solution with 1 M Cl^-

Selective dissolution was also evident in pit cross sections in tested 2101 and 2304 specimens. Figures 6.25 and 6.26 show typical occluded pit cross sections in 2101 and 2304, respectively. In microstructures shown in Figures 6.25 and 6.26, brighter regions correspond to the austenite phase, darker regions correspond to the ferrite phases, and voids (black by backscattered imaging) correspond to the location of precipitates. Selective dissolution of the ferrite phase was observed in 2101 and 2304 in alkaline and carbonated solutions at all Cl^- concentrations that resulted in corrosion initiation. This selective dissolution is clearly shown in the pit cross sections which had ragged perimeters with protrusions of austenite and depressions of ferrite. In some cases, large corrosion pits with selective dissolution were observed. Figure 6.27 shows one such corrosion pit in 2101 where ferrite has selectively dissolved, leaving islands of austenite.

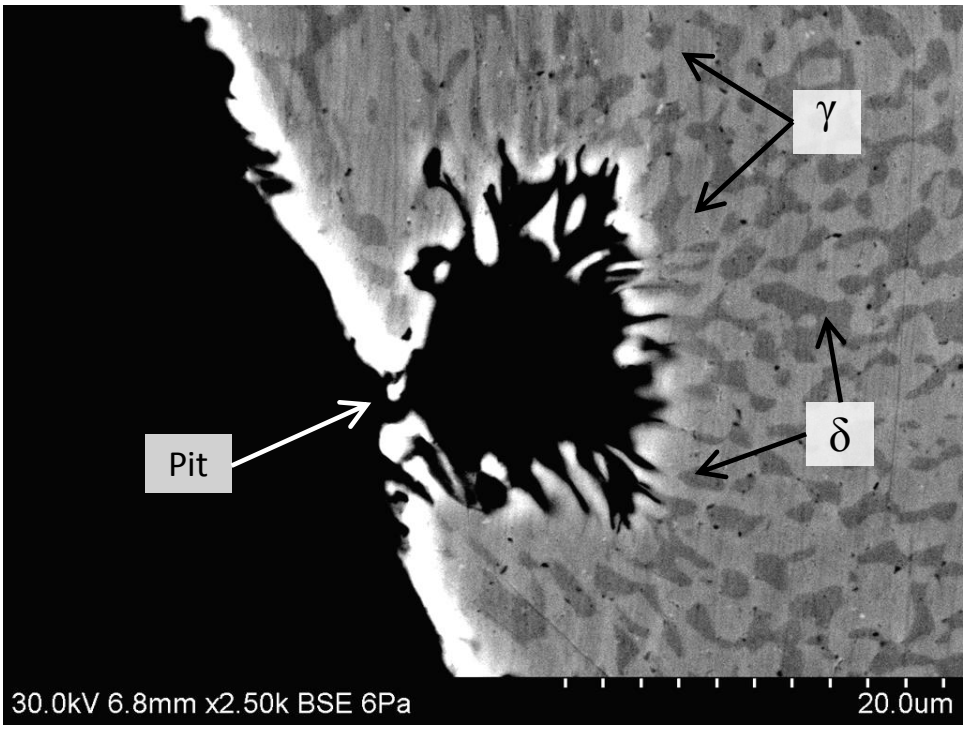

Figure 6.25 Dissolution of ferrite in 2101 HSSS tested in alkaline solution with 1M Cl^-

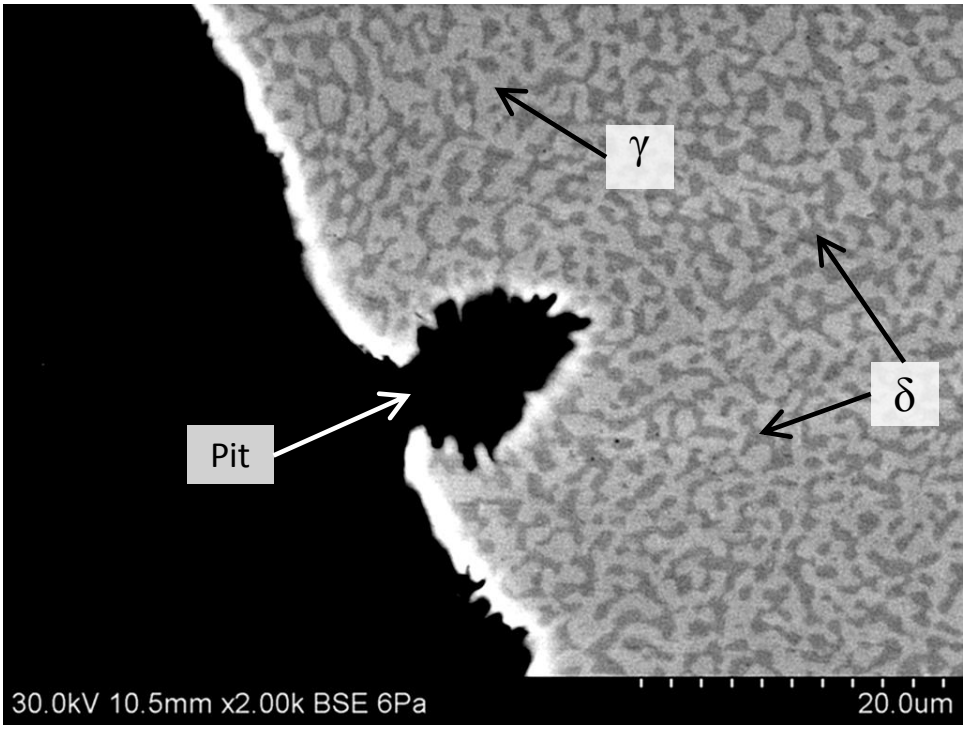

Figure 6.26 Dissolution of ferrite in 2304 HSSS tested in carbonated solution with 1M Cl^-

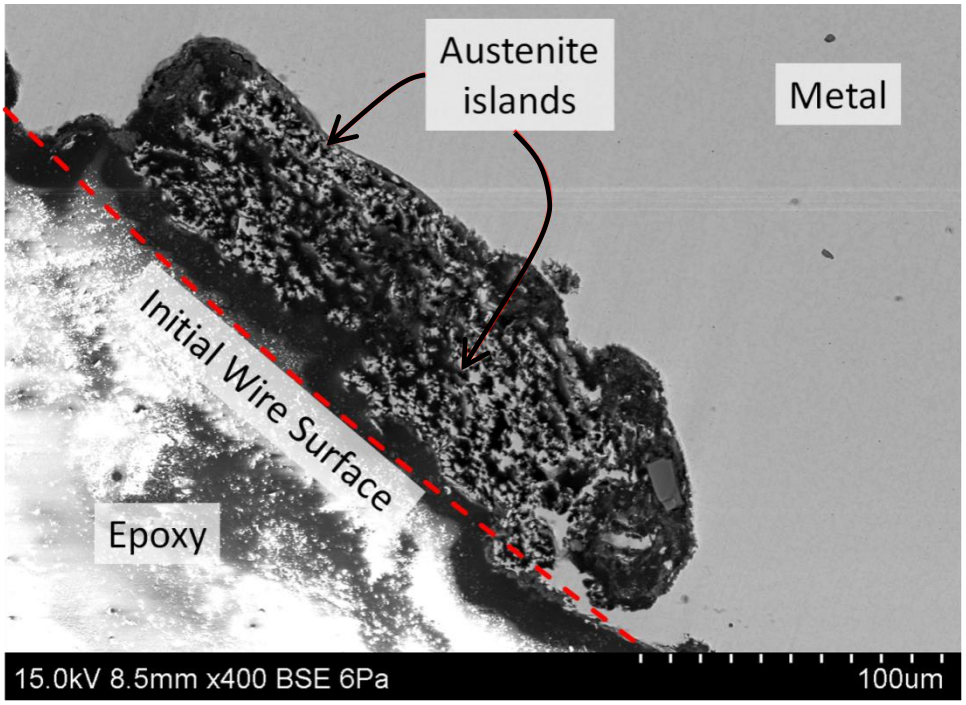

Figure 6.27 Selective dissolution of ferrite in large corrosion pit in 2101 HSSS tested in carbonated solution with 1 M Cl^-

Selective dissolution has been reported previously in duplex stainless steels. However, the phase attacked varies greatly depending on the exposure condition and the electrochemical potential. Selective dissolution is also intrinsically related to changes in chemical composition as austenite stabilizers Ni and N are enriched in the austenite phase and ferrite stabilizers Cr and Mo are enriched in the ferrite phase. Most previous research on selective dissolution in duplex stainless steels has been conducted in acidic Cl^- bearing solutions, typically finding preferential attack of the austenite phase (Femenia, et al., 2001; Fu, et al., 2005). Selective dissolution of ferrite has been observed in 2205 and 2304 in alkaline and carbonated Cl^- bearing solutions (Alvarez, et al., 2011), corroborating the selective dissolution of ferrite noted in the present study. Dissolution of ferrite in 2101 and 2304 HSSSs tested in alkaline and carbonated solutions suggests that increased Ni and N composition in the austenite phase results in superior corrosion resistance when compared with the ferrite phase which is enriched with Cr and Mo. This hypothesis may also explain the enhanced corrosion resistance of 2205 containing 3.2 % Mo which will be enriched in the ferrite phase and contribute to its corrosion resistance.

6.1.2.3.3 Precipitation Hardened Martensitic Grade 17-7

The morphology of corrosion damage in 17-7 HSSS was similar to that observed in austenitic 304 and 316, with large corrosion pits distributed across the surface of the wire following CPP testing. In addition, lacy pitting was also observed in 17-7 (see mechanism in Section 6.1.2.3.1). Figures 6.28 and 6.29 depict a typical corrosion pit in 17-7 and lacy pitting on the rim of the pit, respectively. Pit cross sections revealed hemispherical pits with derivative saucer-shaped pits (see Figure 6.30). No determination of selective dissolution could be made as the surface of 17-7 is largely martensitic.

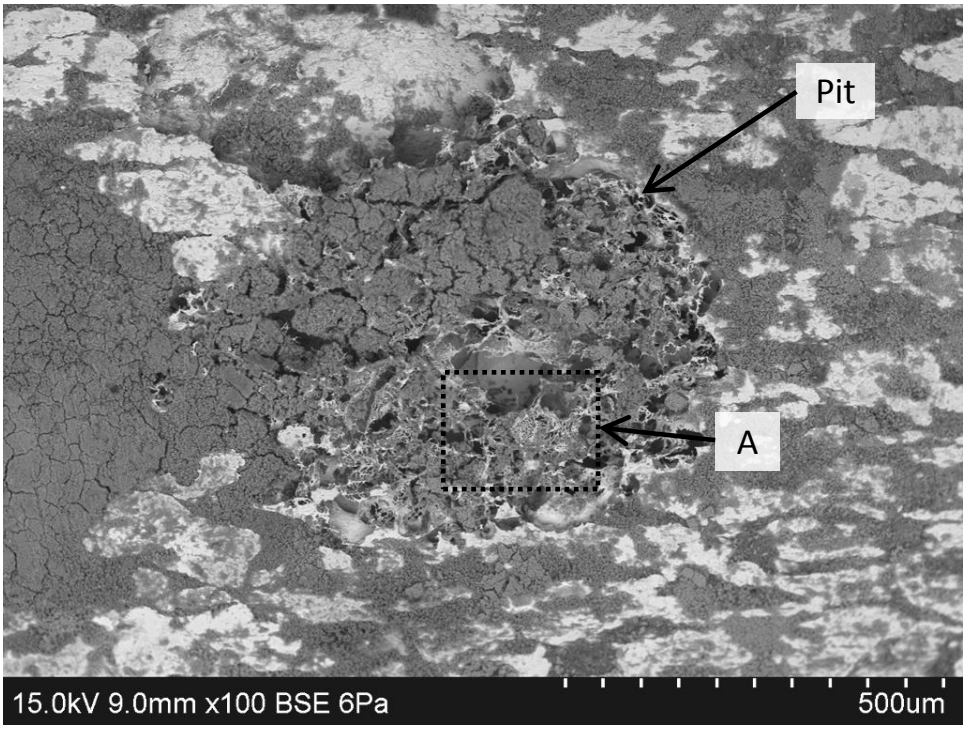

Figure 6.28 Corrosion pit in 17-7 HSSS tested in carbonated solution with 1 M Cl^-

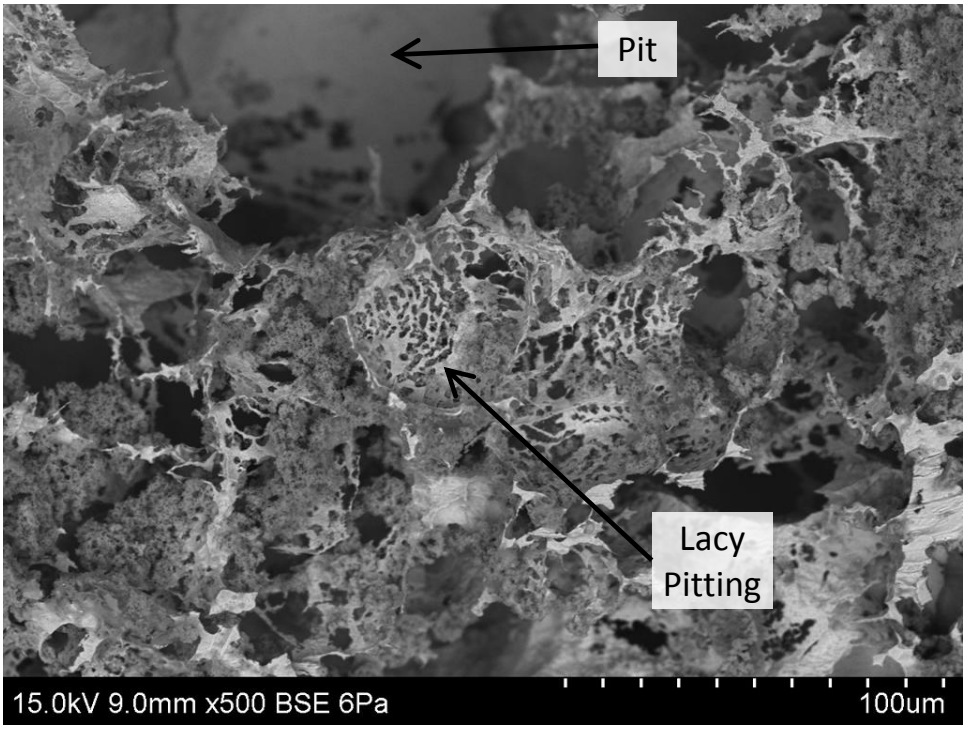

Figure 6.29 Lacy pitting in region A of the corrosion pit shown in Figure 6.30

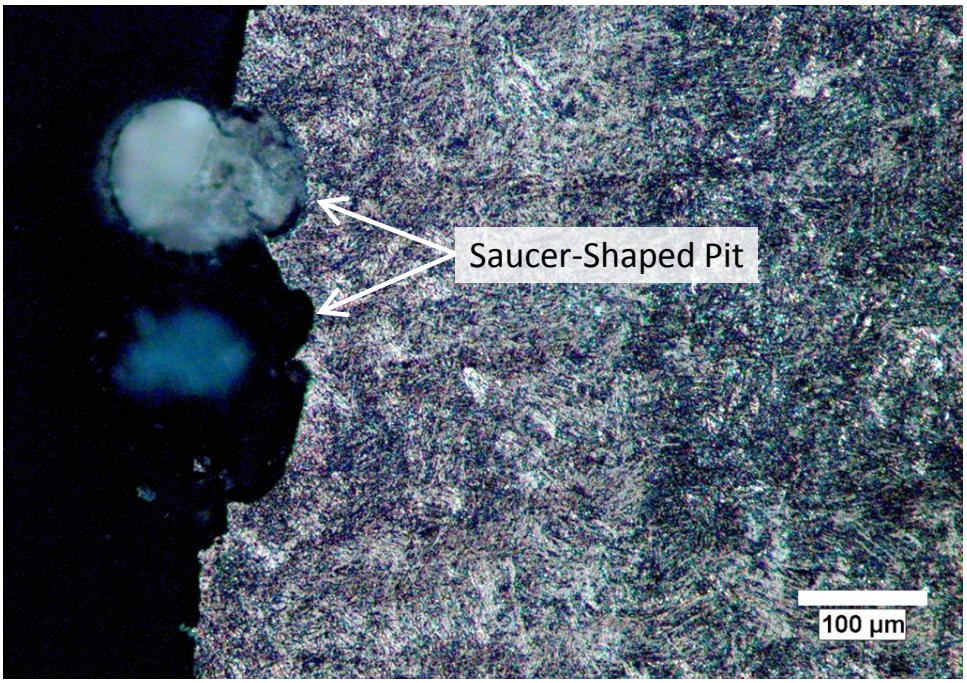

Figure 6.30 Cross section of pit in 17-7 HSSS tested in alkaline solution with 0.5 M Cl^-

6.1.2.3.4 Remarks on Morphology of Corrosion Damage

The optical microscopy and SEM/EDX studies discussed above provide many useful insights into the fundamental mechanisms of corrosion initiation and propagation in HSSSs. This knowledge can be useful for materials selection and optimization. However, the damage morphology presented in micrographs in Section 6.1.2.3 results from corrosion initiated during CPP scans. When corrosion initiates in the CPP scan, the potential is held at high levels of anodic polarization as the scan proceeds. At these high levels of anodic polarization, current densities may remain high (greater than 10 mA/cm^2) for extended periods of time, leading to significant dissolution of metal and large pit sizes. Therefore, the results of these characterization studies may not be fully applicable for the description of corrosion damage morphology which occurs in the field over much longer periods of time.

6.1.3 Summary of Results

The primary goal of CPP experiments presented in Section 6.1 was to identify optimal HSSS alloys based on corrosion resistance from the list of potential candidates. The results of all CPP experiments conducted are shown in Figure 6.31. Results for each HSSS in a given solution and Cl^- concentration have been classified according to the corrosion behavior observed in the electrochemical data and through forensic investigation of tested specimens. Corrosion behavior has been categorized as: (1) no corrosion initiation observed, (2) metastable pitting observed, and (3) stable pitting observed. Behaviors 1 and 3 clearly indicate low and high corrosion susceptibility, respectively. Behavior 2 indicates that metastable pitting was observed in the electrochemical data along with minor surface pitting on at least one of the triplicate test specimens. These metastable pits repassivate at potentials more active than the open circuit potential.

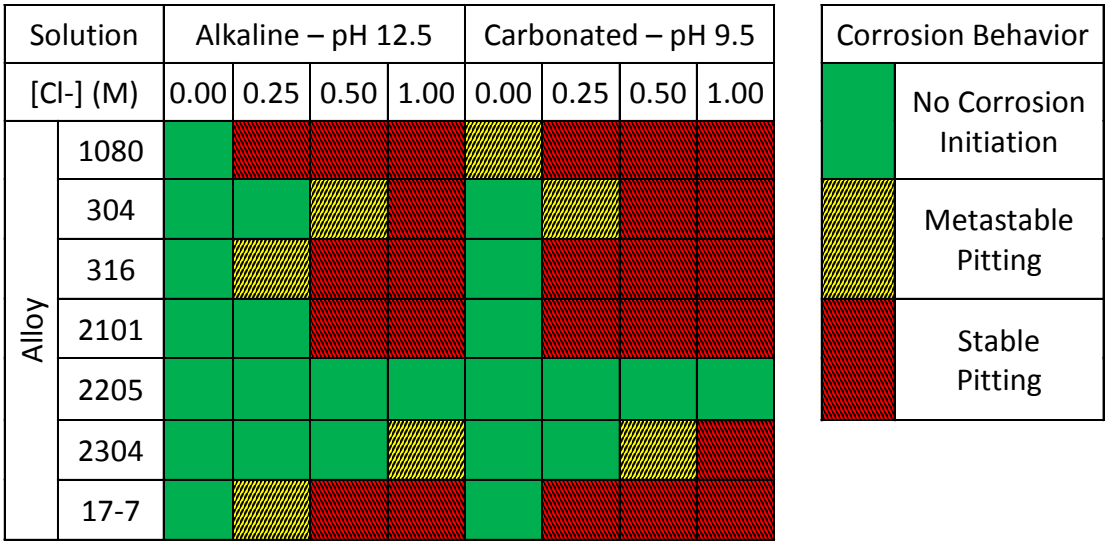

Figure 6.31 Summary of CPP experimental results

As anticipated, the 1080 prestressing steel was found to be susceptible to corrosion initiation in alkaline and carbonated concretes at Cl^- concentrations of 0.25 M. Provided that the alkalinity in the concrete can be maintained throughout the intended service life of the PSC structure, 2205, 2304, and possibly 304 are acceptable at Cl^- concentrations up to 0.5 M. If Cl^- concentrations can be suppressed below brackish water levels (0.25 M) in alkaline concrete, all candidate HSSSs tested exhibit low corrosion susceptibility. However, if the concrete becomes carbonated and pH is reduced, 2205 and 2304 are the only candidate HSSSs which exhibit acceptable corrosion resistance at Cl^- concentrations of up to 0.5 M. In all cases examined, 2205 exhibits corrosion resistance which is far superior to all other candidate HSSSs tested (fully resistant in carbonated solution with 1.0 M Cl^-). The improved corrosion resistance of 2205 and 2304 when compared with their austenitic counterparts 316 and 304 is promising as these duplex grades have a lower Ni content (and low Mo in 2304) and, as a result, are available at a lower cost.

Based on these data and the anticipated exposure conditions present at 100+ years of service, duplex HSSS grades 2205 and 2304 show the most promise for use as prestressing reinforcement. If Cl^- exposures are expected to be well below brackish water levels, austenitic grade 304 may also be a viable option. Grades 2205 and 2304 have been identified as “optimal” HSSSs and are the focus of all additional studies of corrosion behavior presented in the following section and investigations directed towards full-scale production as corrosion resistant prestressing strand presented in Chapter 7.

6.2 Additional Studies of Optimal High-Strength Stainless Steels

Two experimental studies were performed to further characterize the corrosion behavior of optimal HSSSs 2205 and 2304. The first series of experiments examined the effect of HSSSs tested in a stranded geometry on Cl^- induced corrosion resistance. The second series of experiments examined susceptibility to environmentally assisted cracking mechanisms in Cl^- containing simulated concrete pore solutions and with cathodic polarization. Results of these studies are presented in the following sections.

6.2.1 Influence of Stranding on Corrosion Resistance

Studies presented in Chapter 3 have shown that the seven-wire strand geometry typically utilized for prestressing reinforcement results in reduced Cl^- induced corrosion resistance of 1080 prestressing due to crevice corrosion phenomena. Based on these observations, similar studies of HSSSs are justified. In order to investigate the influence of stranding on corrosion resistance, 2205 and 2304 simulated prestressing strands were manufactured and evaluated using CPP techniques.

6.2.1.1 Experimental Methods

Simulated prestressing strands were produced of HSSSs 2205 and 2304. Simulated strand specimens evaluated in Chapter 3 were cut directly from A416 prestressing strands. In the HSSSs of interest, no such strands were available. To form a strand, seven HSSS wires were bundled together and secured using plastic cable ties. With the seven-wire bundle of HSSS wires formed, simulated prestressing strand

specimens were manufactured using the same procedures described in Section 3.2.2.2. A total of eight specimens of 2205 and eight specimens of 2304 were produced.

CPP techniques were used to evaluate the influence of stranding on the Cl^- induced corrosion resistance of 2205 and 2304 HSSSs. All experiments were conducted using the same testing parameters (i.e., potential scan rate and range), simulated alkaline and carbonated concrete pore solutions, and sample conditioning procedures described in Section 6.1.1.2. Due to their increased exposed surface area, strand specimens required testing in a larger solution volume of 700 ml (23.67 oz). The first series of CPP experiments were conducted on duplicate specimens in alkaline and carbonated solutions containing 0.5 M Cl^- to provide an initial indication of corrosion resistance. Based on the results of tests in 0.5 M Cl^-, the concentration of Cl^- was either increased or decreased for the remaining tests. For example, if the first series of tests on 2205 strand in 0.5 M Cl^- containing pore solutions showed full repassivation during the CPP scan, the second series of tests would be performed at an increased Cl^- concentration of 1 M.

6.2.1.2 Results and Discussion

Figures 6.32 and 6.33 show results of CPP testing of 2205 and 2304 strand specimens in alkaline solutions. CPP experiments were conducted at Cl^- concentrations of 0.5 and 1 M for 2205 and 0.25, 0.5, and 1 M for 2304. Following the specimen conditioning period, measured values of E_{corr} in 2205 and 2304 strands were shifted negatively by approximately 200 mV when compared with wires. This shift was also observed in tests of A416 prestressing strands (see Section 3.3.1.2) and has been attributed to aeration/concentration cell effects in the stranded geometry which result in a measured cathodic polarization of E_{corr}.

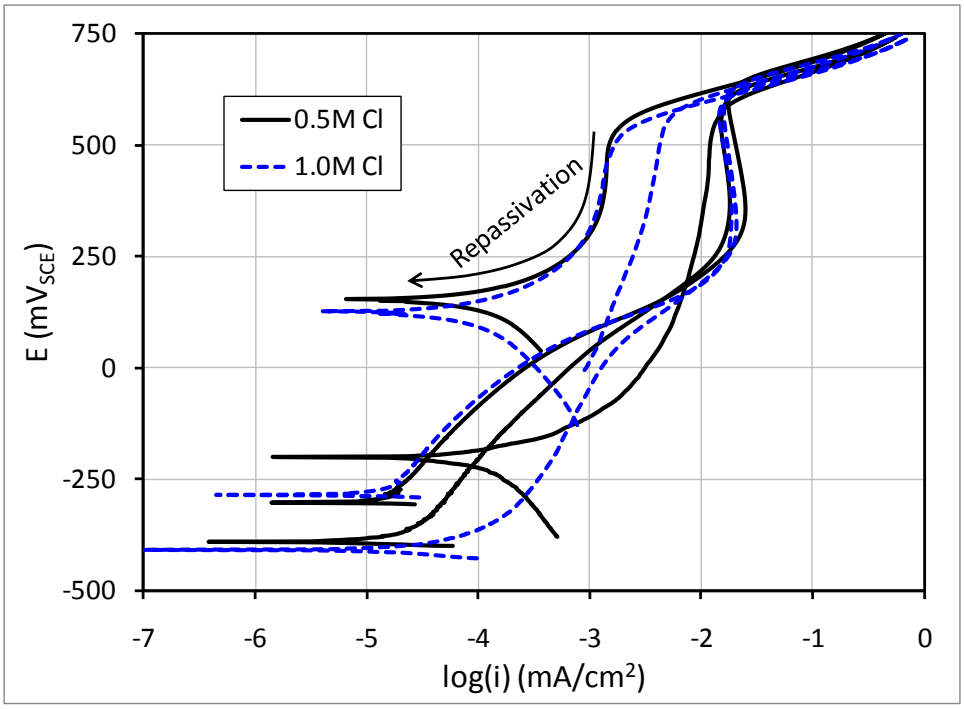

Figure 6.32 Polarization curves of 2205 strand tested in alkaline solutions

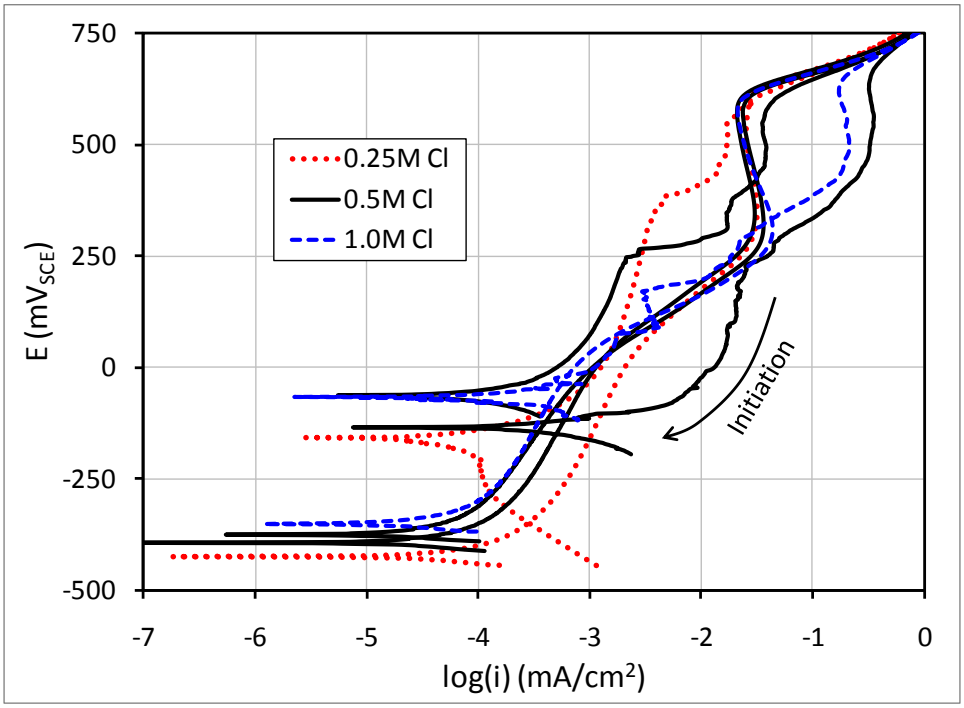

Figure 6.33 Polarization curves of 2304 strand tested in alkaline solutions

In alkaline solutions, no degradation in corrosion resistance was observed in 2205 strand which did not exhibit corrosion initiation at Cl^- concentrations up to 1 M. Stranding did reduce the corrosion resistance of 2304 strand, which at a Cl^- concentration of 0.5 M was not susceptible to corrosion initiation in the single wire geometry (see Figure 6.31) but was when tested in the seven-wire strand geometry. Corrosion initiation in 2304 strands occurred within the O_2 evolution region and lead to repassivation potentials of approximately -100 to -200 mV. Figure 6.34 depicts corrosion damage in a 2304 strand specimen tested in an alkaline solution with 0.5 M Cl^-.

(a) Crevice corrosion

(b) Pitting corrosion

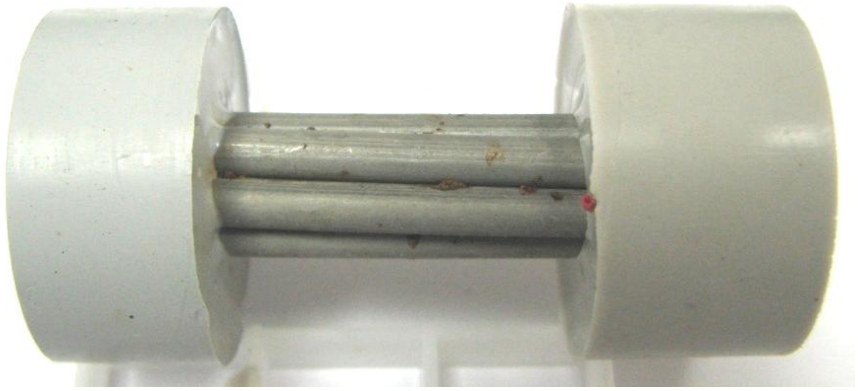

(c) Photo of 2304 strand specimen

Figure 6.34 Corrosion damage in 2304 strand specimen following testing in alkaline solution with 0.5 M Cl^-

Corrosion damage in 2304 strand was largely partitioned to the crevice regions where impingement between the individual wires in the strand occurs (see Figure 6.34 (a)). Moderate pitting corrosion was also observed on the outer wires (see Figure 6.34 (b)). This damage confirms a crevice corrosion mechanism consistent with that proposed in Section 3.3.4 for A416 prestressing strands.

Figures 6.35 and 6.36 show results of CPP testing of 2205 and 2304 strand specimens in carbonated solutions at the same Cl^- concentrations studied in alkaline solutions. The initial E_{corr} of 2205 and 2304 strand in carbonated solutions was shifted negatively by approximately 100 mV relative to single wires of the same alloy. Here again, 2205 strand was fully resistant to corrosion initiation at Cl^- concentrations up to 1 M. The corrosion resistance of 2304 strand was also found to be reduced in carbonated solutions with minor crevice corrosion at Cl^- concentrations of 0.25 M.

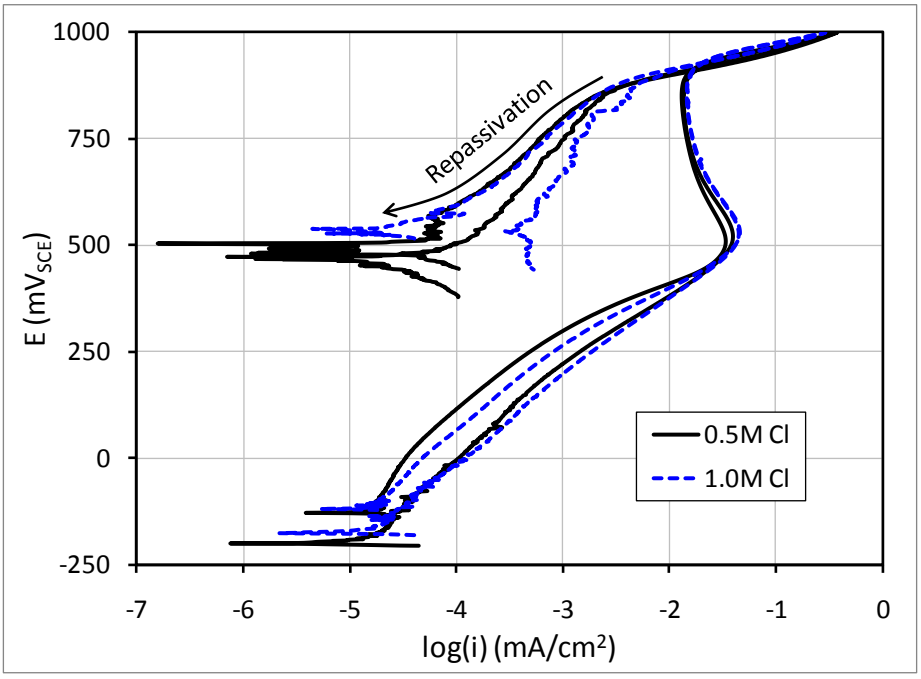

Figure 6.35 Polarization curves of 2304 strand tested in carbonated solutions

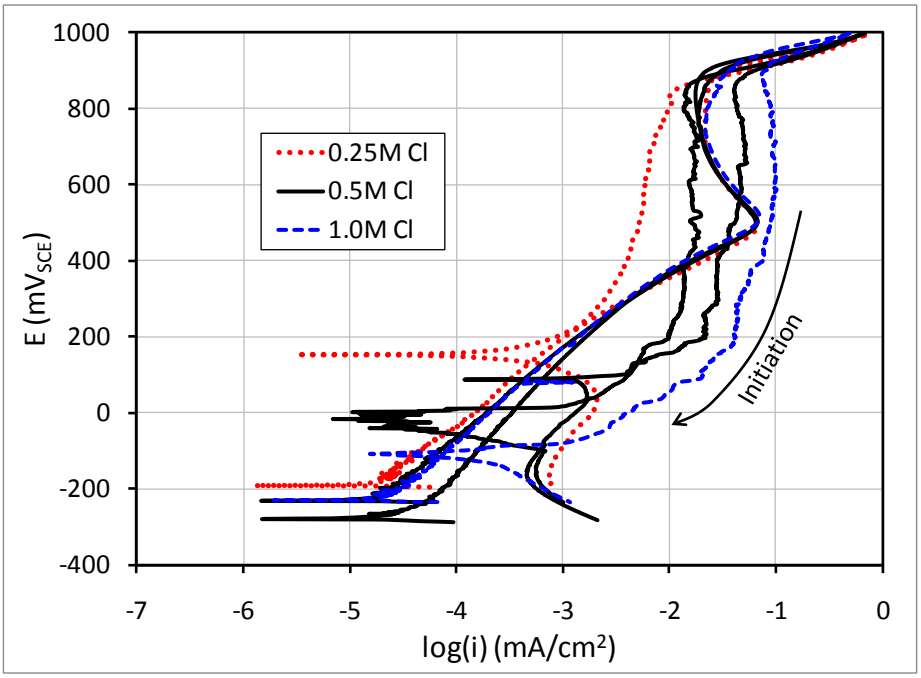

Figure 6.36 Polarization curves of 2304 strand tested in carbonated solutions

Once corrosion initiated in 2304 strands, current densities associated with corrosion propagation were much lower than those measured in single wires (approximately 0.1 mA/cm^2 in strands vs. 10 mA/cm^2 in wires). These low current densities likely correspond to highly localized form of corrosion (crevice / pitting) whose current contributions are negated when normalized against the relatively large exposed surface area of the strand sample.

The results of all CPP experiments on 2205 and 2304 strand are recorded in Figure 6.37 according to corrosion behavior observed (see Section 6.1.3). As discussed above, corrosion resistance of 2304 is jeopardized in the stranded geometry. If alkalinity in the concrete can be maintained and Cl^- concentrations in the pore solution remain below 0.25 M, 2304 will still provide sufficient corrosion resistance in PSC. However, 2304 may be susceptible to corrosion initiation in structures with extended service lives

constructed with poor quality concrete with less resistance to Cl^- ingress and carbonation. Such aggressive conditions necessitate the use of 2205 which exhibits superior corrosion resistance in the stranded geometry even under the most aggressive exposure conditions (carbonated solution with 1 M Cl^-).

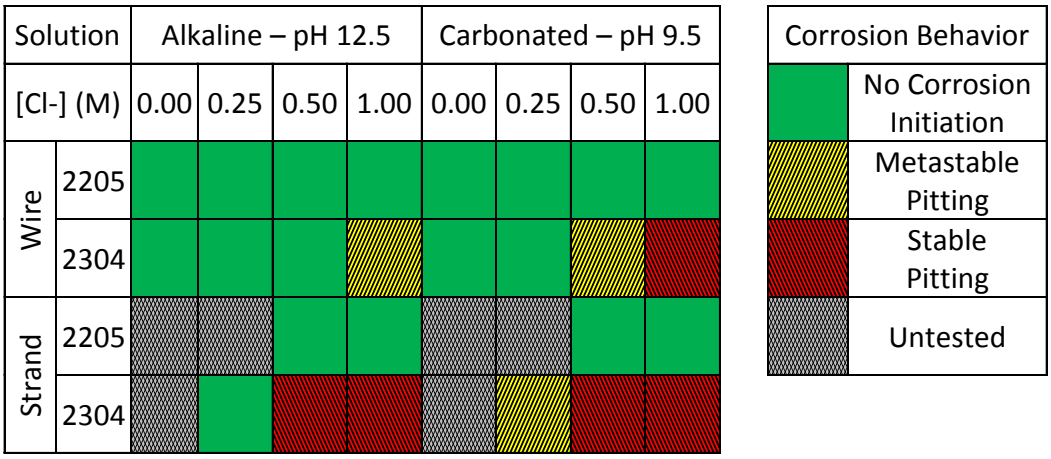

Figure 6.37 Summary of CPP experimental results for 2205 and 2304 strands

The only explanation for the superior performance of 2205 is its chemical composition. As shown in Table 4.3, 2205 contain similar amounts of Ni and Cr as 2304 but increased amounts of Mo (10X higher in 2205) and N (1.6X higher in 2205). Previous studies of the pitting corrosion resistance of duplex stainless steels 2205 and 2304 have found that Mo and N are particularly effective in increasing corrosion resistance in Cl^- containing neutral and acidic solutions (Merello, et al., 2003). The effectiveness of Mo and N is also reflected in the PREN value, with Mo and N making contributions of 3.3 and 30 times that of Cr, respectively (Presuel-Moreno, et al., 2010). Knowing that conditions within the crevice during corrosion propagation are similar to an acidic Cl^- solution (see mechanism in Section 3.3.4), it is hypothesized that the superior

corrosion resistance of 2205 results from its increased Mo and N content. Accordingly, this increased corrosion resistance also comes with increased cost.

6.2.2 Environmentally Assisted Cracking Susceptibility

Brittle environmentally assisted cracking (EAC) caused by the interaction of corrosion initiation and propagation with tensile stress is one of the greatest concerns in prestressed concrete (Nürnberger, 2009). For this reason, it is essential that any new alloy proposed for use as prestressing reinforcement be evaluated for susceptibility to EAC. EAC mechanisms of primary interest are Cl^- assisted stress corrosion cracking (SCC) and hydrogen embrittlement (HE). Previous studies discussed in Section 2.6.1 have shown that austenitic HSSSs are susceptible to SCC and HE at high concentrations of Cl^- and in the presence of H^+, respectively (Alonso, et al., 2008; Wu and Nürnberger, 2009). The lone study which examined 2205 HSSS found significantly higher resistance to HE than 1080 prestressing steel when placed under tensile stress in an aggressive NH_4SCN solution at 50 ˚C (122 ˚F) (Shirahama, et al., 1999). In the present study, slow strain rate test (SSRT) methods were used to evaluate the susceptibility of optimal HSSSs 2205 and 2304 to damage by SCC and HE mechanisms.

6.2.2.1 Experimental Methods

6.2.2.1.1 Manufacture of Test Specimens

Dogbone specimens were machined from 2205 and 2304 wires for use in the SSRT setup. The schematic shown in Figure 6.38 depicts the geometry of the dogbone specimen used for all SSRTs. It was necessary to form a reduced cross section in the center of the specimen to ensure that the high tensile stresses necessary to initiate EAC damage would occur within the testing solution. Two challenges were encountered while

designing and machining the dogbone specimens. First, the high tensile strength of the 2205 and 2304 wires made it necessary to use a small diameter in the reduced cross section of 2.5 mm (0.1 mil) so that the failure load of the specimen would be less than the 8.9 kN (2000 lbf) capacity of the SSRT apparatus. This small diameter caused concerns that the wire would easily flex when secured in the lathe, making it necessary to machine at a slow cutting speed. Second, the residual curvature of the wire required straightening so that the machining could be performed in a lathe. Segments of the wire cut to make dogbone specimens were lightly peened with a hammer and anvil until straight. Additional peening was performed with the specimen secured in the lathe until a transverse wobble less than 0.13 mm (5 mil) was achieved, after which the reduced cross section was machined. Following the creation of the reduced cross section, the specimen was removed from the lathe and 8-32 threads were cut into the ends to be used for securing the specimen in the SSRT apparatus.

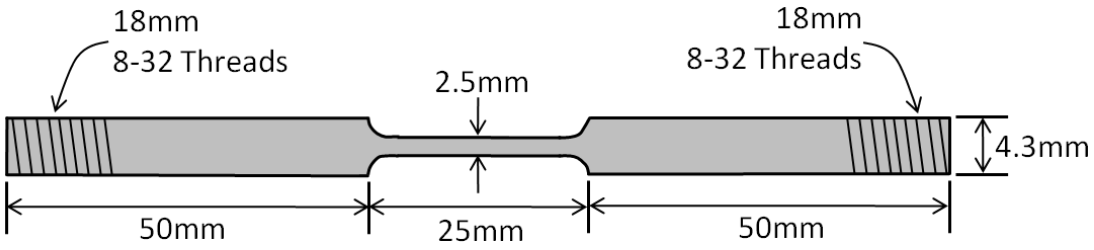

Figure 6.38 Dogbone specimen used for all SSRTs

6.2.2.1.2 Slow Strain Rate Testing Apparatus

Figure 6.39 shows the apparatus used for all SSRTs and the exposure cell used for SCC and HE tests. The apparatus consisted of a rigid steel frame, a variable speed drive motor, and a series of chain-driven speed reducers which eventually connect to a worm

drive screw jack which provides the specified axial displacement rate to the specimen. Pin-connected couplings were used to secure the dogbone test specimen to the screw jack shaft at the top and to the steel frame at the bottom.

Specimens which were exposed to solutions were placed in a 200 ml (6.8 oz) polypropylene exposure cell. Holes were drilled through the lid and bottom of the cell to allow the dogbone specimen to run through its center. In order to prevent the solution leakage, a rubber stopper with a center hole the same diameter as the shoulder of the dogbone specimen (4.2 mm (0.165 in)) was used (see exposure cell in Figure 6.39). Also, silicone sealant was applied circumferentially at the interface between the dogbone specimen and the rubber stopper to prevent solution leakage and the possibility of crevice corrosion. Access holes were drilled in the lid so that testing solutions could be poured into the exposure cell once it was secured in the SSRT apparatus and for reference and counter electrodes, if necessary.

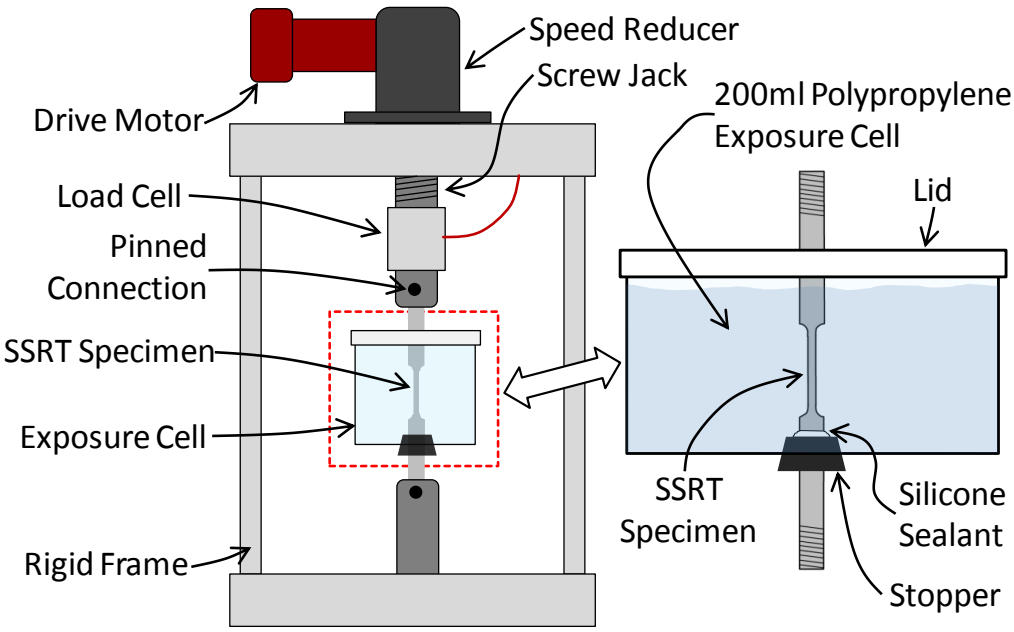

Figure 6.39 Apparatus and exposure cell used for SSRTs

Once the specimen and exposure cell were secured in the SSRT apparatus, the testing solution was added to the cell, any instrumentation was connected, and the SSRT was commenced. A constant displacement rate was applied using an RPM calibration of the variable speed drive motor. A constant displacement rate of $25 \cdot 10^{-6}$ mm/s ($1 \cdot 10^{-6}$ in/s) was used for all SSRTs. This displacement rate corresponds to a strain rate of 10^{-6} s^{-1} for the 25 mm (1 in) gage length with reduced cross section. The 10^{-6} s^{-1} strain rate was selected as it has been shown to result in the most significant damage by SCC and HE and, thus, provides a conservative assessment of EAC susceptibility (Ugiansky and Payer, 1977). The duration of each SSRT was approximately 50 hr. During the SSRT, load in the specimen was monitored using a calibrated tension load cell connected between the screw jack shaft and the coupler used to secure the dogbone specimen. Load data were collected using a DATAQ USB data acquisition device which was monitored using WinDaq.

Details on the SSRT experimental setup used for evaluating SCC and HE susceptibility of 2205 and 2304 are provided in the next two sections. SSRTs were also performed in air to provide a baseline for comparison. For each SSRT, the exposed region of the dogbone specimen was polished with SiC paper up to 600 grit followed by 6 μm (0.24 mil) diamond paste. Following the SSRT, fractured specimens were examined using optical and SEM. Damage was quantified by interpretation of the stress vs. strain behavior and measurements of the reduction in area of the fracture surface.

6.2.2.1.3 Experimental Methods for Stress Corrosion Cracking Tests

The SSRT method was used to evaluate the SCC susceptibility of 2205 and 2304 HSSSs in alkaline and carbonated solutions (see solution details in Section 6.1.1.2) with

the addition of 0.5 M Cl^-. All SSRTs were conducted at open circuit; that is to say, no external potential was applied to the specimens. Figure 6.40 depicts the experimental setup used to evaluate SCC susceptibility.

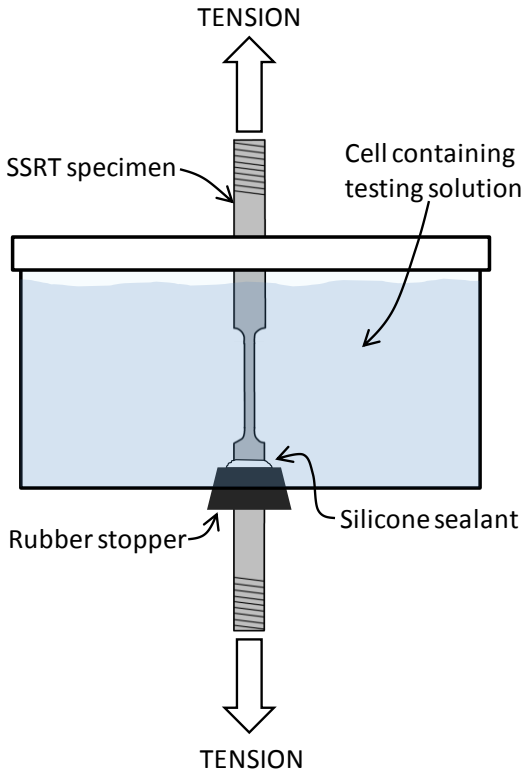

Figure 6.40 Experimental setup for SCC SSRTs

6.2.2.1.4 Experimental Methods for Hydrogen Embrittlement Tests

The SSRT method was used to evaluate the HE susceptibility of 2205 and 2304 HSSSs in alkaline and carbonated solutions (see solution details in Section 6.1.1.2) with an applied cathodic polarization to generate hydrogen. While the exposure cell design used was similar to Figure 6.40, additional electrodes and a potentiostat were necessary to apply the potential to the specimen. Figure 6.41 shows the experimental setup used for HE SSRTs.

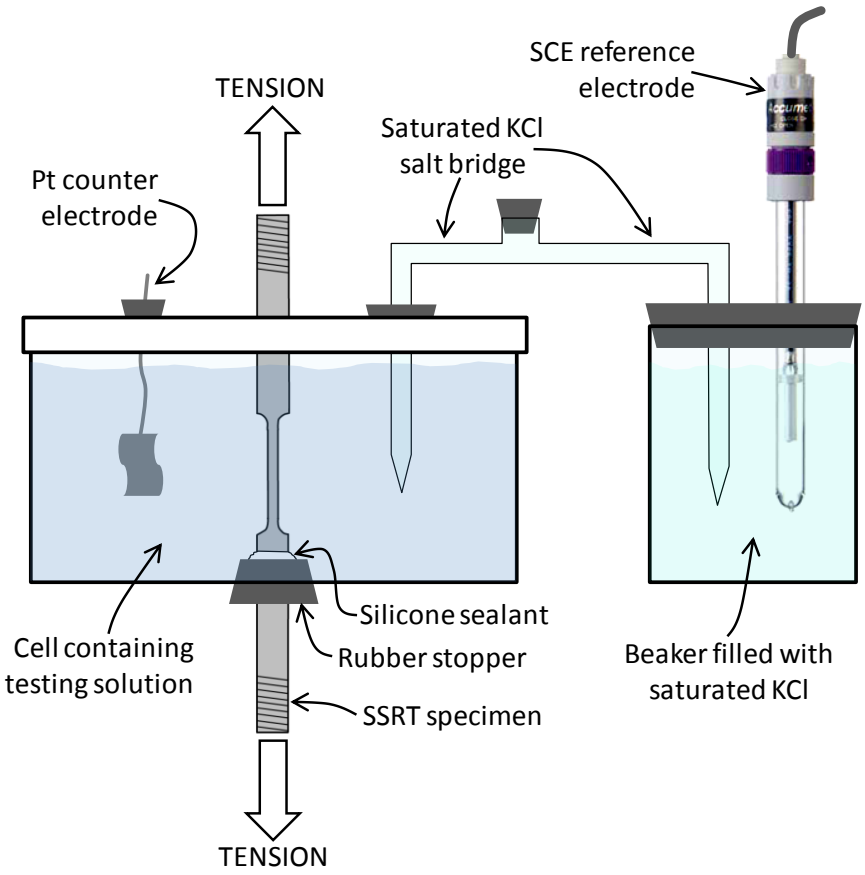

Figure 6.41 Experimental setup for HE SSRTs

A Pt foil counter electrode with surface area of 4 cm^2 (0.62 in^2) was placed through an access hole in the lid of the exposure cell. An SCE reference electrode was placed in an adjacent beaker filled with saturated KCl (a low ohmic resistance solution) and sealed with a rubber stopper. The reference electrode was electrolytically connected to the exposure cell with a salt bridge filled with saturated KCl. The dogbone specimen acted as the working electrode. The counter, reference, and working electrode were connected to a GAMRY Reference 600 potentiostat which was used to apply the potentiostatic cathodic polarization (i.e., apply a constant cathodic polarization of the potential relative to the SCE reference electrode and measure current).

HE tests were performed at potentials of -1.00 V and -0.82 V in alkaline and carbonated solutions, respectively. These potentials lie 20 mV below the E_{H^+/H_2} "Hydrogen" line at the pH of 12.5 in alkaline solutions and 9.5 in carbonated solutions (on the SCE scale: $E_{applied} = 0.242 - 0.059 \cdot pH$ in volts). With the potential shifted to below E_{H^+/H_2}, H_2 is generated on the surface of the working electrode which simulates a cathodic overprotection of the steel which is known to cause HE damage.

6.2.2.2 Results and Discussion

The results of all SSRTs performed on 2205 and 2304 are plotted in Figures 6.42 and 6.43, respectively. One difficulty encountered when interpreting the results of SSRTs was small changes in compliance during the initial portion of the test as the connections seated. This increased compliance resulted in irregular stress vs. strain behavior in the elastic range. In addition, because the strain was calculated based on the specified displacement rate and time stamp of each load reading, changes in compliance also resulted in changes in strain. In order to eliminate these abnormalities and make each set of SSRT results more comparable, the elastic portion of the curve was truncated at a given stress level and the data were shifted.

Similar to the stress vs. strain behavior noted in Chapter 5, 2205 and 2304 HSSSs exhibited non-ductile failures in SSRTs, with immediate necking after yield and no strain hardening. Little evidence of SCC and HE damage was present in any of the SSRTs which all had similar times to failure. The only indication of damage was increased compliance in HE SSRTs just prior to failure. Measurements of area reduction at fracture were far better indicators of damage by SCC and HE. The results of area reduction measurements from all SSRTs performed are shown in Figure 6.44.

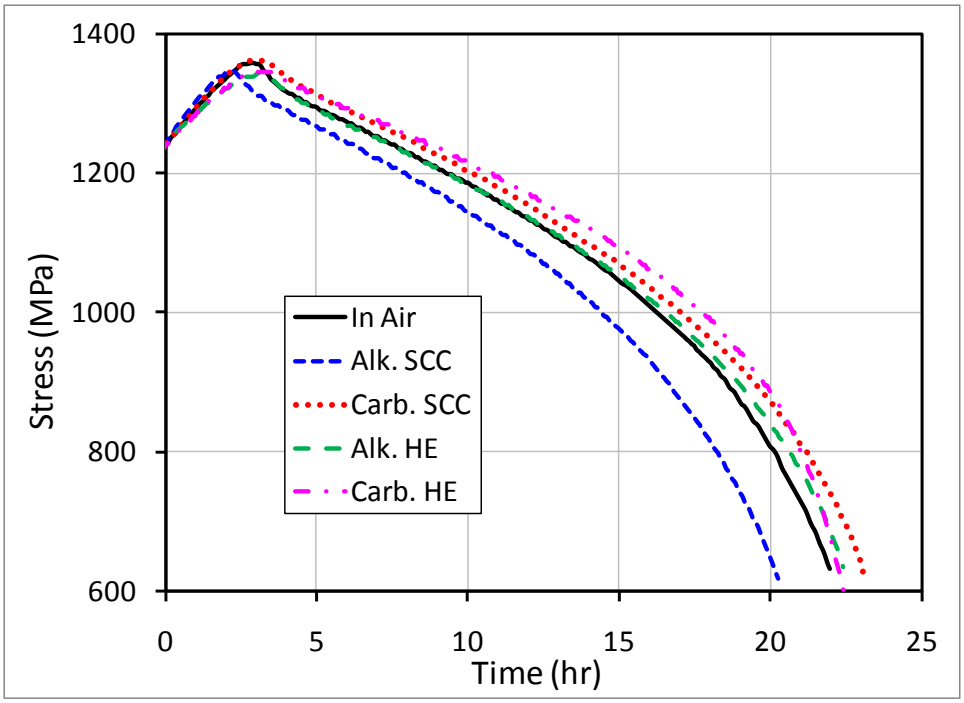

Figure 6.42 SSRT results for 2205 HSSS

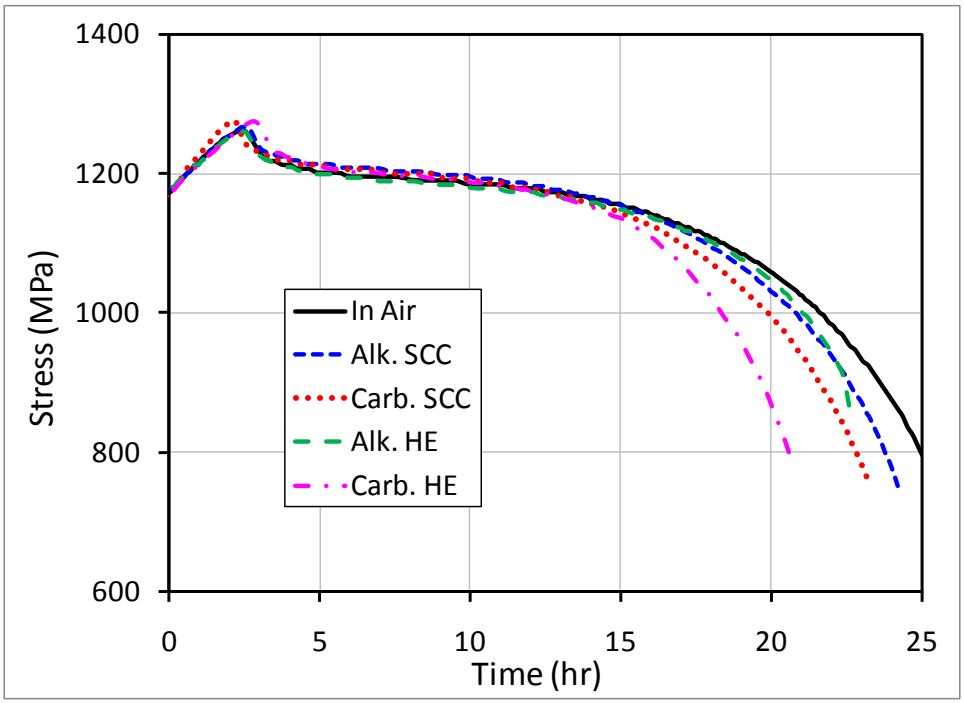

Figure 6.43 SSRT results for 2304 HSSS

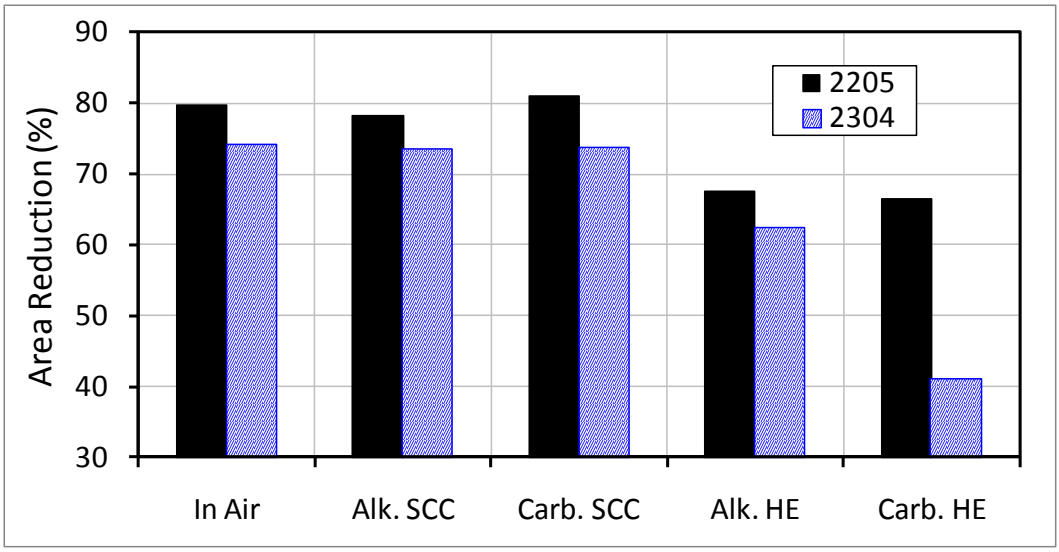

Figure 6.44 Area reductions of 2205 and 2304 SSRTs

SCC SSRTs of 2205 and 2304 showed similar area reductions as in air (approximately 80 % in 2205 and 73 % in 2304), indicating no damage by SCC in alkaline and carbonated solutions. Also, area reductions in these SSRTs were similar to traditional tensile tests presented in Table 5.1 (85 % in 2205 and 77 % in 2304). Damage by HE was evident in measured area reductions of 2205 and 2304 HSSSs in alkaline and carbonated solutions. With the generation of H_2 by cathodic polarization, area reductions decreased to approximately 67 % in 2205 and to less than 63 % in 2304. The most significant HE damage was in 2304 tested in carbonated solutions which resulted in an area reduction of 41 %, almost half of when tested in air.

The trends in area reduction were confirmed when tested specimens were forensically examined with SEM. Figure 6.45 depicts the typical failure observed in SCC SSRTs (2205 shown). In all cases, no damage (i.e., cracking) resulting from SCC was evident in 2205 and 2304. Conversely, significant cracking, delamination, and blistering were evident in all HE SSRTs (see typical damage in Figure 6.46).

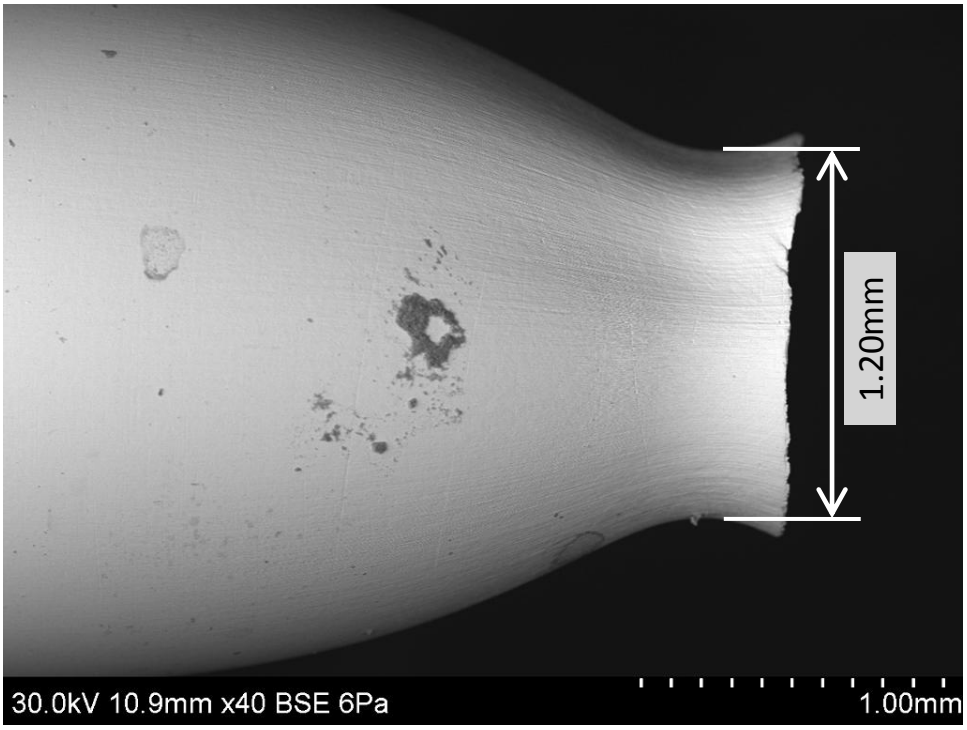

Figure 6.45 No damage 2205 SCC SSRT specimen in carbonated solution

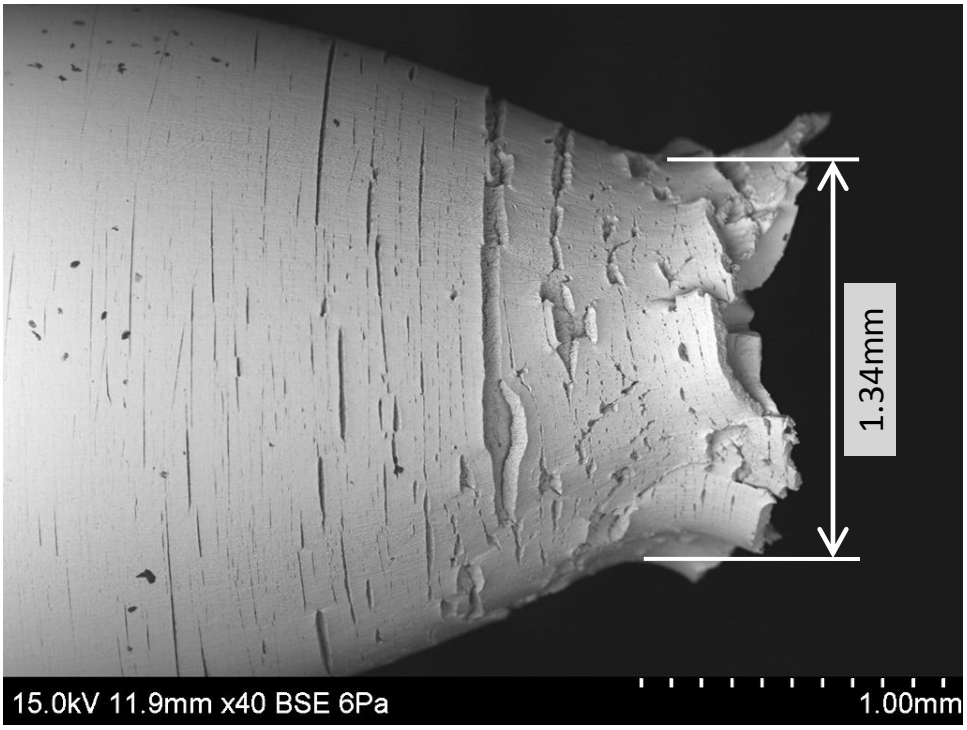

Figure 6.46 Cracking in 2205 HE SSRT specimen in carbonated solution

Cracks in HE specimens were only present in the necked region and increased in size nearer to the fracture surface, suggesting that significant plasticity was required to cause crack initiation and propagation. The most interesting observations of HE damage were made on the fracture surface itself. The SEM micrograph in Figure 6.47 shows the fracture surface of the specimen in Figure 6.46. Here, two distinct fracture morphologies are present. The center of the specimen displayed a ductile cup and cone failure with a shear lip around the perimeter and coalesced voids at the center. Around the perimeter of the specimen, a layer at the surface had fully delaminated from the ductile region at the center. Brittle cleavage fracture of this delaminated surface layer was discovered at higher magnifications. This is clearly shown in the SEM micrograph in Figure 6.48 which corresponds to region A in Figure 6.47.

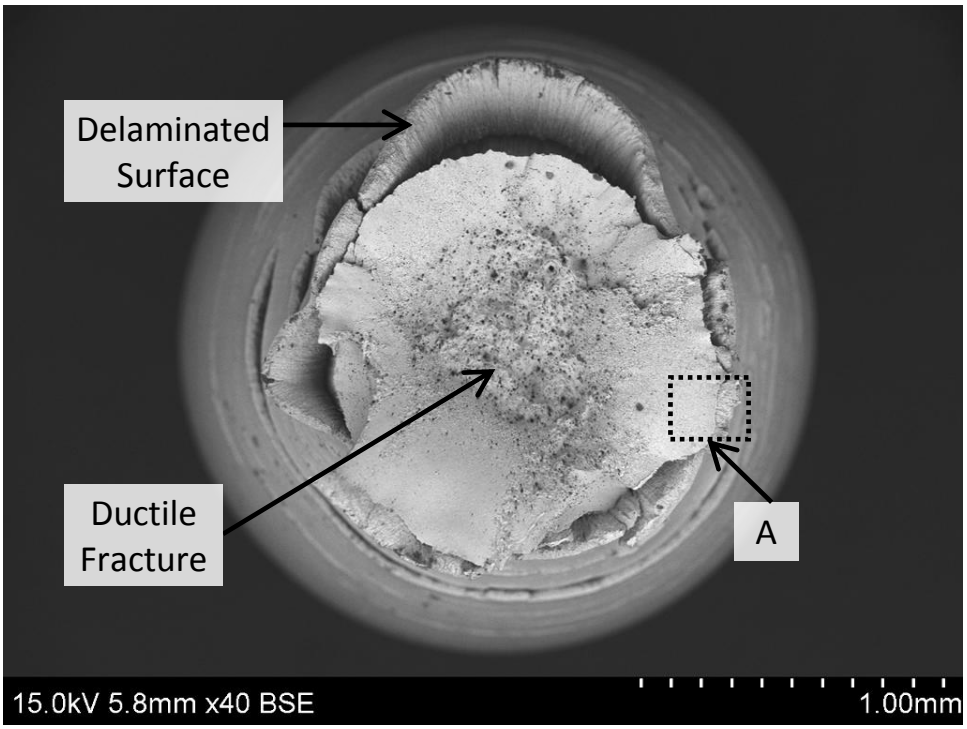

Figure 6.47 Fracture surface of 2205 HE SSRT specimen in carbonated solution

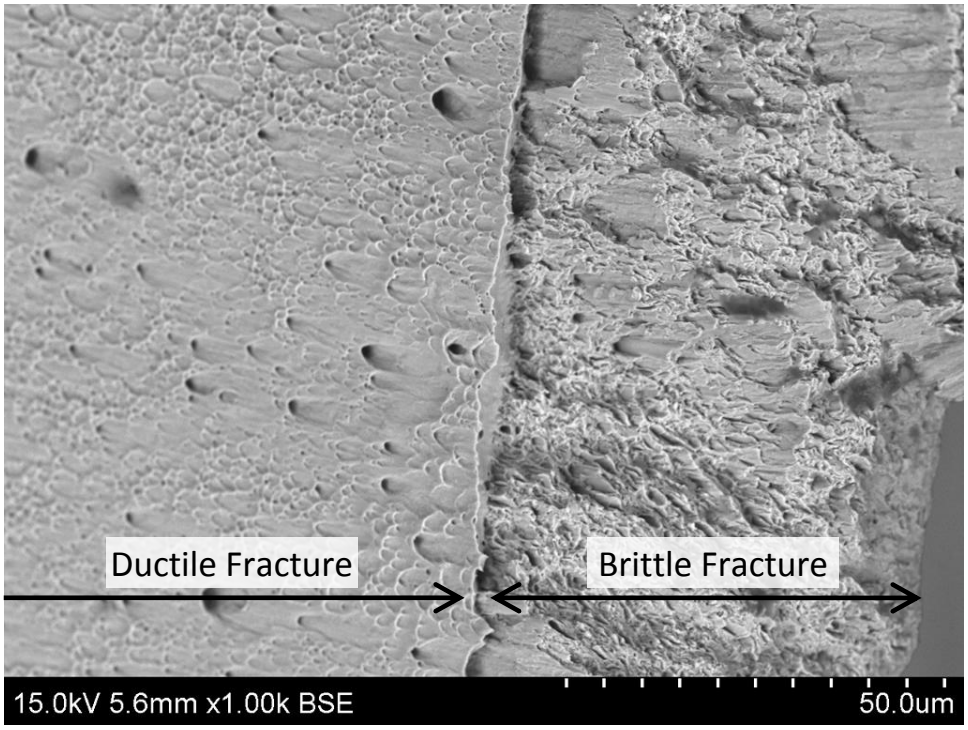

Figure 6.48 Fracture surface of 2205 HE SSRT specimen in carbonated solution corresponding to region A in Figure 6.46

In Figure 6.47, there is a definite transition between the ductile fracture in the center of the specimen and the brittle cleavage fracture at the surface. This transition likely indicates that H has only partially diffused into the specimen. In this case, HE occurred to a depth of approximately 60 μm (2.4 mil) from the surface during the 50 hr SSRT. This means that only 9.4 % of the cross section of the specimen was affected by HE. Therefore, it can be anticipated that if cathodic overprotection which results in the generation of H_2 occurs over extended periods of time in service, H may saturate the steel, promoting fully brittle fracture of the cross section.

CHAPTER 7

DEVELOPMENT OF HIGH-STRENGTH STAINLESS STEEL PRESTRESSING STRAND

With optimal high-strength stainless steels (HSSSs) identified based on their mechanical properties and corrosion resistance, the final objective of the research was to investigate techniques for the production of HSSS prestressing strand. This chapter presents a review of the techniques used for the production of A416 prestressing strands and identifies the potential challenges in producing HSSS prestressing strands using existing A416 prestressing strand production techniques and facilities. The results of studies which investigated techniques for applying low-relaxation thermomechanical heat treatments to HSSS prestressing strands and their effect on stress vs. strain behavior and stress relaxation are also presented.

7.1 Overview of A416 Prestressing Strand Production Process

The production of A416 prestressing strand is a highly optimized process which, with the exception of increased efficiency and improved heat treatments, has changed very little since its introduction in the 1950s (Anderson, 1964). First, high-C 1080 steel rod coil is received and prepped for drawing into wire. The rod coil is prepped by washing followed by pickling in a HCl solution to remove surface oxidation and mill scale. Once the steel is clean, it is submerged into a $ZnPO_4$ solution which reacts with the 1080 steel to form a $ZnPO_4$ coating on the surface which aids in the wire drawing process

and provides some resistance to atmospheric corrosion (Diaz, et al., 2009). A final washing is performed to clean any remaining phosphating solution off of the rod coil. This process is typically performed using an overhead crane which submerges the rod coil into tanks at each step in the prepping process (see Figure 7.1).

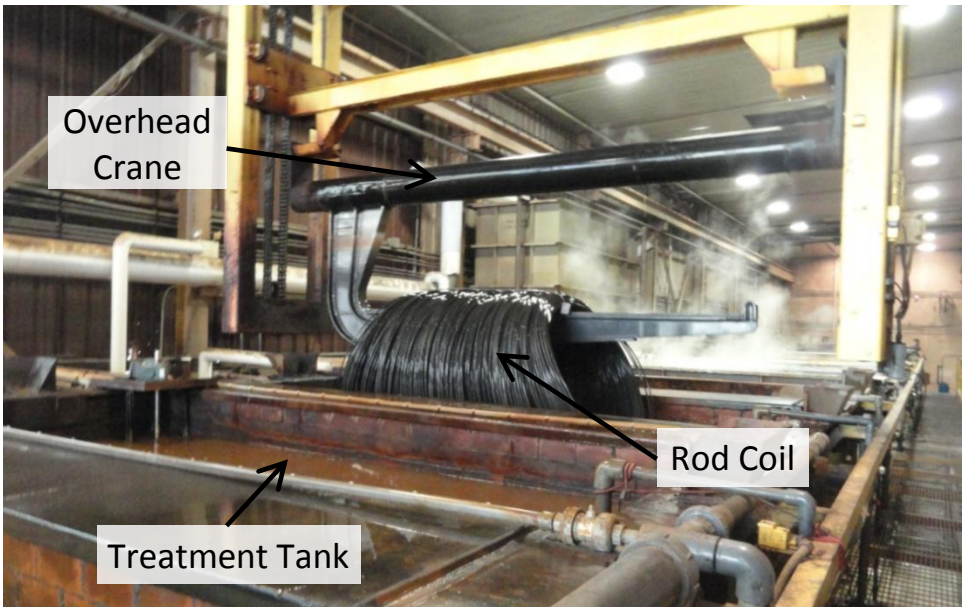

Figure 7.1 Prepping of High-C 1080 steel rod coil at RettCo Steel (Newnan, GA)

Once the rod coil has been fully prepped, it is drawn into wire of the proper diameter. The wire is fed into one end of a multi-block wire drawing machine (see Figure 7.2) wherein its cross section is reduced by pulling through a series of dies. Details on the wire drawing process are presented in Section 4.2.2. The diameter of the center wire of the strand is typically 5 % larger than the six outer wires so that the strand tightens onto itself when loaded in tension, ensuring that all wires in the strand act compositely (Osborn, et al., 2008). The drawn wire is collected on spools like those shown in Figure 7.3 which are specifically designed to be loaded into the equipment used for stranding.

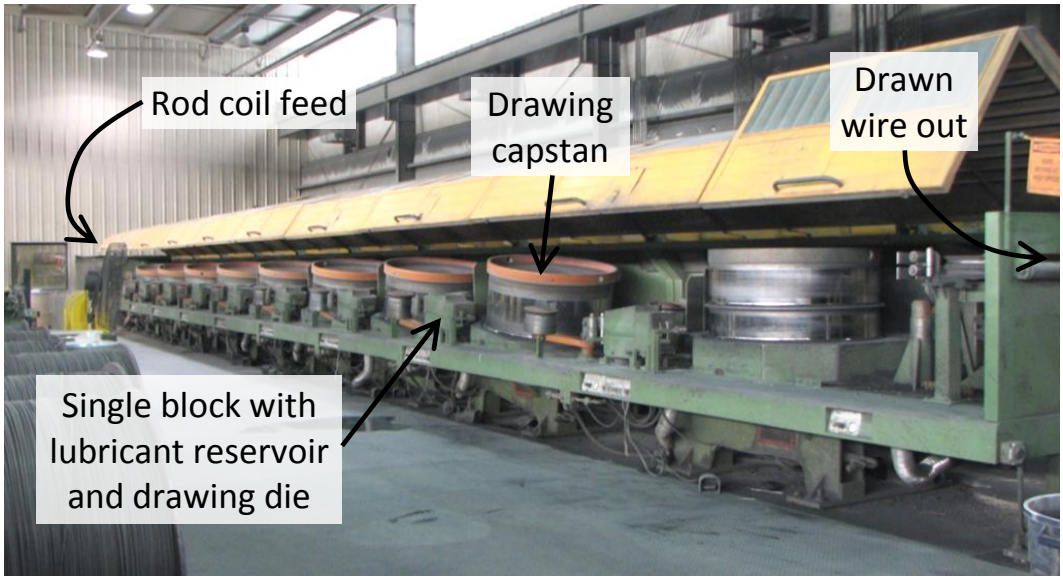

Figure 7.2 Wire drawing machine, Sumiden Wire Products Corp. (SWPC, Dickson, TN)

Figure 7.3 Cold drawn wire on spools specific to skip strander at SWPC

Spools loaded with wire are then loaded into a skip strander. Six spools are loaded to form the six outer wires of the strand and one spool is loaded to serve as the center "king" wire. Wire is fed off of all of the spools simultaneously to form the seven-wire strand. Wire from each spool is diverted around the subsequent spools using bows which have guides for the wires. As the wire is being payed off of the spools, the bows spin at a

rate that varies based on the production speed in order to form a seven-wire strand with the correct helical twist / pitch. Figure 7.4 shows one section of a typical skip strander.

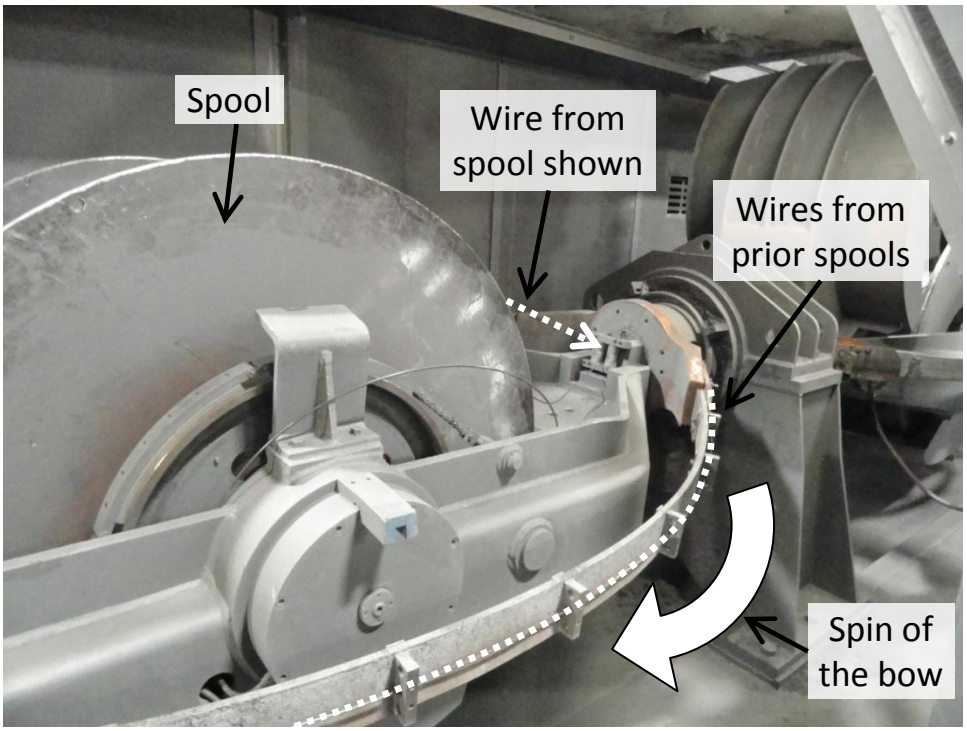

Figure 7.4 Typical configuration of bow strander at SWPC

The remaining portion of the strand production follows the process diagram shown in Figure 7.5 (all dimensions in mm). The following describes the process:

1. The seven-wire helically twisted strand is formed in the skip strander.
2. The strand is run through a pulling unit which provides the necessary pull force to pay wire off of the spools and form the strand. This pulling unit also provides the back tension necessary for the rest of the strand production process.
3. The strand is run through a pulley which reverses the working direction.

4. The strand is now in the reverse direction. This reversal of the working direction is done primarily to better utilize space. In addition, the large reverse pulleys provide precise control of the pull force in the strand.
5. A low-relaxation thermomechanical heat treatment is performed by passing the strand through a three-coil induction furnace under tension. The induction furnace is placed on tracks, allowing it to move with the strand during startups and shutdowns to ensure that the entire length of strand receives the same heat treatment. This heat treatment is performed to reduce stress relaxation and improve mechanical properties. In addition, the low-relaxation heat treatment causes the strand to creep into the helical geometry. Otherwise, it would just unravel when cut.
6. The strand is cooled and cleaned in a water quench tank followed by a drying unit.
7. The strand is run through another pulling unit which provides the pull force necessary for the low-relaxation heat treatment (40 % of the ultimate tensile strength). This pulling unit must also run at a higher speed to account for high-temperature creep which occurs during the low-relaxation heat treatment in the induction furnace.
8. The final strand is collected on two large spools at the end of the production process. One spool is used to collect strand which is being produced. While this occurs, strand is payed-off to smaller size 2900 kg (6400 lb) “packs” from the second, full spool (see Figure 7.6). This process allows for the uninterrupted production of A416 prestressing strand.

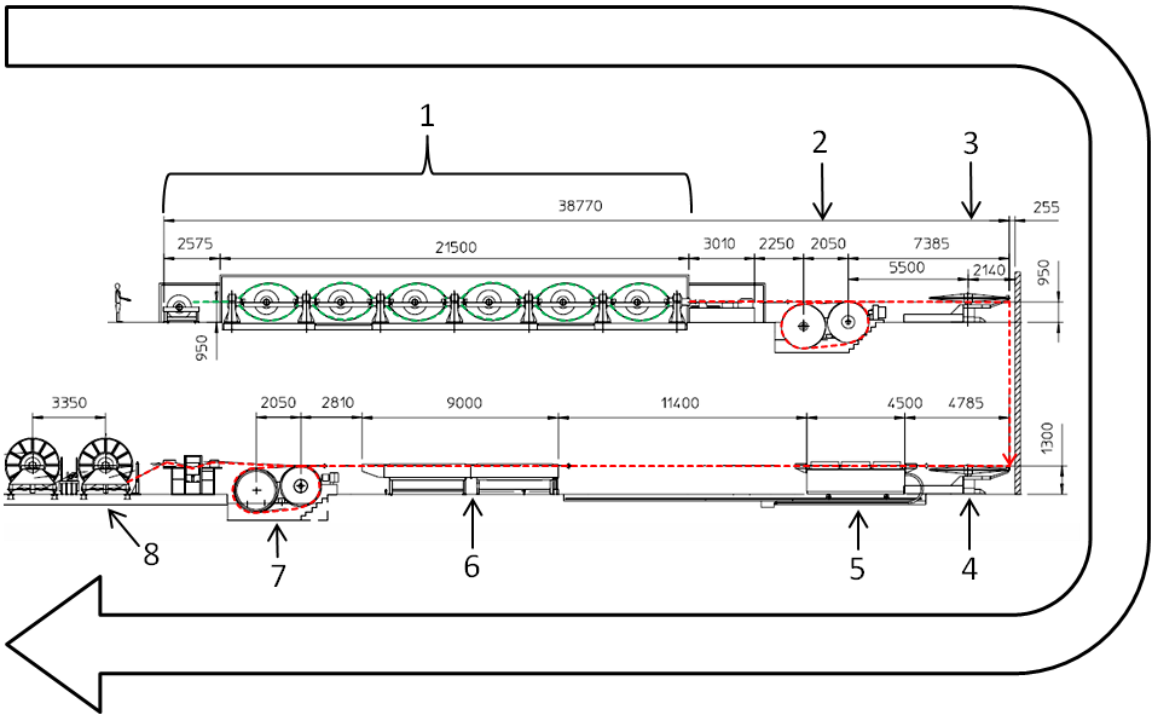

Figure 7.5 Production of A416 seven-wire prestressing strand. Green and red dashed lines indicate wire and strand position, respectively. (Adapted from (Artuso, et al., 2004b))

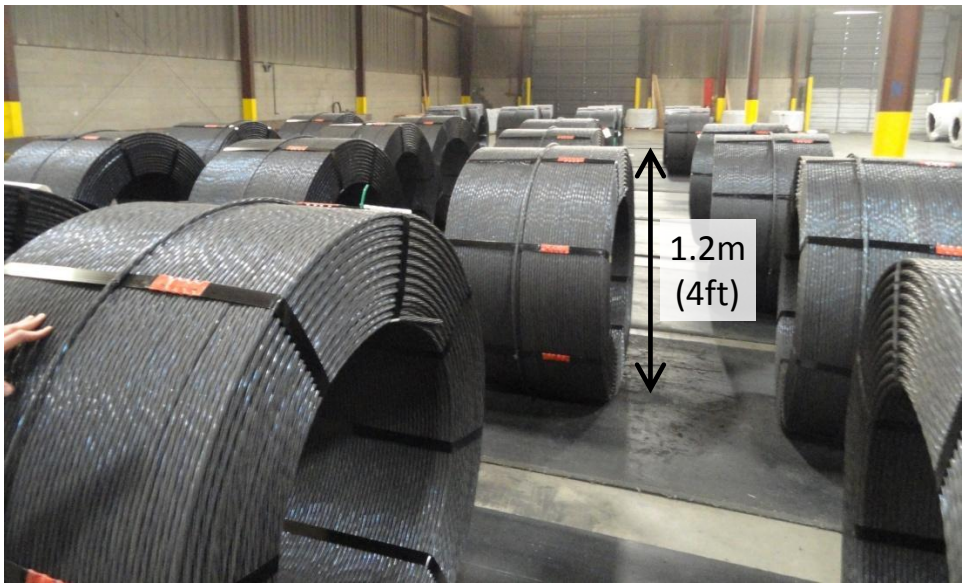

Figure 7.6 Packs of prestressing strand ready for shipment at RettCo Steel

7.1.1 Potential Challenges with High-Strength Stainless Steels

With an understanding of the techniques used to produce A416 prestressing strands, potential challenges which may arise when producing HSSS prestressing strands were identified. HSSS wire is produced by many manufacturers (primarily for spring wire) around the world in wire diameters similar to those used for prestressing strands; thus, there are no production concerns. The process of assembling the helical strand geometry using the skip strander should not change when using HSSS wire. The greatest challenge when switching the production of prestressing strand from High-C 1080 steel to HSSS is the low-relaxation thermomechanical heat treatment and, in particular, the inductive heating behavior of the HSSS wires. Producers of austenitic Nitronic® 33 (see Section 2.6.2), 304, and 316 HSSS prestressing strands have circumvented this challenge by using a preforming method to cause the strand to retain its helical geometry. This preforming method does not provide the improved mechanical properties which result from the low-relaxation process. The following sections provide an overview of the preforming and low-relaxation process.

7.1.1.1 The Preforming Process

Prior to the development of the low-relaxation process, all prestressing strands were produced using a preforming method. Preformed strand is produced by plastically deforming the six outer wires of the strand into a helix which is then wound around the center wire to form the strand (see preformed wire rope in Figure 7.7) (Anderson, 1964). Figure 7.8 shows a typical preforming head located at the end of a strander. The six outer wires of the strand are deformed by rollers on the preforming head. Once the wires have been deformed, they are run through a closure die that compacts the strand.

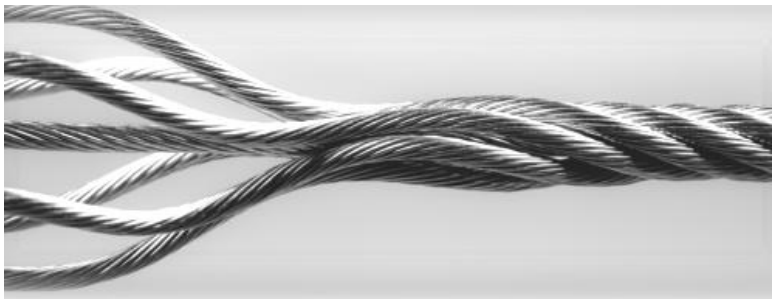

Figure 7.7 Strand produced using preforming method (from (Bragshaw, 2011))

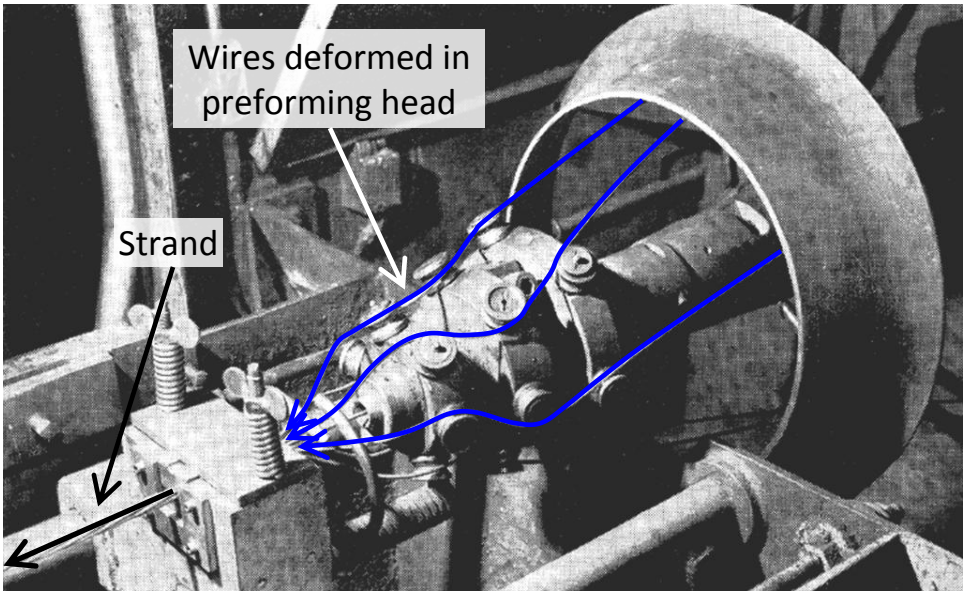

Figure 7.8 Typical preforming head (adapted from (Anderson, 1964))

While this method is effective in creating a seven-wire prestressing strand, preforming heads have largely been replaced in modern A416 prestressing strand production facilities which rely on the low-relaxation process to form the helical strand geometry. Because preforming is no longer used, development of a low-relaxation process is essential so that HSSS prestressing strands may be manufactured in modern production facilities. The low relaxation process should be optimized to reduce stress relaxation and improve mechanical properties of the HSSSs.

7.1.1.1 The Low-Relaxation Process

The low-relaxation thermomechanical heat treatment used for the production of A416 prestressing strands consists of heating the strands to 380 to 400 ˚C (716 to 752 ˚F) while the strand is stressed in tension at 40 % of the ultimate tensile strength (σ_{ult}) (ACI 222.2, 2001). This thermomechanical process reduces residual stresses and also accelerates dislocation creep during production, resulting in improved stress vs. strain linearity, increased yield strength, and reduced stress relaxation (Atienza and Elices, 2007). In addition to these benefits, the low-relaxation process also causes the strand to creep into the helical geometry such that when it is cut no unraveling occurs. Modern A416 prestressing strand production facilities utilize in-line induction furnaces to perform low-relaxation heat treatments as it provides a fast (production speeds as high as 420 m/min (1400 ft/min)), non-contact, and efficient means for heating of the strand (Artuso, et al., 2004b). Figure 7.9 shows a typical three-coil induction furnace used for performing low-relaxation heat treatments.

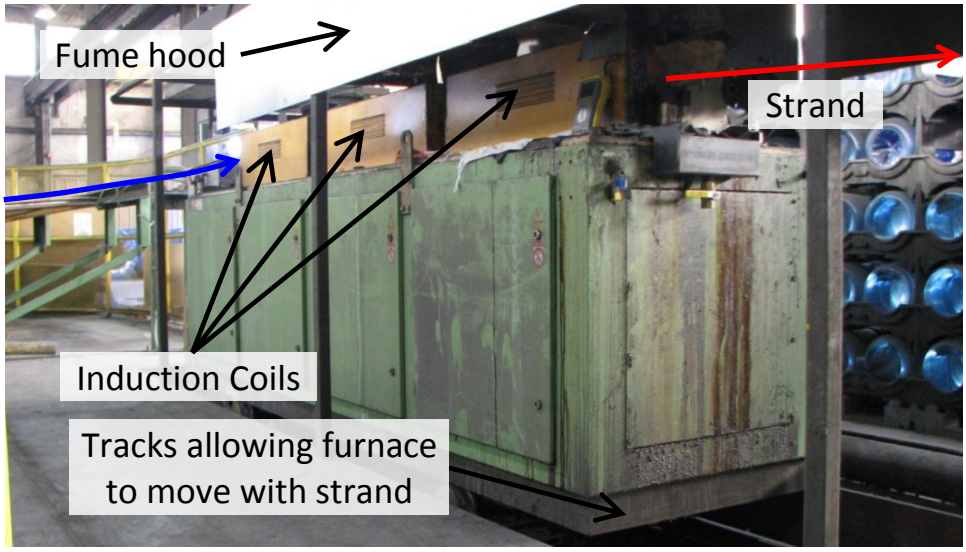

Figure 7.9 Three-coil induction furnace for low-relaxation heat treatment

Using these furnaces, inductive heating is accomplished by exploiting the electromagnetic properties (e.g., magnetic permeability and electrical resistivity) of the steel prestressing strand. Figure 7.10 shows the mechanism by which inductive heating occurs within an induction coil. An alternating current is applied to the coil which generates an alternating magnetic field. Inductive heating of material placed within the coil occurs through both Joule heating (i.e., resistance heating by eddy currents induced in the material by the alternating magnetic field) and hysteresis losses (i.e., internal frictional heating caused by electron spin flipping in the presence of an alternating magnetic field) (Rapoport and Pleshivtseva, 2006). The hysteresis loss mechanism can account for up to 40 % of heating at temperatures below the Curie point (the temperature at which a ferromagnetic material becomes nonmagnetic, approx. 700 to 800 ˚C (1290 to 1470 ˚F) in steels (Semiatin and Stutz, 1986)). As a result, ferromagnetic alloys can be heated more efficiently than paramagnetic alloys to temperatures below the Curie point.

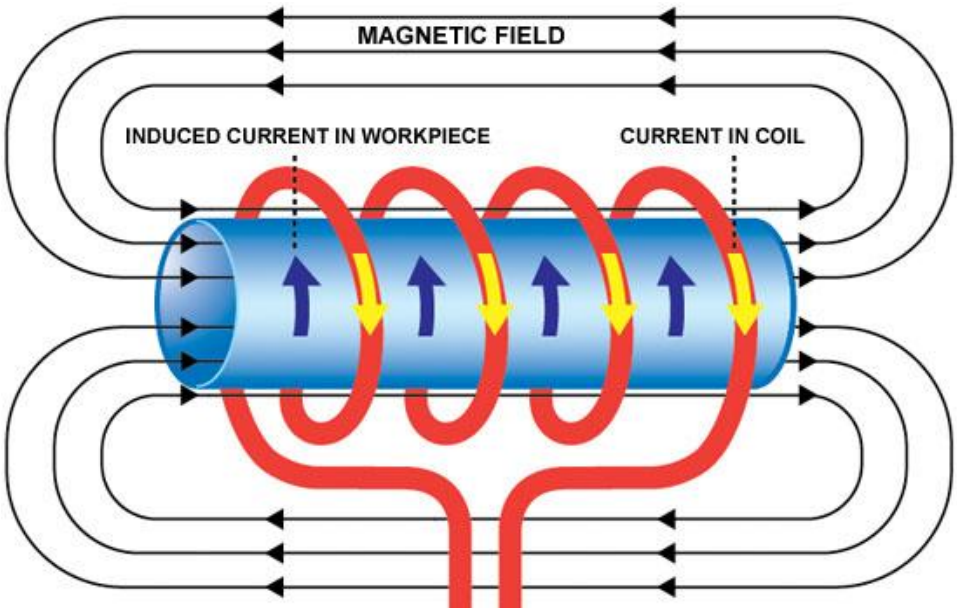

Figure 7.10 Mechanism of heating using an induction coil (from (Shah, 2011))

Due to their chemical composition and crystal structure, the electromagnetic properties of stainless steels differ significantly from those of carbon steels. Stainless steels exhibit electrical resistivities (ρ) of $7.3 \cdot 10^{-5}$ to $8 \cdot 10^{-5}$ $\Omega \cdot$cm (approximately 4.4 times greater than 1080 steel) (Outokumpu, 2010). Values of the relative magnetic permeability (μ_r) of stainless steel vary by crystal structure. Face centered cubic austenitic stainless steels in the annealed condition exhibit a μ_r of 1.0 (Artuso, et al., 2004b), indicating that they are fully paramagnetic. Body centered ferritic and martensitic stainless steels exhibit ferromagnetic behavior. Duplex stainless steels exhibit a composite ferromagnetic (from the ferrite phase) and paramagnetic (from the austenite phase) microstructure. Being ferritic, the 1080 prestressing steel is ferromagnetic with a μ_r of approximately 20 (Artuso, et al., 2004b). Deformation also influences magnetic properties, primarily due to the formation of ferromagnetic strain-induced α'-martensite in the austenite phase of austenitic (Wu and Nürnberger, 2009) and duplex stainless steels (Tavares, et al., 2006).

The effect of these changes in ρ and μ_r in stainless steels when compared with 1080 prestressing steel is shown in Equation 7.1, which should equal 2.5 to 4.5 in order for energy to be efficiently transferred from the induction coil to the strand (Artuso, et al., 2004a). In Equation 7.1, it is clear that as μ_r decreases and ρ increases, the only way to operate efficiently is to use a higher operating frequency, f. In order to conduct low-relaxation heat treatments on paramagnetic or semi-ferromagnetic austenitic HSSSs at similar efficiencies as A416 prestressing strand, excitation frequencies in excess of 150 kHz are necessary (Artuso, et al., 2004b).

$$\frac{D\sqrt{\pi \cdot f \cdot \mu_r \cdot \mu_o}}{\sqrt{2 \cdot \rho}} = 2.5 \; to \; 4.5 \qquad (7.1)$$

Where:
D = wire diameter
f = frequency of induction coil
μ_o = magnetic permeability of free space = $4\pi \cdot 10^{-7}$ N/A^2

Induction furnaces typically used for the production A416 prestressing strand operate on solid state power supplies which cannot vary frequency depending on the alloy being produced; most furnaces operate at approximately 5 kHz. Because of this fixed operating frequency, low-relaxation heat treatments have not been applied to HSSS prestressing strands which, as discussed above, have been produced with austenitic grades using preforming methods.

Optimal HSSSs 2205 and 2304 identified in the present study exhibit ferromagnetic behavior due to the presence of the ferrite phase in the duplex microstructure. Previous studies have shown that 2205 wire can have μ_r as high as 60 in the annealed condition (Sandvik, 2008). When cold drawing is performed to achieve similar strengths as those investigated herein (1300 MPa (188 ksi)), μ_r can increase to as high as 120 (Sandvik, 2008). According to Equation 7.1, this increase in μ_r (in the numerator) nearly equals the increase in ρ, indicating that optimal HSSSs can likely be heated efficiently without changing the operating frequency. However, no previous research has investigated the actual induction heating behavior of duplex HSSSs. Section 7.2 presents the results of a study which investigated the induction heating behavior of 2205 and 2304 HSSSs at temperatures necessary for low-relaxation thermomechanical heat treatments.

7.2 Induction Heating Behavior of 2205 and 2304 High-Strength Stainless Steels

In order to develop a low-relaxation process which can be applied to optimal HSSSs 2205 and 2304, it was necessary to determine their induction heating behavior. A series of trials were conducted with an induction furnace used for low-relaxation heat treatments at the A416 prestressing strand production facility of SWPC in Dickson, TN. All trials were performed during a routine plant maintenance shutdown.

7.2.1 Experimental Methods

HSSS prestressing strands were simulated with two 1.8 m (6 ft) long, seven-wire bundles which were produced with 2205 and 2304 wires. The resulting seven-wire bundles were similar in geometry to a 12.7 mm (0.5 in) prestressing strand. In the coiled form, both 2205 and 2304 wire exhibited residual curvature which had to be removed in order for a straight seven-wire bundle to be produced. Wires were straightened by light peening with a hammer. A 2205 HSSS wire before and after straightening is shown in Figure 7.11.

Once the wire had been straightened, seven-wire bundles were produced. The wires were secured together using hose clamps of 316 stainless steel which is less susceptible to inductive heating than duplex grades 2205 and 2304. Two Type-K thermocouples capable of measuring temperatures of up to 500 ˚C (932 ˚F) were embedded near the mid-length of each wire bundle prior to tightening of the hose clamps. A completed simulated HSSS prestressing strand is shown in Figure 7.12.

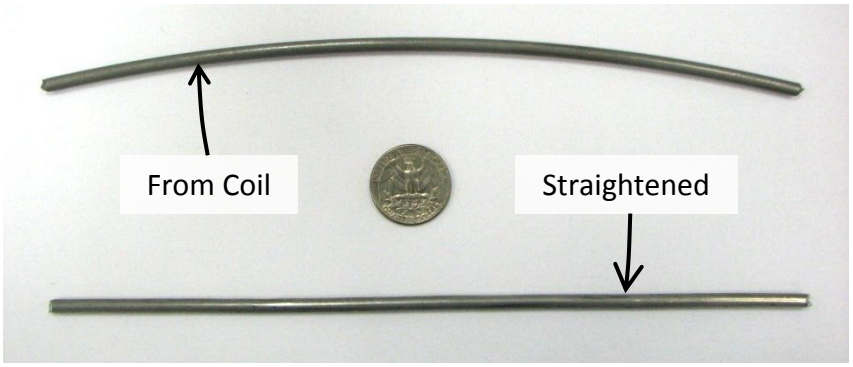

Figure 7.11 Stainless steel wire before and after straightening

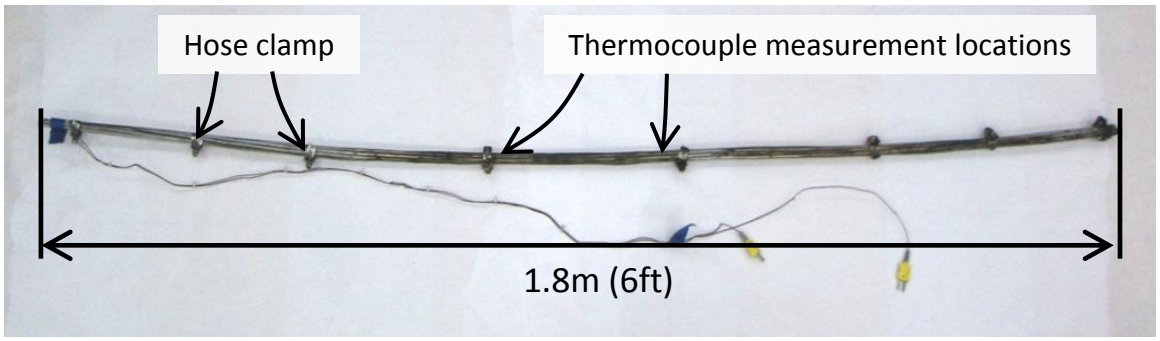

Figure 7.12 Simulated HSSS prestressing strand segment with embedded thermocouples

The induction furnace used for all trials was manufactured by Applicazioni Termo Elettroniche (ATE) with a maximum power supply of up to 450 kW while operating at a constant frequency of 5.5 kHz. This type of furnace is typical for A416 prestressing strand production facilities. The furnace consists of three in-line induction heating coils embedded in a protective ceramic tube which operate under the same power and frequency settings. In order to conserve material, only one of the three induction coils was used in the trial. The stainless strand was placed in the coil and connected to a thermocouple reader which could be monitored at the furnace control station. The experimental setup used is shown in detail in Figure 7.13.

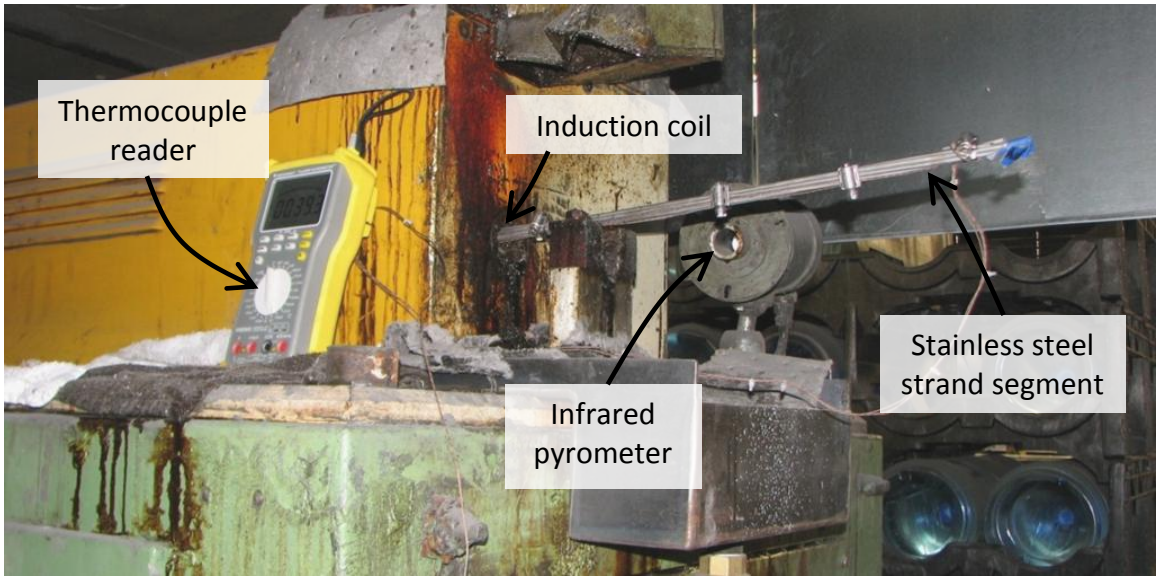

Figure 7.13 Experimental setup to evaluate response of HSSS strand to inductive heating

Using a manual control override, the power level of the induction furnace was increased incrementally with the HSSS prestressing strand placed in last induction coil. While the original intent was to use predefined power levels (e.g., 5 kW, 10 kW, and so on), this was difficult to achieve in practice. As a result, the power was slightly increased manually for each test and the actual power supplied to the strand was recorded from the furnace control readout. For each power level, the time was measured between when the furnace turned on and when the strand reached a temperature of 400 ˚C (752 ˚F), after which the furnace was turned off. Based on the geometry of the furnace (total induction coil length of 3.3 m (10.8 ft)) the time to reach 400 ˚C (752 ˚F) was then converted into an equivalent production speed. The temperature versus time following heating to 400 ˚C (752 ˚F) was also measured to determine the expected reduction in temperature between the induction furnace and quench tank (a distance of 12.1 m (40 ft)).

7.2.2 Results and Discussion

Figure 7.14 depicts the power level versus time to reach a temperature of 400 ˚C (752 ˚F) for both 2205 and 2304 HSSS prestressing strands. The inductive heating behavior of 2205 and 2304 was found to be similar. At power levels below 20 kW, reductions in heating time had an approximately 1:1 correlation with increases in power (e.g., if power was doubled, the heating time was cut in half). However, at power levels above 20 kW, there seemed to be a diminishing effect on reductions in heating time. While this may be due to decreased induction heating efficiency, it is also likely that the startup time of the furnace (i.e., time to reach operating power level) and response time of the thermocouples may have also influenced measurements at high power levels where heating times were less than 10 s. Therefore, the true time required to reach 400 ˚C (752 ˚F) at high power levels likely is less than that which was measured.

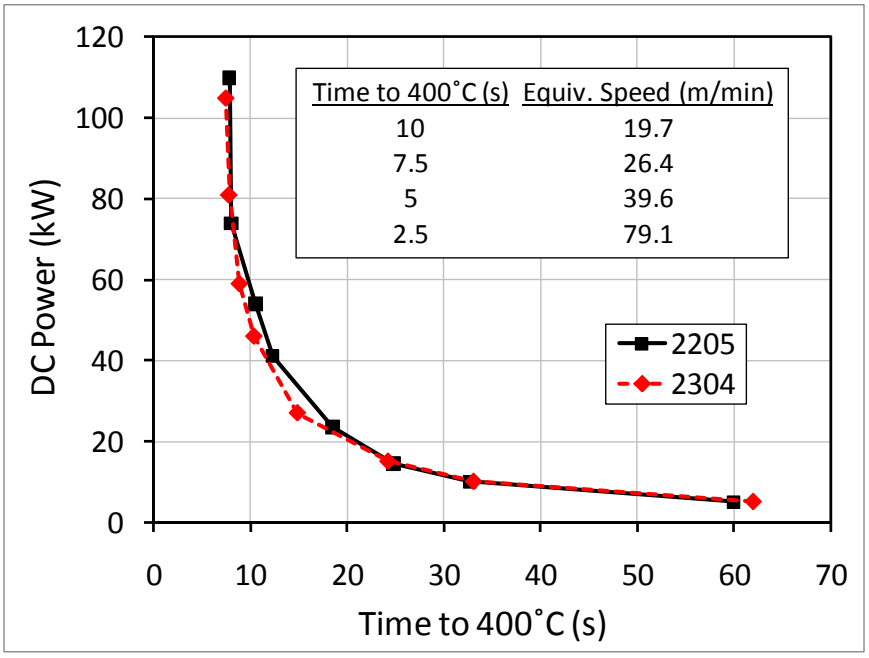

Figure 7.14 Induction furnace power level vs. time to reach 400 ˚C (752 ˚F)

Figure 7.15 shows the temperature of the 2205 and 2304 HSSS prestressing strands after heating to 400 ˚C (752 ˚F) and shutting off the furnace. Both 2205 and 2304 were found to cool in air at a rate of approximately 1 ˚C/s (1.8 ˚F/s) following heating to 400 ˚C (752 ˚F).

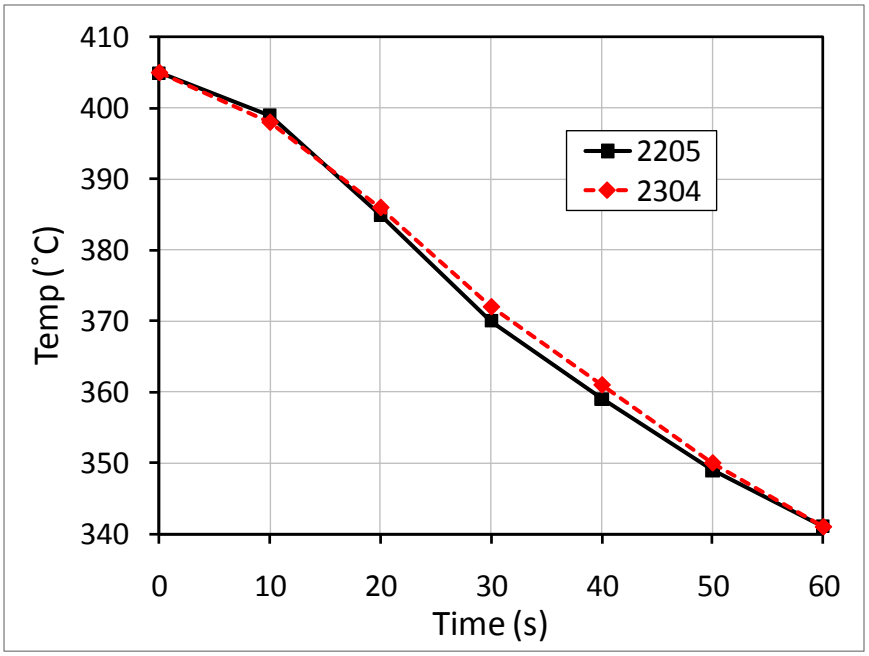

Figure 7.15 Cooling of 2205 and 2304 in air following heating to 400 ˚C (752 ˚F)

7.2.3 Conclusions

The HSSS prestressing strands produced using duplex grades 2205 and 2304 were found to heat effectively using the induction method. Furthermore, both 2205 and 2304 were found to exhibit similar heating and cooling trends. At a trial prestressing strand production speed of 30 m/min (99 ft/min), power levels of approximately 100 kW would be necessary in order to heat 12.7 mm (0.5 in) diameter 2205 and 2304 seven-wire prestressing strand to 400 ˚C (752 ˚F) during the 6.6 s it resides in the furnace. At a

production speed of 30 m/min (100 ft/min), the strand will cool to approximately 380 ˚C (716 ˚F) in the 24.2 s prior to quenching in water. Based on these trials, it is likely that a low-relaxation thermomechanical heat treatment can be developed and applied to duplex grade 2205 and 2304 HSSS prestressing strands manufactured at existing A416 prestressing strand production facilities.

7.3 Low-Relaxation Heat Treatment of 2205 and 2304 High-Strength Stainless Steels

With the feasibility of a low-relaxation heat treatment for optimal HSSSs verified, a series of exploratory experiments were conducted to evaluate the effect of such a heat treatment on mechanical properties and stress relaxation.

7.3.1 Experimental Methods

Wire segments were heated using a heat gun capable of reaching temperatures of 650 ˚C (1200 ˚F). The heat gun was fitted with a T-shaped nozzle made out of 2.54 cm (1 in) steel pipe fittings (see Figure 7.16). The T-shaped nozzle created a 25 cm (10 in) long heating zone which could be placed around the wire segment. Figure 7.17 shows the temperature increase with time of HSSS wire segments placed in the heating zone of the nozzle. Temperatures within the nozzle were less than typical for low-relaxation heat treatments and began to plateau at approximately 325 ˚C (617 ˚F), indicating significant heat loss between the heat gun and the heating zone of the nozzle. In addition, the rate of heating using the heat gun was also reduced when compared with the induction furnace which causes heating of the entire cross section rather than just the surface.

Figure 7.16 Heat gun with T-shaped nozzle attachment

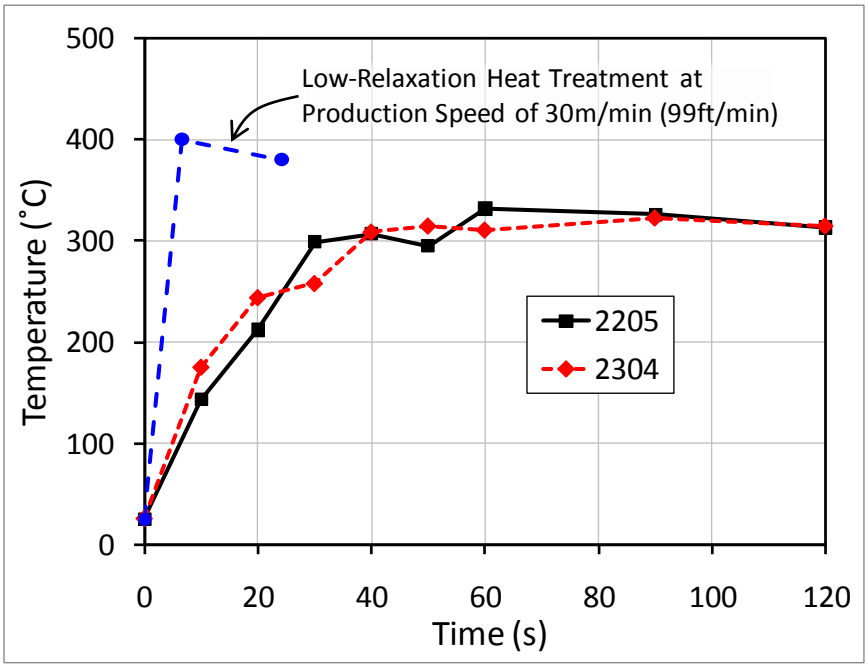

Figure 7.17 Temperature vs. time within 25 cm (10 in) nozzle

Segments of 2205 and 2304 HSSS wire were cut to a length of 90 cm (36 in). The cut segments were inserted through the heating nozzle and secured in universal testing

frame as discussed in Section 5.1.1. Approximately 15 cm (6 in) of the wire length was located within the wedge grip, resulting in a gage length between grips of 75 cm (30 in). This gage length allowed for three 25 cm (10 in) heating zones. Each of the 25 cm (10 in) heating zones was held within the nozzle for 60 s, allowing it to reach the maximum temperature of 325 ˚C (617 ˚F) for approximately 30 s. During the heat treatment, the testing frame was programmed to maintain a constant load in the wire segment of 40 % of σ_{ult} (to simulate a low-relaxation process) to account for thermal expansion and creep effects. Once the entire wire segment had been treated, is was quenched using an H_2O soaked cloth until a temperature less than 50 ˚C (122 ˚F) was achieved, after which it was unloaded and removed from the testing frame. Two segments were cut from the heat treated 75 cm (30 in) gage length. A 25 cm (10 in) long segment was used to perform a tensile test (see techniques in Section 5.1.1) and the remaining 50 cm (20 in) long segment was used to perform a 120 min stress relaxation experiment.

7.3.2 Results and Discussion

Figure 7.18 shows the stress vs. strain curves of 2205 and 2304 HSSS wires which have and have not received the simulated low-relaxation heat treatment described above. The heat treatment resulted in an increase in σ_{ult} of approximately 100 MPa (14.5 ksi) in 2205 and 2304 HSSSs. In addition, the stress vs. strain linearity was improved below yield. Both of these results likely correspond to a reduction in residual stresses following the thermomechanical heat treatment (Elices, 2004). One unfavorable outcome of the heat treatment was a reduction in ultimate strain (ϵ_{ult}). Reductions in ϵ_{ult} may be attributed to the decrease in compressive residual stresses in the center of the wire which would normally have to be overcome prior to failure.

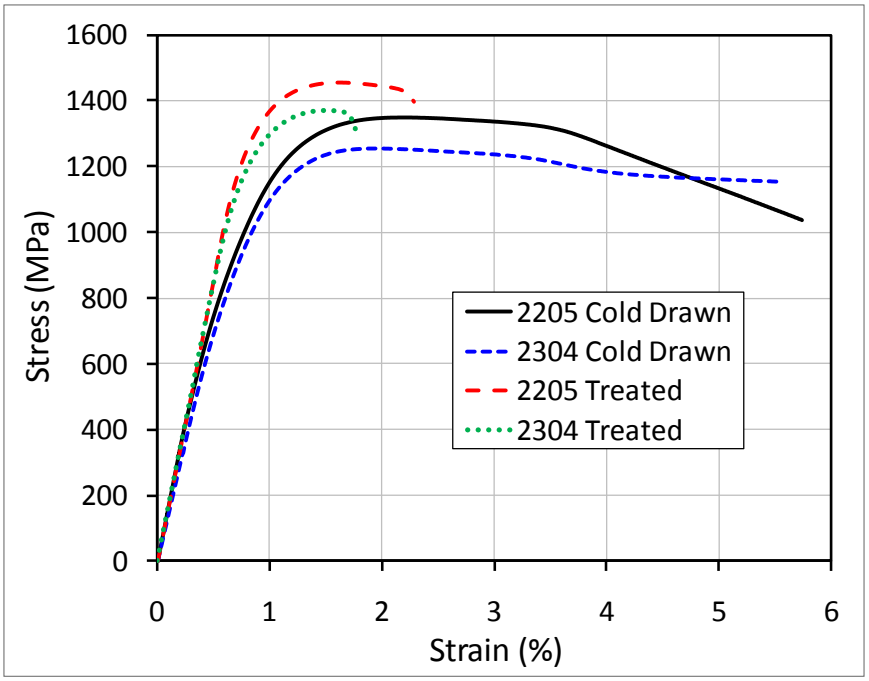

Figure 7.18 Stress vs. strain curves of cold drawn and heat treated 2205 and 2304 HSSSs

Figure 7.19 shows the stress relaxation with time of 2205 and 2304 HSSS wires which have and have not received the simulated low-relaxation heat treatment. Stress relaxation trends were similar to the long-term stress relaxation tests on cold drawn 2205 and 2304 HSSSs presented in Section 5.3.2. The simulated low-relaxation heat treatment resulted in a 79 % decrease in stress relaxation from 2.8 % in the cold drawn condition to 0.6 % in the heat treated condition. These results further indicate that the heat treatment reduced residual stresses and accelerate the creep of highly mobile dislocations (see Section 5.3.2 for discussion of stress relaxation mechanism). Interestingly, in 2205 and 2304 heat treated samples, the relaxation behavior deviates from typical logarithmic creep at approximately 40 min. It is unlikely that this deviation derives from error in the experimental setup or changes in ambient temperature as both tests were conducted at different times. Also, no such deviation was observed in cold drawn HSSSs tested using

the same method. Additional stress relaxation tests are recommended to determine the origin of this deviation in heat treated HSSSs.

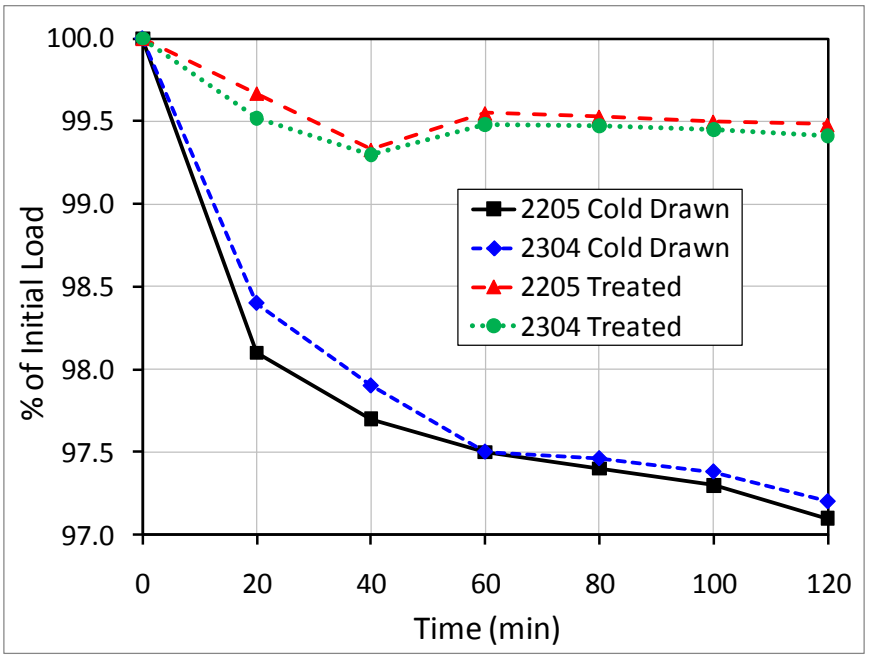

Figure 7.19 Stress relaxation of cold drawn and heat treated 2205 and 2304 HSSSs

Nonetheless, the application of a simulated low-relaxation heat treatment did result in an improvement in mechanical properties and reduction of stress relaxation. These results further support the development of low-relaxation heat treatments which can be utilized in the production of HSSS prestressing strands. In addition, benefits of the low-relaxation heat treatment presented above derive from a simulated heat treatment which was performed at a temperature of 325 ˚C (617 ˚F). Knowing that creep rates are exponentially related to temperature (Ashby and Jones, 1998), it is likely that low-relaxation heat treatments conducted at 400 ˚C (752 ˚F) using an induction furnace would further reduce stress relaxation and improve mechanical properties.

CHAPTER 8

CONCLUSIONS, RECOMMENDATIONS, AND FUTURE RESEARCH

8.1 Conclusions

The primary goal of this research was to develop corrosion mitigation techniques for implementation in coastal prestressed concrete (PSC) bridge substructures. Based on the literature review presented in Chapter 2, two primary deficiencies in knowledge were identified: (1) an understanding of the fundamental mechanisms of corrosion initiation and propagation in prestressing reinforcements and (2) the mitigation of such corrosion using high-strength stainless steels (HSSS). In order to address these deficiencies, an experimental study was conducted which investigated both high-C 1080 prestressing steels (used in A416 prestressing strand) and a variety of candidate HSSS alloys. The study consisted primarily of electrochemical corrosion testing, mechanical testing, and microstructural characterization. The following sections present key conclusions of each portion of the experimental study.

8.1.1 Corrosion Behavior of A416 Prestressing Strands and Influence of Stranding

The influence of crevices present in stranded geometries and as-received surface coatings on the corrosion resistance of prestressing steels was evaluated using cyclic potentiodynamic polarization (CPP) techniques. Prestressing wire and strand specimens were exposed to a simulated concrete pore solution with Cl^- added as NaCl up to 1.0 M.

1. Specimen geometries and experimental techniques were developed which were useful for evaluating the corrosion resistance of 1080 steels used for the production of A416 prestressing strands. These specimen geometries and experimental techniques were subsequently used for evaluating the corrosion resistance of HSSSs being investigated for applications in PSC.
2. The presence of crevices in the prestressing strand geometry significantly influenced corrosion resistance. Corrosion initiation in strand specimens began at a Cl^- concentration 67 % less than that which resulted in corrosion initiation in wire specimens. Once above a Cl^- concentration at which corrosion initiated, repassivation did not occur. These results support the reduction of the chloride threshold level (CTL) for PSC present in most building codes.
3. Corrosion initiation in prestressing wires occurred primarily at imperfections in the as-received $ZnPO_4$ coated steel surface. These imperfections may result from wearing of the die during wire drawing and fretting between wires in the strand.
4. Corrosion initiation in prestressing strands was found to occur initially in crevices located at the impingement sites between adjacent wires.
5. The morphology of corrosion propagation following initiation was observed to be similar in both wires and strands, transitioning from localized corrosion into more uniform surface attack.
6. Additional CPP corrosion initiation experiments indicated that imperfections in the as-received $ZnPO_4$ surface coating provide preferential sites for localized corrosion to initiate. These effects would not be detected by experiments conducted on polished prestressing steel specimens.

7. Based on the results of CPP studies and characterization of corrosion damaged specimens, a hypothetical model was developed to describe the mechanisms of corrosion initiation in prestressing strands. Traditional crevice corrosion mechanisms likely interact with surface imperfections and result in the significant reduction in corrosion resistance found for prestressing strand specimens.
8. Analytical studies that the reduced corrosion resistance of prestressing strands resulted in a decrease in the time-to-corrosion initiation of 34 % when compared with wires. In order to accurately predict the field performance of PSC structures exposed to corrosive environments, service life models must take into account the influence stranding on reductions in the CTL.

8.1.2 Candidate Stainless Steels for Prestressing Strand

Six stainless steel alloys were selected for experimental investigation based on their mechanical properties, corrosion resistance, cost, and availability; austenitic grades 304 and 316; duplex grades 2101, 2205, and 2304; and precipitation hardened martensitic grade 17-7 were identified as candidate HSSSs for the investigation. All candidate HSSS wires exhibited a heterogeneous and deformed as-received surface. The morphology of the wire surface differed depending on manufacturer. In many cases, residual drawing lubricants were also present on the surface of the wires. Corrosion experiments were conducted on the as-delivered wires.

1. With the exception of 316, all candidate HSSSs were effectively cold drawn to achieve a target ultimate tensile strength (σ_{ult}) of 1500 MPa (217 ksi) in wire diameters similar to the 4.2 mm (0.17 in) diameter used for 12.7 mm (0.5 in)

prestressing strand. Due to limited work hardening by the formation of strain-induced α′-martensite, 316 HSSS required additional drawing to achieve the desired σ_{ult}.

2. All six candidate HSSSs exhibited a highly oriented microstructure with elongated grains preferentially aligned with the longitudinal drawing direction.
3. Austenitic grades 304 and 316 were found to have significant inclusions of α′-martensite. The presence of α′-martensite was also verified using X-ray diffraction (XRD) techniques. These deformation phases are known to degrade resistance to Cl^- induced corrosion and stress corrosion cracking. In 316 HSSS specimens, distributed precipitates were observed in etched microstructures. Based on measured bulk chemical composition, the precipitates were likely S-containing. The presence of such precipitates may further degrade the corrosion resistance of 316 HSSS.
4. XRD patterns obtained from duplex HSSSs indicated the presence of α′-martensite. In addition, precipitates were observed at austenite/ferrite phase boundaries in 2101 and 2304 lean duplex HSSSs. Like 316, the presence of these precipitiates, along with α′-martensite, likely leads to decreased corrosion resistance. Few precipitates were found in 2205.
5. Distributed Al-based precipitates were observed in the martensitic 17-7 HSSS specimens resulting from the precipitation hardening heat treatment.

8.1.3 Mechanical Properties of High-Strength Stainless Steels

Experimental studies were performed to evaluate the stress vs. strain behavior and stress relaxation of the six candidate HSSSs and of the 1080 prestressing steel control. A series of experiments were also conducted to compare the stress vs. strain behavior of 1080 prestressing steel wires with that of A416 prestressing strands.

1. Tensile strengths of 1250 to 1550 MPa (181 to 225 ksi) were achieved in the six candidate HSSSs. Even though microstructural ductile fracture was observed, non-ductile behavior was evident in the stress vs. strain curves which exhibited no strain hardening.
2. All candidate HSSS failures occurred by immediate strain localization (i.e., necking) following yielding. This behavior suggested that as the length of the specimen increases, the ultimate strain (ϵ_{ult}) likely approaches the strain corresponding to σ_{ult}. This hypothesis was confirmed through additional tensile tests performed with various gage lengths. As a result, any measure of ductility in HSSSs should be based on the strain at σ_{ult}. Furthermore, the non-ductile behavior of HSSSs when compared with A416 prestressing strands will likely require the development of reduced resistance factors and/or allowable stresses for use in structural design.
3. Nonlinear stress vs. strain behavior observed below yield was indicative of significant residual stresses due to cold drawing. These residual stresses could likely be lessened with the application of a low-relaxation thermomechanical heat treatment similar to that used for A416 prestressing strands.
4. The stress relaxation observed in candidate HSSSs and the 1080 prestressing steel followed classic logarithmic viscoelastic creep / stress relaxation models.
5. The stress relaxation of candidate HSSSs was 3 to 4 times that of the 1080 prestressing steel which had undergone a low-relaxation heat treatment. The presence of residual stresses along with highly mobile dislocations likely contributed to the high stress relaxation of candidate HSSSs.

8.1.4 Corrosion Behavior of High-Strength Stainless Steels

The corrosion resistance of the six candidate HSSSs was evaluated using CPP techniques in solutions simulating alkaline and carbonated concrete with the addition of Cl^- as NaCl. From these studies, two "optimal" HSSSs were identified: duplex grades 2205 and 2304. Additional studies were performed on these to determine the influence of stranding on corrosion resistance and susceptibility to brittle fracture by stress corrosion cracking (SCC) and hydrogen embrittlement (HE).

1. In alkaline solutions, all candidate HSSSs were found to exhibit acceptable corrosion resistance at Cl^- concentrations of zero 0.25 M. As Cl^- concentrations increased to 0.5 M, only 2205 and 2304 exhibited low corrosion susceptibility. Grade 2205 was still resistant to corrosion at 1.0 M Cl^-.
2. In carbonated solutions, corrosion resistance was reduced in all but the 2205 HSSS tested. Grades 2205 and 2304 exhibited low and moderate corrosion susceptibility at 0.5 M Cl^-, respectively. Again, the 2205 HSSS cold drawn wire exhibited superior corrosion resistance.
3. Corrosion initiation in all candidate HSSSs occurred exclusively above the Cr_2O_3 oxidation potential of 200 mV_{SCE} in alkaline solutions and above 400 mV_{SCE} in carbonated solutions, indicating that the passive film must be destabilized for metastable pitting to transform into stable pit propagation.
4. The corrosion resistance of 316 HSSS cold drawn wire was found to be less than its austenitic counterpart 304. This result was not anticipated given the typically higher pitting resistance of 316 bar and plate stock. The poor corrosion resistance of 316 can be attributed to the presence of S-bearing precipitates along with ά-martensite.

5. Corrosion damage in austenitic and martensitic HSSSs was similar, with large pits distributed across the wire surface. A lacy pitting mechanism was identified around the rim of the pit which may be caused by the aggressive nature of the CPP technique used. Similar to reports by other researchers, preferential attack of heavily slip banded austenite and α′-martensite was observed in austenitic HSSSs.
6. Selective dissolution of ferrite in pits was observed in duplex HSSSs 2101 and 2304. Similar damage has been reported by other researchers and indicates that the enrichment of Ni and N in the austenite phase enhance its corrosion resistance in alkaline and carbonated solutions. This hypothesis supports the increased corrosion resistance of 2205 that contains Mo which will partition to the ferrite phase.
7. Based on the results of all CPP experiments conducted, 2205 and 2304 showed the most promise as corrosion-resistant prestressing reinforcement and, thus, were identified as optimal HSSSs for further investigation.
8. Stranding reduced the corrosion resistance of 2304 specimens due to crevice corrosion. Grade 2205 strand specimens were still fully resistant to corrosion at Cl^- concentrations up to 1.0 M in alkaline and carbonated solutions. It is hypothesized that the superior corrosion resistance of 2205 derives from its 3.2 % Mo content which contributes to its corrosion resistance in the acidic conditions that develop within the crevice region of the strand during corrosion propagation.
9. Slow strain rate testing (SSRT) of 2205 and 2304 HSSSs showed no damage by SCC at Cl^- concentrations of 0.5 M in alkaline and carbonated solutions.
10. Damage by HE was observed in 2205 and 2304 SSRTs. HE cracking was isolated to the necked region of SSRT specimens. Examination of the fracture surface showed

that brittle fracture by HE had only occurred in the surface of the specimen, with the rest of the fracture being ductile. If the entire sample was to become saturated with hydrogen due to long periods of cathodic overprotection, brittle fracture of the entire cross section would occur.

8.1.5 Development of High-Strength Stainless Steel Prestressing Strand

The greatest challenge when producing HSSS prestressing strand was identified as the low-relaxation induction heat treatment. Austenitic HSSS prestressing strands which do not efficiently heat using induction methods have instead been produced using a preforming method. However, preforming equipment is not present in most modern A416 prestressing strand production facilities. This makes ferromagnetic materials like the optimal HSSSs 2205 and 2304 identified in the present study a much more viable option for production as prestressing strand using modern low-relaxation heat treatments. In order to investigate the feasibility of performing low-relaxation heat treatments on HSSS prestressing strands, a series of trials were conducted at an A416 prestressing strand production facility to determine the induction heating behavior of simulated 2205 and 2304 prestressing strands. In addition, the effects of a simulated low-relaxation heat treatment on stress vs. strain behavior and stress relaxation were studied.

1. Both 2205 and 2304 HSSSs heated effectively using induction methods, and they showed similar heating and cooling trends.
2. At DC power levels above 20 kW, nonlinearity in the induction heating trends was observed. This nonlinearity may be due to losses in the induction coil itself and possibly to delays in thermocouple temperature measurement.

3. Due to the slow reaction time of the thermocouples used, the results obtained from the induction heating trials are best applied to production speeds less than 30 m/min (99 ft/min). Additional studies will be necessary to develop induction heating parameters which are valid at higher production speeds.
4. The simulated low-relaxation heat treatment increased σ_{ult} by approximately 100 MPa (14.6 ksi) in 2205 and 2304 HSSSs. In addition, stress vs. strain linearity was improved below yield. Both results suggest a reduction in residual stresses.
5. The simulated low-relaxation heat treatment reduced the stress relaxation of 2205 and 2304 HSSSs by 79 %, indicating a reduction in residual stresses and highly mobile dislocations.

8.1.6 Overarching Conclusions

High-strength stainless steels, especially duplex grades 2205 and 2304, show excellent promise to mitigate corrosion if utilized as prestressing reinforcement in PSC bridge substructures (e.g., precast PSC piling) exposed to severe marine environments. In addition, the full-scale production of 2205 and 2304 prestressing strands using existing A416 prestressing strand production facilities is feasible.

8.2 Recommendations

8.2.1 Production of High-Strength Stainless Steel Prestressing Strand

From previous experience, the tensile strength of 2205 and 2304 rod coil can be increased to 1600 MPa (232 ksi) by cold drawing to an area reduction of approximately 80 % (see Figure 4.1). This 80 % area reduction will require rod coil diameters of 9 to 10

mm (0.35 to 0.39 in) in order to achieve maximum tensile strength in wire sizes commonly used for the production of prestressing strands. Significant additional research (i.e., mechanical and corrosion testing) will be necessary if even higher tensile strengths are desired.

Studies presented in Chapter 7 have shown that low-relaxation heat treatments are a viable option which should be applied for the production of HSSS prestressing strand using duplex grades 2205 and 2304. This heat treatment may result in an additional 100 MPa (14.5 ksi) tensile strength and reduced stress relaxation, both of which are economically beneficial from a raw materials cost standpoint. At a production speed of 30 m/min (99 ft/min), the induction furnace should be operated at a DC power level of 100 kW to reach a temperature of 400 ˚C (752 ˚F) during the 6.6 s residence time of the strand in the induction furnace. These induction heating parameters are specific to the alloys investigated and the operating frequency of the induction furnace used during the trials (5.5 kHz). Additional research will be required to develop and optimize techniques for producing HSSS prestressing strands at higher speeds.

8.2.2 Implementation of High-Strength Stainless Steel Prestressing Strand

Based on the results of the present study, duplex grades 2205 and 2304 displayed the most promise as corrosion-resistant prestressing reinforcement. Grade 2205 should be used in cases where exposure conditions are more severe and extended service lives are desired, such as high priority bridges exposed to seawater. This increased corrosion resistance comes with increased cost (January 2011 pricing of 2.91 $/lb for 2205 vs. 2.06 $/lb for 2304). In many cases, the increased cost of using stainless reinforcing steels can be decreased by specifying its use only in critical regions of a structure. For example, in

an elevated bridge structure along the Georgia coast, the bridge superstructure will likely see negligible exposure to Cl^- when compared with the substructure which is in direct contact with brackish and/or sea water. Therefore, stainless steel reinforcement may only be necessary in substructure elements like precast PSC piles, pile caps, and piers.

If the decision is made that stainless steel reinforcing is to be used in a reinforced or prestressed concrete element, all of the reinforcing steel in the critical region of the structure (e.g., prestressing strands, ties, and stirrups) should be stainless steel as it will all be exposed to the same corrosive conditions. Non-prestressed stainless steel reinforcing bars are currently produced in grades 304, 316, 2101, 2205, and 2304 (other grades have lower availability). Stainless steel grades 316 and 2205 are the most commonly specified reinforcing bars for corrosion mitigation in concrete bridges. Ideally, the same stainless steel alloy which is known to provide adequate corrosion resistance under the anticipated exposure conditions should be used for all reinforcement (i.e., prestressed and non-prestressed) to ensure a consistent level of durability and to limit any galvanic effects which may further accelerate corrosion if initiation were to occur. All elements used to support and secure the reinforcement (e.g., wire ties and chairs) should be made of corrosion-resistant materials (e.g., stainless steel or plastic).

Much information exists regarding the design of reinforced concrete structures using stainless steels. In contrast, no standards exist regarding the design of PSC structures using HSSS prestressing strands. While this research examined the stress vs. strain behavior and stress relaxation of HSSSs, many properties more specifically related to PSC design remain unknown. The results of the present study have shown that HSSSs exhibit lower strengths and ductility when compared with A416 prestressing strands.

Therefore, depending on the anticipated loading condition, it may be necessary to develop resistance factors or allowable stresses which account for the lack of ductility and low toughness of HSSSs.

8.3 Future Research

The present study has addressed many deficiencies in the knowledge of HSSSs. However, much future research will be necessary in order to further develop HSSSs as an effective means to corrosion mitigation in PSC structures. Some key topics requiring additional research are listed below:

1. Additional research is necessary to more accurately determine the corrosion resistance of HSSSs (e.g., CTL measurements). With a more accurate prediction of the CTL of different HSSSs, service life modeling can be used to determine if a lower cost HSSS like 2101 will provide sufficient corrosion resistance over the specified service life of a PSC structure. These future research efforts should consider the actual heterogeneous surface condition of cold-drawn HSSSs and stranded geometry of prestressing strands, both of which were found to influence corrosion resistance in the present study.
2. Studies are also needed which correlate the corrosion resistance of HSSSs in simulated concrete pore solutions with that derived from testing conducted in Cl^- contaminated concrete specimens.
3. The present study has shown that duplex HSSSs 2101, 2205, and 2304 provide superior corrosion resistance. These results support the investigation of newer duplex

grades, such as 2003, 2202, and 2404. In particular, duplex grade 2003 currently being produced by Allegheny Technologies Incorporated may be well suited for corrosion-resistant prestressing reinforcement due to its moderate 1.5 to 2 % Mo content.

4. The effect of surface condition on corrosion resistance should also be investigated (i.e., polished vs. as-received). These studies will be useful for specifying surface roughness criteria and cleaning methods for the production of HSSS wire and strand.
5. SSRTs of 2205 and 2304 have found high resistance to SCC under open-circuit conditions. However, these studies have assumed that corrosion initiation will not occur based on the results of CPP experiments on HSSS wires. While this is a valid assumption for 2205, 2304 was found to be susceptible to corrosion initiation in the stranded geometry. Therefore, additional SSRTs of 2304 under potentials which result in corrosion initiation are necessary to evaluate susceptibility to SCC.
6. Additional research on HSSS prestressing strand production techniques is also needed. The magnitude and speed of prestressing strand production makes this type of research impossible to accurately simulate in a laboratory setting. Therefore, this research will likely require a full-scale trial production run of HSSS prestressing strand at an A416 prestressing strand production facility. These studies should also focus on optimization of the low relaxation heat treatment process for HSSS prestressing strands produced using ferromagnetic alloys.
7. Once HSSS prestressing strand has been produced, experimental studies will be necessary to determine stress vs. strain behavior and stress relaxation of the full

prestressing strands. In addition, properties which dictate the design of PSC elements should also be determined, including transfer length and pullout strength.

8. Consideration should also be given to the limited ductility and toughness of HSSSs. These factors may necessitate the use of reduced allowable stresses or changes in design methodology to assure similar structural safety in structures built with A416 strand and those built with HSSS strand.
9. In the author's opinion, one of the most important topics requiring future research is the integration of highly corrosion-resistant reinforcing and prestressing steels into an optimized durable structural design methodology. For example, when utilizing highly corrosion-resistant reinforcing and prestressing steels, code requirements such as minimum cover thicknesses, concrete quality, and crack sizes may no longer be necessary. If these considerations are factored into the structural design, it will make the use of corrosion-resistant steels much more economically feasible.

APPENDIX A: CHEMICAL COMPOSITION OF MATERIALS

APPLIED TECHNICAL SERVICES, INCORPORATED

1049 Triad Court, Marietta, Georgia 30062 • (770) 423-1400 Fax (770) 424-6415

CHEMICAL TEST REPORT

Ref. C157384 **Date** September 15, 2010 **Page** 1 **of** 1

Customer: Georgia Tech Civil Engineering, 790 Atlantic Drive, Atlanta, GA 30332

Attention: Robert Moser

Purchase Order #: Credit Card Part #/Name: Carbon Steel wire

Material Designation: SAE 1080 Carbon Steel [2]

Special Requirement: N/A

Lab Comment: Analyzed by combustion and ICP atomic emission techniques.

Test Results

Composition: Weight %

Identification	C	Mn	P	S	Si	Cr	Ni	Mo	Cu	V
1080 Carbon Steel chemical req. [1]	0.75 0.88	0.60 0.90	0.040 Max.	0.050 Max.	—	—	—	—	—	—
Sample	0.81	0.73	0.009	0.005	0.24	0.04	0.06	0.01	0.11	0.08

(1) *ASM Metals Handbook, Vol. 1, 10th Edition*

(2) Sample also meets 1084 and 1085 Carbon Steel chemical requirements.

ISO 9001

Prepared by: T. Gholar, Senior Chemist

Approved by: D. M. McKay, Supervisor

Figure A.1 Chemical composition of 1080 prestressing steel

APPLIED TECHNICAL SERVICES, INCORPORATED

1049 Triad Court, Marietta, Georgia 30062 • (770) 423-1400 Fax (770) 424-6415

CHEMICAL TEST REPORT

Ref. C160604 **Date** December 10, 2010 **Page** 1 **of** 7

Customer: Georgia Institute of Tech., 790 Atlantic Dr. Atlanta, GA 30332

Attention: Robert Moser

Purchase Order #: Credit Card Part #/Name: 302

Material Designation: 302 Stainless Steel

Special Requirement: N/A

Lab Comment: Analyzed by XRF, combustion, inert gas fusion, and ICP atomic emission techniques.

Test Results

Composition: Weight %

Identification	C	Mn	P	S	Si	Ni	Cr	Mo	Cu	V	N
Alloy or Spec. Req. (1)	0.15 Max.	2.00 Max.	0.045 Max.	0.030 Max.	1.00 Max.	8.0 10.0	17.0 19.0	—	—	—	0.10 Max.
302	0.07	1.02	0.028	0.001	0.33	8.3	17.8	0.33	0.47	0.10	0.09

(1) ASTM A276-08a

ISO 9001

Prepared by: J. Hardaway
Technician

Approved by: D. M. McKay
Supervisor

Figure A.2 Chemical composition of 304 HSSS (referred to as "302" here)

APPLIED TECHNICAL SERVICES, INCORPORATED

1049 Triad Court, Marietta, Georgia 30062 • (770) 423-1400 Fax (770) 424-6415

CHEMICAL TEST REPORT

Ref. C160604 **Date** December 10, 2010 **Page** 2 **of** 7

Customer: Georgia Institute of Tech., 790 Atlantic Dr. Atlanta, GA 30332

Attention: Robert Moser

Purchase Order #: Credit Card Part #/Name: 316

Material Designation: 316 Stainless Steel

Special Requirement: N/A

Lab Comment: Analyzed by XRF, combustion, inert gas fusion, and ICP atomic emission techniques.

Test Results

Composition: Weight %

Identification	C	Mn	P	S	Si	Ni	Cr	Mo	Cu	V	N
Alloy or Spec. Req. (1)	0.08 Max.	2.00 Max.	0.045 Max.	0.030 Max.	1.00 Max.	10.0 14.0	16.0 18.0	2.00 3.00	—	—	—
316	0.03	1.67	0.030	0.030	0.21	10.8	16.4	2.23	0.46	0.16	0.05

(1) ASTM A276-08a

ISO 9001

Prepared by: J. Hardaway, Technician

Approved by: D. M. McKay, Supervisor

Figure A.3 Chemical composition of 316 HSSS

APPLIED TECHNICAL SERVICES, INCORPORATED

1049 Triad Court, Marietta, Georgia 30062 • (770) 423-1400 Fax (770) 424-6415

CHEMICAL TEST REPORT

Ref. C160604 **Date** December 10, 2010 **Page** 3 **of** 7

Customer: Georgia Institute of Tech., 790 Atlantic Dr. Atlanta, GA 30332

Attention: Robert Moser

Purchase Order #: Credit Card Part #/Name: 2101

Material Designation: Similar to 2101 Duplex Stainless Steel (UNS S32101)

Special Requirement: N/A

Lab Comment: Analyzed by XRF, combustion, inert gas fusion, and ICP atomic emission techniques.

Test Results

Composition: Weight %

Identification	C	Mn	P	S	Si	Ni	Cr	Mo	Cu	V	N
Alloy or Spec. Req. (1)	0.040 Max.	4.0 6.0	0.040 Max.	0.030 Max.	1.00 Max.	1.35 1.70	21.0 22.0	0.10 0.80	0.10 0.80	—	0.20 0.25
2101	0.027	5.0	0.018	<0.001	0.71	1.56	20.9[2]	0.16	0.25	0.12	**0.29**

***Bold number indicates element is above specification.**

(1) ASTM A276-08a

(2) Within product analysis tolerance, ±0.25%, ASTM A484/A484M-08

ISO 9001

Prepared by: J. Hardaway, Technician

Approved by: D. M. McKay, Supervisor

Figure A.4 Chemical composition of 2101 HSSS

APPLIED TECHNICAL SERVICES, INCORPORATED

1049 Triad Court, Marietta, Georgia 30062 • (770) 423-1400 Fax (770) 424-6415

CHEMICAL TEST REPORT

Ref. C160604 **Date** December 10, 2010 **Page** 4 **of** 7

Customer: Georgia Institute of Tech., 790 Atlantic Dr. Atlanta, GA 30332

Attention: Robert Moser

Purchase Order #: Credit Card Part #/Name: 2205

Material Designation: 2205 Duplex Stainless Steel

Special Requirement: N/A

Lab Comment: Analyzed by XRF, combustion, inert gas fusion, and ICP atomic emission techniques.

Test Results

Composition: Weight %

Identification	C	Mn	P	S	Si	Ni	Cr	Mo	Cu	V	N
Alloy or Spec. Req. (1)	0.030 Max.	2.00 Max.	0.030 Max.	0.020 Max.	1.00 Max.	4.5 6.5	22.0 23.0	3.0 3.5		—	0.14 0.20
2205	0.004	0.82	0.023	<0.001	0.51	5.1	22.1	3.2	0.21	0.12	0.22[2]

(1) ASTM A276-08a

(2) Within product analysis tolerance, ±0.02%, ASTM A484/A484M-08.

ISO 9001

Prepared by: J. Hardaway, Technician

Approved by: D. M. McKay, Supervisor

Figure A.5 Chemical composition of 2205 HSSS

APPLIED TECHNICAL SERVICES, INCORPORATED

1049 Triad Court, Marietta, Georgia 30062 • (770) 423-1400 Fax (770) 424-6415

CHEMICAL TEST REPORT

Ref. C160604 **Date** December 10, 2010 **Page** 5 **of** 7

Customer: Georgia Institute of Tech., 790 Atlantic Dr. Atlanta, GA 30332

Attention: Robert Moser

Purchase Order #: Credit Card Part #/Name: 2304

Material Designation: 2304 Duplex Stainless Steel

Special Requirement: N/A

Lab Comment: Analyzed by XRF, combustion, inert gas fusion, and ICP atomic emission techniques.

Test Results

Composition: Weight %

Identification	C	Mn	P	S	Si	Ni	Cr	Mo	Cu	V	N
Alloy or Spec. Req. (1)	0.030 Max.	2.50 Max.	0.040 Max.	0.030 Max.	1.00 Max.	3.0 5.5	21.5 24.5	0.05 0.60	0.05 0.60	—	0.05 0.20
2304	0.018	0.87	0.011	0.001	0.43	4.8	22.3	0.31	0.23	0.07	0.14

(1) ASTM A276-08a

ISO 9001

Prepared by: J. Hardaway, Technician

Approved by: D. M. McKay, Supervisor

Figure A.6 Chemical composition of 2304 HSSS

APPLIED TECHNICAL SERVICES, INCORPORATED

1049 Triad Court, Marietta, Georgia 30062 • (770) 423-1400 Fax (770) 424-6415

CHEMICAL TEST REPORT

Ref. C160604 **Date** December 10, 2010 **Page** 6 **of** 7

Customer: Georgia Institute of Tech., 790 Atlantic Dr. Atlanta, GA 30332

Attention: Robert Moser

Purchase Order #: Credit Card Part #/Name: 17-7 PH

Material Designation: 17-7 PH Stainless Steel

Special Requirement: N/A

Lab Comment: Analyzed by XRF, combustion, inert gas fusion, and ICP atomic emission techniques.

Test Results

Composition: Weight %

Identification	C	Mn	P	S	Si	Ni	Cr	Mo	Cu	V	N	Al
Alloy or Spec. Req. (1)	0.09 Max.	1.00 Max.	0.040 Max.	0.030 Max.	1.00 Max.	6.50 7.8	16.0 18.0	—	—	—	—	0.75 1.50
17-7 PH	0.07	0.82	0.023	0.001	0.23	7.83[2]	16.1	0.19	0.30	0.15	0.02	0.81

(1) ASTM A313/A313M-08

(2) Within product analysis tolerance, ±0.10%, ASTM A555/A555M-05(2009).

ISO 9001

Prepared by: J. Hardaway, Technician

Approved by: D. M. McKay, Supervisor

Figure A.7 Chemical composition of 17-7PH HSSS

APPENDIX B: METALLOGRAPHY

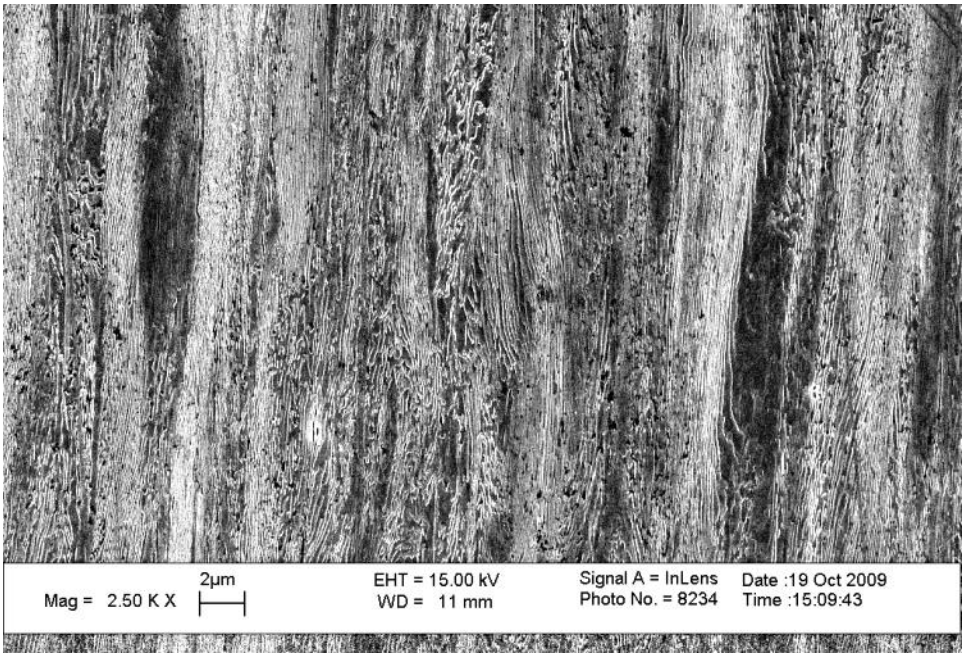

Figure B.1 Longitudinal microstructure of 1080 prestressing steel

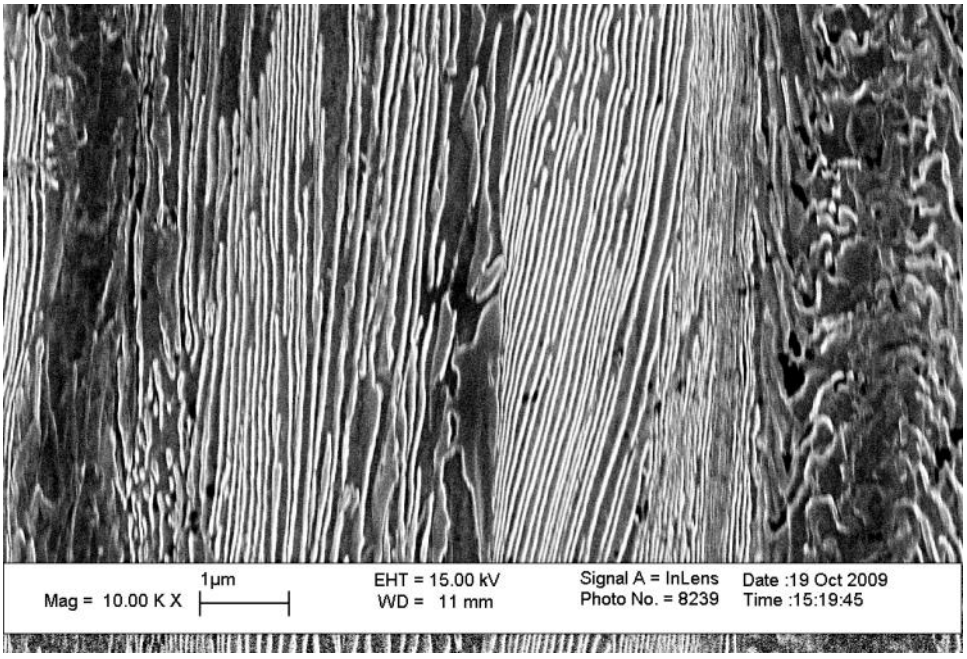

Figure B.2 Pearlite colonies oriented in drawing direction in 1080 prestressing steel

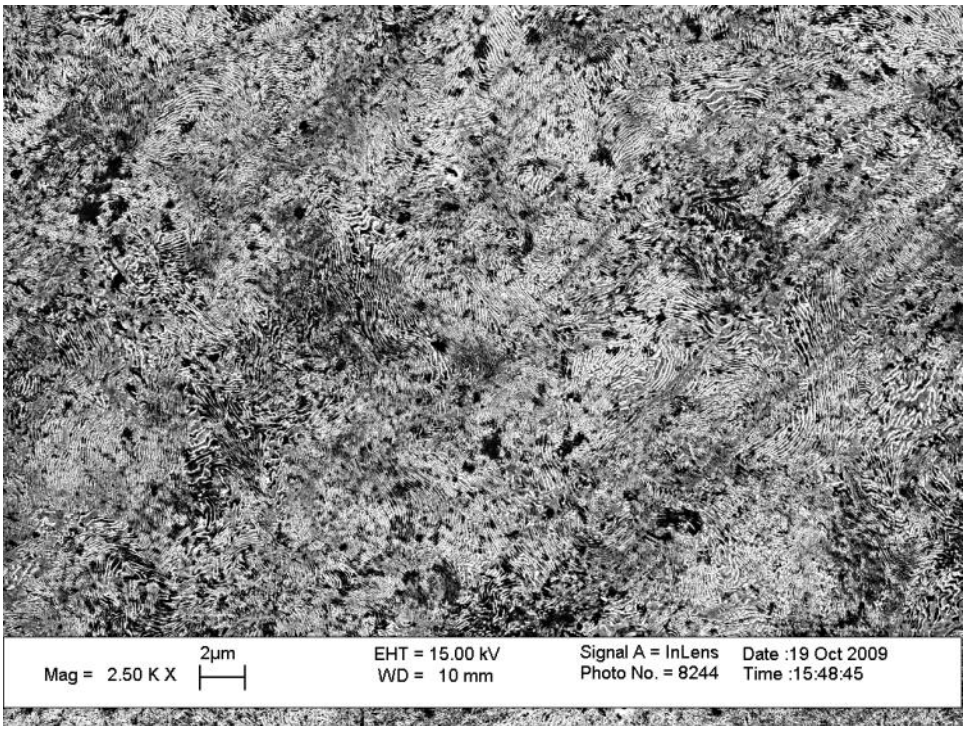

Figure B.3 Transverse microstructure of 1080 prestressing steel

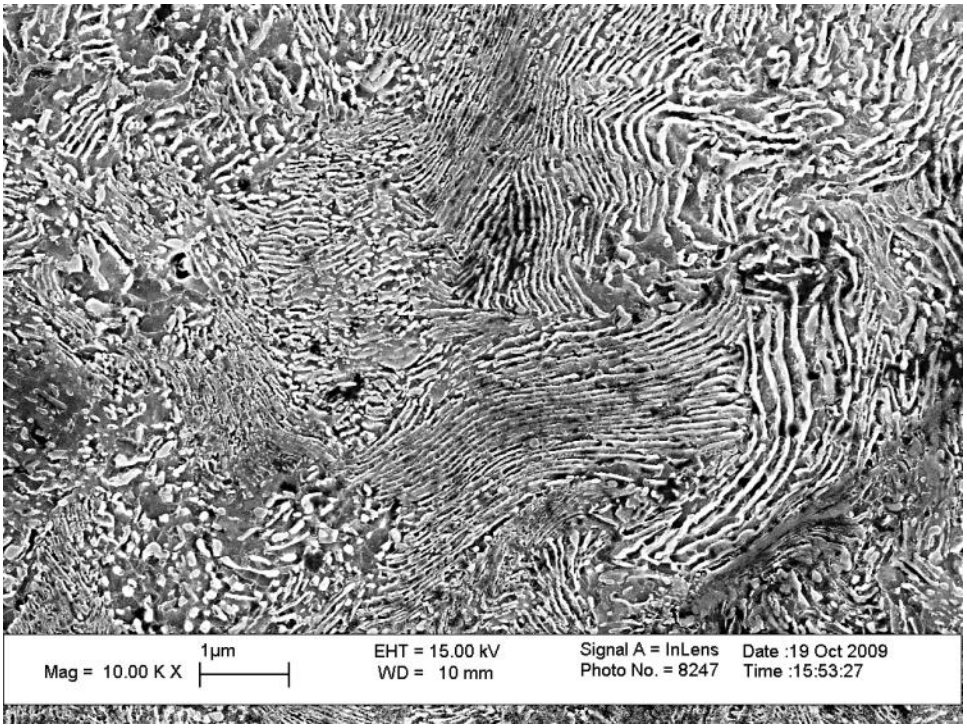

Figure B.4 Transverse microstructure of 1080 prestressing steel

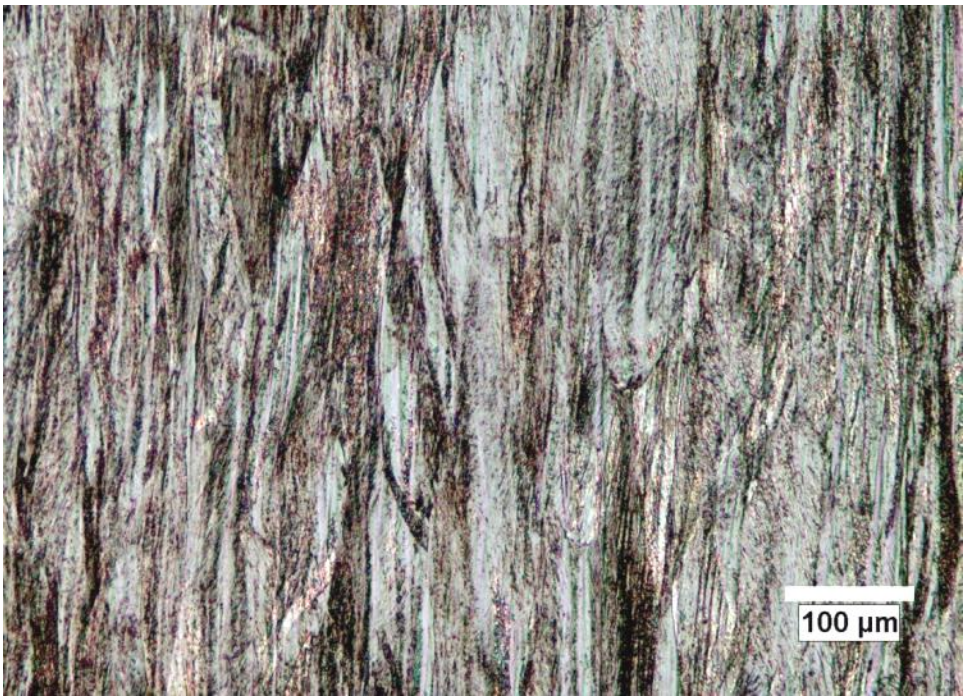

Figure B.5 Longitudinal microstructure of 304 HSSS

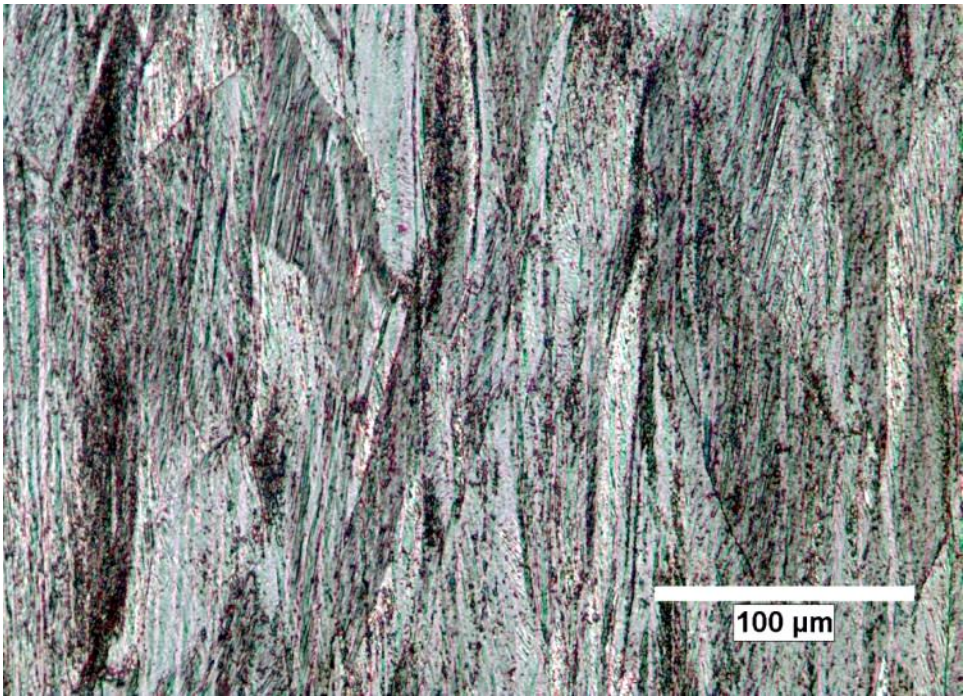

Figure B.6 Longitudinal microstructure of 304 HSSS

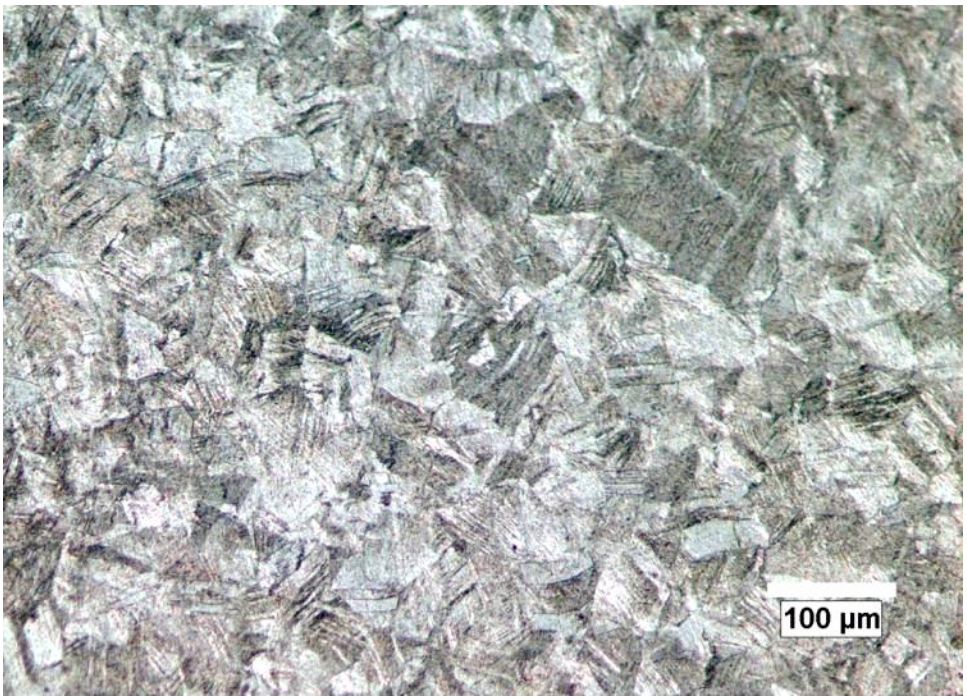

Figure B.7 Transverse microstructure of 304 HSSS

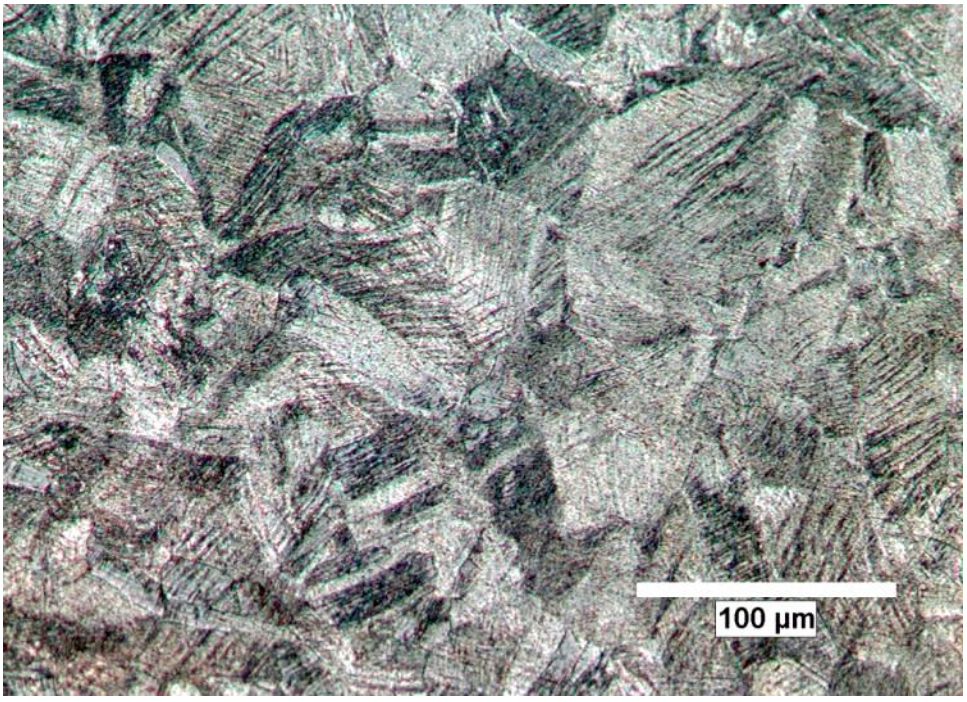

Figure B.8 Transverse microstructure of 304 HSSS

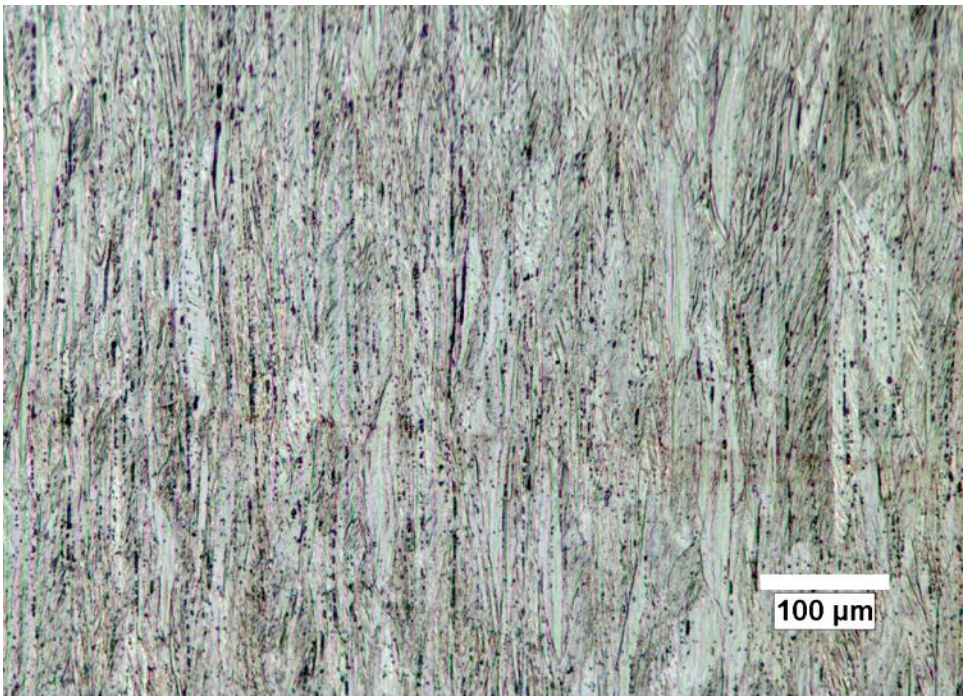

Figure B.9 Longitudinal microstructure of 316 HSSS

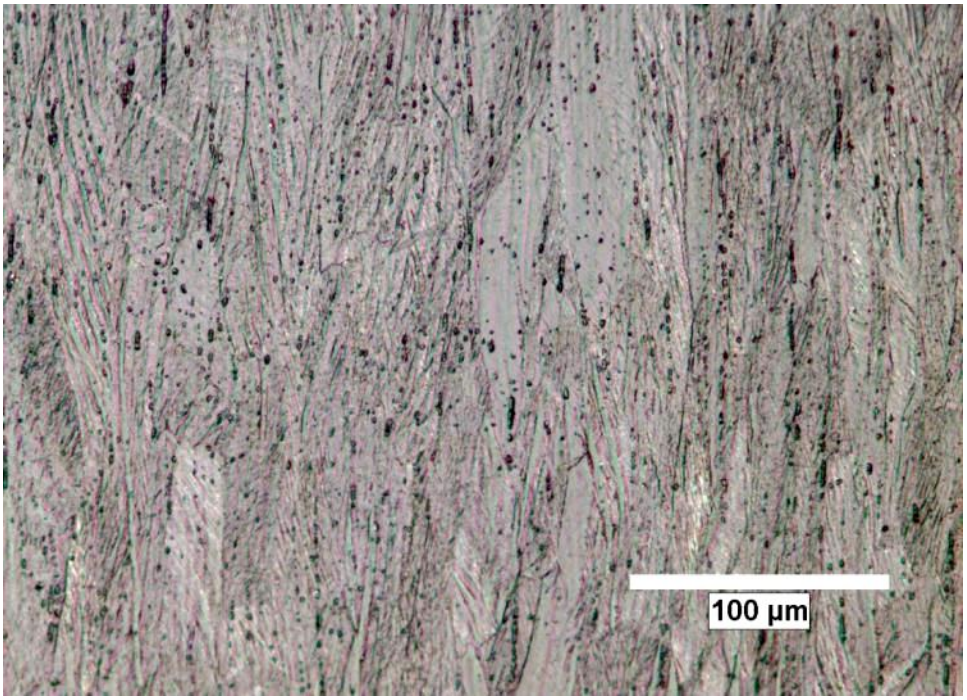

Figure B.10 Longitudinal microstructure of 316 HSSS

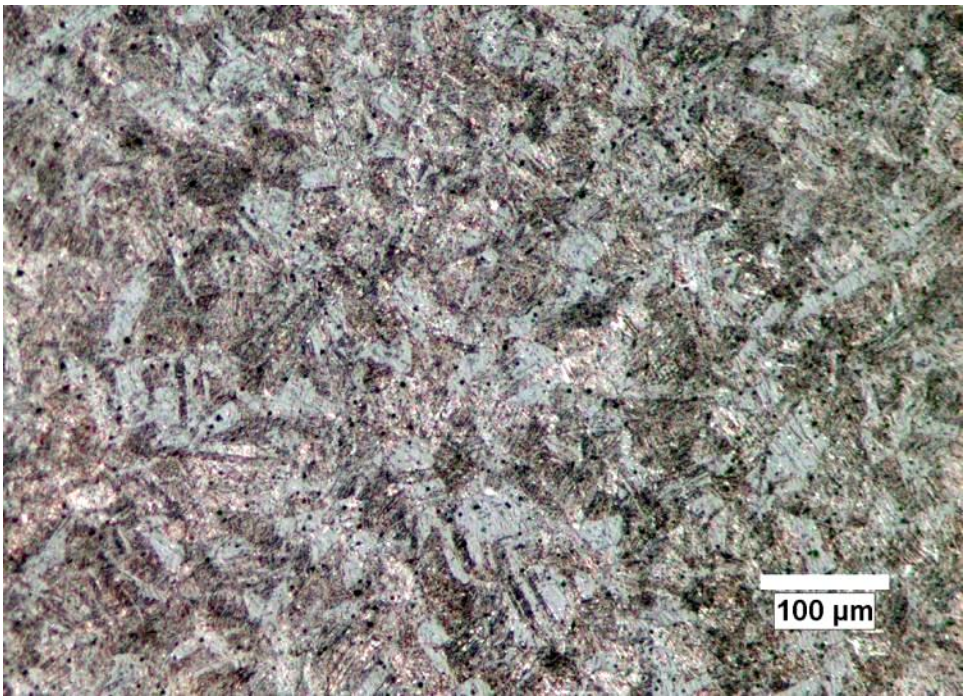

Figure B.11 Transverse microstructure of 316 HSSS

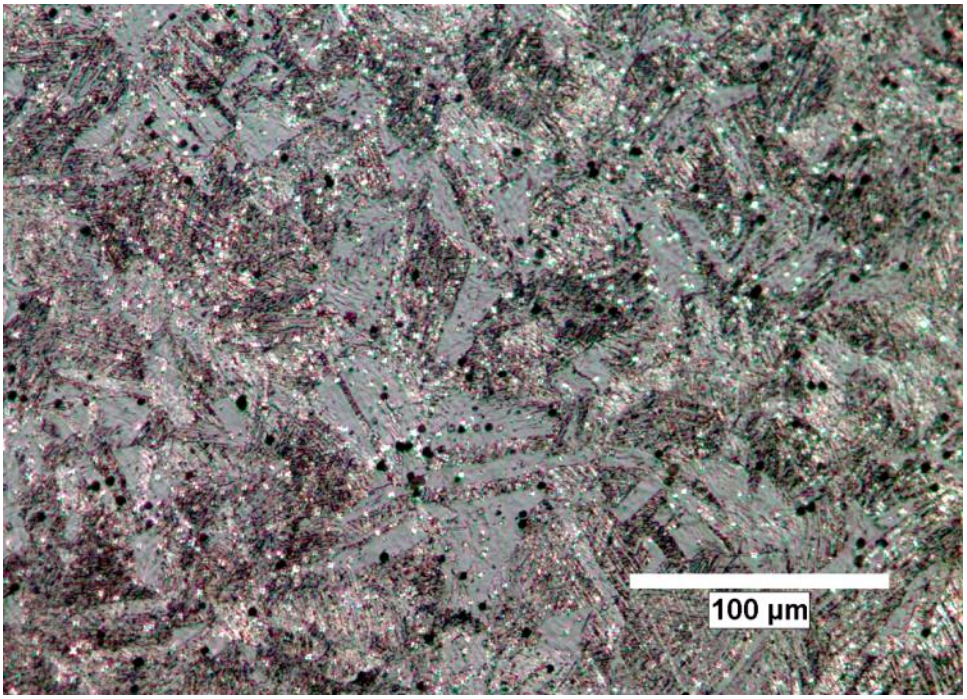

Figure B.12 Transverse microstructure of 316 HSSS

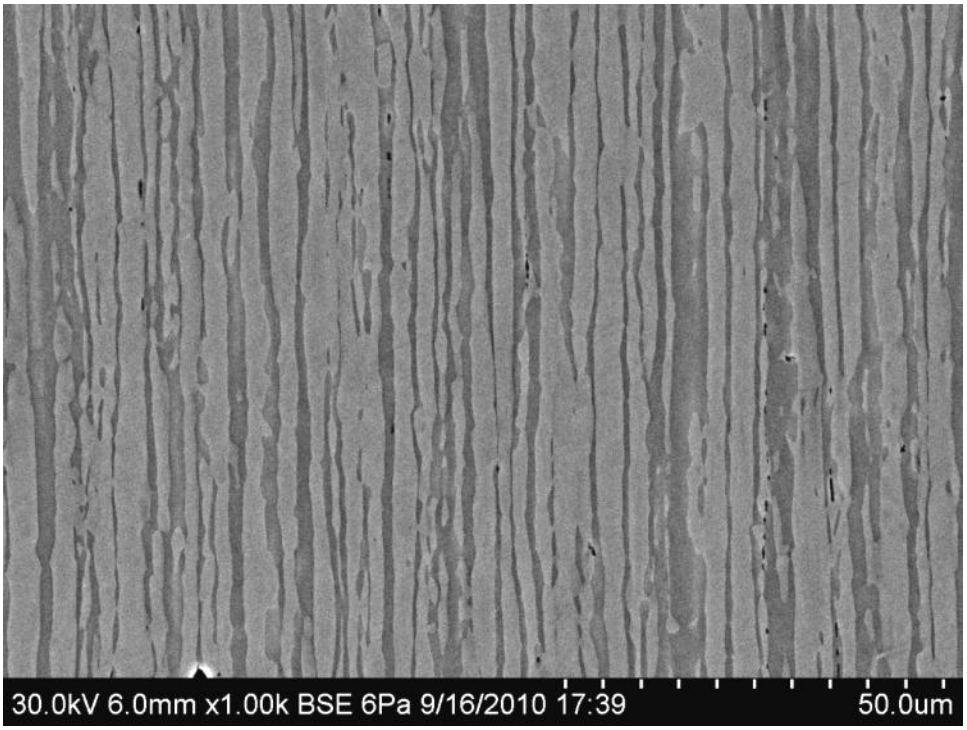

Figure B.13 Longitudinal microstructure of 2101 HSSS

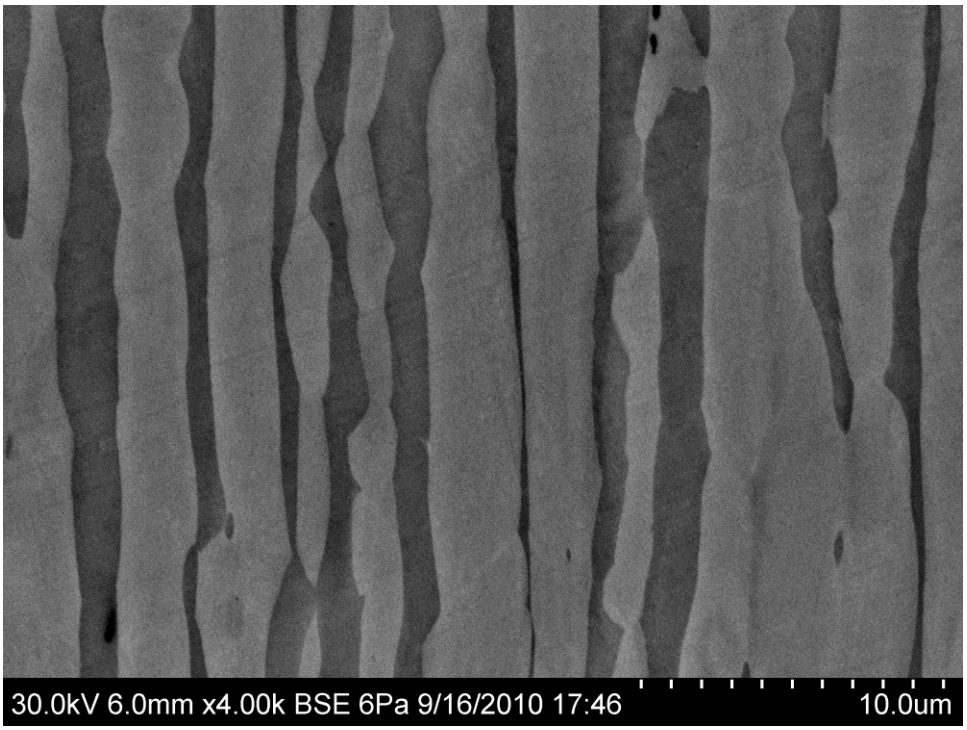

Figure B.14 Longitudinal microstructure of 2101 HSSS

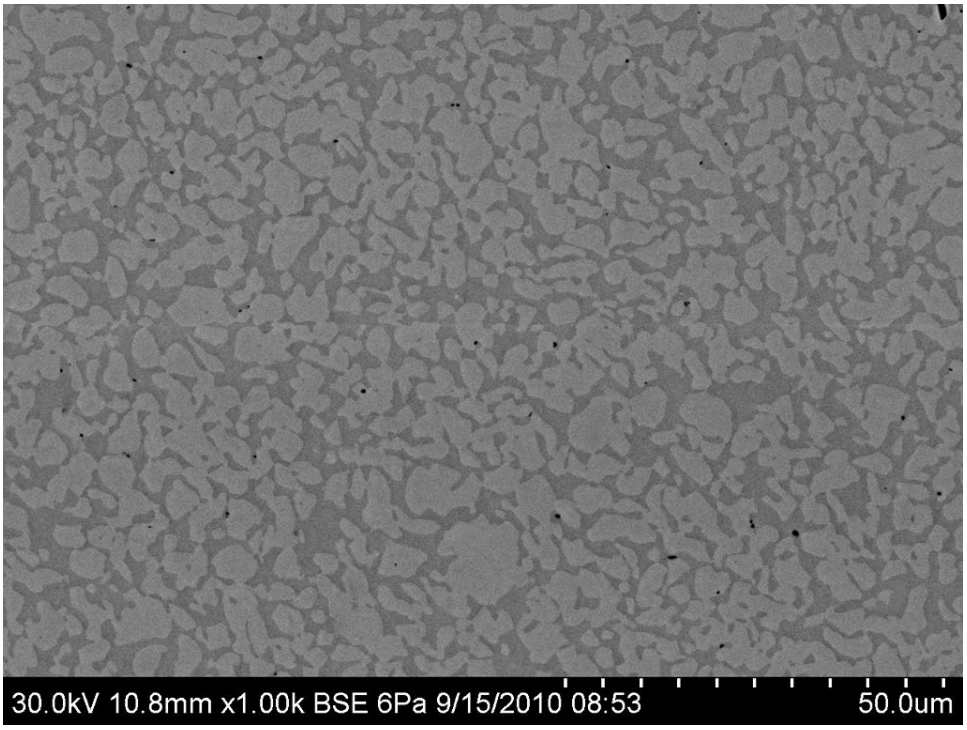

Figure B.15 Transverse microstructure of 2101 HSSS

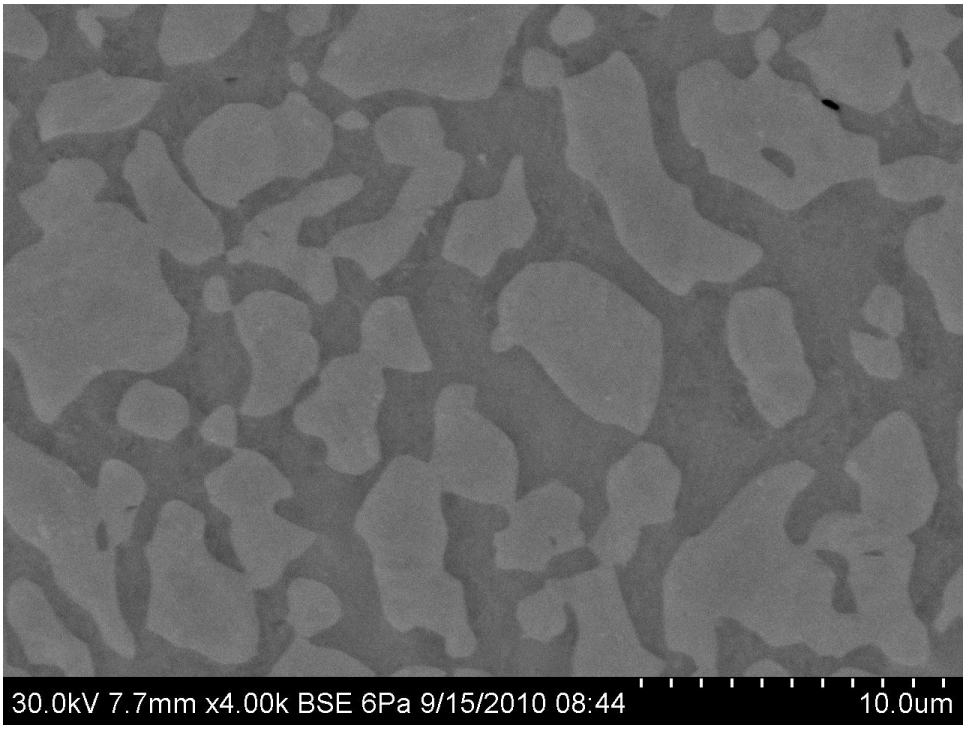

Figure B.16 Transverse microstructure of 2101 HSSS

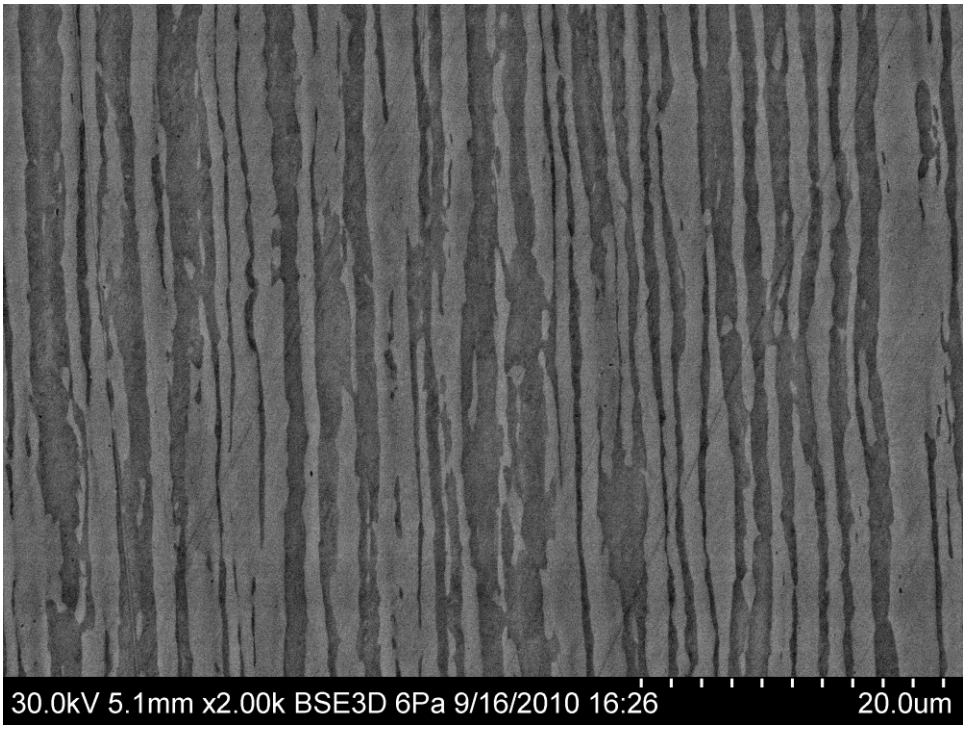

Figure B.17 Longitudinal microstructure of 2205 HSSS

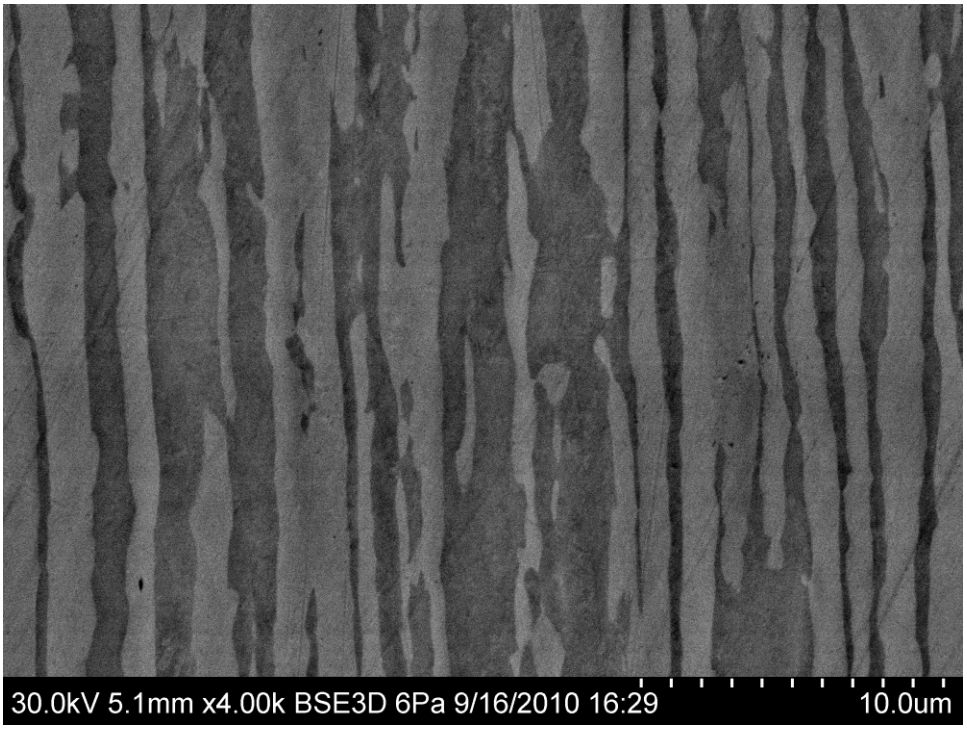

Figure B.18 Longitudinal microstructure of 2205 HSSS

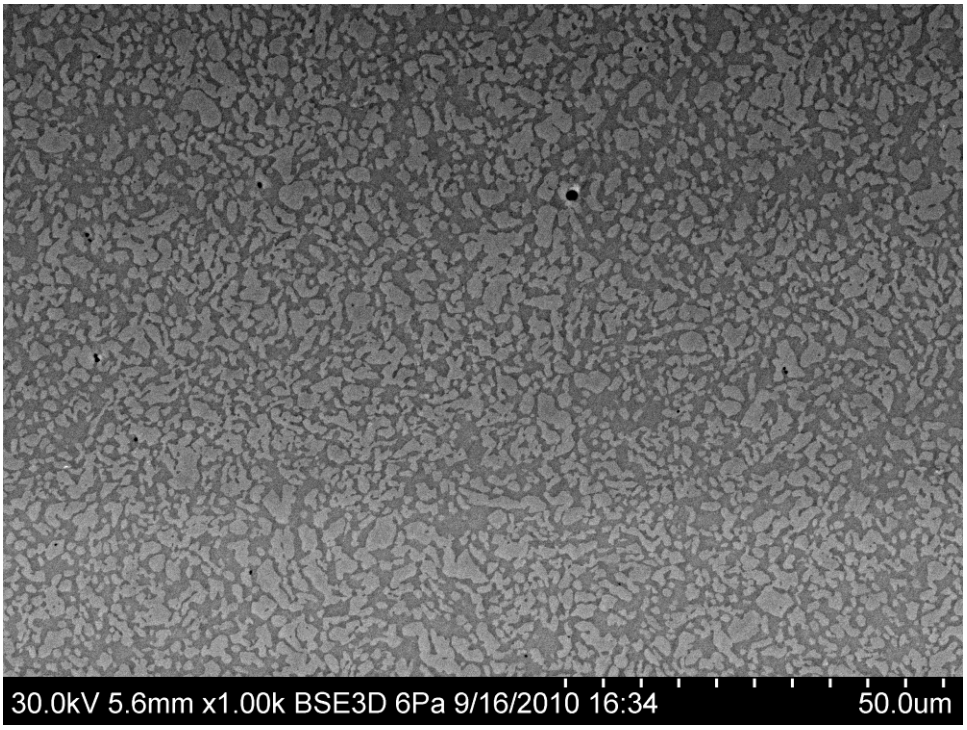

Figure B.19 Transverse microstructure of 2205 HSSS

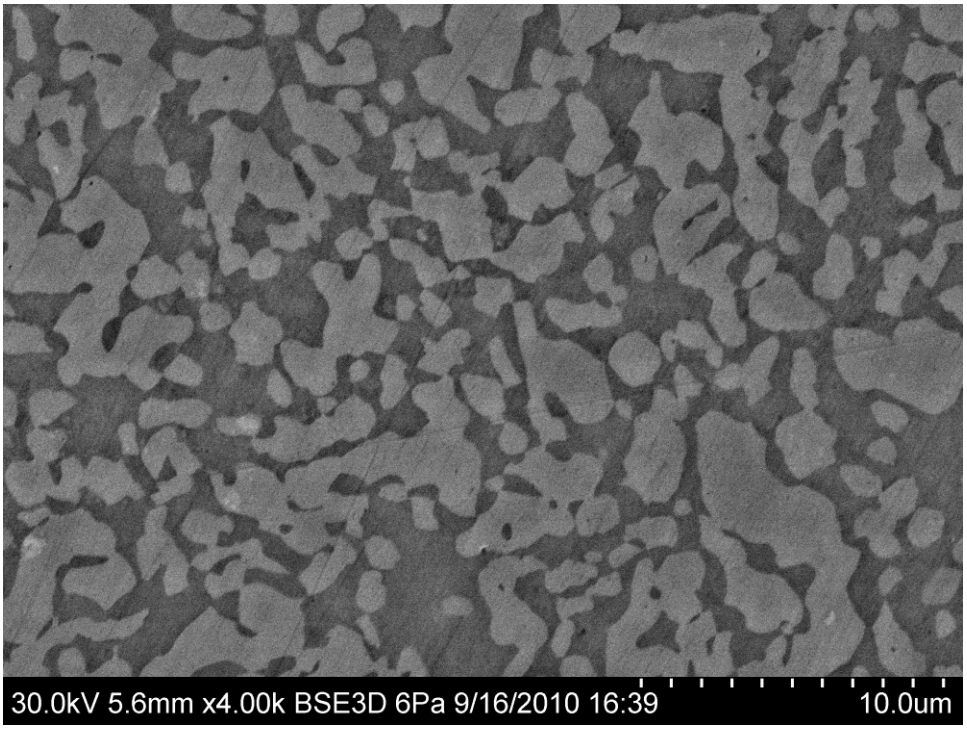

Figure B.20 Transverse microstructure of 2205 HSSS

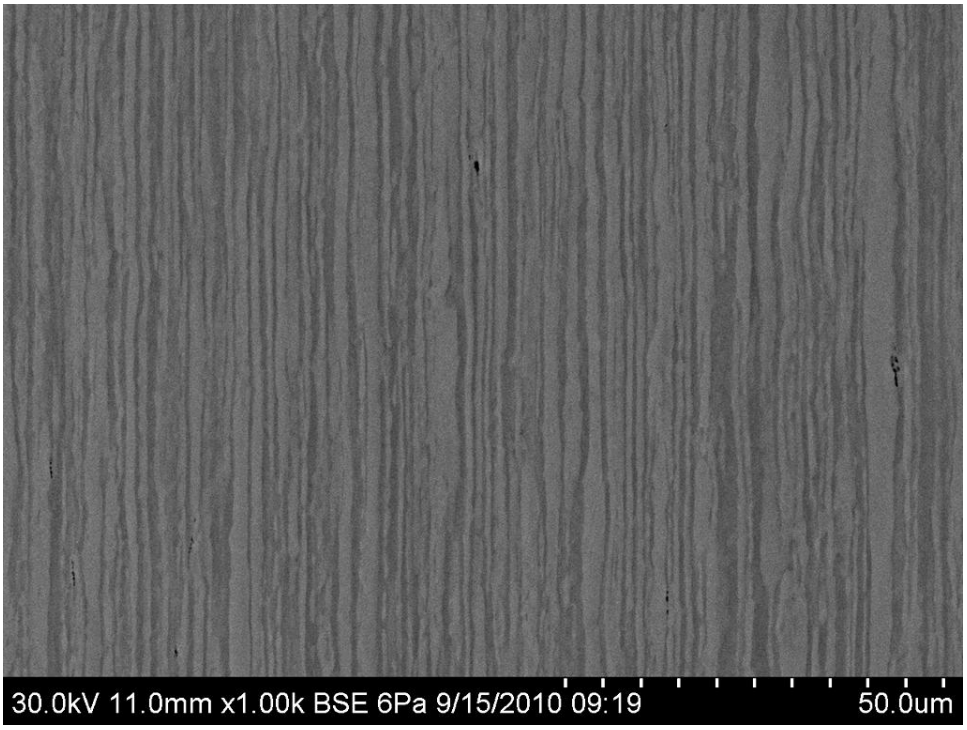

Figure B.21 Longitudinal microstructure of 2304 HSSS

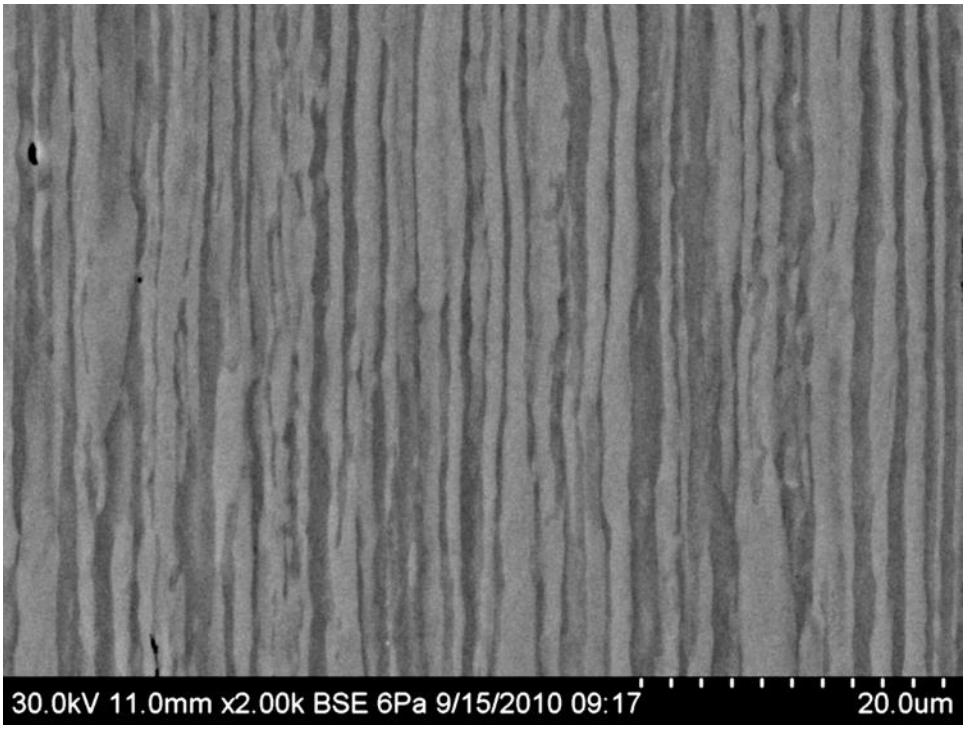

Figure B.22 Longitudinal microstructure of 2304 HSSS

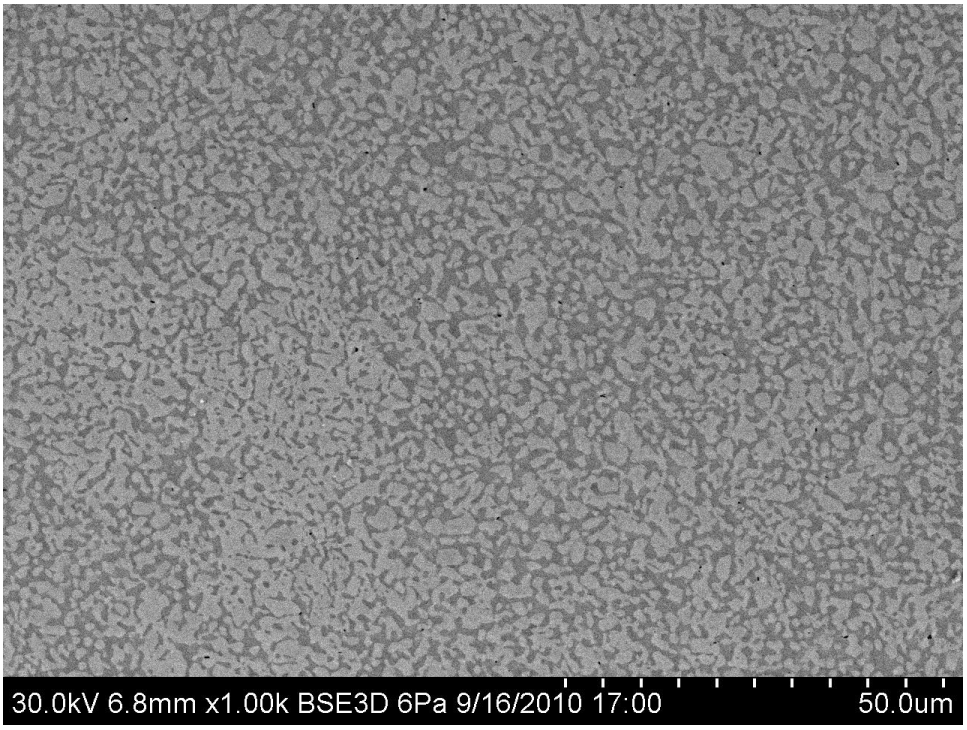

Figure B.23 Transverse microstructure of 2304 HSSS

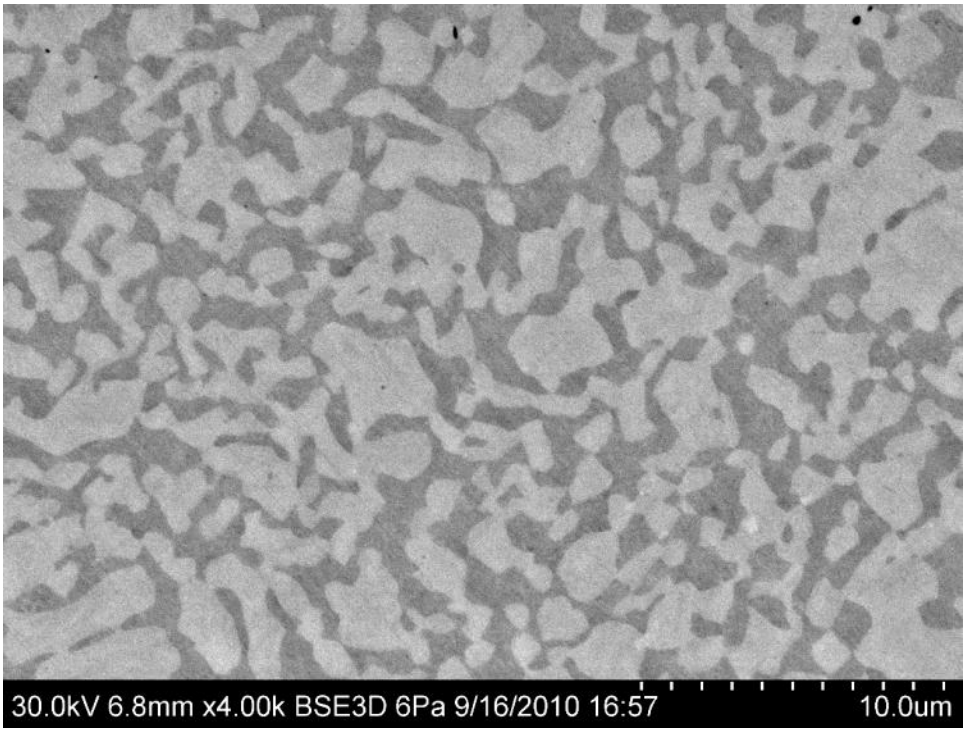

Figure B.24 Transverse microstructure of 2304 HSSS

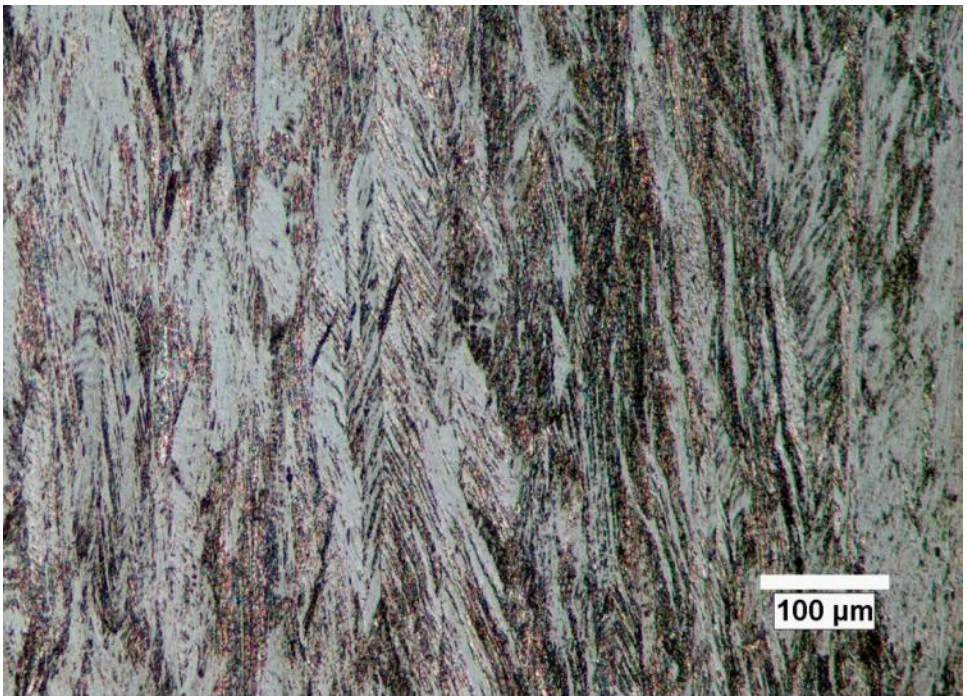

Figure B.25 Longitudinal microstructure of 17-7 HSSS

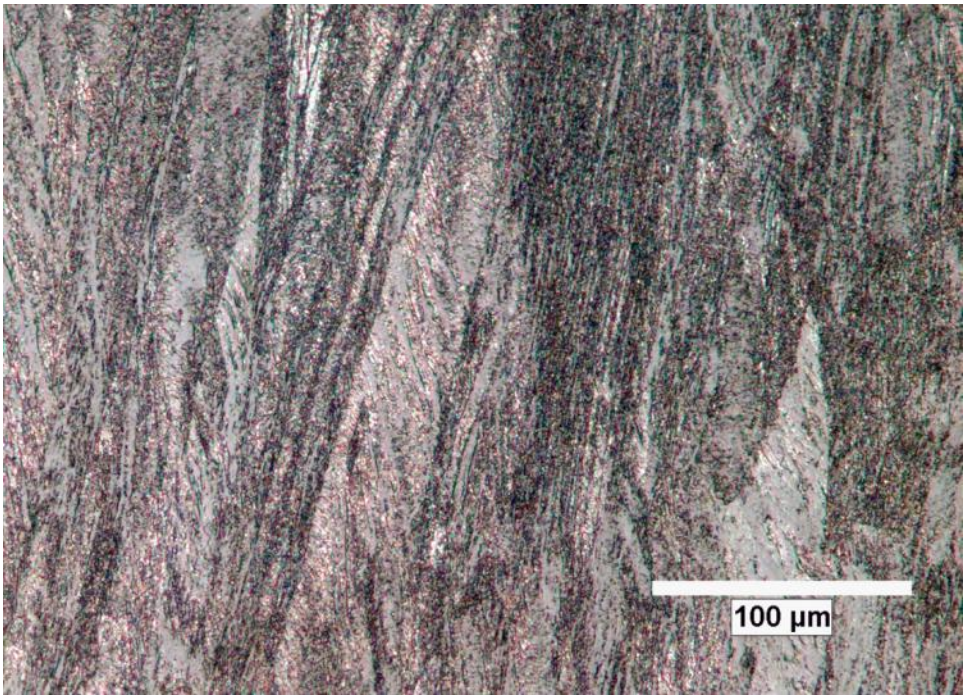

Figure B.26 Longitudinal microstructure of 17-7 HSSS

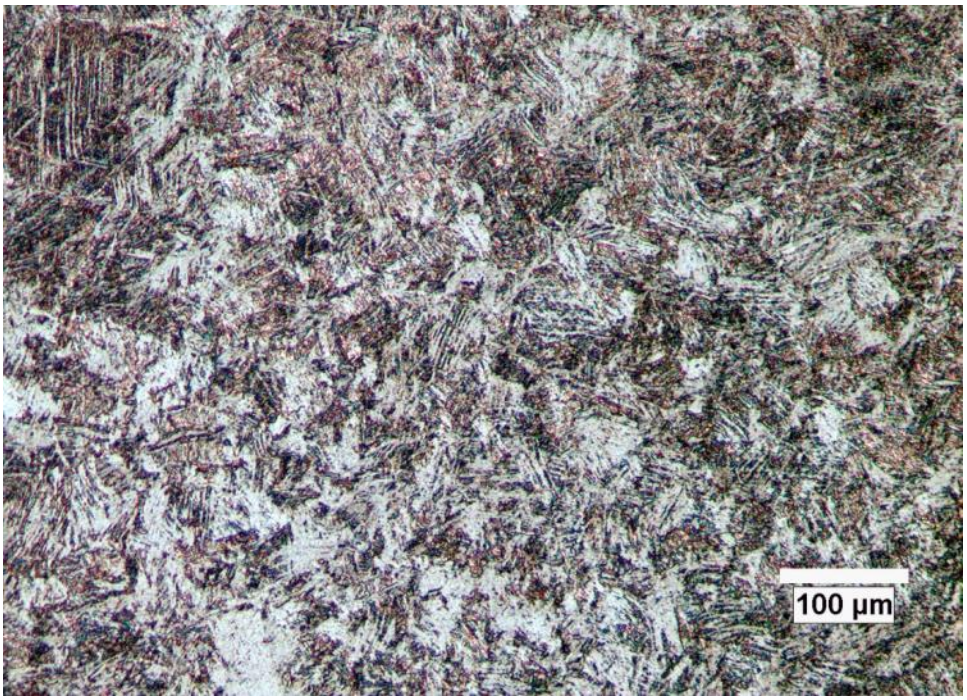

Figure B.27 Transverse microstructure of 17-7 HSSS

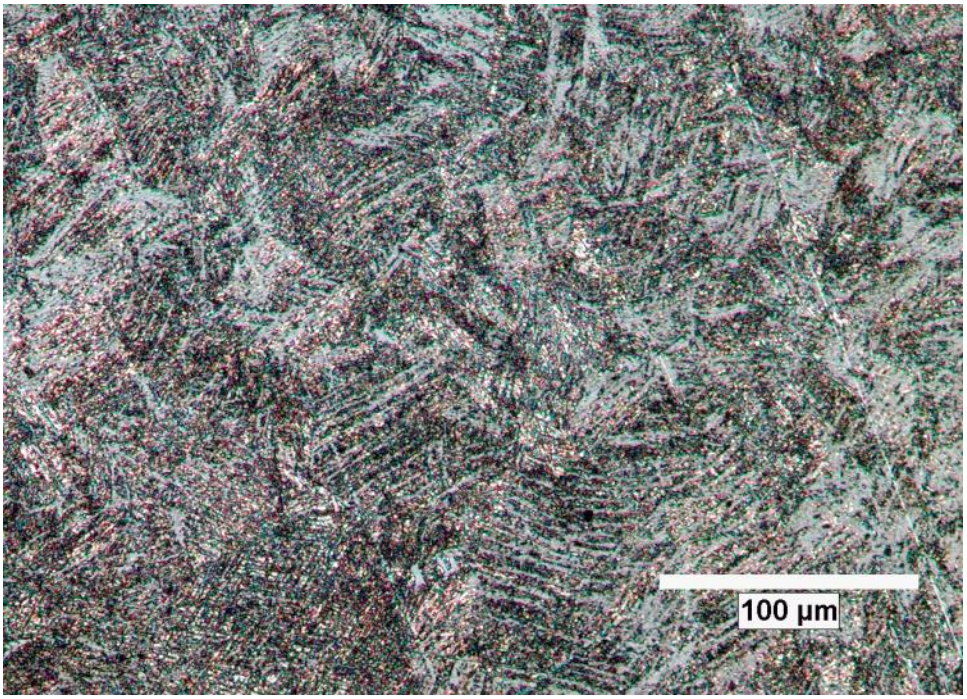

Figure B.28 Transverse microstructure of 17-7 HSSS

APPENDIX C: FRACTURE SURFACES

Figure C.1 Fracture surface of 1080 prestressing steel

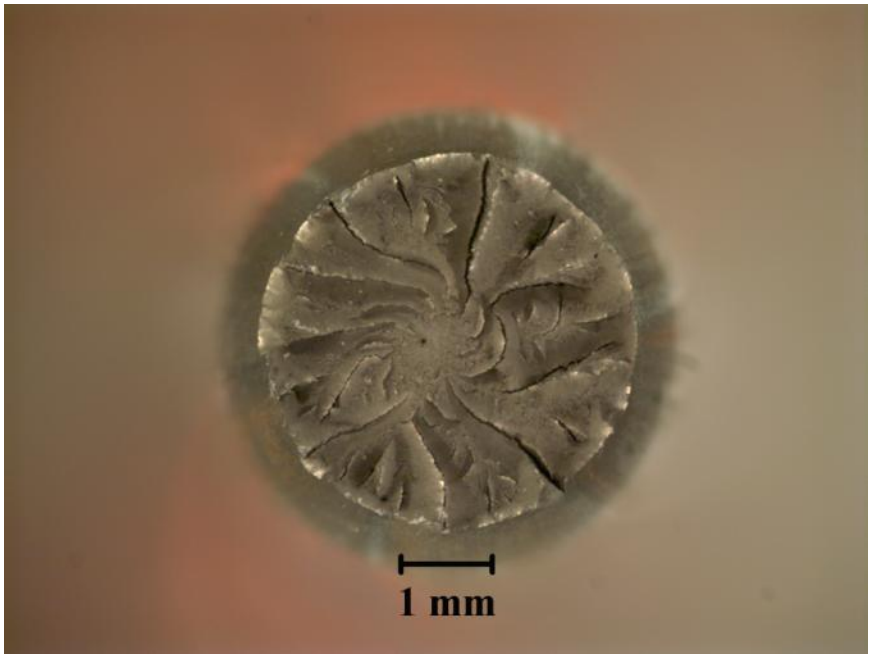

Figure C.2 Fracture surface of 1080 prestressing steel

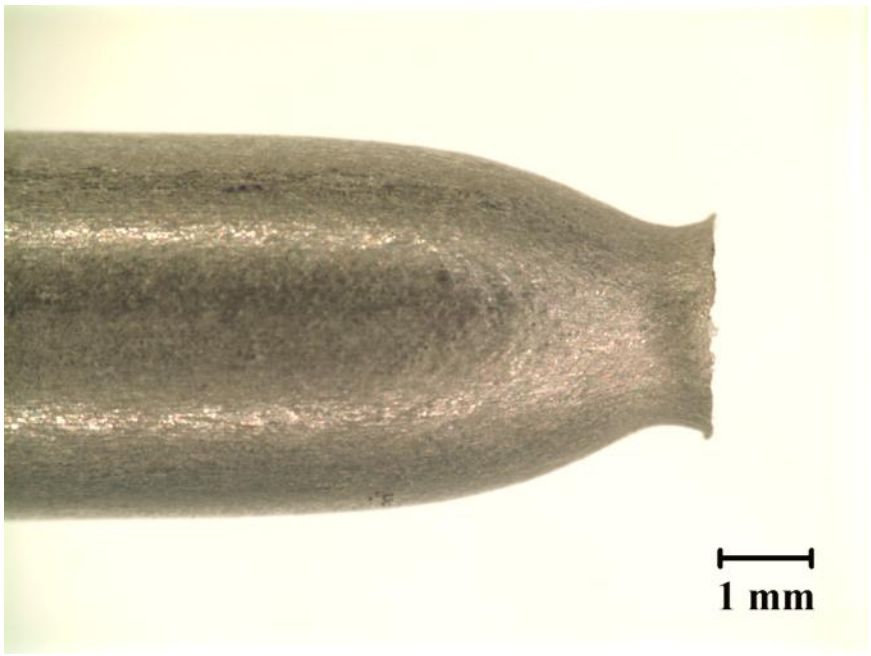

Figure C.3 Fracture surface of 304 HSSS

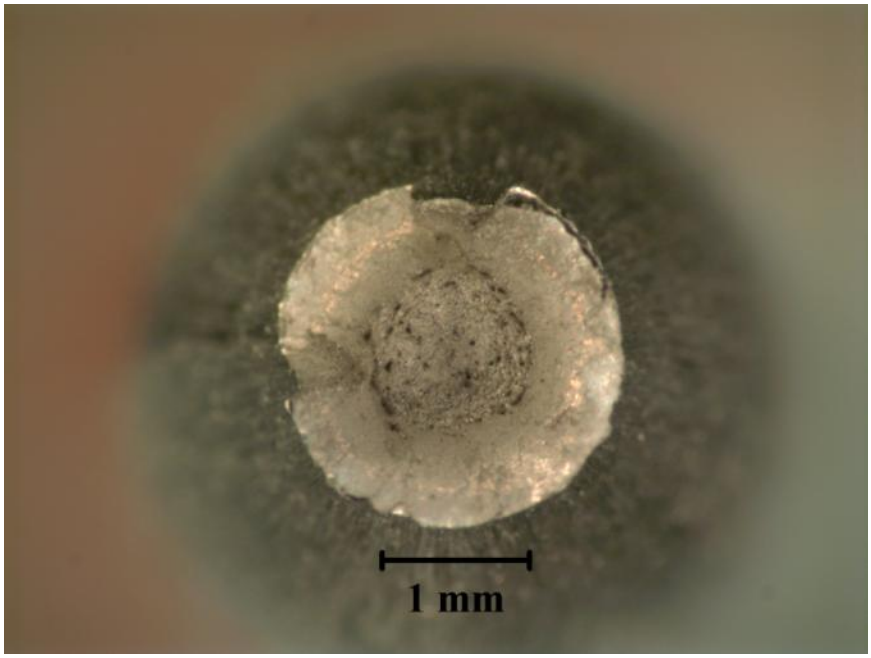

Figure C.4 Fracture surface of 304 HSSS

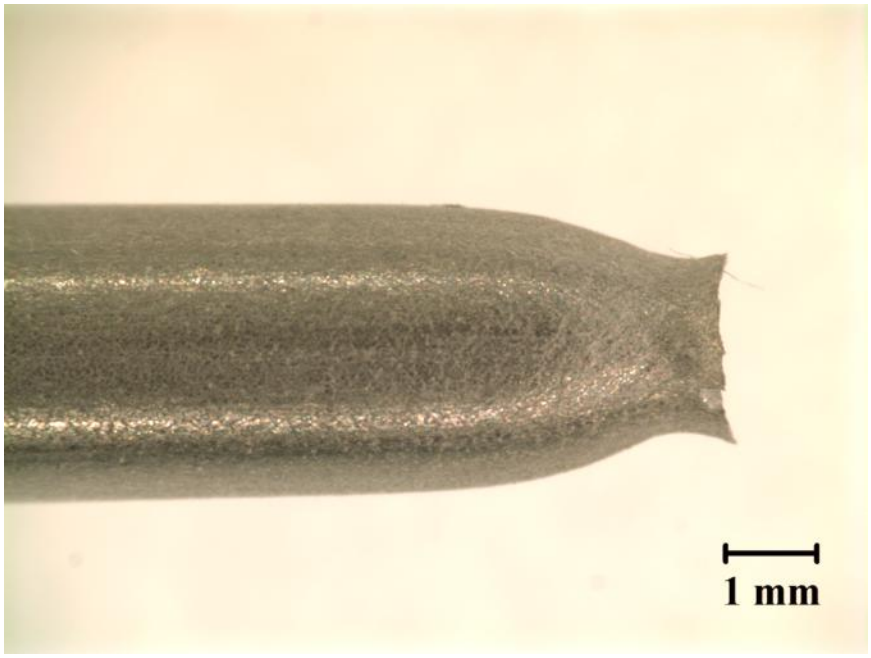

Figure C.5 Fracture surface of 316 HSSS

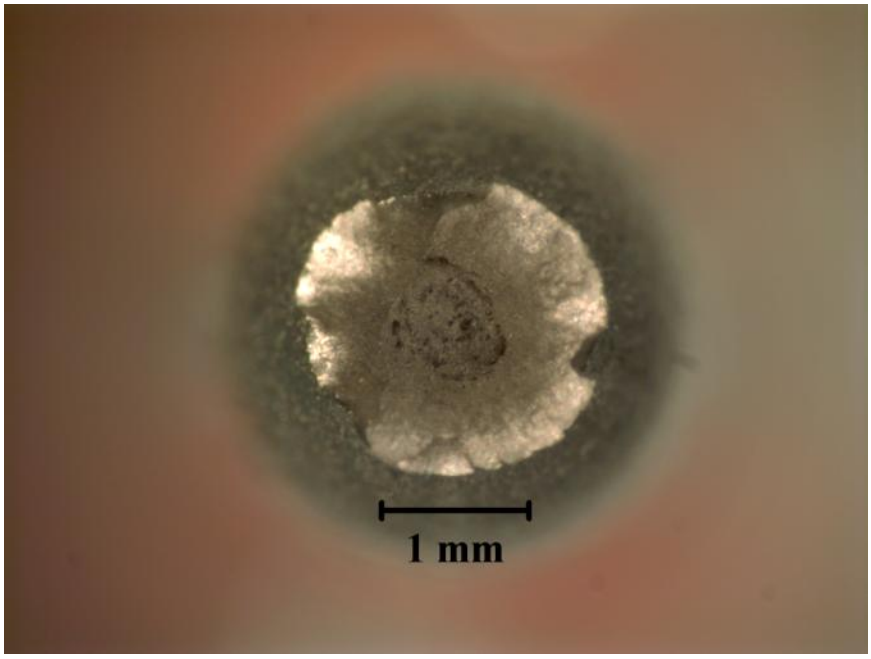

Figure C.6 Fracture surface of 316 HSSS

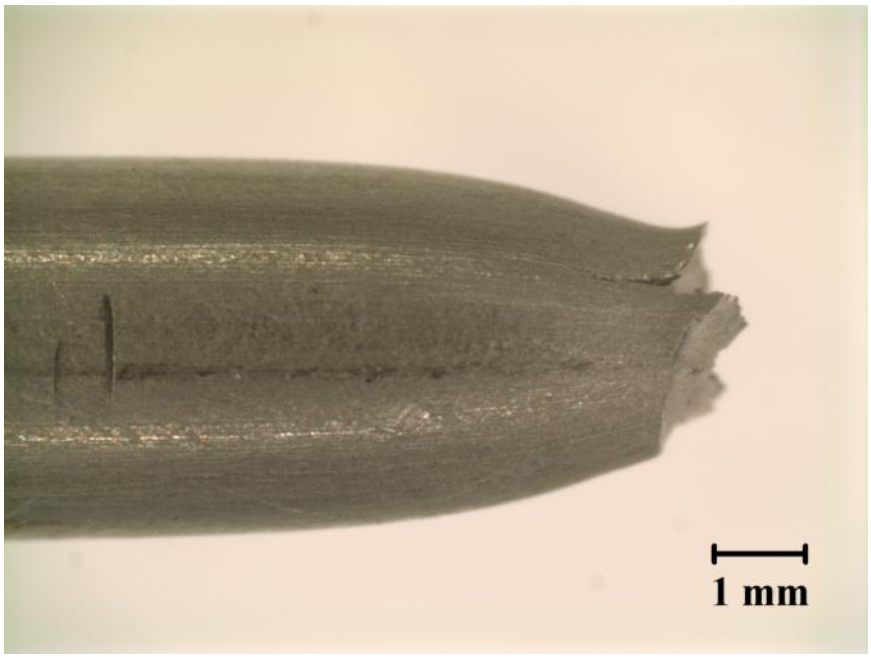

Figure C.7 Fracture surface of 2101 HSSS

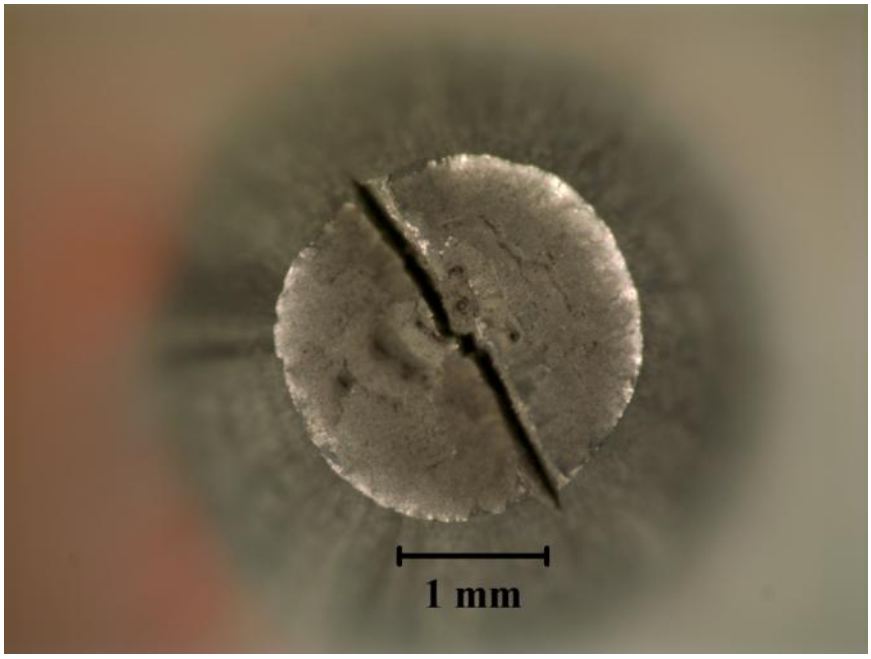

Figure C.8 Fracture surface of 2101 HSSS

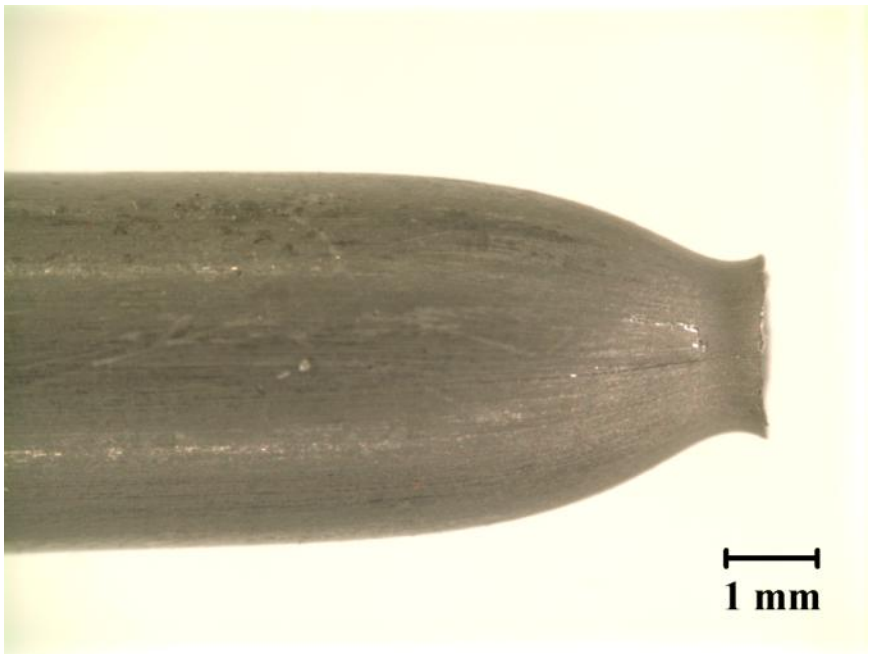

Figure C.9 Fracture surface of 2205 HSSS

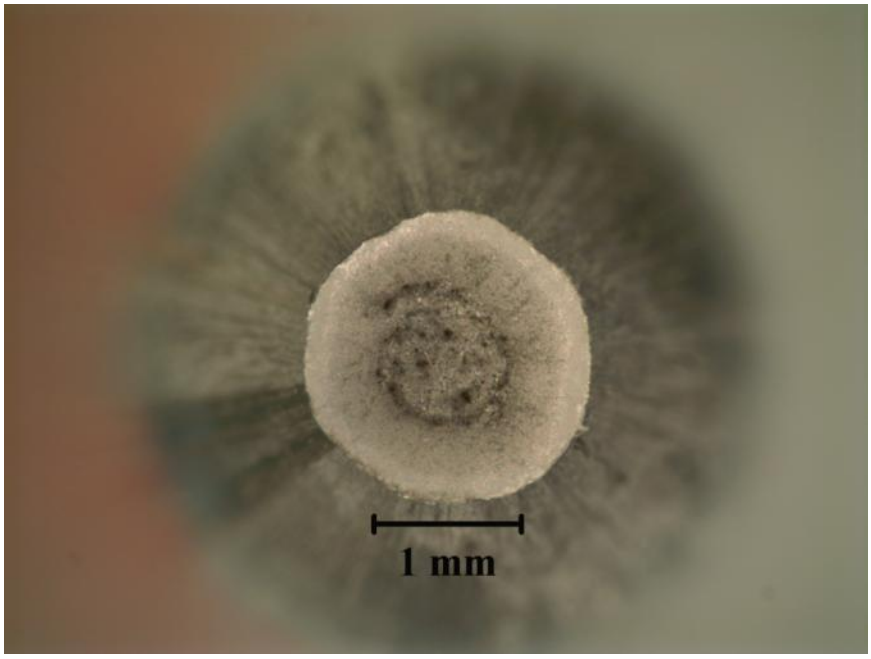

Figure C.10 Fracture surface of 2205 HSSS

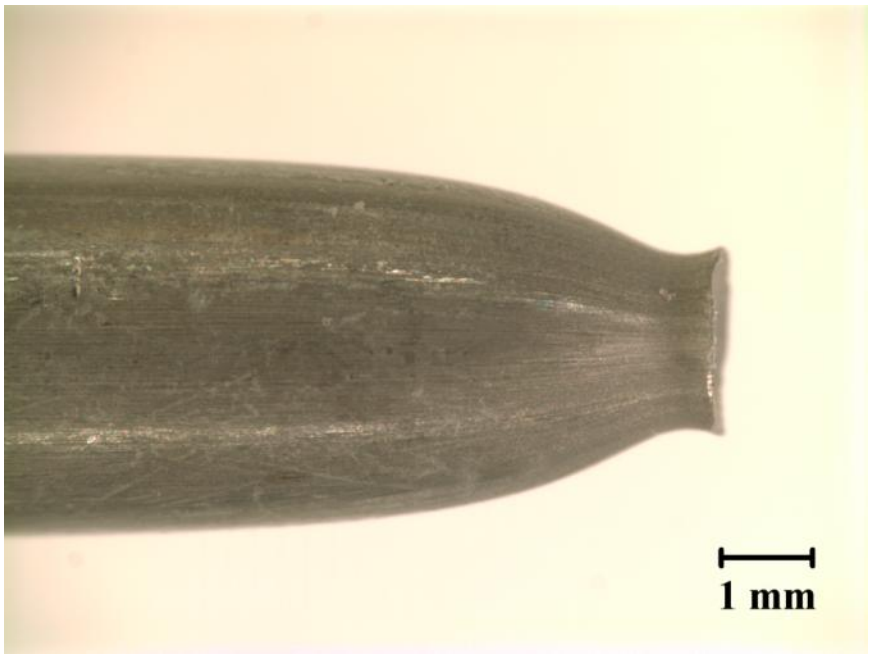

Figure C.11 Fracture surface of 2304 HSSS

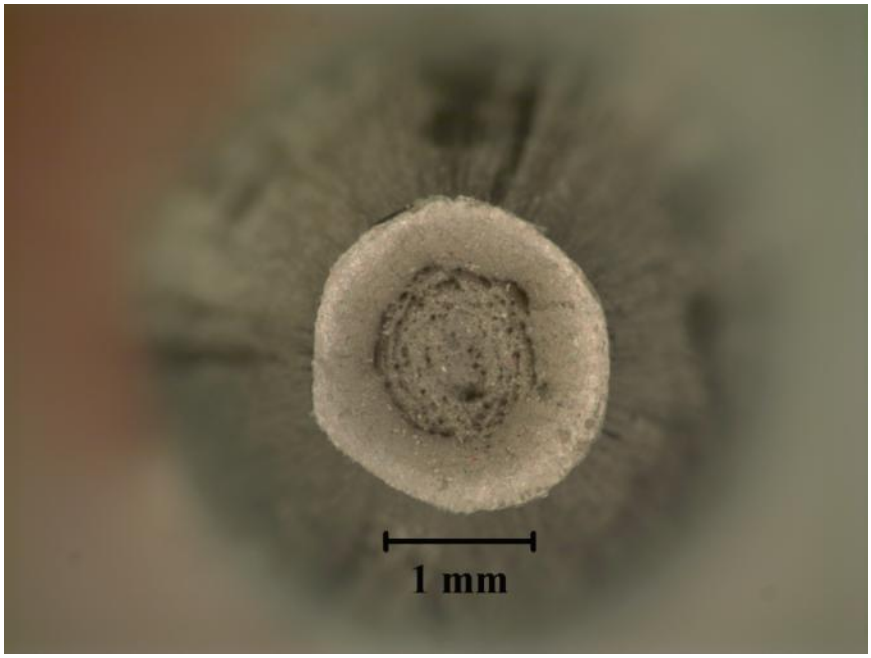

Figure C.12 Fracture surface of 2304 HSSS

Figure C.13 Fracture surface of 17-7 HSSS

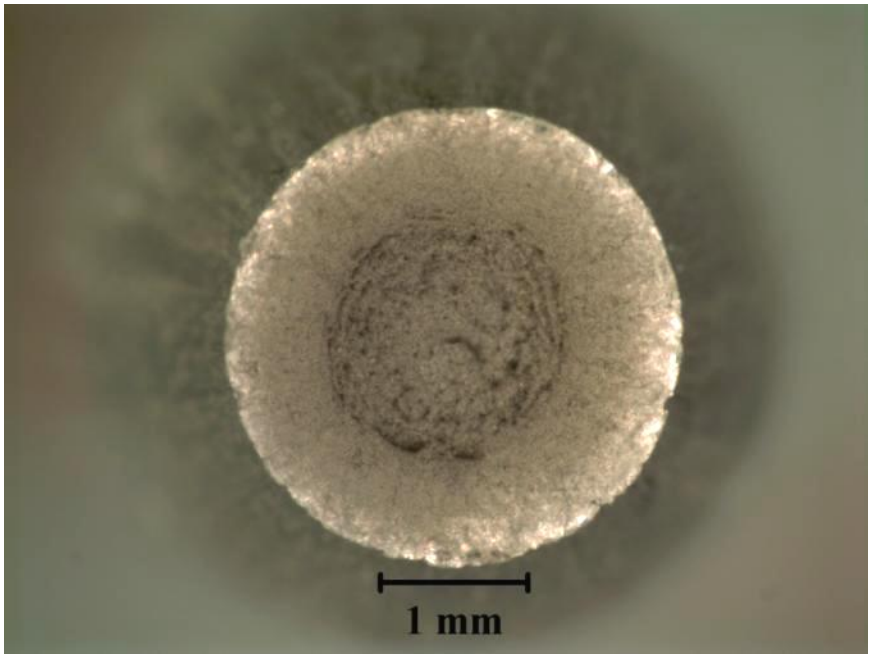

Figure C.14 Fracture surface of 17-7 HSSS

APPENDIX D: WIRE SPECIMEN PREPARATION TECHNIQUES

The following figures and captions describe the procedures used to make wire geometry test specimens used in all corrosion studies.

Figure D.1 Wire rod cut using slow-speed water-cooled diamond saw

Figure D.2 Cut wire specimen along with heat-shrink tubing and PTFE plug to be epoxied to the end of the wire segment

Figure D.3 Securing heat shrink tubing to wire segment with heat gun

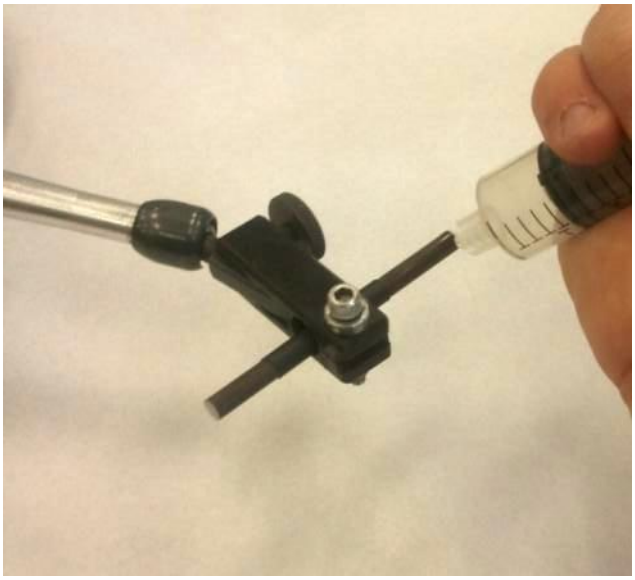

Figure D.4 Application of silicone sealant circumferentially at crevice site located at heat-shrink tubing and PTFE plug interface with wire segment

Figure D.5 Completed wire corrosion test specimen

APPENDIX E: STRAND SPECIMEN PREPARATION TECHNIQUES

The following figures and captions describe the procedures used to make strand geometry test specimens used in all corrosion studies.

Figure E.1 Strand segments cut using slow-speed water-cooled diamond saw. Two plastic wire ties are secured around the seven-wire strand to prevent relative movement of the wires from their as-received geometry.

Figure E.2 Strand segments ultrasonicated in ethanol for 1 min following cutting to remove and debris from the interstices of the strand.

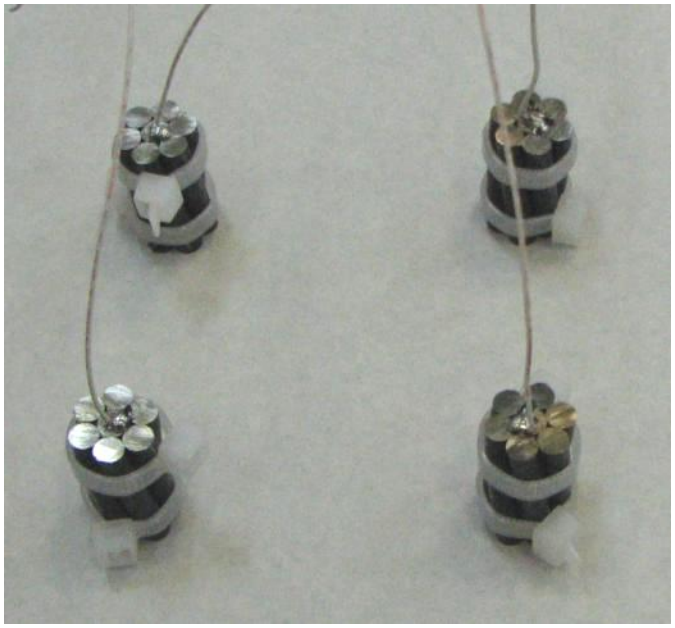

Figure E.3 Segments of insulated wire soldered onto the top of the strand segments to provide an electrical connection for us in corrosion experiments.

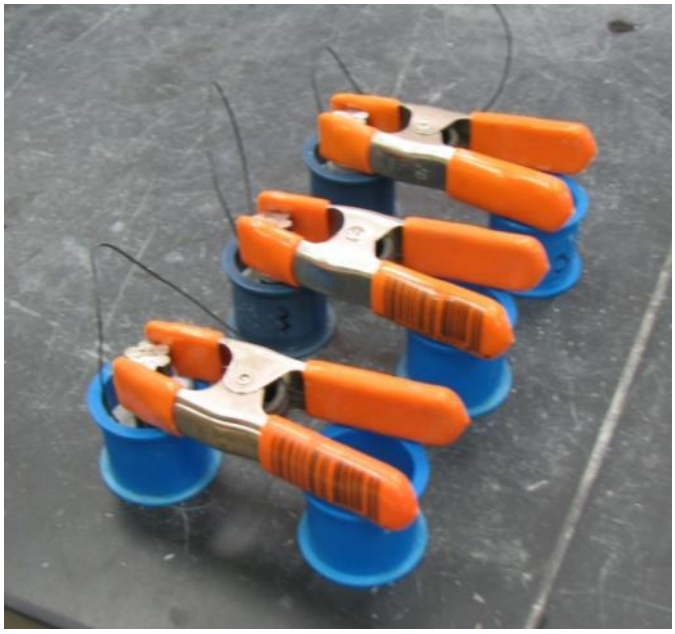

Figure E.4 Strand segments embedded in epoxy while being secured with spring clamps. Epoxy was allowed to “set up” for approximately 30 min prior to immersing strand segments.

Figure E.5 Completed strand corrosion test specimen

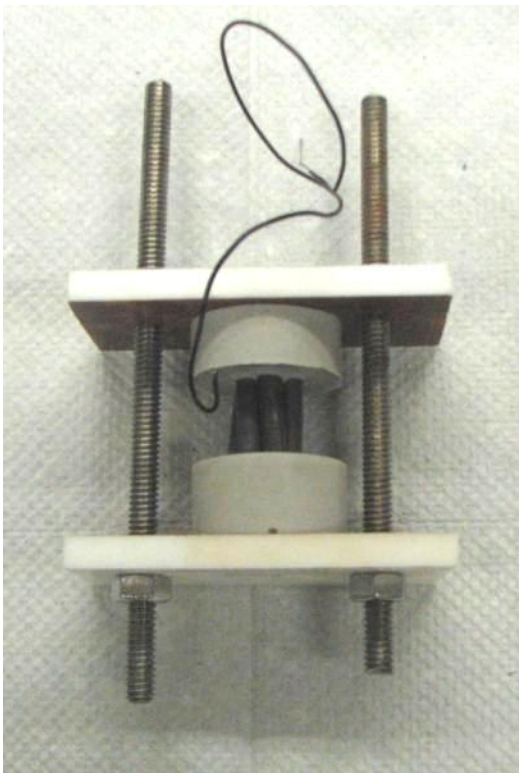

Figure E.6 Strand specimen placed in frame of PTFE sheets and secured using threaded rods and nuts of Hasteloy C276

APPENDIX F: ASTM G48 MASS LOSS

Preliminary testing to comparatively evaluate corrosion susceptibility was performed using ASTM G48 – *Standard Test Methods for Pitting and Crevice Corrosion Resistance of Stainless Steels and Related Alloys by Use of Ferric Chloride Solution*. Triplicate HSSS samples were cut to 6 in (152.4 mm) length in immersed in a $FeCl_3$ solution maintained at 50 ˚C for 72 hours in an environmental chamber. All HSSSs produced in Phase 3 were tested in addition to a sample of Nitronic® 33 prestressing wire received from Insteel Wire Products Corporation. The experimental setup used is shown in Figure F.1.

Mass loss results from ASTM G48 tests are shown in Figure F.2. HSSSs 304, 2101, 2304, and 17-7 showed similar mass loss values. Interestingly, 316 HSSS exhibited higher mass loss than 304, an outcome which is unexpected and may be the result of microstructural features caused by the heavy cold drawing of 316 HSSS in order to achieve strengths greater than 1380 MPa (200 ksi). This reduced corrosion resistance of 316 also likely derives from the precipitates and high sulfur content discussed in Chapter 4. Duplex grade 2205 was the only HSSS which suffered little damage under this extremely aggressive exposure.

(a) Triplicate wire segments placed in $FeCl_3$ exposure cell

(b) Wire segments with $FeCl_3$ solution added to exposure cell

(c) Containers in environmental chamber

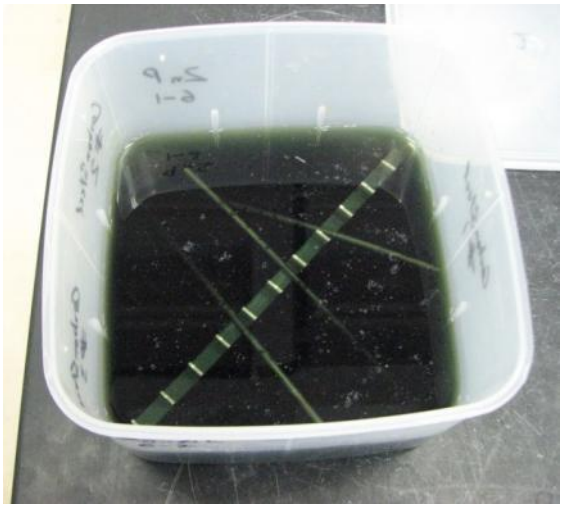

(d) Solution following testing

Figure F.1 ASTM G48 experimental setup

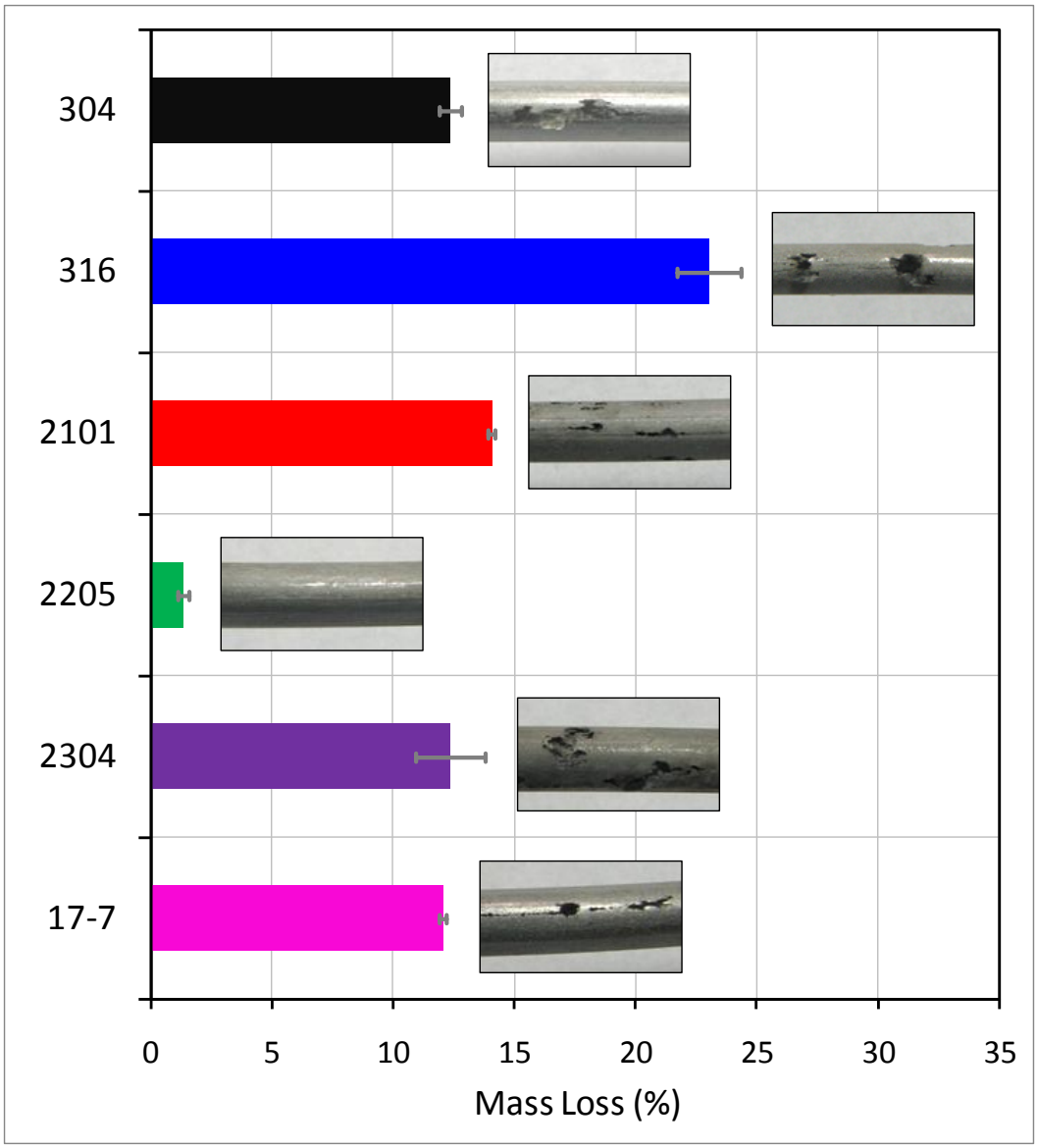

Figure F.2 ASTM G48 Mass loss results and surface corrosion damage

APPENDIX G: PASSIVATION OF 2205 AND 2304 STRANDS

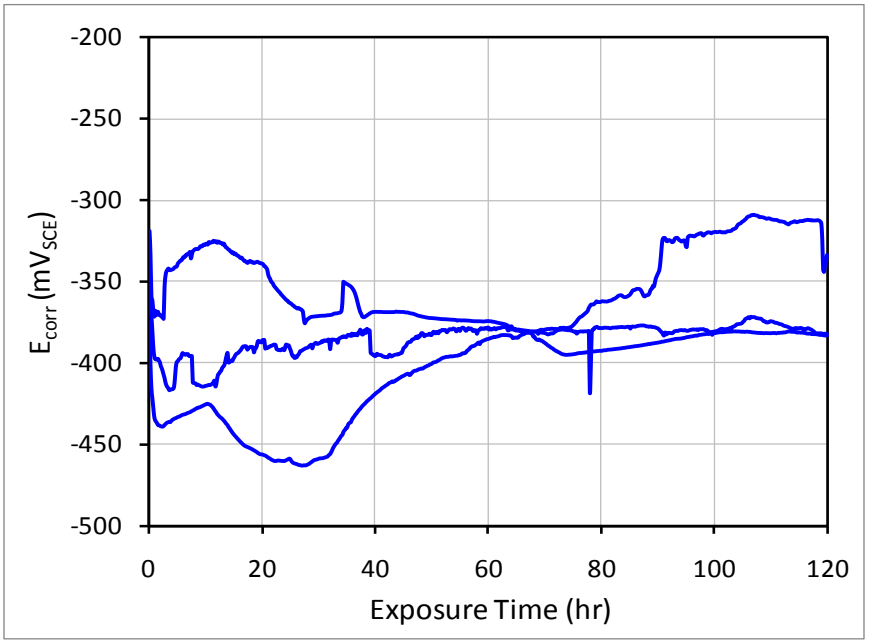

Figure G.1 E_{corr} vs. time of triplicate 2205 strand specimens in alkaline solutions

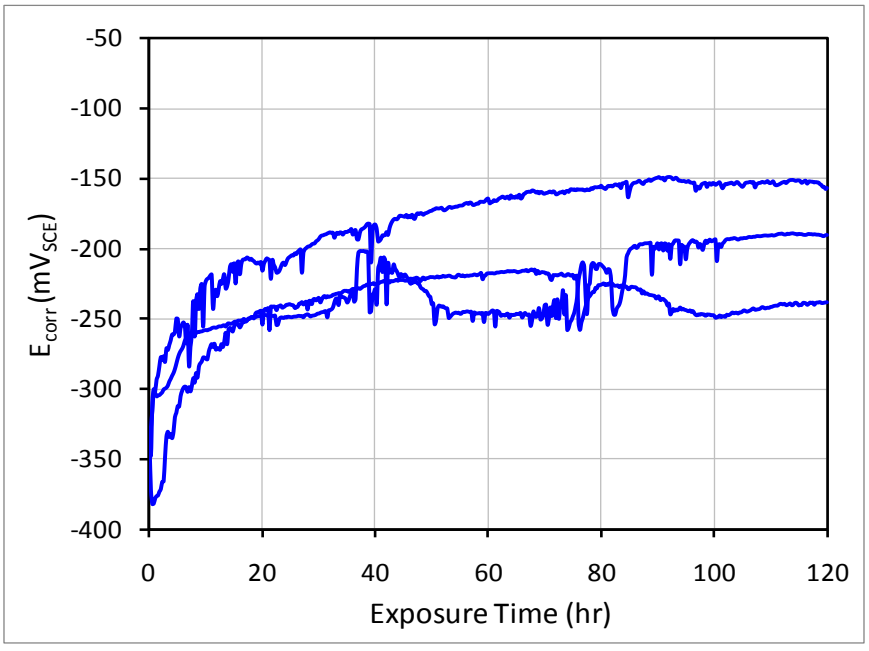

Figure G.2 E_{corr} vs. time of triplicate 2205 strand specimens in carbonated solutions

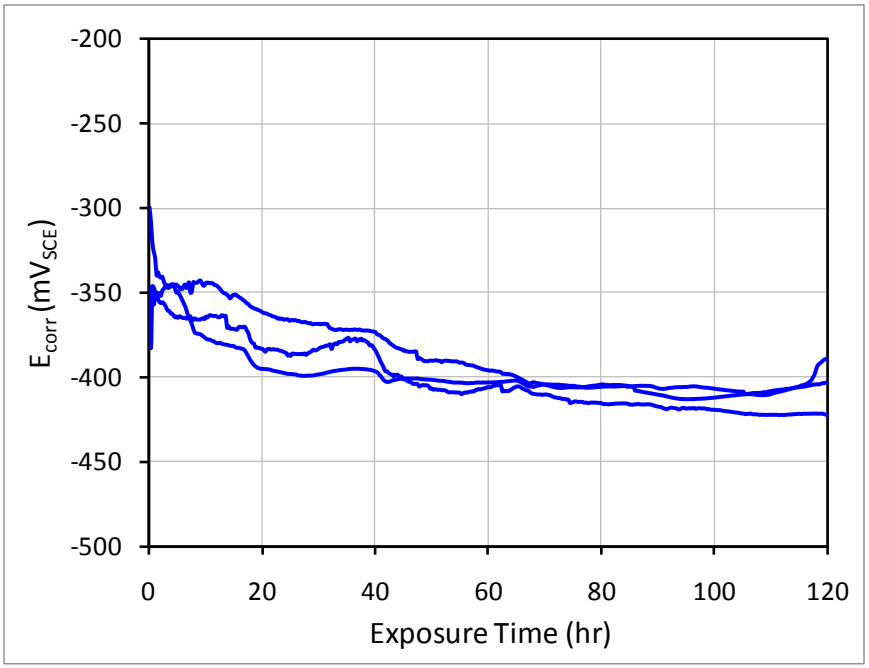

Figure G.3 E_{corr} vs. time of triplicate 2304 strand specimens in alkaline solutions

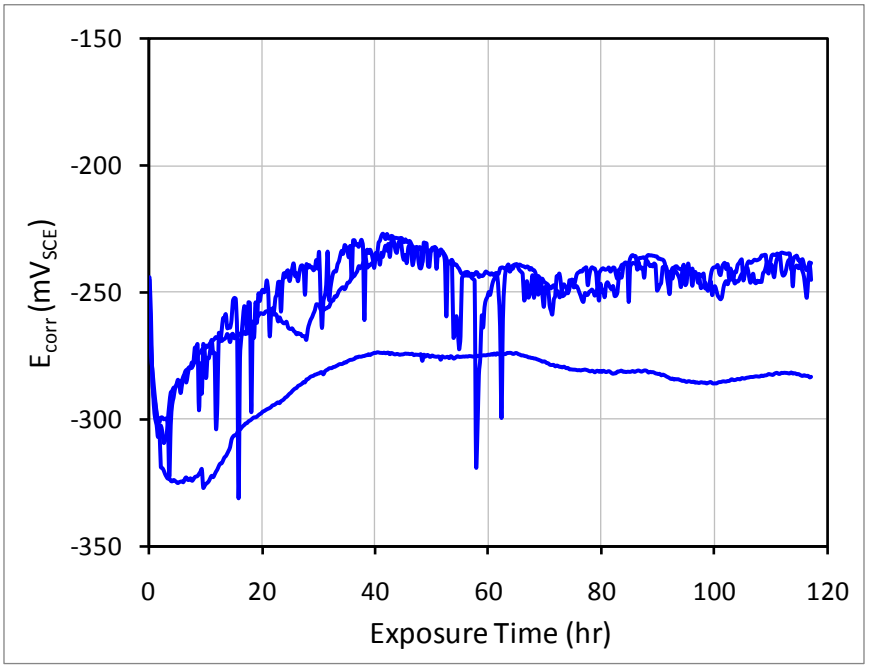

Figure G.4 E_{corr} vs. time of triplicate 2304 strand specimens in carbonated solutions

APPENDIX H: INFLUENCE OF SULFATES ON PASSIVATION

Water samples recovered during bridge inspections along Georgia's coast showed high sulfate contents ([SO_4^{2-}] as high as 2000 ppm). Sulfates are also typically present in the concrete pore solution due to the presence of ettringite, monosulfate hydrate, and residual gypsum. Previous studies in the pulp and paper industry have shown that, depending on alloy composition, sulfates can promote passivation in caustic environments but may hinder passivation in acidic environments. These effects have seen limited investigation in concrete systems.

In order to investigate the influence of sulfates on electrochemical behavior, specimens were exposed to alkaline and carbonated concrete pore solutions with of 0, 1000, and 2000 ppm of SO_4^{2-} added as Na_2SO_4. Studies were limited to the 1080 prestressing steel and 304, 2205, and 2304 HSSSs. Passivation behavior was monitored with open circuit potential measurements for 120 hr, along with polarization resistance and potentiodynamic polarization measurements on selected specimens. The following figures show the effect of sulfate addition on passivation of the alloys evaluated.

The addition of sulfates was found to have little impact on the passivation of 1080 and 304 in carbonated and alkaline solutions. However, sulfates did influence the passivation behavior of duplex HSSSs 2205 and 2304. At lower concentrations (1000 ppm), the passivation of 2205 and 2304 was accelerated to more noble (positive) potentials, particularly in alkaline solutions. However, at the increased sulfate concentration of 2000 ppm, passivation of 2205 and 2304 was hindered and more active (negative) potentials were achieved, suggesting a decrease in corrosion resistance.

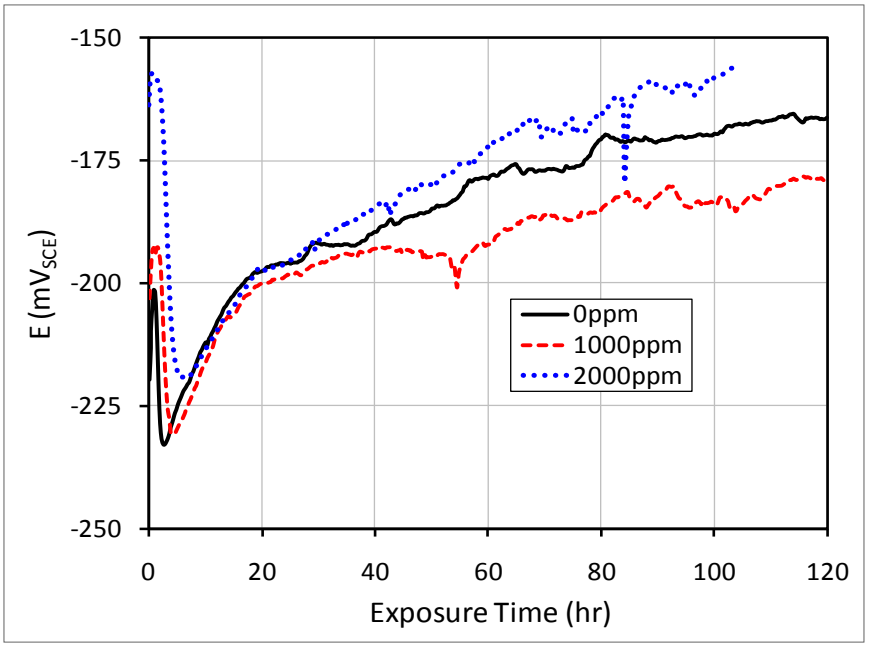

Figure H.1 1080 HSSS exposed to alkaline solutions with 0, 1000, and 2000ppm SO_4^{2-}

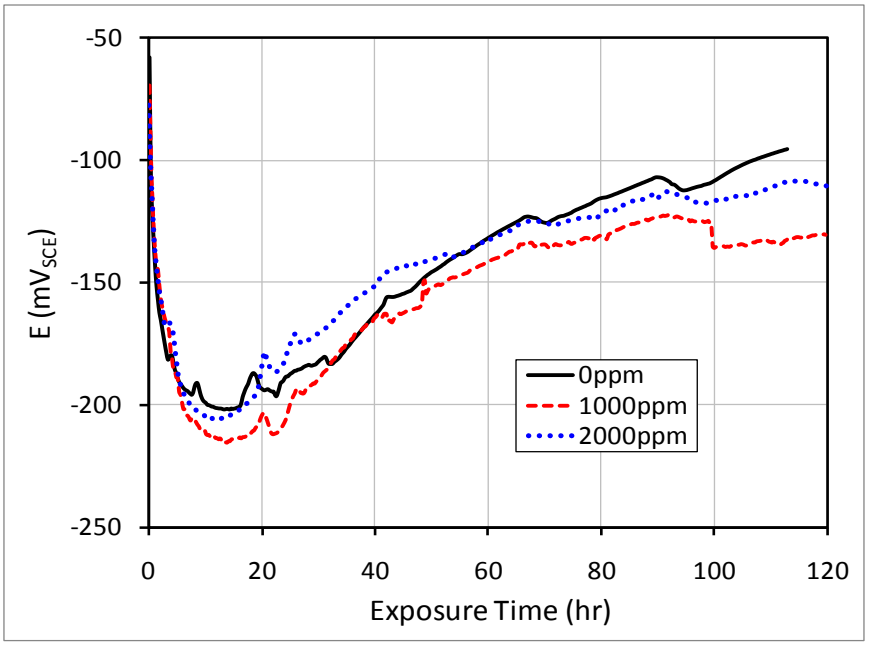

Figure H.2 1080 HSSS exposed to carbonated solutions with 0, 1000, and 2000ppm SO_4^{2-}

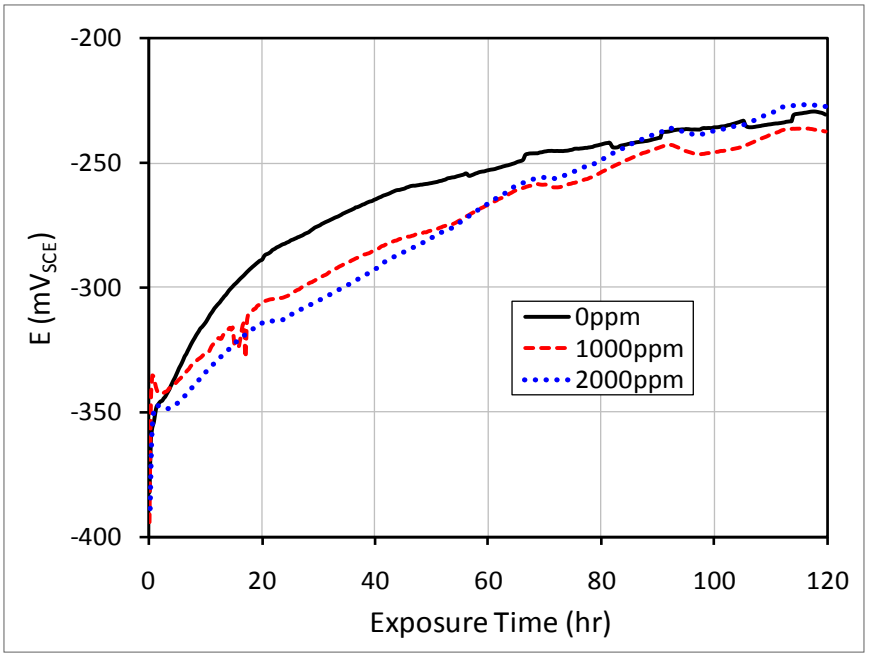

Figure H.3 304 HSSS exposed to alkaline solutions with 0, 1000, and 2000ppm SO_4^{2-}

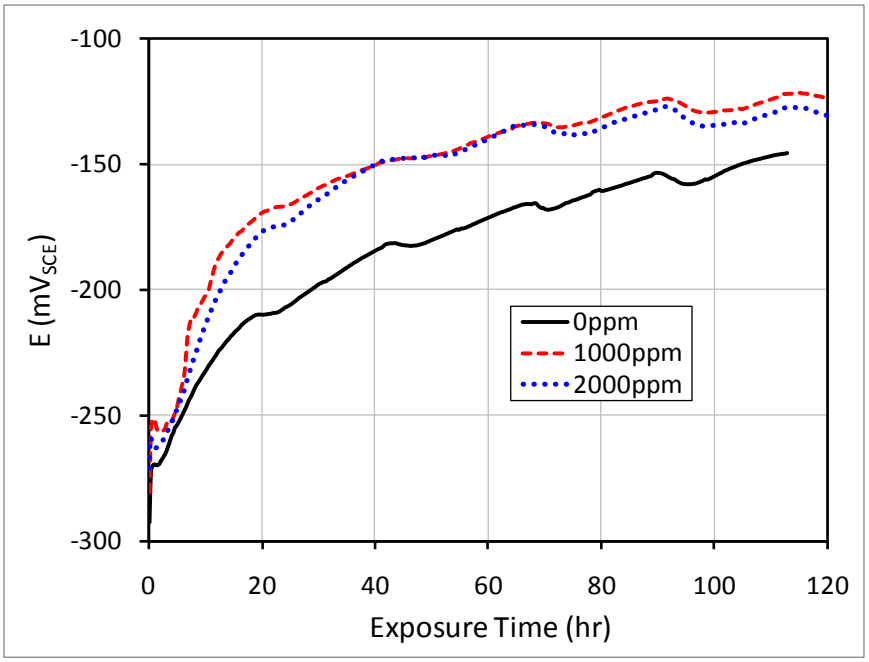

Figure H.4 304 HSSS exposed to carbonated solutions with 0, 1000, and 2000ppm SO_4^{2-}

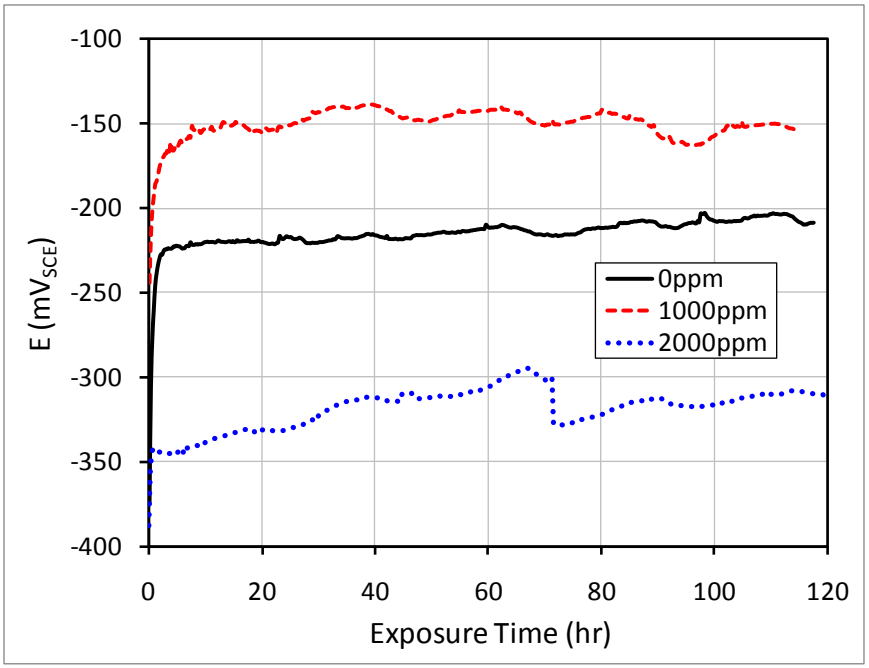

Figure H.5 2205 HSSS exposed to alkaline solutions with 0, 1000, and 2000ppm SO_4^{2-}

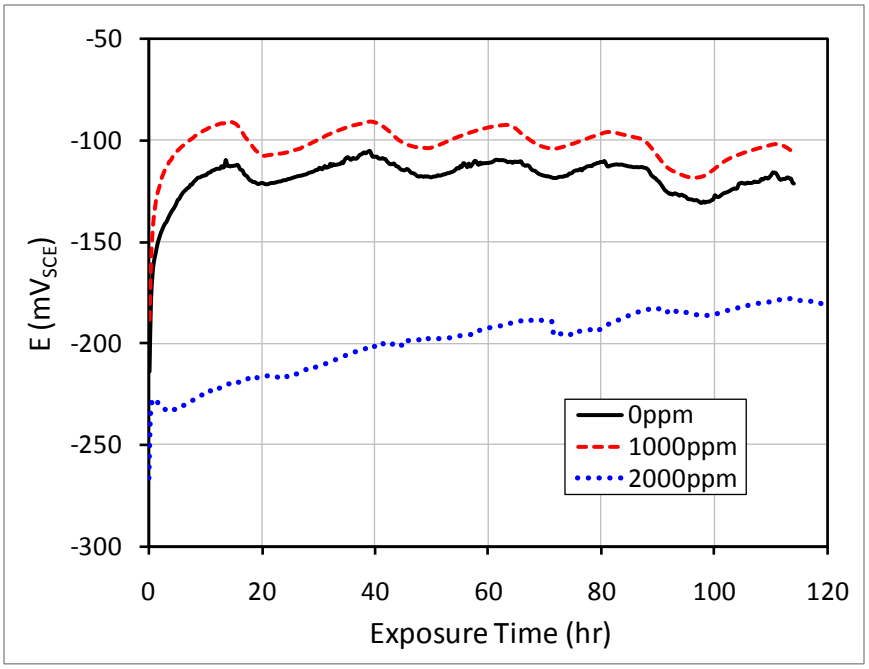

Figure H.6 2205 HSSS exposed to carbonated solutions with 0, 1000, and 2000ppm SO_4^{2-}

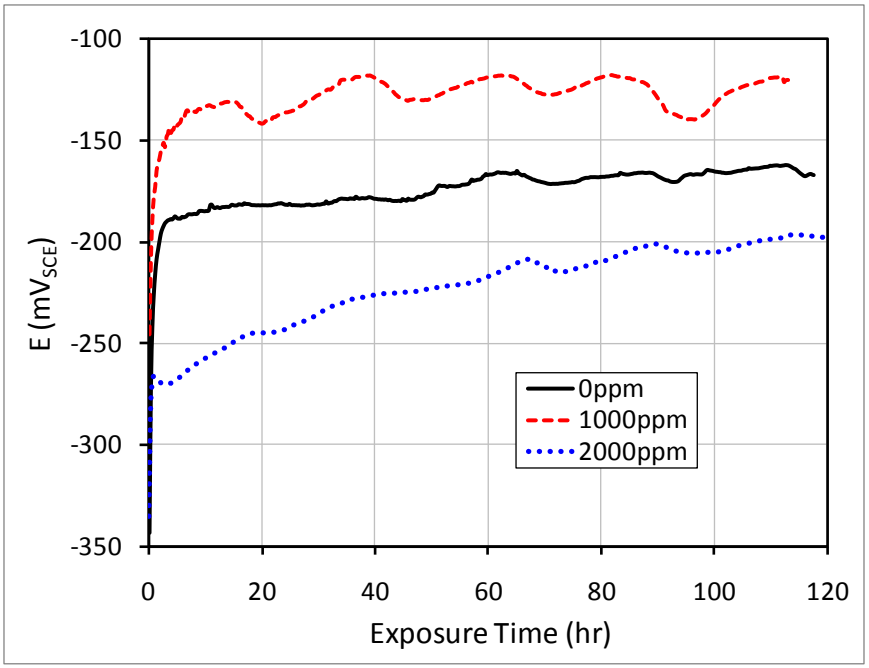

Figure H.7 2304 HSSS exposed to alkaline solutions with 0, 1000, and 2000ppm SO_4^{2-}

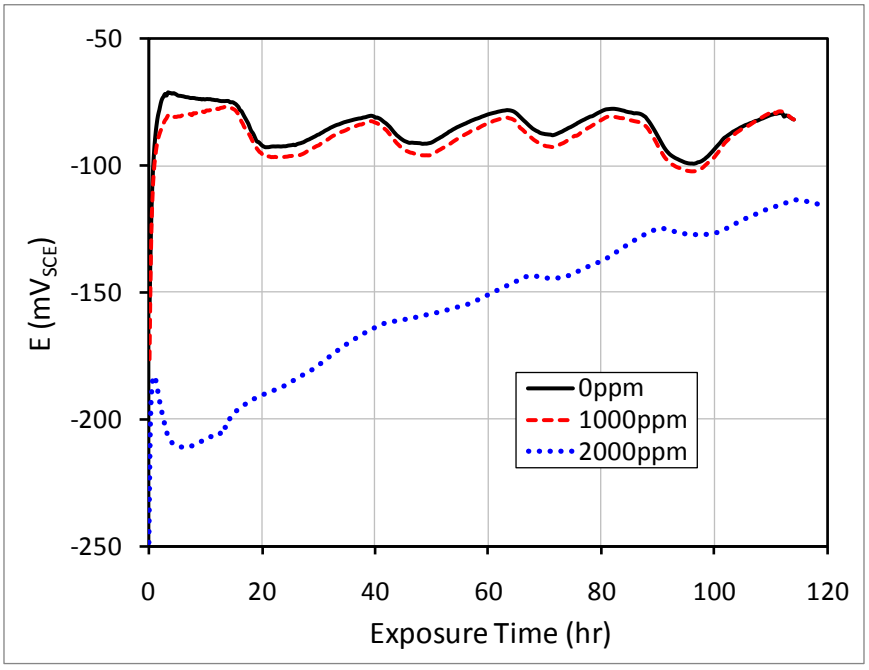

Figure H.8 2304 HSSS exposed to carbonated solutions with 0, 1000, and 2000ppm SO_4^{2-}

Even though the addition of sulfates was found the influence the passivation behavior of duplex grades 2205 and 2304, there seemed to be little effect on observed polarization behavior. Figure H.9 depicts potentiodynamic polarization curves obtained from 2304 HSSS specimens immersed in carbonated solutions with 0, 1000, and 2000 ppm SO_4^{2-}. Here, the addition of SO_4^{2-} has a negligible effect on polarization behavior. Further research is necessary to determine the mechanism by which sulfates influence the passivation behavior of HSSSs, especially duplex grades. This research may include microstructural characterization of the passive film formed as well as electrochemical chloride threshold testing to determine the impact of sulfates on corrosion resistance.

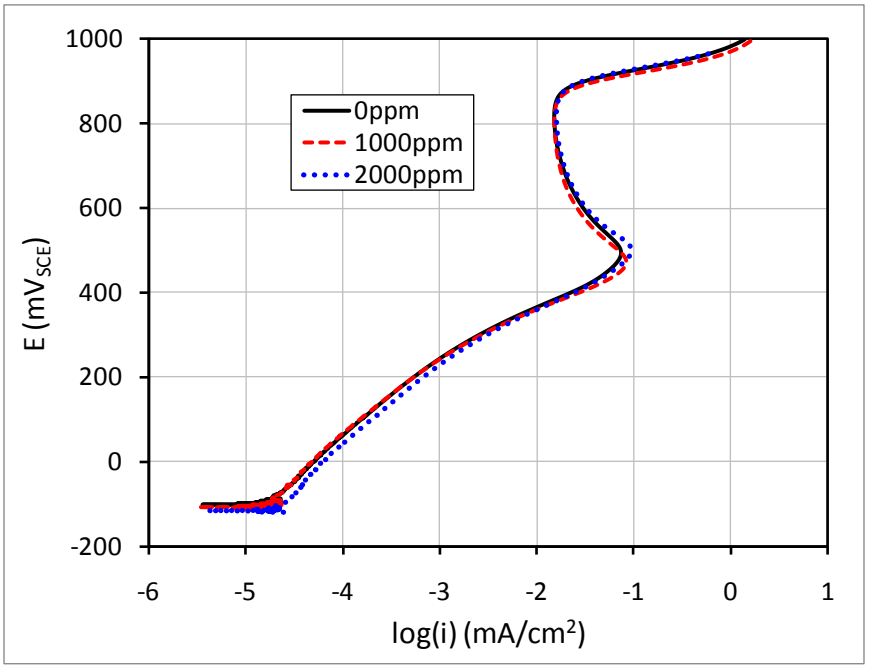

Figure H.9 2304 HSSS exposed to carbonated solutions with 0, 1000, and 2000ppm SO_4^{2-}

APPENDIX I: ENVIRONMENTALLY ASSISTED CRACKING IN SLOW-STRAIN RATE TEST SPECIMENS

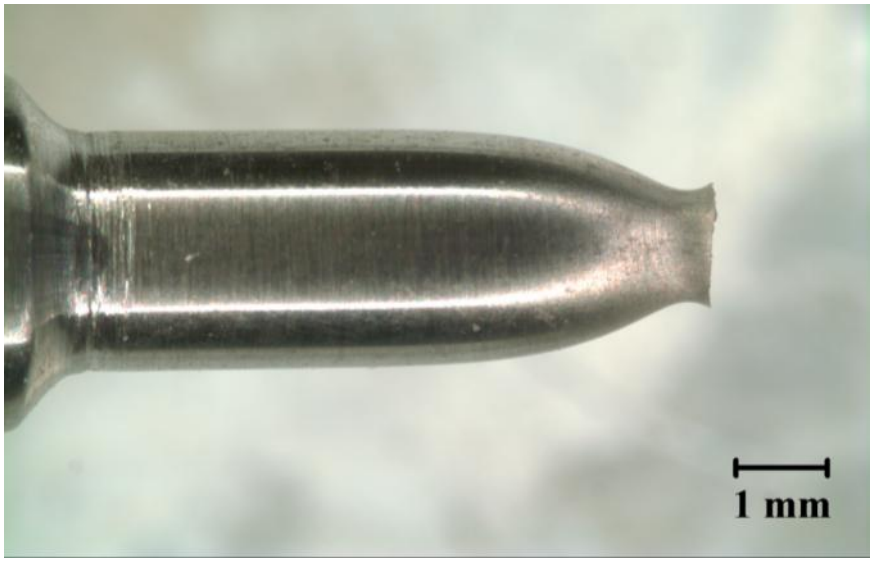

Figure I.1 2205 slow-strain rate test (SSRT) specimen tested in air

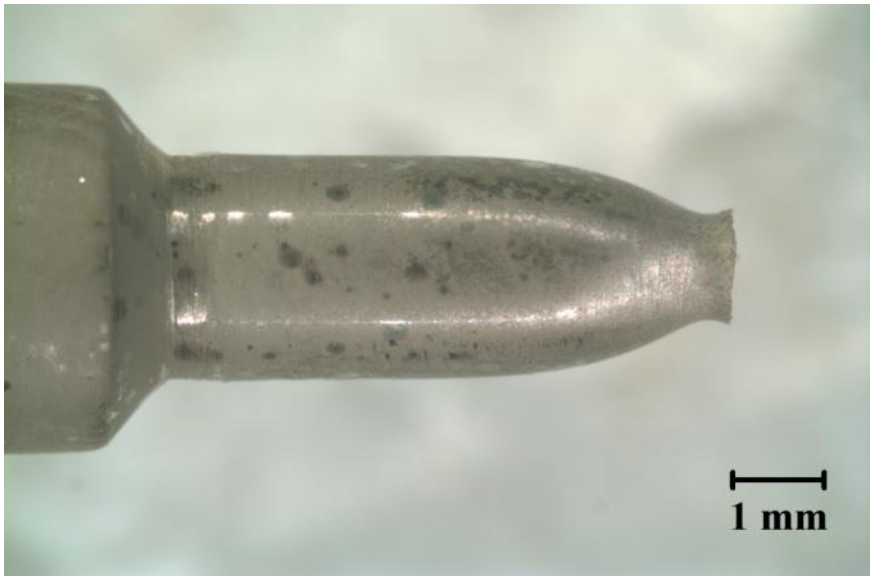

Figure I.2 2205 SSRT specimen tested in an alkaline solution with 0.5 M Cl^-

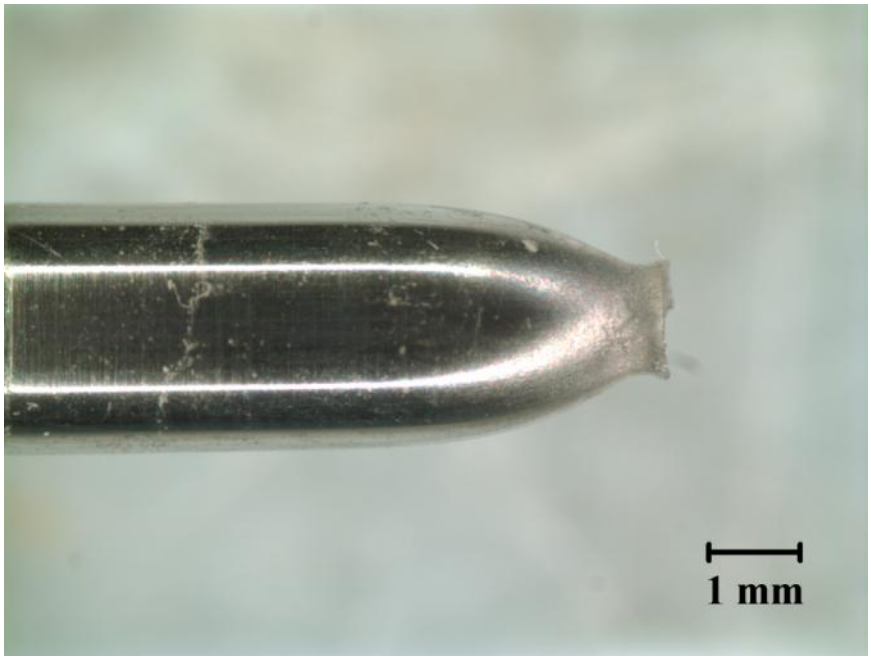

Figure I.3 2205 SSRT specimen tested in a carbonated solution with 0.5 M Cl^-

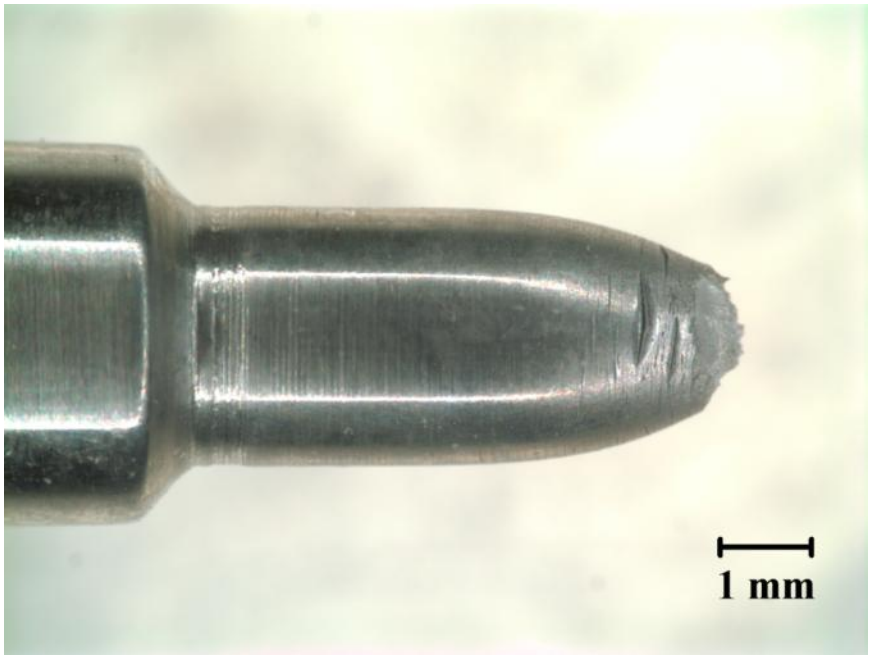

Figure I.4 2205 SSRT specimen tested in an alkaline solution with an applied cathodic potential of -1000 mV_{SCE}

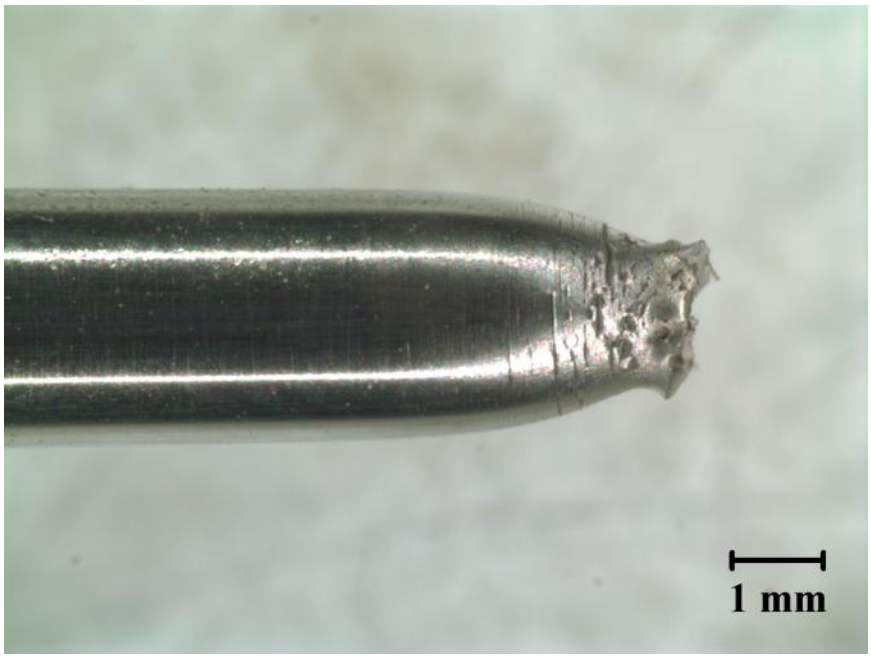

Figure I.5 2205 SSRT specimen tested in a carbonated solution with an applied cathodic potential of -820 mV_{SCE}

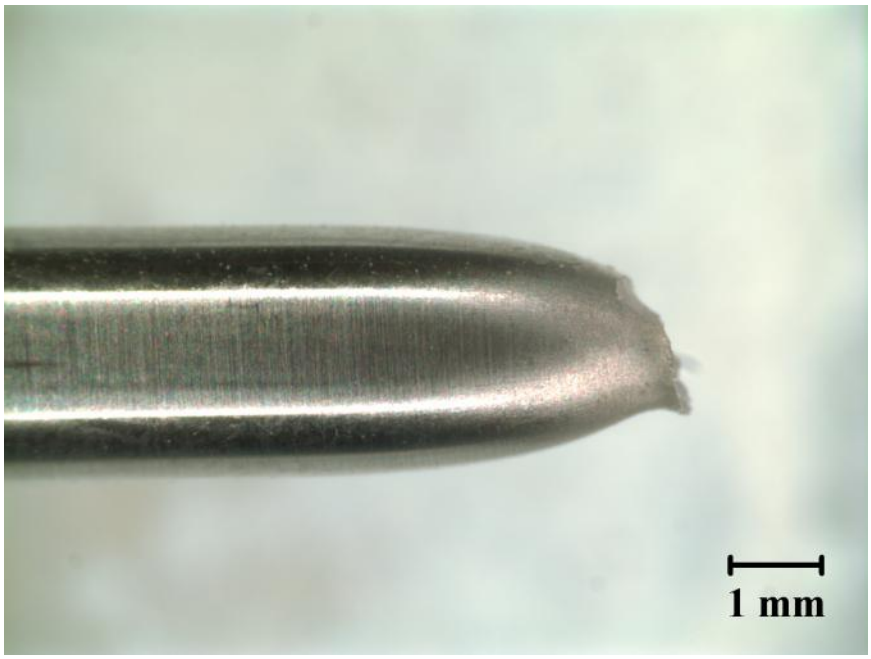

Figure I.6 2304 SSRT specimen tested in air

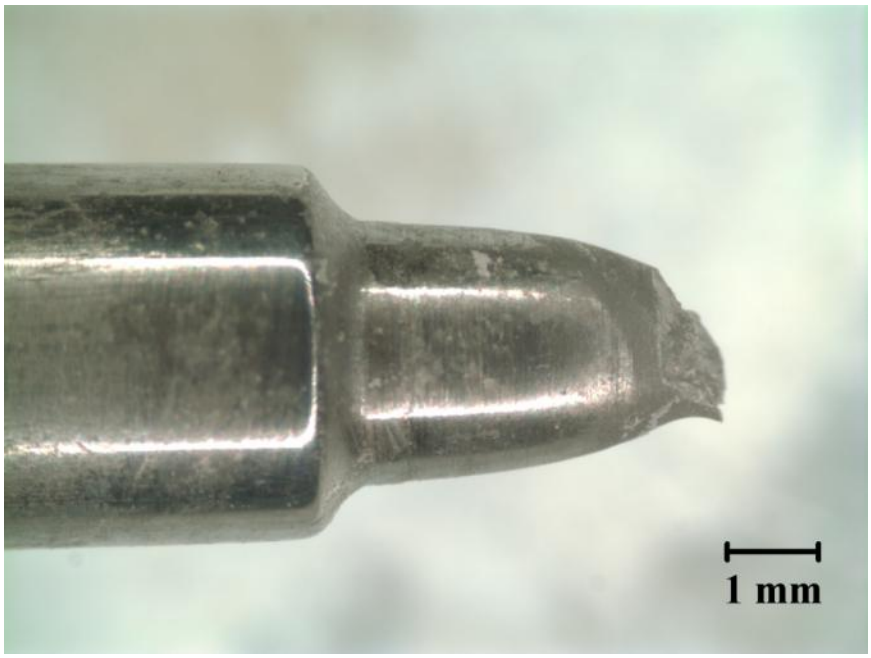

Figure I.7 2304 SSRT specimen tested in an alkaline solution with 0.5 M Cl^-

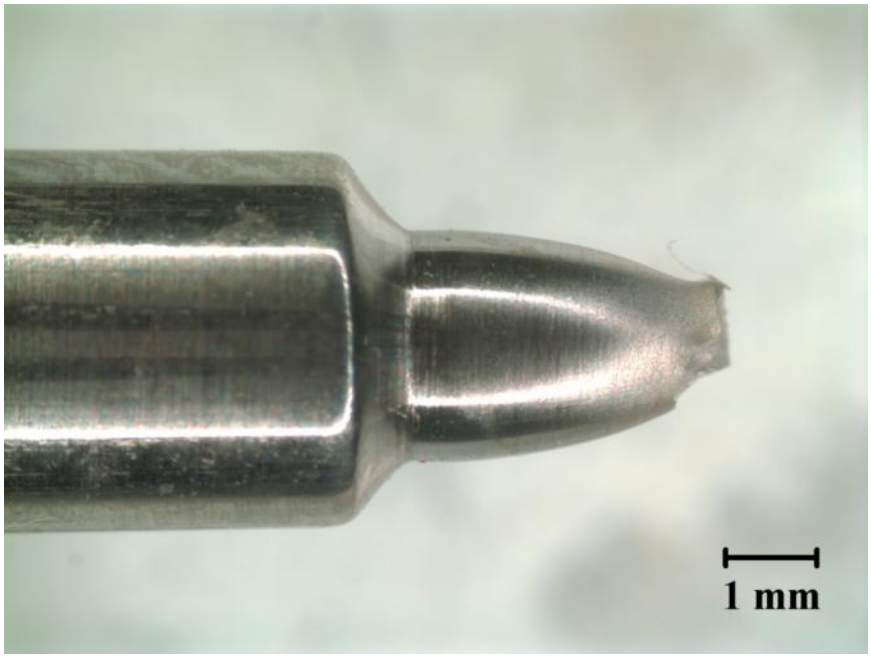

Figure I.8 2304 SSRT specimen tested in a carbonated solution with 0.5 M Cl^-

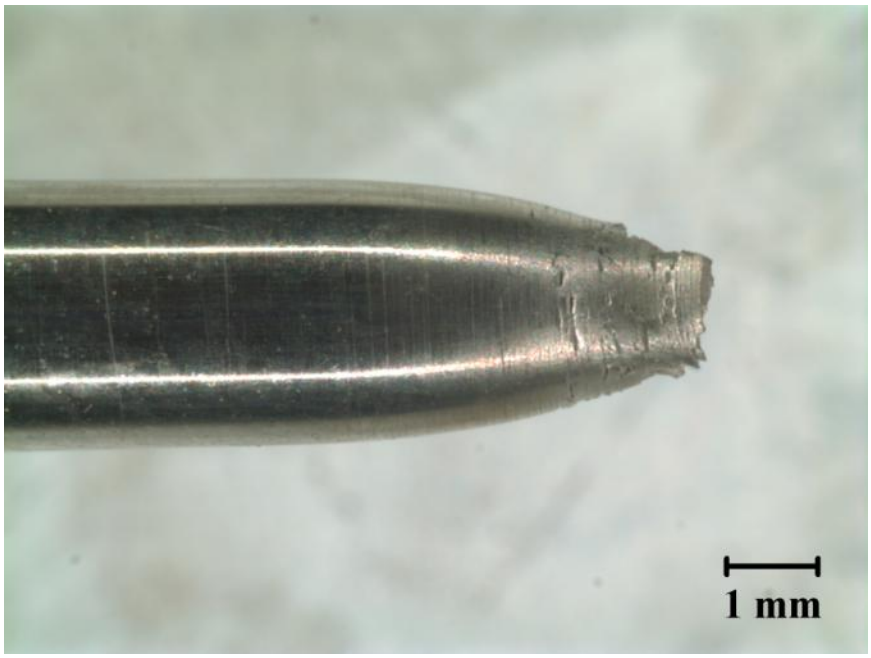

Figure I.9 2304 SSRT specimen tested in an alkaline solution with an applied cathodic potential of -1000 mV_{SCE}

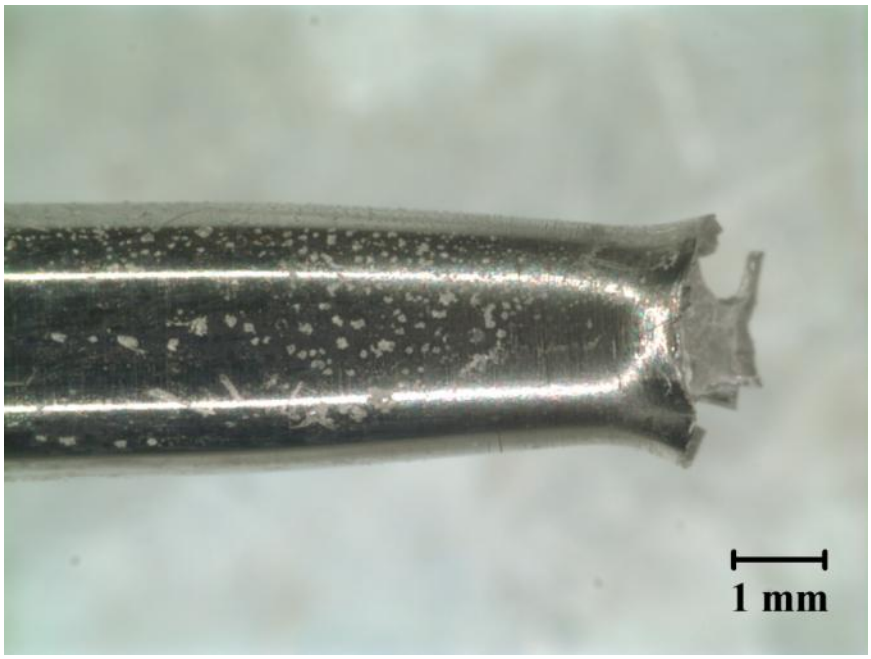

Figure I.10 2304 SSRT specimen tested in a carbonated solution with an applied cathodic potential of -820 mV_{SCE}

REFERENCES

ACI 222 (2001), "Protection of Metals in Concrete Against Corrosion," American Concrete Institute, Farmington Hills, MI.

ACI 222.2 (2001), "Corrosion of Prestressing Steels," American Concrete Institute, Farmington Hills, MI.

ACI 318 (2008), "Building Code Requirement for Structural Concrete and Commentary," American Concrete Institute, Farmington Hills, MI.

Addari, D., Elsener, B., and Rossi, A. (2008), "Electrochemistry and surface chemistry of stainless steels in alkaline media simulating concrete pore solutions," *Electrochimica Acta*, V. 53 (27), pp. 8078-8086.

Ahern, M. E. (2005), "Design and Fabrication of a Compact Specimen for Evaluation of Corrosion Resistance of New Post-Tensioning Systems," MS Thesis, University of Texas at Austin, Austin, TX.

Alonso, C., Castellote, M., and Andrade, C. (2002), "Chloride Threshold Dependence of Pitting Potential of Reinforcements," *Electrochimica Acta*, V. 47 (21), pp. 3469-3481.

Alonso, M. C. (2007), "Corrosion Performance of High Strength Stainless Steel for Tendon Applications," Proceeding of the Final Conference of COST Action 534, Toulouse, France.

Alonso, M. C., and Recio, F. J. (2007), "Aceros Inoxidables De Alta Resitencia Mecanica En Medios Alcalinos con Cloruros," *Anales de la Mecánica de Fractura*, V. 2, pp. 649-654.

Alonso, M. C., Recio, F. J., and Sanchez, M. (2008), "High Strength Stainless Steels for Prestressed Concrete Structures in Marine Environment," Proceedings of the 1st International Conference on Construction Heritage in Coastal and Marine Environments: Damage, Diganosis, Maintenance and Rehabilitation, Lisbon, Portugal.

Alonso, M. C., and Sanchez, M. (2009), "Analysis of the Variability of Chloride Threshold Values in the Literature," *Materials and Corrosion*, V. 60 (8), pp. 631-637.

Alvarez-Armas, I. (2008), "Duplex Stainless Steels: Brief History and Some Recent Alloys," *Recent Patents on Mechanical Engineering*, V. 1, pp. 51-57.

Alvarez, S. M., Bautista, A., and Velasco, F. (2011), "Corrosion Behaviour of Corrugated Lean Duplex Stainless Steels in Simulated Concrete Pore Solutions," *Corrosion Science*, V. 53 (5), pp. 1748-1755.

Anderson, W. R. (1964), "Steel for Prestressed Concrete," *PCI Journal*, V. 9 (2), pp. 108-116.

Angst, U., Elsener, B., Larsen, C. K., and Vennesland, Ø. (2009), "Critical Chloride Content in Reinforced Concrete - A Review," *Cement and Concrete Research*, V. 39 (12), pp. 1122-1138.

Ann, K. Y., and Song, H.-W. (2007), "Chloride Threshold Level for Corrosion of Steel in Concrete," *Corrosion Science*, V. 49 (11), pp. 4113-4133.

Arnvig, P. E., and Houska, C. (2010). "Stainless Steel Specification for Corrosive Environments." ACI Fall 2010 Convention, Pittsburgh, PA.

Artuso, I., Dughiero, F., Lupi, S., Partisani, S., and Facchinelli, P. (2004a), "Installation for the Continuous Induction Heat Treatment of Wires," Applicazioni Termo Elettroniche, Brendola, Italy.

Artuso, I., Ghedin, S., Siega, P., and Visconti, A. (2004b), "Induction Furnace for Heat Treatment of Austenitic and/or Ferritic Steel Wires and Strands," Applicazioni Termo Elettroniche, Brendola, Italy.

Ashby, M. F., and Jones, D. R. H. (1998), Engineering Materials 1, Butterworth-Heinemann, Woburn, MA.

ASTM A276 (2008), "Standard Specification for Stainless Steel Bars and Shapes," American Society for Testing and Materials, West Conshohocken, PA.

ASTM A416 (2006), "Standard Specification for Steel Strand, Uncoated Seven-Wire for Prestressed Concrete," American Society for Testing and Materials, West Conshohoken, PA.

ASTM A751 (2008), "Standard Test Methods, Practices, and Terminology for Chemical Analysis of Steel Products." American Society of Testing and Materials, ed.West Conshohocken, PA.

ASTM A1035 (2009), "Standard Specification for Deformed and Plain, Low-carbon, Chromium, Steel Bars for Concrete Reinforcement." American Society of Testing and Materials, ed.West Conshohocken, PA.

ATI (2008), "AL 17-7 Precipitation Hardening Alloy Datasheet." Allegheny Ludlum Technologies Inc., Brackenridge, PA.

Atienza, J. M., and Elices, M. (2007), "Role of Residual Stresses in Stress Relaxation of Prestressed Concrete Wires," *Journal of Materials in Civil Engineering*, V. 19 (8), pp. 703-708.

Baldo, S., and Meszaros, I. (2010), "Effect of Cold Rolling on Microstructure and Magnetic Properties in a Metastable Lean Duplex Stainless Steel," *Journal of Materials Science*, V. 45 (19), pp. 5339-5346.

Bard, A. J., and Faulkner, L. R. (2001), "Electrochemical Methods", John Wiley & Sons, Inc., Hoboken, NJ.

Bertolini, L., Elsener, B., Pedeferri, P., and Polder, R. (2004), "Corrosion of Steel in Concrete", Wiley-VCH, Weinheim, Germany.

Bertolini, L., and Redaelli, E. (2009), "Depassivation of Steel Reinforcement in Case of Pitting Corrosion: Detection Techniques for Laboratory Studies," *Materials and Corrosion*, V. 60 (8), pp. 608-616.

Bhattacharya, A. (2008), "Stress Corrosion Cracking of Duplex Stainless Steels in Caustic Solutions," PhD Dissertation, Georgia Institute of Technology, Atlanta, GA.

Boddy, A., Bentz, E., Thomas, M. D. A., and Hooton, R. D. (1999), "An Overview and Sensitivity Study of a Multimechanistic Chloride Transport Model," *Cement and Concrete Research*, V. (29), pp. 827-837.

Böhni, H. (2005), Corrosion in Reinforced Concrete Structures, Woodhead Publishing Ltd., Cambridge, UK.

Bragshaw, P. (2011), "Preforming," Loos HotWire, Loos and Company, Pomfret, CT.

Brooks, M. A. (2003), "Influence of Interstitial Crevice Corrosion in Accelerated Corrosion Testing," BS Thesis, Penn State University, State College, PA.

Broomfield, J. P. (2007), Corrosion of Steel in Concrete, Taylor and Francis Group, New York, NY.

Chai, G., Soderman, A., and Etheridge, P. (2007), "High and Super-High-Strength Duplex Stainless Steels for Wire Applications," Sandvick Materials Technology, Sandviken, Sweden.

Chandler, K. A. (1984), Marine and Offshore Corrosion, Butterworth & Company Ltd., Surrey, UK.

Chang, C. F., and Chen, J. W. (2006), "The Experimental Investigation of Concrete Carbonation Depth," *Cement and Concrete Research*, V. 36 (9), pp. 1760-1767.

Cherry, B. W., and Price, S. M. (1980), "Pitting, Crevice and Stress-Corrosion Cracking Studies of Cold Drawn Eutectoid Steels," Corrosion Science, V. 20 (11-12), pp. 1163.

Clemena, G. G. (2003), "Investigation of the Resistance of Several New Metallic Reinforcing Bars to Chloride-Induced Corrosion in Concrete," Virginia Transportation Research Council, Charlottesville, VA.

Cook, D. C. (1987), "Strain Induced Martensite Formation in Stainless-Steel," *Metallurgical Transactions A-Physical Metallurgy and Materials Science*, V. 18 (2), pp. 201-210.

Cottrell, A. H. (1997), "Logarithmic and Andrade creep," *Philosophical Magazine Letters*, V. 75 (5), pp. 301-307.

Cramer, S. D., Jr., B. S. C., Bullard, S. J., Holcomb, G. R., Russell, J. H., Nelson, F. J., Laylor, H. M., and Soltesz, S. M. (2002), "Corrosion Prevention and Remediation Strategies for Reinforced Concrete Coastal Bridges," *Cement and Concrete Composites*, V. 24, pp. 101-117.

Crank, J. (1980), The Mathematics of Diffusion, Oxford University Press, New York, NY.

Dash, J., and Otte, H. M. (1963), "Martensite Transformation in Stainless Steel," *Acta Metallurgica*, V. 11 (10), pp. 1169-1178.

DeLong, W. T., Ostrom, G. A., and Szumachowski, E. R. (1956), "Measurement and calculation of ferrite in stainless steel weld metal," *Journal of Welding*, V. 35 (11), pp. 521-528.

Diaz, B., Freire, L., Novoa, X. R., and Perez, M. C. (2009), "Electrochemical behaviour of high strength steel wires in the presence of chlorides," *Electrochimica Acta*, V. 54 (22), pp. 5190-5198.

Dupoiron, F., and Audouard, J. P. (1996), "Duplex Stainless Steels: a High Mechanical Properties Stainless Steel Family," *Scandinavian Journal of Metallurgy*, V. (25), pp. 95-102.

Edvardsen, C. (1999), "Water Permeability and Autogenous Healing of Cracks in Concrete," *ACI Materials Journal*, V. July-August, pp. 448-456.

Elices, M. (2004), "Influence of Residual Stresses in the Performance of Cold-Drawn Pearlitic Wires," *Journal of Materials Science*, V. 39 (12), pp. 3889-3899.

Elices, M., Cabllero, L., Valiente, A., Ruiz, J., and Martin, A. (2008), "Hydrogen Embrittlement of Steel for Prestressing Concrete: The FIP and DIBt Tests," *CORROSION* V. 64 (2), pp. 164-174.

Elsener, B., Addari, D., Coray, S., and Rossi, A. (2011), "Stainless Steel Reinforcing Bars – Reason for Their High Pitting Corrosion Resistance," *Materials and Corrosion*, V. 62 (2), pp. 111-119.

Ernst, P., Laycock, N. J., Moayed, M. H., and Newman, R. C. (1997), "The Mechanism of Lacy Cover Formation in Pitting," *Corrosion Science*, V. 39 (6), pp. 1133-1136.

Ernst, P., and Newman, R. C. (2002), "Pit Growth Studies in Stainless Steel Foils: Introduction and Pit Growth Kinetics," *Corrosion Science*, V. 44 (5), pp. 927-941.

Fagersta Stainless (2007), "Material Datasheet for SAF 2205 and SAF 2304," Fagersta Stainless AB, Fagersta, Sweden.

Federal Highway Administration (2006), "Status of the Nation's Highways, Bridges, and Transit: Report to Congress." FHWA, Washington, DC.

Femenia, M., Pan, J., Leygraf, C., and Luukkonen, P. (2001), "In Situ Study of Selective Dissolution of Duplex Stainless Steel 2205 by Electrochemical Scanning Tunnelling Microscopy," *Corrosion Science*, V. 43 (10), pp. 1939-1951.

FIP (1992), "Design Guide for Durable Concrete Structures," T. T. Publishers, ed., Comité Euro-International du Béton - Fédération Internationale du Béton, Lausanne, Switzerland.

Frankel, G. S. (1998), "Pitting Corrosion of Metals," *Journal of the Electrochemical Society*, V. 145 (6), pp. 2186-2198.

Frederiksen, J. M. (2009), "On the Need for More Precise Threshold Values for Chloride Initiated Corrosion," *Materials and Corrosion*, V. 60 (8), pp. 597-601.

Fu, Y., Lin, C. J., and Tsai, W. T. (2005), "A Study of The Selective Dissolution Behavior of Duplex Stainless Steel by Micro-Electrochemical Technique," *Acta Metallurgica Sinica*, V. 41 (3), pp. 302-306.

Garas, V. Y. (2009), "Multi-Scale Investigation of Tensile Creep of Ultra-High Performance Concrete for Bridge Applications," PhD Dissertation, Georgia Institute of Technology, Atlanta, GA.

García-Alonso, M. C., Escudero, M. L., Miranda, J. M., Vega, M. I., Capilla, F., Correia, M. J., Salta, M., Bennani, A., and González, J. A. (2007), "Corrosion Behaviour of New Stainless Steel Reinforcing Bars Embedded in Concrete," *Cement and Concrete Research*, V. 37, pp. 1463-1471.

Gardner, L. (2005), "The Use of Stainless Steel in Structures," *Progress in Structural Engineering and Materials*, V. 7 (2), pp. 45-55.

Griggs, R. D. (1987), "Structural Concrete in the Georgia Coastal Environment." Georgia Department of Transportation, Atlanta, GA.

Hamilton III, H. R. (2007), "St. George Island Bridge Pile Testing," Florida Department of Transportation, Tallahassee, FL.

Hansson, C. M. (2005), "Effects of High Performance Concrete on Corrosion of Reinforcement," Portland Cement Association, Skokie, IL.

Hansson, C. M., Poursaee, A., and Laurent, A. (2006), "Macrocell and Microcell Corrosion of Steel in Ordinary Portland Cement and High Performance Concretes," *Cement and Concrete Research*, V. 36, pp. 2098-2102.

Hartt, W. H. (2005), "Jobsite Evaluation of Corrosion Resistant Alloys for use as Reinforcement in Concrete," Florida Atlantic University, Dania Beach, FL.

Hartt, W. H. (2010), "Protocol for Projecting Time-to-Corrosion of Reinforcing Steel in Concrete Exposed to Chlorides," *CORROSION*, V. 66 (8), pp. 086002.

Hartt, W. H., Kumria, C. C., and Kessler, R. J. (1993), "Influence of Potential, Chlorides, pH, and Precharging Time on Embrittlement of Cathodically Polarized Prestressing Steel," *CORROSION*, V. 49 (5), pp. 377-385.

Hartt, W. H., and Nam, J. (2004), "Critical Parameters for Corrosion Induced Deterioration of Marine Bridge Substructures in Florida," Florida Atlantic University, Dania Beach, FL.

Hartt, W. H., Powers, R. G., Leroux, V., and Lysogorski, D. K. (2004), "Critical Literature Review of High-Performance Corrosion Reinforcements in Concrete Bridge Applications," Florida Atlantic University, Dania Beach, FL.

Heide, N. T. (2005), "Crack Healing in Hydrating Concrete." MS Thesis, Delft University of Technology, Delft, Netherlands.

Hill, A. T. (2006), "Material Properties of the Grade 300 and Grade 270 Prestressing Strands and Their Impact on the Design of Bridges," MS Thesis, University of Texas at Austin, Austin, TX.

Hooton, R. D., and Titherington, M. P. (2004), "Chloride Resistance of High-Performance Concretes Subjected to Accelerated Curing," *Cement and Concrete Research*, V. 34 (9), pp. 1561-1567.

Hurley, M. F., and Scully, J. R. (2006), "Threshold Chloride Concentrations of Selected Corrosion-Resistant Rebar Materials Compared to Carbon Steel," *CORROSION*, V. 62 (10), pp. 892-904.

Inst. Für Elektrochemie (2011), "Schematic of metal/electrolyte interface," http://www.uni-ulm.de/echem/index.html?id=1029002.

Insteel (2002), "1/2 inch 240ksi Stainless Steel Strand," Insteel Industries, Sanderson, FL.

Isecke, B. (1982), "Collapse of the Berlin Congress Hall Prestressed Concrete Roof," *Materials Performance*, V. (December), pp. 36-39.

Izumida, H., Kawabe, N., Takamura, S., Morita, H., and Murai, T. (2005), "Development of High-tensile-strength Stainless Steel Wire," *Sumitomo (SEI) Steel Wire Corp. Technical Review*, V. 60.

Jacobs, A., and Wozadlo, G. (1988). "Irradiation-Assisted Stress Corrosion Cracking as a Factor in Nuclear Power Plant Aging." Journal of Materials Engineering, V. 9 (4), pp. 345-351.

Jenkins, J. F. (1987), "Validation of Nitronic 33 in Reinforced and Prestressed Concrete," Naval Facilites Engineering Command, Jacksonville, FL.

Jones, D. A. (1996), Principles and Prevention of Corrosion, Prentice Hall, Upper Saddle River, NJ.

Knudson, A., and Skovsgaard, T. (1999), "The Optimal Use of Stainless Steel Reinforcement in Concrete Structures," Ramboll Arminox, Mønsted, Denmark.

Koch, G. H., Brongers, M. P. H., Thompson, N. G., Virmani, Y. P., and Payer, J. H. (2008), "Corrosion Costs and Preventive Strategies in the United States," National Association of Corrosion Engineers, Houston, TX.

Kurtis, K. E., and Mehta, K. (1997), "A Critical Review of Deterioration of Concrete Due to Corrosion of Reinforcing Steel." ACI Special Publication, V. 170, 535-554.

Landolt, D. (2007). Corrosion and Surface Chemistry of Metals, EPFL Press, Laussanne, Switzerland.

Li, L., and Sagues, A. A. (2002), "Chloride Corrosion Threshold of Reinforcing Steel in Alkaline Solutions - Cyclic Polarization Behavior," *CORROSION*, V. 58 (4), pp. 305-316.

Lv, Z. Q., Jiang, P., Wang, Z. H., Zhang, W. H., Sun, S. H., and Fu, W. T. (2008). "XRD Analyses on Dissolution Behavior of Cementite in Eutectoid Pearlitic Steel During Cold Rolling," *Materials Letters*, V. 62 (17-18), pp. 2825-2827.

Manera, M., Vennesland, Ø., and Bertolini, L. (2008), "Chloride Threshold for Rebar Corrosion in Concrete with Addition of Silica Fume," *Corrosion Science*, V. 50 (2), pp. 554-560.

Markeset, G. (2009), "Critical Chloride Content and its Influence on Service Life Predictions," *Materials and Corrosion*, V. 60 (8), pp. 593-596.

Markeset, G., Rostam, S., and Klinghoffer, O. (2006), "Guide for the Use of Stainless Steel Reinforcement in Concrete Structures," Norwegian Building Research Institute, Oslo, Norway.

Matta, Z. G. (1993), "More Deterioration of Concrete in the Arabian Gulf," *Concrete International*, V. (November), pp. 50-51.

Mehta, P. K. (1991), Corrosion in the Marine Environment, Elsevier Applied Science, New York, NY.

Mehta, P. K., and Monteiro, P. J. M. (2006), Concrete: Microstructure, Properties, and Materials, McGraw-Hill Companies Ltd., Columbus, OH.

Merello, R., Botana, F. J., Botella, J., Matres, M. V., and Marcos, M. (2003), "Influence of Chemical Composition on the Pitting Corrosion Resistance of Non-Standard Low-Ni High-Mn-N Duplex Stainless Steels," *Corrosion Science*, V. 45 (5), pp. 909-921.

Mietz, J. (2000), "Investigations on Hydrogen-Induced Embrittlement of Quench and Tempered Prestressing Steels," *Materials and Corrosion*, V. 51, pp. 80-90.

Mietz, J., Elsener, B., and Polder, R. (1997), Corrosion of Reinforcement in Concrete - Monitoring, Prevention, and Rehabilitation, The Institute of Materials, London, UK.

Milad, M., Zreiba, V., Elhalouani, F., and Baradai, C. (2008), "The Effect of Cold Work on Structure and Properties of AISI 304 Stainless Steel," *Journal of Materials Processing Technology*, V. 203 (1-3), pp. 80-85.

Moser, R. D., Holland, R. B., Kahn, L. F., Singh, P. M., and Kurtis, K. E. (2010). "Durability of Precast Prestressed Concrete Piles in Marine Environments: Reinforcement Corrosion and Mitigation - Part 1." Georgia Institute of Technology, Atlanta, GA.

Nabarro, F. R. N. (2001), "The Time Constant of Logarithmic Creep and Relaxation," *Materials Science and Engineering – A*, V. 309, pp. 227-228.

NACE (2008), "How Much Can a Bridge Take," National Association of Corrosion Engineers, Houston, TX.

Nawy, E. G. (2000), Prestressed Concrete - A Fundamental Approach, Prentice Hall, Upper Saddle River, NJ.

Newman, R. C. (2001), "2001 W.R. Whitney Award Lecture: Understanding the Corrosion of Stainless Steel," *CORROSION*, V. 57 (12), pp. 1030-1041.

Nilsson, L.-O. (2009), "Models for Chloride Ingress into Concrete - From Collepardi to Today," *International Journal of Modelling, Identification and Control*, V. 7 (2), pp. 129-134.

Nürnberger, U. (2002), "Corrosion Induced Failures of Prestressing Steels," *Otto-Graf Journal*, V. 13.

Nürnberger, U. (2003), "High Strength Stainless Steel - Alternative Materials for Tension Members in Civil Engineering," *Otto-Graf-Journal*, V. 14.

Nürnberger, U. (2009), "Hydrogen Induced Cracking of Prestressing Steel in Concrete Constructions," Proceedings of Eurocorr, Nice, France.

Nürnberger, U., and Wu, Y. (2005), "High-Strength Stainless Steel in Prestressed Concrete," Proceedings of the Workshop of COST 534 on NTD Assessment and New Systems in Prestressed Concrete Structures, Institute for Terotechnology, Radom, Poland.

Nürnberger, U., and Wu, Y. (2008), "Stainless Steel in Concrete Structures and in the Fastening Technique," *Materials and Corrosion*, V. 59 (2), pp. 144-158.

Osborn, A. E. N., Lawler, J. S., and Connolly, J. D. (2008), "Acceptance Tests for Surface Characteristics of Steel Strand in Prestressed Concrete," NCHRP, Washington, DC.

Outokumpu (2010), "Steel Grades, Properties, and Global Standards," Outokumpu Stainless, Avesta, Sweden.

Page, C., and Vennesland, Ø. (1983), "Pore Solution Composition and Chloride Binding Capacity of Silica-Fume Cement Pastes," *Materials and Structures*, V. 16 (1), pp. 19-25.

Papadakis, V. G., Vayenas, C. G., and Fardis, M. N. (1991), "Fundamental Modeling and Experimental Investigation of Concrete Carbonation," *ACI Materials Journal*, V. 88 (4), pp. 363-373.

Pfeifer, D. W. (2000), "High Performance Concrete and Reinforcing Steel with a 100-Year Service Life," *PCI Journal*, V. 45 (3), pp. 46-54.

Pourbaix, M. (1974), Atlas of Electrochemical Equilibria in Aqueous Solutions, National Association of Corrosion Engineers, Houston, TX.

Poursaee, A., and Hansson, C. M. (2009), "Potential Pitfalls in Assessing Chloride-Induced Corrosion of Steel in Concrete," *Cement and Concrete Research*, V. 39 (5), pp. 391-400.

Poursaee, A., and Hansson, C. M. (2007), "Reinforcing Steel Passivation in Mortar and Pore Solution," *Cement and Concrete Research*, V. 37 (7), pp. 1127-1133.

Presuel-Moreno, F., Scully, J. R., and Sharp, S. R. (2010), "Literature Review of Commercially Available Alloys That Have Potential as Low-Cost Corrosion-Resistant Concrete Reinforcement," *CORROSION*, V. 68 (8), pp. 1-13.

Proverbio, E., and Bonaccorsi, L. M. (2002), "Failure of Prestressing Steel Induced By Crevice Corrosion in Prestressed Concrete Structures," 9th International Conference on Durability of Materials and Components, Brisbane, Australia.

Raharinaivo, A. (2005), "Galvanised Carbon Steel Tendons," Proceedings of the Workshop of COST 534 on NTD Assessment and New Systems in Prestressed Concrete Structures, Institute for Terotechnology, Radom, Poland.

Rapoport, E., and Pleshivtseva, Y. (2006), Optimal Control of Induction Heating Processes, CRC Press, Boca Raton, FL.

Revie, R. W. (2000), Uhlig's Corrosion Handbook, John Wiley & Sons Inc., Hoboken, NJ.

Rodriguez, O. G., and Hooton, R. D. (2003), "Influence of Cracks on Chloride Ingress into Concrete," *ACI Materials Journal*, V. 100 (2), pp. 120-126.

Rossi, A., Tulifero, R., and Elsener, B. (2001), "Surface Analytical and Electrochemical Study on the Role of Adsorbed Chloride Ions in Corrosion of Stainless Steels," *Materials and Corrosion*, V. 52 (3), pp. 175-180.

Rourke, D. (2008), "Galvanized Rebar Resource Center," http://www.galvanizedrebar.com/.

Saadatmanesh, H., and Tannous, F. E. (1999), "Relaxation, Creep, and Fatigue Behavior of Carbon Fiber Reinforced Plastic Tendons," *ACI Materials Journal*, V. 96 (2), pp. 143-153.

Salas, R. M., Schokker, A. J., West, J. S., Breen, J. E., and Kreger, M. E. (2004), "Conclusions, Recommendations and Design Guidelines for Corrosion Protection of Post-Tensioned Bridges," Center for Transportation Research, Austin, TX.

Salas, R. M., Schokker, A. J., West, J. S., Breen, J. E., and Kreger, M. E. (2008), "Corrosion Risk of Bonded, Post-Tensioned Concrete," *PCI Journal*, V. 53 (1), pp. 89-107.

Sandberg, P., Tang, L., and Andersen, A. (1998), "Recurrent Studies of Chloride Ingress in Uncracked Marine Concrete at Various Exposure Times and Elevations," *Cement and Concrete Research*, V. 28 (10), pp. 1489-1503.

Sandvik (2008), "Duplex Stainless Steel - Springflex SH Datasheet," Sandvik Materials Technology, Sandviken, Sweden.

Schaeffler, A. L. (1949), "Constitution Diagram for Stainless Steel Weld Metal," Metals Progress, V. 56 (11), pp. 680.

Schießl, P., and Raupach, M. (1997), "Laboratory Studies and Calculations on the Influence of Crack Width on Chloride-Induced Corrosion of Steel in Concrete," *ACI Materials Journal*, V. 94 (1), pp. 56-62.

Schroeder, R. M., and Müller, I. L. (2003), "Stress Corrosion Cracking and Hydrogen Embrittlement Susceptibility of an Euctectoid Steel Employed in Prestressed Concrete," *Corrosion Science*, V. 45, pp. 1969-1983.

Schupack, M. (2001), "Prestressing Reinforcement in the New Millennium," *Concrete International*, V. 23 (12), pp. 38-45.

Schweitzer, P. A. (2003), Metallic Materials: Physical, Mechanical, and Corrosion Properties, Marcel Dekker Inc., New York, NY.

Semiatin, S. L., and Stutz, D. E. (1986), Induction Heat Treatment of Steel, American Society for Metals, Metals Park, Ohio.

Shah, K. P. (2011), "Case Hardening Methods," http://practicalmaintenance.net/?p=1543.

Shanina, B. D., Gavriljuk, V. G., Berns, H., and Schmalt, F. (2002), "Concept of a New High-Strength Austenitic Stainless Steel," *Steel Research International*, V. 73 (3), pp. 105-113.

Sharland, S. M. (1992), "A Mathematical-Model of the Initiation of Crevice Corrosion in Metals," *Corrosion Science*, V. 33 (2), pp. 183-201.

Shirahama, S., Fang, S., Kobayashi, T., and Miyagawa, T. (1999), "Basic Properties of Duplex Stainless Prestressing Steel and Flexural Behaviors of Prestressed Concrete Beams Using the Tendon," *Journal of the Society of Materials Science of Japan*, V. 48 (10), pp. 1199-1206.

Shyr, T. W., Shie, J. W., Huang, S. J., Yang, S. T., and Hwang, W. S. (2010), "Phase Transformation of 316L Stainless Steel from Wire to Fiber," *Materials Chemistry and Physics*, V. 122 (1), pp. 273-277.

Simmons, J. W. (1996), "Overview: High-nitrogen alloying of stainless steels," *Materials Science and Engineering – A*, V. 207 (2), pp. 159-169.

Skorchelletti, V. V. (1976), Theory of Metal Corrosion, Israel Program for Scientific Translations, Jerusalem, Israel.

Stein, G., and Witulski, H. (1990), High Nitrogen Steels, Verlag Stahleisen GmbH, Aachen, Germany.

Suzuki, T., Kojima, H., Suzuki, K., Hashimoto, T., and Ichihara, M. (1977), "Experimental-Study of Martensite Nucleation and Growth in 18-8 Stainless-Steel," *Acta Metallurgica*, V. 25 (10), pp. 1151-1162.

Tavares, S. S. M., da Silva, M. R., Pardal, J. M., Abreu, H. F. G., and Gomes, A. M. (2006), "Microstructural Changes Produced by Plastic Deformation in the UNS S31803 Duplex Stainless Steel," *Journal of Materials Processing Technology*, V. 180 (1-3), pp. 318-322.

Thangavel, K., and Rengaswamy, N. S. (1998), "Relationship Between Chloride / Hydroxide Ratio and Corrosion Rate of Steel in Concrete," *Cement and Concrete Composites*, V. 20, pp. 283-292.

Thomas, M. D. A., Bamforth, P. B., and Banerjee, M. K. (1999), "Modeling Chloride Diffusion in Concrete Effect of Fly Ash and Slag," *Cement and Concrete Research*, V. (29), pp. 487-495.

Trejo, D., Monteiro, P. J. M., Ben C. Gerwick, J., and Thomas, G. (2000), "Microstructural Design of Concrete Reinforcing Bars for Improved Corrosion Performance," *ACI Materials Journal*, V. 97 (1), pp. 78-84.

Trejo, D., and Pillai, R. G. (2004), "Accelerated Chloride Threshold Testing – Part II: Corrosion-Resistant Reinforcement," *ACI Materials Journal*, V. 101 (1), pp. 57-64.

Trejo, D., Pillai, R. G., Hueste, M. B. D., Reinschmidt, K. F., and Gardoni, P. (2009), "Parameters Influencing Corrosion and Tension Capacity of Post-Tensioning Strands," *ACI Materials Journal*, V. 106 (2), pp. 144-153.

Ugiansky, G. M., and Payer, J. H. (1977), Stress Corrosion Cracking - The Slow Strain-Rate Technique, American Society for Testing and Materials, West Conshohocken, PA.

Virmani, Y. P., and Clemena, G. G. (1998), "Corrosion Protection: Concrete Bridges," Turner-Fairbank Highway Research Center, McLean, VA.

Wensley, A., and Dykstra, H. (1997), "Corrosion of Bleach Washers." *Pulp and Paper – Canada*, V. 98 (9), pp. 40-42.

Wierig, H. J. (1984), "Long-Time Studies on the Carbonation of Concrete Under Normal Outdoor Exposure," Proceedings of the RILEM Seminar on Durability of Concrete Structures Under Normal Outdoor Exposure, Hannover, Germany.

Wu, Y., and Nürnberger, U. (2009), "Corrosion-Technical Properties of High-Strength Stainless Steels for the Application in Prestressed Concrete Structures," *Materials and Corrosion*, V. 60 (10), pp. 771-780.

Zhang, P., Wittmann, F. H., Zhao, T., and Lehmann, E. H. (2010), "Neutron Imaging of Water Penetration into Cracked Steel Reinforced Concrete," *Physica B*, V. 405 (7), pp. 1866-1871.

VITA

ROBERT D. MOSER

Robert Moser was born on May 19th, 1985 in Stuart, Florida. He graduated from Towns County High School in Hiawassee, Georgia in 2003. Robert attended Young Harris College from 2003 to 2005. In 2007, he graduated with a B.S. in Civil Engineering from the Georgia Institute of Technology in Atlanta, GA. Following his undergraduate studies, Robert began conducting graduate research at the Georgia Institute of Technology, receiving an M.S. in Civil Engineering in 2009 and Ph.D. in Civil Engineering in 2011, both with an emphasis on Structural Engineering and Materials Science. Robert is currently employed as a Research Civil Engineer in the Geotechnical and Structural Laboratory of the U.S. Army Engineer Research and Development Center.